PARAMETRIC DYNAMIC LOAD PREDICTION OF A NARROW GAUGE

ROCKET SLED

BY

JOHN SCOTT FURLOW, B.S., M.S.

A dissertation submitted to the Graduate School

in partial fulfillment of the requirements

for the degree

Doctor of Philosophy, Engineering

Specialization in: Mechanical Engineering

New Mexico State University

Las Cruces, New Mexico

December 2006

Report Documentation Page		*Form Approved* *OMB No. 0704-0188*

Public reporting burden for the collection of information is estimated to average 1 hour per response, including the time for reviewing instructions, searching existing data sources, gathering and maintaining the data needed, and completing and reviewing the collection of information. Send comments regarding this burden estimate or any other aspect of this collection of information, including suggestions for reducing this burden, to Washington Headquarters Services, Directorate for Information Operations and Reports, 1215 Jefferson Davis Highway, Suite 1204, Arlington VA 22202-4302. Respondents should be aware that notwithstanding any other provision of law, no person shall be subject to a penalty for failing to comply with a collection of information if it does not display a currently valid OMB control number.

1. REPORT DATE **DEC 2006**	2. REPORT TYPE **N/A**	3. DATES COVERED **-**	
4. TITLE AND SUBTITLE **Parametric Dynamic Load Prediction of a Narrow Gauge**		5a. CONTRACT NUMBER	
		5b. GRANT NUMBER	
		5c. PROGRAM ELEMENT NUMBER	
6. AUTHOR(S)		5d. PROJECT NUMBER	
		5e. TASK NUMBER	
		5f. WORK UNIT NUMBER	
7. PERFORMING ORGANIZATION NAME(S) AND ADDRESS(ES) **New Mexico State University Las Cruces, NM**		8. PERFORMING ORGANIZATION REPORT NUMBER	
9. SPONSORING/MONITORING AGENCY NAME(S) AND ADDRESS(ES)		10. SPONSOR/MONITOR'S ACRONYM(S)	
		11. SPONSOR/MONITOR'S REPORT NUMBER(S)	
12. DISTRIBUTION/AVAILABILITY STATEMENT **Approved for public release, distribution unlimited**			
13. SUPPLEMENTARY NOTES			
14. ABSTRACT			
15. SUBJECT TERMS			

16. SECURITY CLASSIFICATION OF:			17. LIMITATION OF ABSTRACT **SAR**	18. NUMBER OF PAGES **261**	19a. NAME OF RESPONSIBLE PERSON
a. REPORT **unclassified**	b. ABSTRACT **unclassified**	c. THIS PAGE **unclassified**			

Standard Form 298 (Rev. 8-98)
Prescribed by ANSI Std Z39-18

"Parametric Dynamic Load Prediction of Narrow Gauge Rocket Sleds," a dissertation prepared by John Scott Furlow in partial fulfillment of the requirements for the degree, Doctor of Philosophy, Engineering, has been approved and accepted by the following:
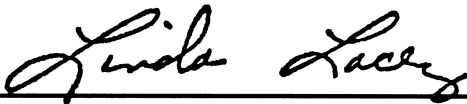
_____ 10/10/06

Linda Lacey

Dean of the Graduate School

_____

Gabe V. Garcia

Chair of the Examining Committee

_____

Date

Committee in charge:

     Dr. Gabe V. Garcia, Chair

     Dr. Michael D. Hooser

     Dr. David V. Jáuregui

     Dr. Ou Ma

     Dr. Young H. Park

DEDICATION

This work is dedicated to all my family most especially my wife, Debbie, and children, Steven and Morgan, as they were the ones who truly sacrificed for the completion of this work. This work is also dedicated to the promise of God as: 'No eye has seen, no ear has heard, no mind has conceived what God has prepared for those who love Him.' 1 Cor 2:9.

ACKNOWLEDGEMENTS

VITA

March 19, 1975   Born in Lubbock, Texas

1993   Graduated from Brownfield High School,

                        Brownfield, Texas

1997   Bachelor of Science, Mechanical Engineering,

                        Texas Tech University

1999   Master of Science, Mechanical Engineering,

                        Texas Tech University

1999-Present   Mechanical Engineer, United States Air Force,

                        Holloman Air Force Base, New Mexico

PROFESSIONAL AND HONORARY SOCIETIES

AIAA

Tau Beta Pi

Pi Tau Sigma

PUBLICATIONS

Furlow, J. S. and James, D. L., Convective Heat Transfer Characteristics from Combined Mechanical and Supply Pulsed Radial Reattaching Jets, International Journal of Heat and Fluid Flow, Accepted for Publication 8 February 2006.

Furlow, J.S. and James, D.L., Local Instantaneous Convective Heat Transfer Characteristics of Radial Reattaching Nozzles, 33rd National Heat Transfer Conference, Albuquerque, NM, NHTC99-151, August, 1999.

ABSTRACT

PARAMETRIC DYNAMIC LOAD PREDICTION OF A NARROW GAUGE

ROCKET SLED

BY

JOHN SCOTT FURLOW, B.S., M.S.

Doctor of Philosophy, Engineering

Specialization in Mechanical Engineering

New Mexico State University

Las Cruces, New Mexico, 2006

Dr. Gabe V. Garcia, Chair

Dynamic load prediction of rocket sleds has been of interest to sled designers and analysts since the inception of the Holloman High Speed Test Track, (HHSTT). Dynamic loading along with thrust and aerodynamic loading is a primary contributor to sled design load cases. Dynamic loading comes directly from the rocket sled

traversing the gap between the slipper and rail and the resulting sliding impacts. The current study investigates the prediction of narrow gauge sled dynamic loads by applying a systematic process of modeling validation, design parameter variation and dynamic load correlation.

Numerical modeling was employed to simulate the Land Speed Record (LSR) test and the model data was validated by comparing it to the data taken from the sled during the LSR test. Modeling methods validated against the test data were applied to a reduced complexity narrow gauge sled representing a generic version of the LSR sled. Design parameters were identified that contributed to the generation of dynamic loading. The design parameters are: sled mass, slipper gap, vertical rail roughness, lateral rail roughness, vertical sled natural frequency, lateral sled natural frequency, torsional sled natural frequency, and sled velocity. Peak dynamic load results (from evaluating the reduced complexity model while varying the design parameter values over high, low, and typical ranges) were computed at the sled center of Gravity (CG). This peak dynamic loading, η force, constituted the dynamic load prediction. The correlation of η to its respective design parameters showed that a multivariate interpolation method was the most accurate method to relate η force to its respective design parameters. The study revealed a heavy dependence of dynamic load on velocity, rail roughness, slipper gap, and translational sled natural frequencies. The study also showed a favorable comparison of η force prediction over previously used methods at the HHSTT.

TABLE OF CONTENTS

LIST OF TABLES

xvii

LIST OF FIGURES

1. INTRODUCTION

The Holloman High Speed Test Track (HHSTT) propels test items along a steel rail using rocket sleds. This range of test items and test velocities is very broad. Typical test items include aircraft egress systems, aerothermal test samples and ballistic impact items. Test velocities range from static, 0 feet per second (fps), to hypersonic in ground level air. A sled is a structure designed to interface with a payload while being propelled by a rocket motor and its trajectory is controlled by slippers whose inside profiles are slightly larger than the rail over which it slides. This profile difference is shown in Figure 1.1 and allows the sled to fly through the slipper gap should impact, inertia, and/or lift forces incline the sled to do so. Three distinct sled configurations are used: monorail, dual rail wide gauge, and dual rail narrow gauge. Of the three, the narrow gauge configuration has been used most recently for high velocity impact tests and was the configuration used to set the current land speed record, Figure 1.2.

1.1 Existing Theory

Since the inception of the HHSTT in 1950, sled designers have sought to accurately predict structural loading experienced by the sled as it moves down the track. The accepted design process is to hold the sled in dynamic equilibrium at significant events during the sled test and analyze force and stress distribution throughout the sled. Significant events have been identified from measurements and

1

Figure 1.1 Slipper Rail Interaction
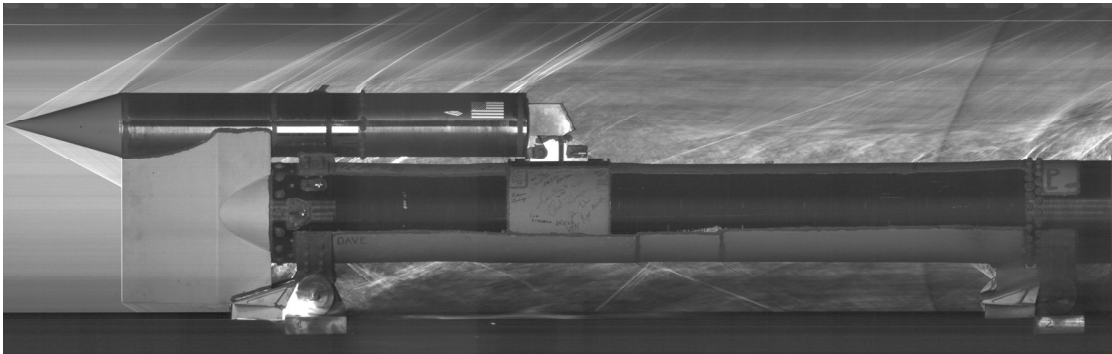
Figure 1.2 Hypersonic Narrow Gauge Sled

represent design conditions that reduce the infinite number of possible time steps during a test to about seven cases. This allows a designer to define load conditions and then choose extreme design load cases to begin structural analysis. Design loads are divided into two categories, quasi-steady-state and dynamic. Quasi-steady-state loading is defined as loading that is well defined in magnitude and time of application. This loading type, although time varying, may be applied at instants in time as if essentially static with an applicable dynamic load factor to compensate for its application time. Examples of this loading type are aerodynamic, thrusting, inertial, and braking. Dynamic loading is defined as loading due to flexible body interaction, slipper/rail interface, and rocket motor transients. Dynamic loading for the current design process is applied as a static load factor, λ units of gs, through the Center of Gravity (CG) of the free body diagram or as an acceleration vector in a Finite Element Model (FEM). This process allows design engineers to quickly analyze a design using static sled models. A quick process is needed since during the course of a design cycle the analysis is typically performed several times on converging iterations of the final sled design.

1.1.1 Lambda, λ

Dynamic load prediction on rocket sleds has a history as long as the HHSTT itself. The earliest organized effort was accomplished by the Interstation Supersonic Track Conference Structures Working Group, ISTRACON, in 1961 with the publishing of the ISTRACON handbook (ISTRACON Handbook 1961). This

handbook comprehensively detailed track testing among the major test tracks of the United States and recommended using 'Rail Roughness Load Factor' (ISTRACON Handbook, 1961, p. 4-1-19), λ, to account for the rail roughness effects imparted to the sled. It was defined as a function of velocity only and applied to the sled CG. This was the first statement of the dual rail λ factor and its original intent to account for rail roughness. In the development of λ, very basic load measurements were taken for a wide range of speeds for different sled designs as shown in, Figure 1.3. Typically a load sensor, force transducer or strain gage, was placed somewhere on a sled and the reaction forces were measured and recorded during the course of a sled test. To analyze the force data, known forces were then applied to a sled free body diagram in static equilibrium for a given fixed time step. The forces measured at different points on the sled were balanced and any unbalance was corrected by applying a force at the CG to bring the forces back into equilibrium. The force applied to the CG was divided by the sled weight and the resulting value was termed λ. Monorail λ factor loading was first documented by Mixon (1971) where a few measured data points were reported. The monorail λ factor was shown to be significantly higher than dual rail λ factor. Narrow gauge λ factor was first stated by Krupovage, Mixon & Bush (1985) and studied in the context of a damped sled test by Hooser (1989). The listing by Krupovage et al. (1985) was a simple fit of narrow gauge λ factor essentially halfway through that of the monorail and dual rail wide gauge λ values as seen in Figure 1.4. This methodology was loosely confirmed

4

through one sled test by Hooser (1989). In all three sled configurations lateral values

of λ were prescribed as 0.6 of vertical λ values.

1.1.2 SIMP/SLEDYNE

The absence of known dynamic load data combined with the need for high

velocity testing prompted Mixon (1971) to undertake his work in the area of high

fidelity modeling of monorail sleds which began the next significant area of dynamic

load prediction: transient FEM modal analysis. Transient FEM modal analysis is a

numerical method where rocket sled flexibility is represented as a modal model and

excited by traversing a section of rough rail. The interaction between the sled and rail
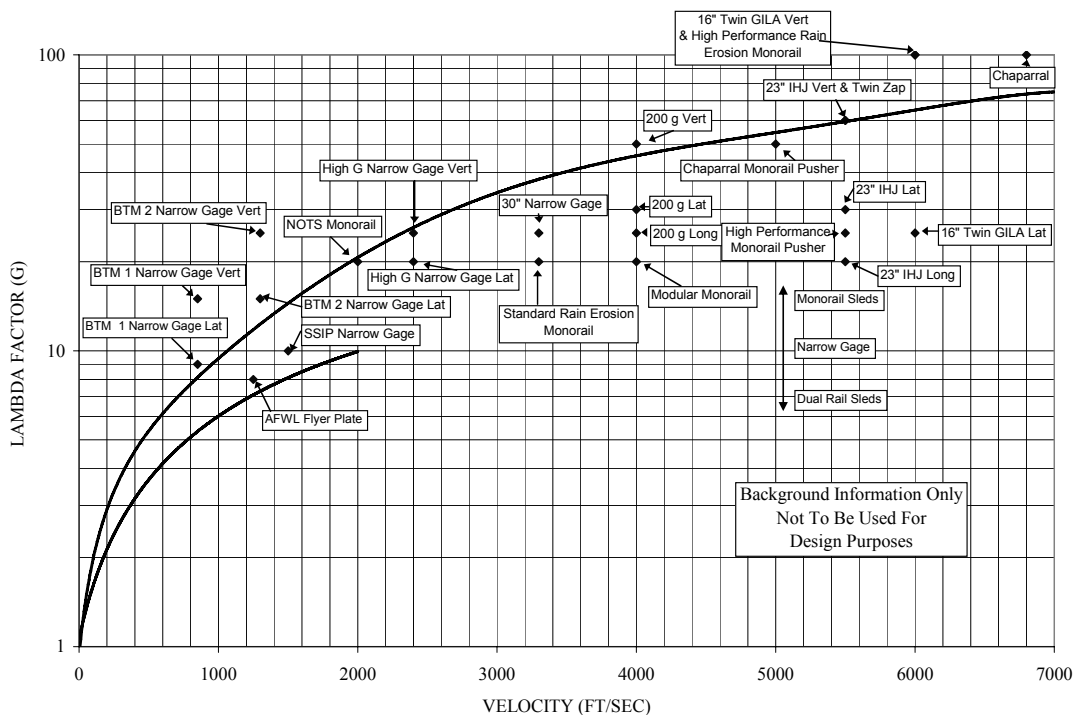
Figure 1.3 λ vs. Velocity with Measured Sled Data (Mixon and Hooser 2002)
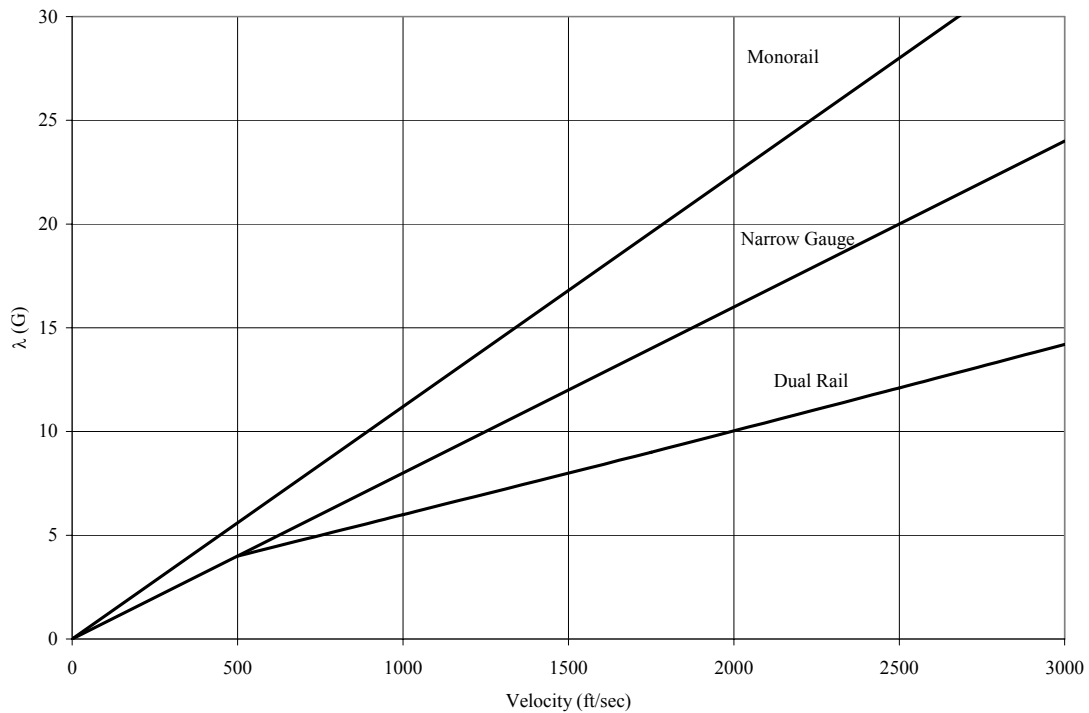
Figure 1.4 λ vs. Velocity

is approximated by using a coefficient of restitution formation (Abbot 1967) or

stiffness and damping formation (Mixon 1971; Greenbaum, Garner & Platus 1973;

Tischler, Venkayya & Palazotto 1981). Typically, a flexible modal model of a rocket

sled is loaded with thrust and drag as it travels along the rough rail profile (Abbot

1967; Greenbuam et al. 1973; Tischler et al. 1981). Mixon (1971) divided the

problem into two parts; the first part consists of a rigid body representation of a sled

that traverses the rough rail generating a force time history at each slipper. In the

second part, the force time histories are applied to a flexible modal model of the

rocket sled to generate force time histories at discretized sled masses. All of the

preceding methods utilized surveyed rail roughness data in only the vertical direction;

6

monorail sleds were studied by Abbot (1967), Mixon (1971), and Greenbaum et al. (1973) and wide gauge dual rail sleds were analyzed by Mixon (1971), Greenbaum et al. (1973), and Tischler et al. (1981). Transient FEM modal analysis was shown to produce inertial loading that was verified with corresponding sled tests for vertical and pitching motion. Mixon (1971) used a measurement scheme where a custom transducer was built into the front and aft slippers of the sled. This transducer featured three self-compensated strain gage bridges which made it possible to directly measure the vertical and lateral force and pitching moment. The force data was used to correlate a mathematical model in the time and frequency domains. However, the computational and rail survey limitations that existed over 20 years ago prevented any large scale design parameter variations and subsequent correlation. The only studies that sought to significantly study parameter variation were those by Greenbaum et al. (1973) and Tischler et al. (1981). The work by Greenbaum et al. (1973), a published software package SLEDYNE, was parametrically varied to produce Sled IMpact Parameter (SIMP) which used a series of slipper impact velocity estimates, sled mass, and vertical stiffness to produce a SIMP factor and ultimately a maximum slipper force. SIMP has two major drawbacks: it uses only 400 feet of vertical rail roughness data and does not correlate well to sled test data in the lateral degree of freedom. The parametric study of a dual rail wide gauge sled by Tischler et al. (1981) utilized SLEDYNE and a statistical representation of rail roughness while varying slipper beam stiffness This study did not present any correlation between peak loading and design parameters.

1.1.3 Numerical Integration of Equations of Motion, NIEOM

Recently dynamic sled prediction has advanced where modeling was improved by incorporating higher fidelity models which utilize more design parameters and more detailed rail survey information by using Numerical Integration of Equations of Motion (NIEOM). This method utilizes a numerical solution of the equations of motion as generated by a commercial-off-the-shelf-package, in this case Dynamic Analysis and Design System (DADS) (Hooser 2000, 2002b, Hooser and Schwing 2000), to produce displacement, velocity, acceleration, forces, and moments at each discretized mass. Rail roughness was defined in the vertical and lateral directions using actual survey data for the length of rail the sled will traverse. Slipper impacts were approximated using Hertzian contact theory, coefficient of restitution, or springs and dampers. NIEOM has been successfully used to verify numerical predictions with measured sled test data on monorail sleds (Hooser and Schwing 2000) and for narrow gauge sleds (Hooser 2002b; Minto 2004, 2002, 2000). Sleds may be modeled as Spring Mass Damper (SMD) systems (Hooser and Schwing 2000, Hooser 2002b, Furlow 2004), imported modal representations (Furlow 2004), or combinations of both. DADS has been shown to match favorably to other numerical solutions for a basic step loaded cantilever beam by Furlow (2004) and in approximating small deflections of a vibrating nonlinear flexible body by Eskridge (1998).

1.2 Limitations of Current Methods

HHSTT design engineers are currently using λ generated dynamic loads (Krupovage, Mixon & Bush 1991) even though a significant amount of work has been done to study the nature and parameters influencing dynamic loading. The primary reason for this occurrence is the basic one step process associated with λ factor as opposed to an advanced empirical method such as SIMP. Also computational studies such as SLEDYNE rely on computing platforms and FEM code that is no longer operational and custom computer codes have been lost or are no longer functional. Additionally the λ method has proven to be successful in many past sled designs. However, Mixon (1971), Mixon and Hooser (2002), and Hooser (1989) have shown that, for certain sled configurations, λ under predicts measured dynamic loading. This is best demonstrated in a focused look at monorail and narrow gauge λ data versus sled test data as shown in Figures 1.5 and 1.6. The intent of λ was to bound the highest dynamic values. In Figures 1.5 and 1.6, it can be seen that λ significantly under predicts dynamic loading in some cases and over predicts in others. Also in many cases the widely used ratio of lateral to vertical λ of 0.6 is not present. The sensitivity of dynamic loading to design parameter variation was investigated numerically by Nedimovic (2004), and sensitivity to changes in rail roughness, slipper gap, and slipper beam stiffness were documented through a limited design parameter study in DADS for a hypersonic narrow gauge sled. Even though the λ method in the past has been successful, it does not account for all significant

9

design parameters nor does it produce optimized sled designs. Mixon and Hooser (2002) attribute its success to overly conservative material safety factors and assumed worst case load conditions that compensate for its lack of specific accuracy.

1.3 Problem Statement

Sled designers need a dynamic load prediction tool that is easily applied while maintaining accuracy over the range of significant design parameters. The λ factor method is extremely efficient and easily used but does not account for sled design parameters other than velocity and mass where it has been shown experimentally
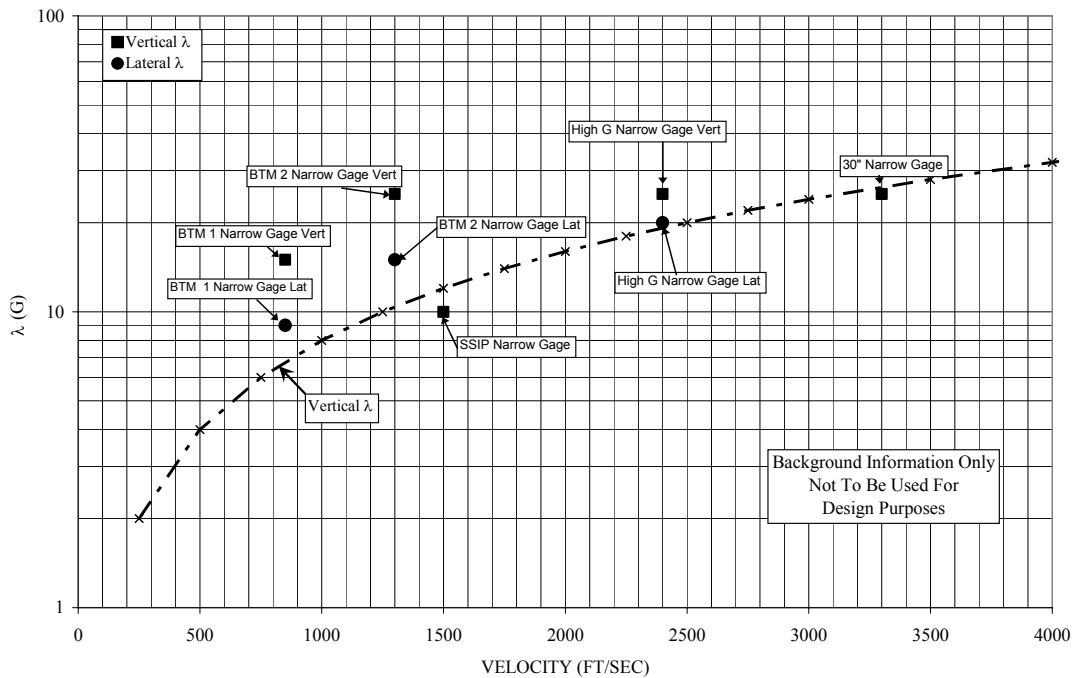
Figure 1.5 Narrow Gauge λ Compared to Sled Tests
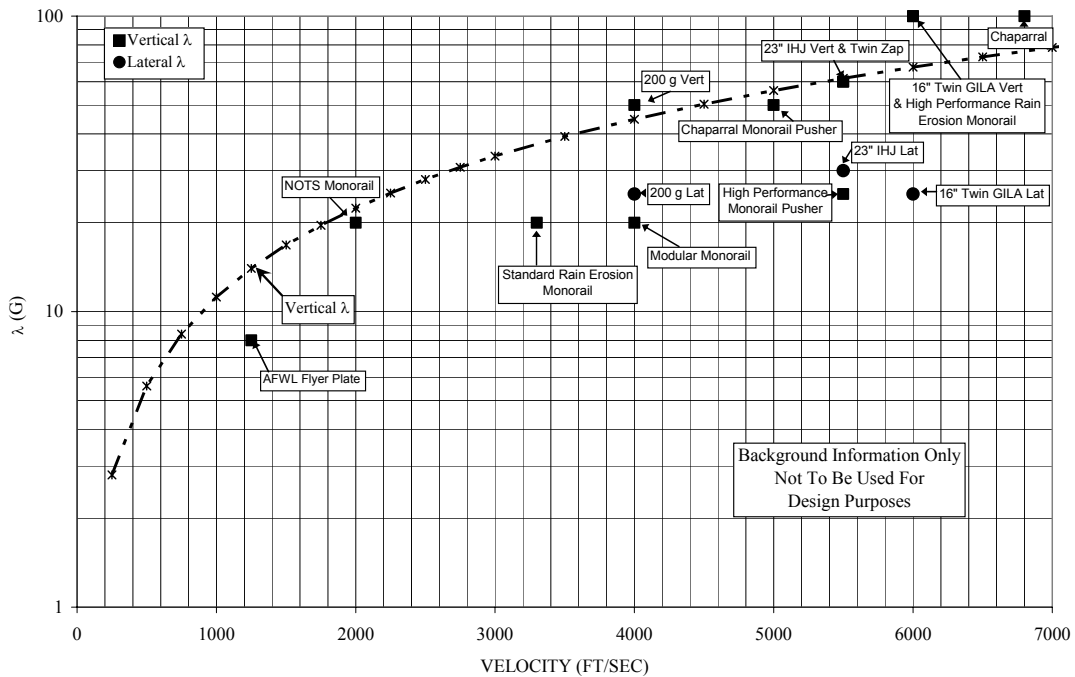
Figure 1.6 Monorail λ Compared to Sled Tests

(Mixon 1971, Hooser 1989, ISTRACON 1961) and numerically (Nedimovic 2004) that slipper gap, sled flexibility, slipper/rail interaction, and rail roughness are also significant and worthy of inclusion. Previous numerical and experimental attempts to produce a dynamic load prediction tool have not thoroughly accounted for a broad spectrum of design parameters since computational tools were not adequate or the sheer number of experimental data points was impossible to obtain. The use of a validated numerical model as a platform to conduct large scale parameter variation studies solves the initial problem of obtaining a large enough sample of dynamic load data. The next step, to produce a dynamic load prediction tool, is to correlate the numerical data to the sled design parameters. Finally the development of a factor or

11

load to be applied at the sled CG in the manner of λ must be completed. A design

prediction tool which marries the efficiency of λ with the robustness of a detailed

wide ranging numerical study would produce an efficient and accurate tool which

would ultimately make HHSTT sled designs more optimized and reliable thus

reducing cost and increasing performance.

2. DYNAMIC LOAD PREDICTION OF NARROW GAUGE SLEDS

Rocket sled dynamic load prediction in its various forms from λ (ISTRACON 1961), to SLEDYNE/SIMP (Mixon 1971; Greenbaum, Garner & Platus 1973; Tischler, Venkayya & Palazotto 1981) to NIEOM (Hooser 2000, 2002b, Hooser and Schwing 2000) has at its core the goal to make use of known values in order to accurately extrapolate or interpolate to unknown values of design parameters and associated loading. The successful characterization of known dynamic loads serves as a verification process tool for a prediction tool. The characterization criteria have varied with each method and were heavily dependent upon the measurement technology available at that time.

2.1 Narrow Gauge Sled Dynamic Load Prediction

Dynamic load prediction is necessary and essential for a sled designer. The intense dynamic environment generates significant loading in comparison to aerodynamic, thrusting and braking loads. The current method to generate a dynamic load, which is applied statically on a sled representation in dynamic equilibrium, is depicted in Figure 2.1. The dynamic load is applied to the sled CG and reacted by the front and aft slippers. The generation and utilization of this dynamic load comes from one of the three methods currently employed at the HHSTT, with λ being the most common.
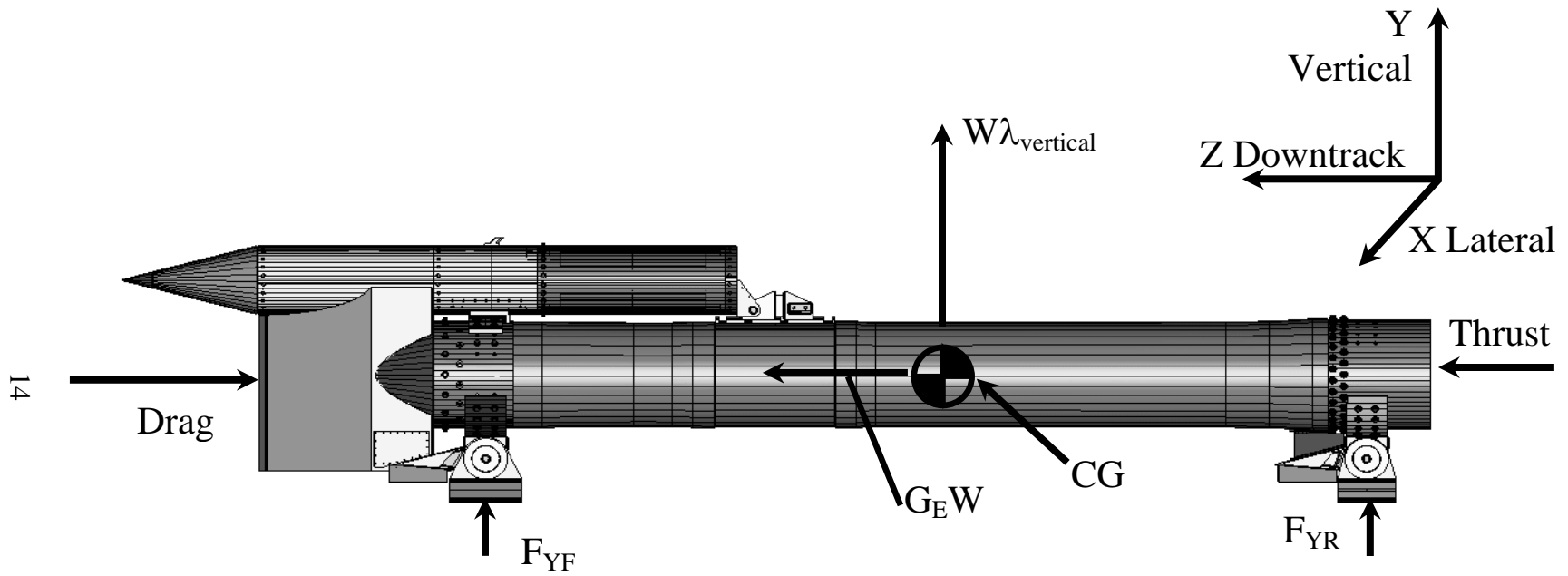
Figure 2.1 Application of Vertical λ to a Narrow Gauge sled

The application of λ involves the calculation of the λ factor from the appropriate value (monorail, narrow gauge, or dual rail) and applying the factor to the mass of the sled. Early on in its formation, λ was applied only at the sled CG. With wide spread use of FEM, λ has been applied as an acceleration vector to all masses in a linear static model.

The development of SLEDYNE and SIMP (Mixon 1971; Greenbaum et al. 1973; Tischler et al. 1981) was a more involved process where initial verification was performed by Mixon (1971). Subsequent development of SLEDYNE and SIMP relied heavily on the initial work performed by Mixon and ultimately came full circle with the publishing of SIMP factors (Greenbaum et al. 1973, Krupovage, Mixon & Bush 1991) and the implementation of SLEDYNE at the HHSTT.

The application of SIMP is for preliminary design and is a two step process. The first step involves the estimation of a slipper impact velocity based on lift-to-weight and effective impact frequency. In the second step, the impact velocity is then applied to a SIMP chart or equation resulting in the calculation of a maximum force located at the slipper beam is calculated (Greenbaum et al. 1973, Krupovage et al. 1991). SLEDYNE is a more involved extension of SIMP and utilizes a modal representation of the sled and then outputs loads at slipper beams for analysis (Greenbaum et al. 1973, Krupovage et al. 1991). SLEDYNE considers the test conditions for a FEM generated flexible body where SIMP is a rough estimate of the same for a rigid body. Both methods are well correlated in the vertical direction.

NIEOM utilizes a flexible structural representation of a sled traversing a

15

rough rail. This dynamic loading calculation method is verified using an array of measurement points located across a sled that include accelerometers, force transducers, and strain gages. The verification of this method is detailed in Chapter 4 and can be summarized as a comparison of standard deviation in the time domain and spectral power over a range of banded frequencies. Load prediction from this method is accomplished by first constructing a verified model and then varying its design parameters to represent the design in question. Maximum loading and acceleration at critical structural components is the main output of this method and it is most useful to the dynamic equilibrium analysis methods utilized by sled designers.

2.2 Selection of Dynamic Load Prediction Method

In comparing the currently available dynamic load prediction methods, λ, SIMP, and NIEOM, the most easily applied is the λ factor method where the most accurate is NIEOM. The method that is the most efficient in extrapolation and interpolation between design parameter values is SIMP as more design parameters have been factored into its parametric study. The NIEOM method represents an accurate method of modeling to study, in depth, the behavior of the sled. However its current implementation in DADS proves to be cumbersome for the design process.

Considering the strengths and weaknesses of the methods developed over the existence of the HHSTT, a reasonable choice of a dynamic load prediction tool is one that is as easily applied as λ and as accurate as NIEOM. The feature that makes λ not as robust or comprehensive in its accuracy is that it is not based on the results of a

limited number of sled tests where design parameters have not varied greatly. The

parameter variation begun with the development of SIMP lends itself to the idea that

the required sled tests can be performed by numerical simulation using NIEOM and a

robust load prediction tool produced with the proper analysis of the design parameters

and resulting loads. The load prediction tool selected for this study is NIEOM where

its results are to be studied and manipulated into a form that can be applied as easily

as λ.

2.3 Development of Dynamic Load Prediction Method

The development of this new method entails the following tasks: 1)

Construction and validation of a DADS model using reasonable engineering

judgment, valid assumptions, and detailed structural characteristics of a representative

sled test where suitable data exists. 2) Wide scale design parameter variation to

perform many numerical simulations of sled tests. 3) Correlation of contributing

design parameters to dynamic loading outputs; and 4) Evaluation of design tool

effectiveness compared to previous methods.

2.3.1 Construction and Validation of DADS Model

This initial task is essential to the success of the method since methodology

developed in the construction and validation of the representative model will

propagate throughout the entire effort. The representative sled test for this work is

the Land Speed Record (LSR) test conducted 30 April 2003 at the HHSTT where a

narrow gauge forebody achieved a peak velocity of 9,465 fps. Suitable data was

recorded for this test and has been studied in depth along with very detailed

aerodynamic and structural information regarding the forebody sled. Also used in

this effort was a developmental Coast Out (CO) sled test of the same forebody where

suitable data was collected during the peak velocity of 5,343 fps and subsequent coast

out.

2.3.2 Wide Scale Design Parameter Variation

This portion of the dynamic load prediction effort involves identifying design

parameters and documenting a reasonable range for each parameter consisting of a

high, middle, and a low value. The parameter variation will be divided into two

steps. The first step is to assign all design parameters a middle value and document

the peak dynamic force at the sled CG. Then each parameter will be varied

independently to its high and low value. The change of the peak dynamic output at

the sled CG with respect to the middle value will be used to establish the influence

that each design parameter has on peak dynamic load. A suitable threshold will be

established and all parameters whose change is above the threshold will be deemed

contributing and will be retained in the next step, all others will be deemed

noncontributing and will not be considered in the next step. Also at this point any

groupings or nondimensional combinations of parameters should be identified. This

approach has two advantages. The first advantage is that the relationships that might

exist between parameters will give more insight into their influence. The second

advantage is that nondimensional grouping of design parameters may reduce the total number of numerical simulations in the subsequent step of design parameter variation.

The next step of design parameter variation is to vary all remaining parameters through their high, middle, and, low values for all combinations. The peak dynamic loading output associated with the sled CG and slippers will be recorded along with design parameter values. It should be noted that from previous work (ISTRACON 1961, Mixon 1971, Greenbaum et al. 1973, Hooser 1989, Hooser 2000, 2002, Nedimovic 2004) that velocity is a design parameter. Its variation is inherent in every sled run as a sled begins at rest and approaches its maximum velocity over a continuum of velocity values.

2.3.3 Correlation of Design Parameters to Dynamic Loading Outputs

This effort uses the peak dynamic loading values recorded in the previous task to build a relationship between model inputs (design parameters) and outputs (peak dynamic loading) at the sled CG. This relationship is the core of the dynamic load prediction tool and will be utilized by the design engineer to predict dynamic loading for the force/stress analysis in the sled design process. Care should be taken to ensure that the prediction tool does not produce unreasonable values at interpolated or extrapolated points between design parameters.

2.3.4 Evaluation of Design Tool Effectiveness Compared to Previous Methods

This task will document a basic comparison of a typical design where the dynamic load will be generated by the new tool and previous methods, SIMP and λ. The dynamic load values themselves will be compared and then the effect on overall sled design will be noted. It is worth noting that weight, high speed sled design, is the primary design driver. A reduction in weight allows higher velocity and more flexible sleds which in turn produce lower loads and ultimately less stress than their more rigid and heavier counterparts.

3. DEVELOPMENT OF NARROW GAUGE SLED MODEL

The narrow gauge sled model was developed in DADS to replicate the propulsive LSR and CO forebody sleds. The methodology employed was to construct the sled from the same information available to the design engineer using drawings (DWG 2002E37504), Computer Aided Design (CAD) models, and vibration test results. Since the sled in question has been tested several times and studied in depth during its development, there was a large amount of data available to characterize the major sled components. The ultimate goal of the DADS modeling effort was an accurate numerical model of the sled in Figure 3.1 and served as the starting and ending point for model development. The initial effort was to identify all functional aspects of the sled. Several novel design concepts were employed on this particular sled: weight and moment optimized slipper beams, lateral vibration isolation on slipper beams, composite rocket motor case, slipper anti-rotation, lateral and downtrack vibration isolation on the payload. Also the interior contact surface of all slippers was configured to disallow any contact between the slipper and the interior surface of the rail. Thus all lateral contact was on the exterior portion of the rail. Considering all functional aspects of the sled design, several modeling assumptions were made to ensure fidelity to sled function and to discard all noncontributing phenomena.

Figure 3.1 LSR Forebody Sled

3.1 Modeling Assumptions

Initially the simulation boundaries were defined via assumptions as to what the DADS model would and would not contain. Justification of each assumption was tersely stated and measured against common sense. The DADS model accounts for the items in Table 3.1 and excludes items in Table 3.2.

3.2 Design Parameter Selection

Design parameters are defined as any sled or rail characteristic that affects sled performance. Conceivably any parameter from frequency response to sled color could affect performance; however, in the scope of this study only those parameters

Table 3.1 Modeling Assumptions Ensuring Model Fidelity

Assumption	Description
Elastic Slipper Rail Contact	Slipper rail impact does not account for energy loss due to plastic deformation, wear, or gouging
Flexible Body Modeling of Structural Components	Flexible body representation of rocket motor, slipper beams, slippers, and payload
Rough Rail	Use survey data to vary the surface of the ideal rail profile
Rigid Rail	Rail is assumed to be rigid based on data from Baker and Turnbull (1999), Hooser (2000a), Hooser and Mixon (2000), and Graf, K. F., Mahig, J., Wu, T. S., Barnes, R. A., Kowal, C. R. (1966)

Table 3.2 Modeling Assumptions Outside Scope of Present Study

Assumption	Description
No plastic deformation at slipper rail contact	Model only elastic contact
No slipper rail gouging	For all tests in LSR series rail coating and alignment technology have prevented significant gouges (Turnbull and Minto 2003, Cinnamon 2006)
No significant heat transfer from Aerodynamic Heating or friction	Sled test does not last long enough to allow heat transfer that would affect structural properties
No frictional wear of slippers	Slipper wear is not enough to change slipper gap or structural properties of slippers
No variations in rail stiffness	The rail is uniformly rigid

which influence structural response and sled performance are studied as they relate directly to the parameters that design engineers consider. Aerothermal effects are important, but are outside the scope of this investigation. The design parameters chosen in this study are as follows:

1) Slipper Gap, Vertical and Lateral

2) Rail Roughness, Vertical and Lateral

3) Slipper Beam Stiffness

4) Rocket Motor Stiffness

5) Component Connection Structural Characteristics

6) Component Weight

7) Structural Damping

8) Vibration Isolation

9) Component Material

10) Thrust

11) Aerodynamic Lift and Drag Forces

12) Velocity

13) Slipper Rail Contact

14) Combustion Instability

The items contained in this list represent the highest level categorization of design parameters. For example the slipper rail contact category is made up of several variables that include contact scheme and all of the parameters related to it.

3.3 Slipper Rail Impact Modeling

Slipper rail impact describes a range of high sliding velocity contacts from a flat plate on rail, Figure 3.2, to a rotated plate on rail, Figure 3.3. The angle that the sled can move is governed by the distance between the front and aft slipper edges and the slipper gap. For a specialized case with the current study a 10 inch long rotated slipper moving through a 0.125 in gap gives a pitch impact angle of about 1°. The rotated slipper effect is worth mentioning since the impact scenario is different from that of a flat plate with 0° angle of impact. With the rotated slipper, the leading edge will contact first, experience some minor wear, and rotate until a 0° angle is achieved and eventually rebound. An edge contact followed by a momentum dissipation through slipper rotation are two additional elements that occur which affect the before and after impact momentum with a nonzero impact angle.

The end product of slipper rail impact modeling was implemented into DADS in the form of three contact points per slipper surface, Figures 3.4 and 3.5. This required validation against the method used to generate the contact scheme. DADS allows the implementation of a modified Hertzian contact scheme (Stronge 2000), or spring and damper values, linear and nonlinear. The linear and nonlinear contact forces are straightforward as shown in Equations 3.1 and 3.2 respectively (LMS CADSI 2004). The Hertzian contact force is calculated as shown in Equation 3.3 (LMS CADSI 2004) with the inclusion of effective Young's Modulus (Stronge 2000). This range of contact phenomena was investigated from three perspectives: linear, nonlinear and Hertzian.
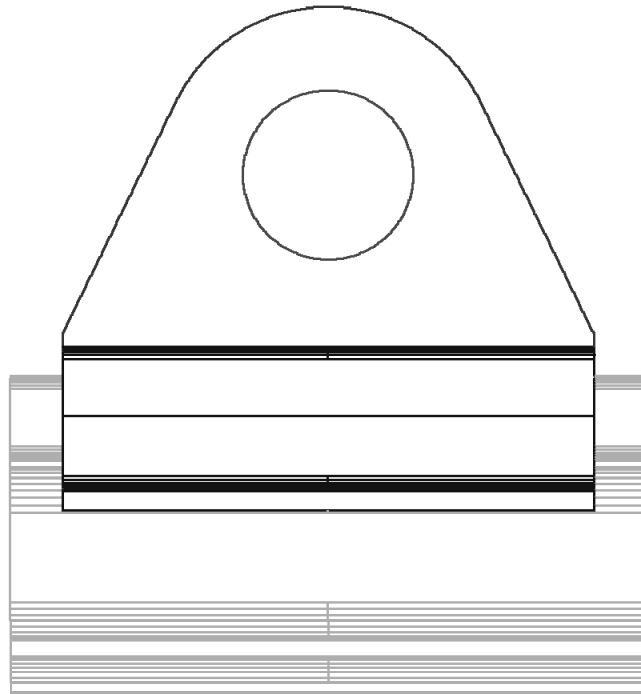
Figure 3.2 Slipper Rail Impact Parallel Orientation
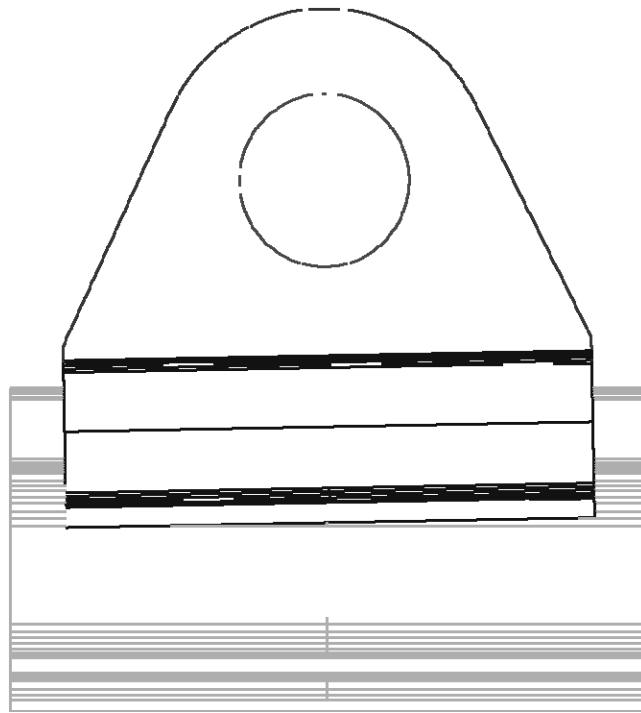
Figure 3.3 Slipper Rail Impact Maximum Angled Orientation 3°
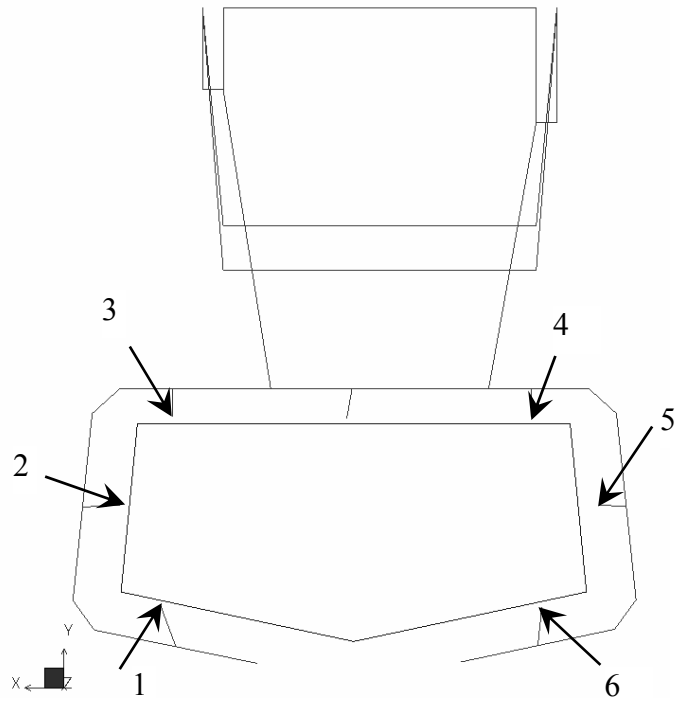
Figure 3.4 Front View of DADS Slipper Rail Contact Depiction
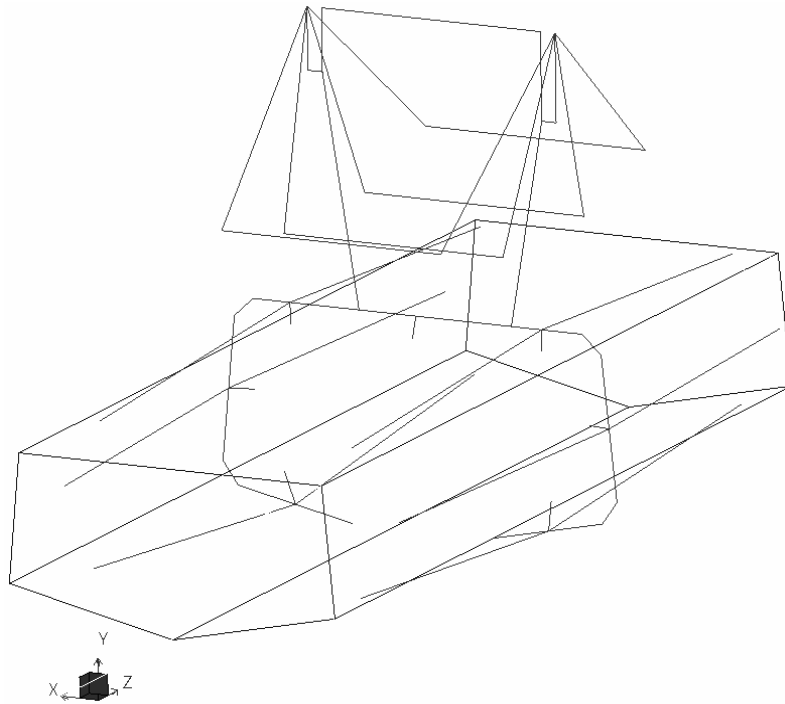
Figure 3.5 Isometric View of DADS Slipper Rail Contact

$$F_n = k\delta - cV_P \tag{3.1}$$

where

V_p is the penetration velocity (in/s)

δ is deflection (in)

k is a linear spring coefficient (lbf/in)

c is a linear damping coefficient (lbf s/in)

$$F_n = k(\delta)\delta - c(V_p)V_P \tag{3.2}$$

where

$k(\delta)$ is a nonlinear stiffness as a function of deflection (lbf/in)

$c(V_p)$ is a nonlinear damping as a function of penetration velocity (lbf s/in)

$$c = \frac{1}{R_1} + \frac{1}{R_2}$$

$$K_{nom} = 0.733E\sqrt{\frac{1}{c}}$$

$$K_{act} = K_{nom}\left[1 + \left(\frac{1 - COR^2}{1 + COR^2}\right)\tanh\left(2.5\frac{V_p}{V_e}\right)\right] \tag{3.3}$$

$$F_n = K_{act}\delta^{1.5}$$

where

R_1 is the Radius of contacting body 1 (in)

R_1 is the Radius of contacting body 2, for flat bodies is 84.245 in

E is the effective Young's Modulus of contacting body (lbf/in^2)

COR is Coefficient of Restitution

V_e is the transitional velocity (in/s)

K_{nom} is the nominal stiffness (lbf/in)$^{-0.5}$

K_{act} is the actual stiffness (lbf/in)$^{-0.5}$

F_n is the normal force as a function of K_{act} and deflection (lbf)

3.3.1 Theoretical Formulation

The first perspective consisted of a purely theoretical standpoint to uncover the nature of slipper rail impact. There were several sources found during the literature review that treated in great detail the theory related to less complicated contact such as two spheres colliding or a single sphere contacting a semi infinite plate, Hertzian contact (Stronge 2000). A theoretical source that dealt directly with high velocity sliding contact was not found. The literature surveyed dealt with elastic impacts of comparatively basic systems or with complex systems that analyzed wave propagation within the material (Zukas, J. A., Nicholas, T., Swift, H. F., Greszczuk, L, B. 1982). Note that the latter system was discounted due to experimental work performed by Hooser (2002a) and Hooser and Mixon (2000) and computational work by Furlow (2006a) that showed that slipper impacts on the rail are of short duration, typically 1 millisecond, so there is not time for the rail response to influence the contact either initial or subsequent at sled velocities above 4,000 fps. The natural mode of the rail in the vertical direction, 310 Hz 1st bending, and lateral direction, 199 Hz 1st bending and 490 Hz 1st torsional, give a minimum response time that cannot structurally affect slipper rail interaction for a 130 in long sled traveling above 4,000 fps. Also shown were the formation of certain elastic waves that propagate along the rail at given velocities (Baker and Turnbull 1999). These waves were shown to quickly decay and not influence slipper rail interaction as it was concluded that if they were significant the front slipper would disturb the rail and induce a response that could destroy the following aft slipper; from observation and decades of testing this

29

scenario does not prevail. It was surmised at this point in the research effort and noted in the literature (Baker and Turnbull 1999) that a considerable study was warranted to truly understand slipper impacts from a theoretical standpoint. The study would involve the broader range of slipper rail contact scenarios and not necessarily the solid mechanics involved in the slipper interpenetrating the rail.

3.3.2 Computational Formulation

The second perspective was to approximate the macro level slipper rail impact by studying the pre- and post-impact conditions of a slipper impacting the rail. Several transient FEM software packages are available to perform the analysis portion of this study. PRONTO, a FEM package developed by Sandia National Labs (SNL) was chosen for its availability and capability to be run locally on a Linux cluster or at the DOD High Performance Computing Center. The PRONTO models were constructed to represent three general cases of slipper rail impact: vertical down, lateral, and vertical up. The slipper rail model was constructed using two solid parts separated by about 0.001 inches in the contact direction. The solid parts were produced in I-DEAS and meshed in CUBIT, a SNL mesher. The mesh size discretization for the slipper was 0.009 in and the rail was 0.35 in and is depicted in Figures 3.6, 3.7, and 3.8. The tie-downs, mechanical fixtures that fasten the rail to a concrete girder, were approximated by fixing four inch sections of the rail every 52 in as depicted in Figure 3.9. Initially the downtrack velocity was studied at 0 fps where several phenomena were noted. The impact of a slipper at a tie-down vs. rail mid-

span of the tie-downs gave different deflections and contact times but yielded similar

CORs. When the downtrack velocity was increased, the impact point became less

significant as the slipper remained in contact with the rail over tie-down and mid-span

alike. In fact at 5,000 fps, the lateral case bounding impact points show very little

difference as depicted in Figure 3.10. As a result of this a downtrack velocity of 5000

fps was used for all subsequent PRONTO analyses. The initial conditions for all

impact cases, vertical down, vertical up, and lateral, were a range of velocities of 10,

25, 50, and 100 ips in the respective impact direction with the downtrack velocity of

5000 fps. These initial conditions were intended to span the range of typical slipper

impacts as noted by Hooser and Mixon (2000). A similar analysis for all cases was

performed where a set of nodes on the slipper were identified that defined the mid-

span and ends of the slipper. The displacement, velocity, acceleration and contact

force of these node sets were monitored to describe the impact behavior of the

slipper; the gross slipper motion was derived from these data values.   The contact

force was used to define the initiation of the contact as force was zero until first

contact. At the first contact point, the approach velocity and relative deflection levels

were noted as they were used in subsequent analyses. The return of the slipper

deflection to the relative deflection point was used to define where the slipper left the

rail. At this point, the rebound velocity was monitored. There was a substantial

amount of high frequency vibration present in velocity data after contact, but

typically for the period immediately after slipper rail separation, the averaged velocity

was used to define the rebound velocity of the slipper. The approach and rebound

velocities were used to define the Coefficient of Restitution. The time where the zero

velocity point occurred was used to ratio the force and relative displacement at this

point to determine a maximum stiffness value if the force data were significant across

the impact duration. These analysis points are depicted in a typical result for the non-

sliding 100 ips vertical up case shown in Figure 3.11 (Furlow 2006a).

The results of this study are shown in Table 3.3 and document the values of

COR. The results are averages over all of the initial conditions for each respective

impact direction. It should be noted that the COR values were simply a ratio of the

pre-impact to post-impact slipper momentum. The values compare well to
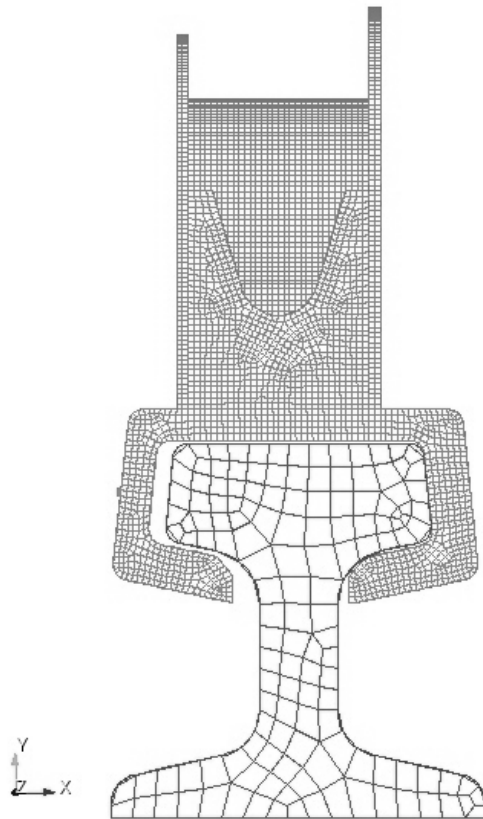
Figure 3.6 Slipper Rail PRONTO Model Front View
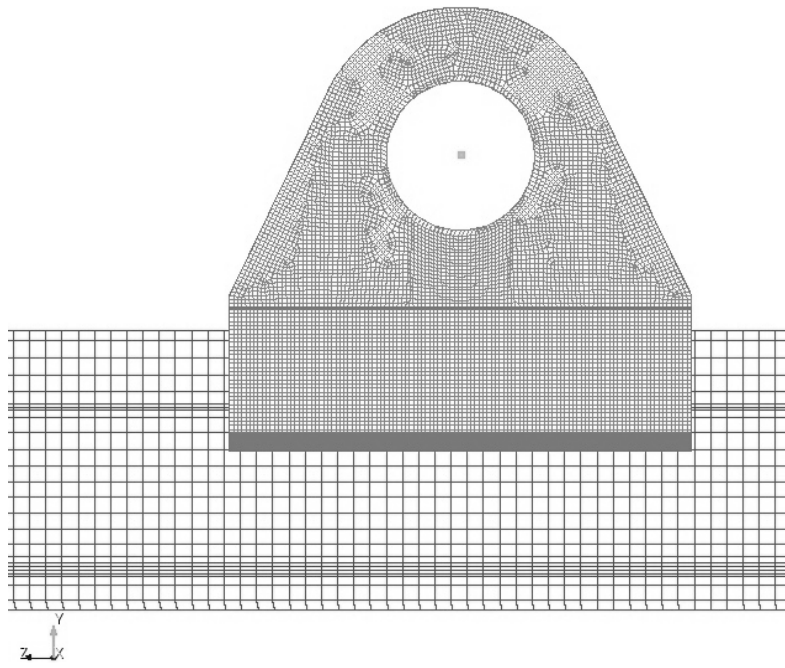
Figure 3.7 Slipper Rail PRONTO Model Side View
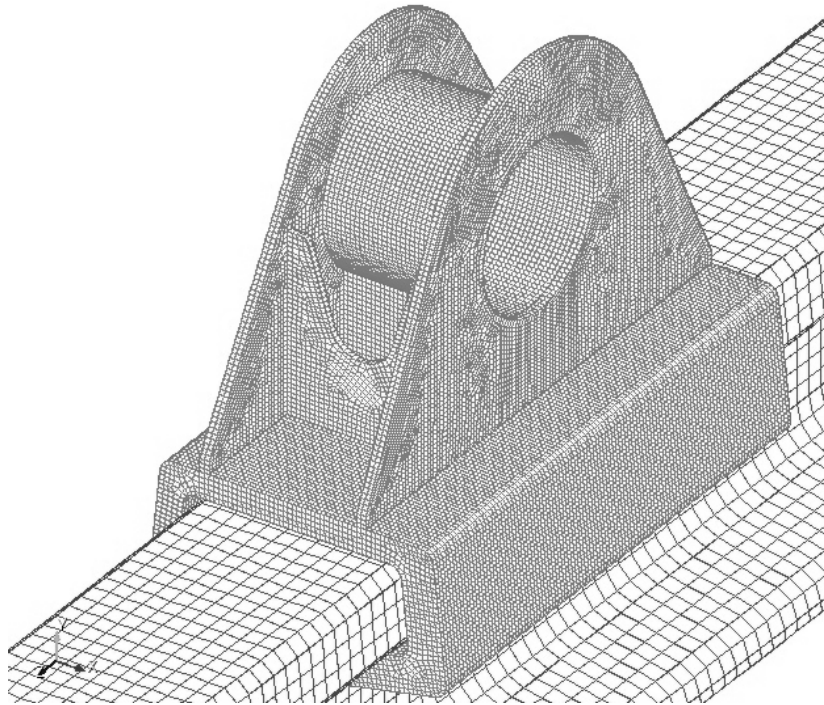
Figure 3.8 Slipper Rail PRONTO Model Isometric View
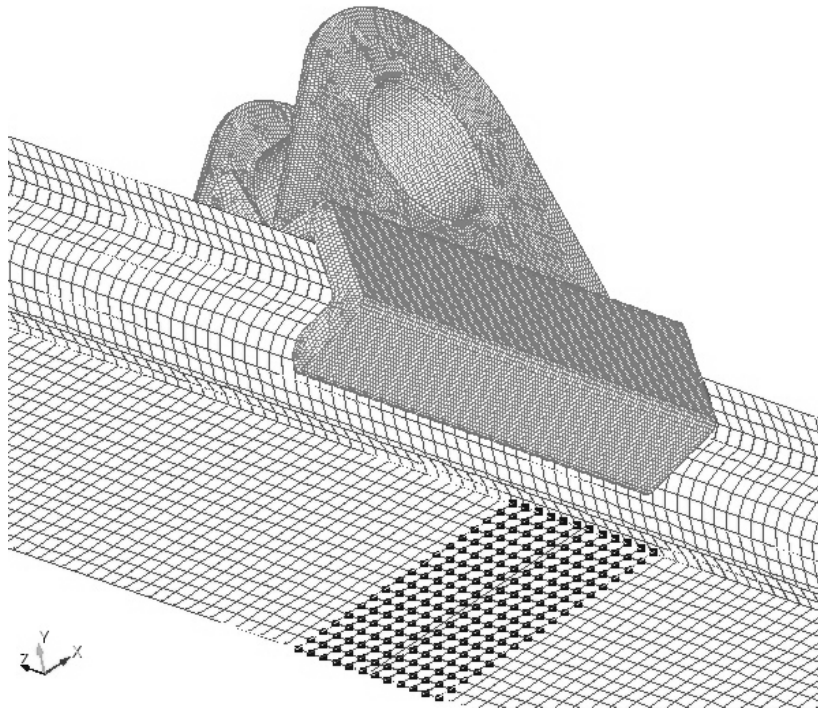
Figure 3.9 Slipper Rail PRONTO Model Boundary Conditions
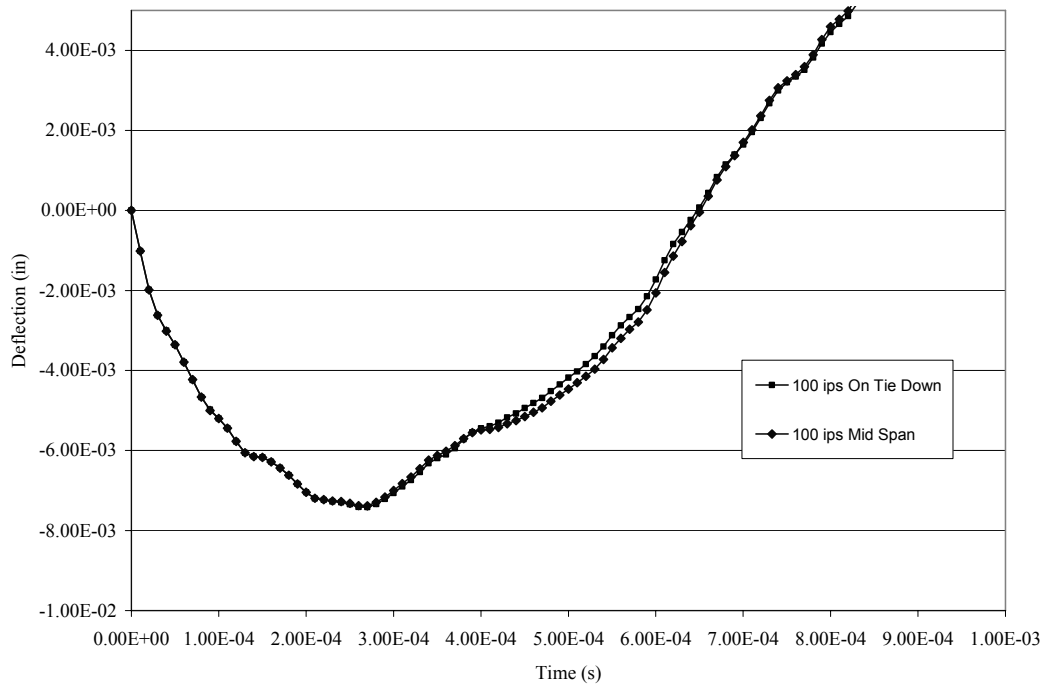
Figure 3.10 Lateral Impact 100 ips, 5000 fps Sliding Velocity Comparison
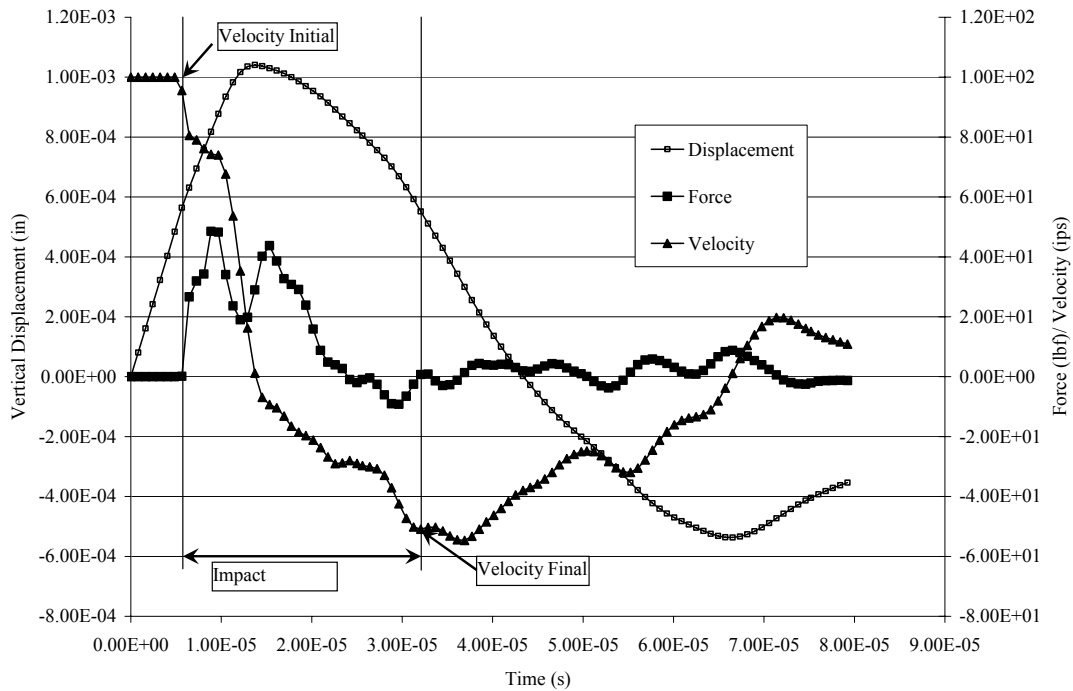
Figure 3.11 Vertical Up Impact 100 ips, 0 fps Sliding Velocity

those derived from the work of Hooser and Mixon (2000) in the vertical up impacts since momentum lost to the rail is typically 2.2 lb$_f$ s and is somewhat lower in the vertical down as the typical momentum loss to the rail was 1.7 lb$_f$ s. The lateral momentum loss was 2.7 lb$_f$ s which is substantially lower than the value of 32.3 lb$_f$ s reported by Hooser and Mixon (2000), this discrepancy is most likely due to the nature of the measured sled test. The sled test generating the experimental data was a monorail where vertical up and down impacts are similar to a single slipper, but lateral impacts are dissimilar in that monorails have a significant roll motion component that adds to torsional and lateral rail deflection. Also discrepancies may arise from assumptions made in using measured flange translational velocities to describe a torsional rail response and too flexible of a model to represent rail motion.

35

The effective mass of both the rail and slipper were calculated and applied to the measured velocity (rail) and SIMP derived velocity (slipper) respectively. The important conclusion of this study was the measurement of the COR. In this study the stiffness and damping values were adjusted since their eventual implementation was on a rigid rail in DADS.

Table 3.3 PRONTO Slipper Impact Results

Impact Direction	Coefficient of Restitution, COR
Lateral	0.24
Vertical Up	0.49
Vertical Down	0.42

3.3.3 DADS Implementation

The results of the PRONTO modeling were emulated in a DADS representation of the test cases conducted in PRONTO. The DADS model included assumptions to be used on the full scale sled test model. The most important among these assumptions was the rigid rail assumption. Three different contact schemes were studied: linear stiffness, nonlinear stiffness, and DADS implemented Hertzian as shown in Equations 3.1, 3.2, and 3.3 respectively. The actual contact scenario is bounded by a semi-infinite cylinder (angled slipper) contacting a semi-infinite plate (rail) and by a finite plate (parallel slipper) contacting a semi-infinite plate (rail). In

contrast Hertzian contact, as implemented by DADS, represents the contact of two

spherical bodies where the contact radius corresponding to a flat surface is 84.245 in.

To represent the contact, values for stiffness, damping, COR, radius contact point,

and Young's modulus were prescribed as necessary. The slipper was modeled as a

flexible body using modal or SMD representations. The rail was described as a rigid

body with the profile shown in Figures 3.4 and 3.5 with no rail roughness. The initial

conditions were 10, 25, 50, and 100 ips in the respective contact direction and 0 fps in

the downtrack direction. The 0 fps downtrack velocity was valid as the rail was

modeled as rigid and friction was not included in this study. The stiffness and

damping for each direction are listed in Tables 3.4, 3.5, and 3.6 for each of the

contact schemes. The measure of correlation in each case is based on a visual

inspection of PRONTO and DADS data overlays of displacement and velocity. It

should be noted that correlation of the Hertzian contact scheme, Table 3.6, was not

acceptable for any case and was thus discarded. In DADS Young's modulus had to

be scaled to get results within a reasonable range of the PRONTO generated results

and the deflection did not correlate well. The linear and nonlinear contact schemes,

Figures 3.12 and 3.13 respectively, yielded good comparisons to the PRONTO data.

The comparisons were evaluated on two criteria: the maximum deflection and impact

duration. The COR values generated in PRONTO were used as a double check to

ensure that the DADS correlation data matched in velocity as well, and that

momentum transfer was similar to that in PRONTO. The experimental study by

Hooser and Mixon (2000) was used as a measure of effectiveness, and the DADS

results compared well as they were similar to the PRONTO results. It should be noted that for nonlinear contact the force-deflection in DADS was described by a force deflection curve from a text file. For some simple contact scenarios, the nonlinear contact scheme produced force error and inexplicably the contact displacement was not affected. It is surmised that this was due to interpolation errors in DADS when calculating force and displacement from the text file, and although the nonlinear contact scheme yielded excellent results it was not used in the complete sled model for this reason.

3.4 Flexible Body Modeling

Flexible body representation was included in the simulation of the LSR test as it was shown to contribute significantly in transient rocket sled models when it was incorporated as a modal representation (Mixon 1971, Greenbaum et al. 1973) or as a SMD representation (Hooser and Schwing 2000, Hooser 2002b, 2000). Modal representation refers to representing a flexible rocket sled by decomposing the sled into major structural components, applying the appropriate boundary conditions and then solving for natural frequencies and mode shapes. Typically the solution of the natural frequencies and mode shapes is accomplished using a finite element technique where the model is formed by resolving mass properties at nodes and developing the stiffness matrix based on the connecting geometry. The SMD system involves prescribing stiffness and damping values for degrees of freedom between point masses. The stiffnesses are formed based on the structural properties between the

Table 3.4 DADS Slipper Impact Results, Linear Contact Model

Impact Direction	Measured Coefficient of Restitution, COR	Stiffness (lb$_f$/in)	Damping (lb$_f$ s/in)	Correlation
Lateral	0.20	1200000	350	Good/Fair
Vertical Up	0.35	38057	60	Good
Vertical Down	0.50	5959008	600	Excellent

Table 3.5 DADS Slipper Impact Results, Nonlinear Contact Model

Impact Direction	Measured Coefficient of Restitution, COR	Stiffness (lb$_f$/in$^{1.5}$)	Damping (lb$_f$ s/in)	Correlation
Lateral	0.18	40000000	400	Fair/Poor
Vertical Up	0.30	1256.5	64	Good/Fair
Vertical Down	0.50	7.39E+08	500	Excellent

Table 3.6 DADS Slipper Impact Results, Hertzian Contact Model

Impact Direction	Measured Coefficient of Restitution, COR	Young's Modulus (lb$_f$/in^2)	Contact Radius (in)	Rail Radius (in)	Transition Velocity (ips)	Correlation
Lateral	0.24	4.0E9	0.001	84.245	1.0	Poor
Vertical Up	0.35	3.50E7	0.001	84.245	1.0	Fair
Vertical Down	0.50	5.29E9	0.001	84.245	1.0	Fair/Poor
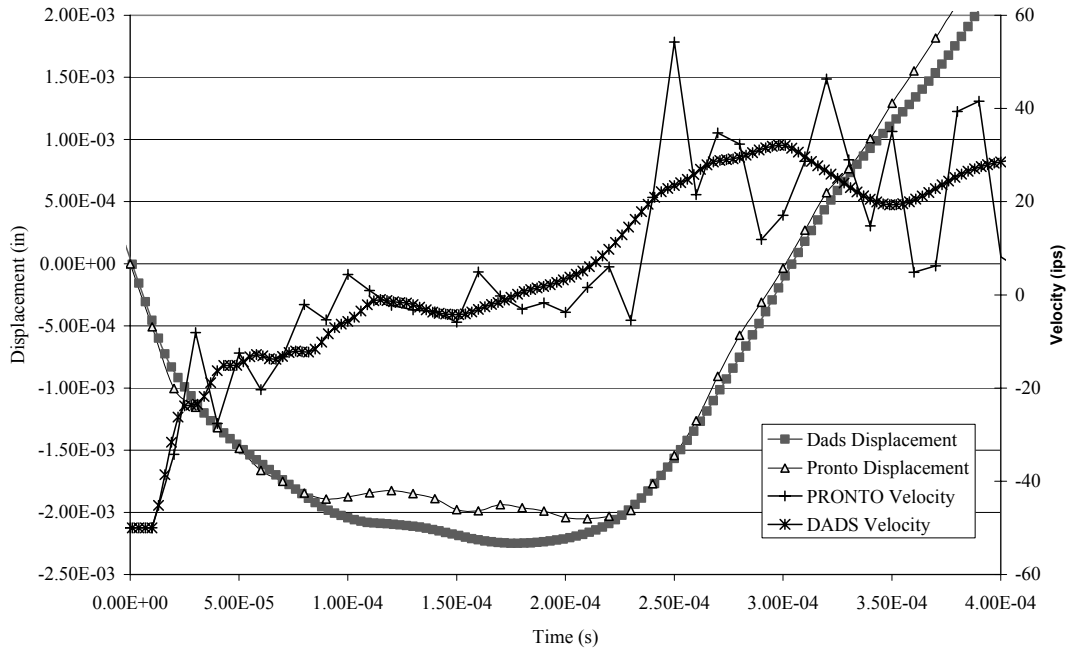
Figure 3.12 Vertical Down Impact 50 ips, Linear Contact
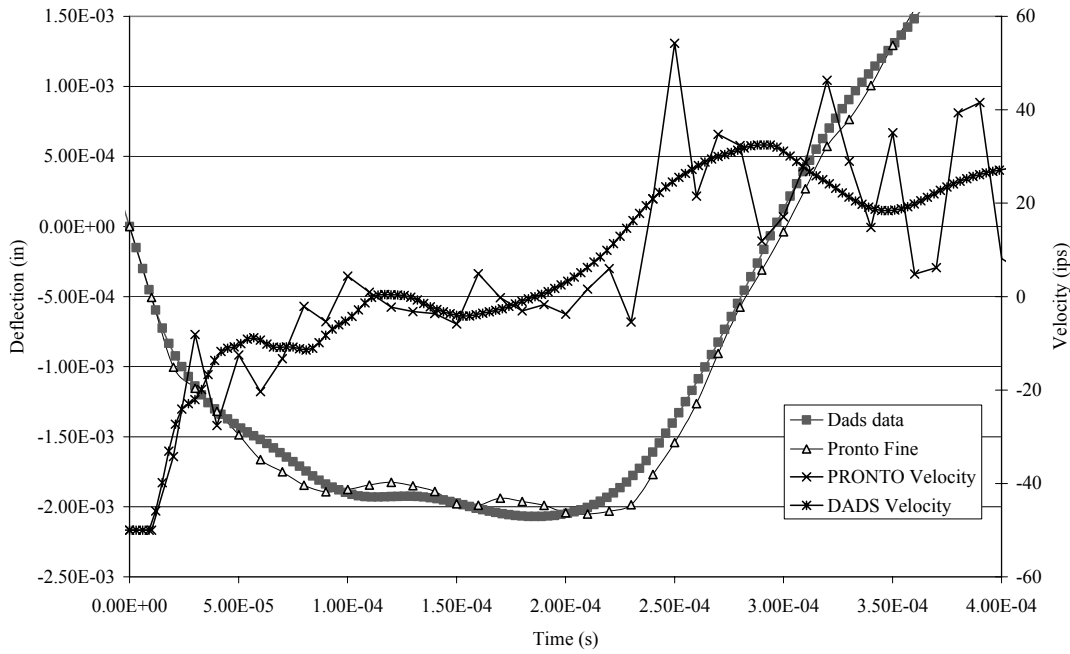
Figure 3.13 Vertical Down Impact 50 ips, Nonlinear Contact

point masses in a manner similar to the finite element technique. The principle

difference between the two methods is that mode shapes are prescribed by their

boundary conditions regardless of their final application; however, it is possible to

group many different boundary conditions in the final application. Both methods will

be considered and analyzed in the current study and the more accurate of the two will

be selected for use in the wide scale parameter variation study.

For both methods the general implementation was to establish a set of

acceptance criteria for each major structural component in order to measure the

fidelity of the flexible body modeling scheme. The properties measured were mass

distribution, static deflection, and natural frequencies and mode shapes. The most

desirable data was that derived during laboratory testing of the actual sled

components. This data was available for natural frequencies and mode shapes for the

rocket motor body. The next most desirable source of data was from a three-

dimensional FEM representation of the component. This allowed three-dimensional

effects to be accounted for in the evaluation of static deflection and frequency data.

When a major structural component was modeled in DADS using either flexible body

representation, the DADS model characteristics were measured against the

acceptance criterion. The acceptance criterion and respective sources are listed in

Table 3.7. The most descriptive example of this method is the validation process of

the rocket motor model.

The geometrical shape of the rocket motor was produced in I-DEAS and a

typical density prescribed. The rocket motor consists of a carbon composite case with

Table 3.7 DADS Model Acceptance Criterion

Major Structural Component	Acceptance Criterion		
	Mass	Static Deflection	Frequency Data
Slipper Beam	FEM Model	FEM Model	FEM Model
Rocket Motor	Laboratory Measurement	Not Used	Laboratory Measurement
Payload	FEM Model	FEM Model	FEM Model
Slipper	FEM Model	FEM Model	FEM Model

insulating layers protecting the inside of the carbon composite from the burning

propellant. The composite lay-up was studied to determine a suitable density for the

I-DEAS model where the rocket motor casing with no propellant weight was

measured in the lab. Using the solid volume calculated in I-DEAS, a weight density

of 0.0672 lb_f/in^3 was prescribed. The total volume was next divided into 12 separate

volumes whose CGs each corresponded to a mass lumped at a node placed at the

corresponding CG location. Beam elements were prescribed to represent the

geometry spanning the CG locations and used area, length, shear area coefficient, and

area moments of inertia based on the cross sectional properties to approximate

flexibility. Polar moment of inertia was exactly one half of the typical value as the

carbon composite lay-up was such that this was necessary. The frequency data

criterion were used to verify a model representing a reproduction of the modal test

accomplished by Mixon (2002b) the results of which are featured in Table 3.8 for the rocket motor entries. From the verified model, frequency data (Mixon 2002b), fabrication information (Track DWG A0406003, Mixon 1999a), and consulting Herakovich (1998) a smeared composite material value for Young's Modulus, 11.75E6 lb_f/in^2, and Poisson's ratio, 0.28, were determined along with an average composite material layup ratio value of 0.473. It was reasoned that if frequency response and mass properties matched laboratory test equivalents then no static deflection validation was needed for the rocket motor. The procedure was executed in a similar fashion for the remaining major structural components whose acceptance criteria are listed for mass properties in Table 3.9, static deflection in Table 3.10, and frequency data in Table 3.8. During the course of performing this analysis, care was taken to ensure the model discretization process was adequate to represent frequency and deflection phenomenon. Any three dimensional effects or such as translational or rotational coupling were included in the modeling through refined substructuring or representative stiffness. The three dimensional FEM models for the payload, slipper beam, and slipper are shown in Appendix A. Studies were conducted on the application of different boundary conditions to the modal model to investigate their effect on the motion of the exported model. The findings of these side studies showed that the boundary condition values should be based on the interfaces of the major structural component, e.g., whether or not a connection could transmit a moment or force. For an interface that was nonlinear it was more desirable to let the major structural component be unconstrained in that degree of freedom so that force

generation would occur within DADS with the application of the nonlinear boundary conditions.

Table 3.8 Major Structural Component Frequency Properties

Major Structural Component	Boundary Condition	Frequency (Hz) and Mode Shape						
Slipper Beam	Fixed at Yoke	259 SS V*	487 SS DT*	650 C DT*	732 1st C V*	1380 1st T*	1860 2nd C V*	2580 1st C L*
Slipper	Fixed at SB interface	708 B L*	2280 B V*					
Rocket Motor	Free – Free	146 1st B V*	146 1st B L*	236 1st T DT*	381 2nd B V*	482 1st DT*		
Payload	Fixed (FWD) – Free (AFT)	151 1st B V*	152 1st B L*	803 2nd B V*	813 2nd B L*	3500 1st DT*		

* V-Vertical; L-Lateral; DT-DownTrack; SS-See Saw; B-Bending; T-Torsional; C-Cantilever

Table 3.9 Major Structural Component Mass Properties

Major Structural Component	Weight (lb_f)	Ixx ($lb_f\ s^2$ in)	Iyy ($lb_f\ s^2$ in)	Izz ($lb_f\ s^2$ in)
Slipper Beam	49.68	1.29	5.29	5.85
Slipper	27.06	0.770	0.803	0.521
Rocket Motor	203.15	1038.46	1033.47	31.00
Payload	145.43	194.00	194.00	7.78

44

Table 3.10 Major Structural Component Static Deflection Properties

Major Structural Component	Load Point	Boundary Condition	Deflection (in)/ Load Direction (lb$_f$)		
			X	Y	Z
Slipper Beam	Inside slipper attachment	Fixed yoke	-4.78E-5 (X) 1.58E-4(Y)/ 100 X	1.58E-4 (X) 9.99E-4 (Y)/ 100 Y	4.10E-4 (Z)/ 100 Z
Slipper	Lip edge	Fixed at SB interface	2.13E-3/ 100 Y	1.77E-3/ 100 Y	N/A
Rocket Motor	N/A	N/A	N/A	N/A	N/A
Payload	N/A	N/A	N/A	N/A	N/A

3.4.1 Modal Representation

Modal representation as applied to this study was implemented in DADS by utilizing natural frequencies and mode shapes generated in I-DEAS using beam elements based on sled geometry. The process of generating the mode shapes in I-DEAS and implementing them in DADS is quite complex and worthy of explanation. Sled geometry was used to generate the length and cross sectional properties of the major structural sled components. This information was used to produce nodes and linear 2-node beam elements. The beam theory used to produce the stiffness properties of the beam elements was the default method in I-DEAS (Unigraphics Solutions Inc. 2002) and was derived from Przemieniecki's (1968) treatment of Timoshenko beam theory more recently documented by Timoshenko, Young, and Weaver (1974). The Timoshenko beam equation is shown in Equation 3.4 and leads

to the elemental stiffness matrix seen in Appendix B. The cross sectional area, area

moments of inertia, and shear area ratios (inverse of the Timoshenko shear area

coefficient) were all computed from the prescribed element cross section. Some

investigation was made into the effect of basing the calculation of shear area

coefficient solely on geometric properties resulting in the shear area ratio being

written as the ratio of shear strain at the cross section centroid to the average shear

strain (Timoshenko et al. 1974). A study by Gruttmann and Wagner (2001)

investigated the effect of including Poisson's ratio in the determination of shear area

coefficient and found that the effect was noticeable only for extreme values of

Poisson's ratio coupled with thick rectangular cross sections where the height was

much less that the width. However, in the present study it was found that the shear

area coefficient calculation used by I-DEAS was more than adequate.

$$
EI\frac{\partial^4 y}{\partial x^4} + \rho A\frac{\partial^2 y}{\partial t^2} - \rho\frac{I}{\Xi G}\left[E\frac{\partial^4 y}{\partial x^2 \partial t^2} - \rho\frac{\partial^4 y}{\partial t^4}\right] - \rho I\frac{\partial^4 y}{\partial x^2 \partial t^2} =
$$
$$
q + \frac{\rho I}{\Xi A G}\frac{\partial^2 q}{\partial t^2} - \frac{EI}{\Xi G A}\frac{\partial^2 q}{\partial x^2}
$$

(3.4)

where
E is Young's modulus
I is the area moment of inertia about the deflected axis
ρ is the density
A is cross sectional area
G is shear modulus
Ξ is the Timoshenko shear area coefficient
q is an applied force

After constructing a beam FEM and validating its mass distribution, static and frequency response to either laboratory measurements or full three dimensional FEMs, its mode shapes, natural frequencies, mass distribution, geometric and other FEM information were exported into several text files to be processed by a command line executable, DFBT.exe (DADS Flexible Body Translator). This executable assembled the text files into a file that was processed using the DADS/Flex program. Within DADS/Flex, the mode shapes and natural frequencies were orthogonalized so that they could be run in a stable and efficient manner within DADS. The theory behind orthogonalization is presented by LMS CADSI (1999) and seeks to 'decouple the modal mass matrix with respect to the modal stiffness matrix' and is seen in Equation 3.5. This process removes rigid body mode shapes and backs out the mass and stiffness matrices from modal information (LMS CADSI 1999). It also may include constraint and static attachment modes in the model so that static stiffness is retained in the DADS model as well if the analyst requires these conditions.

$$\left(\mathbf{K}^{m} - \lambda \mathbf{M}^{m}\right)\chi = \mathbf{0}$$
$$\Psi o = \Psi \chi$$

where

$\mathbf{M}^{m}$ is the modal mass matrix

$\mathbf{K}^{m}$ is the modal stiffness matrix

Ψ are the modes selected for orthogonalization

λ is the vector of eigenvalues

Ψo new modes linearly transformed

χ nxm eigenvector transformation matrix

(3.5)

The next step in the process was to prescribe a flexible body in DADS and use the orthogonalized mode shapes defined in DADS/Flex to represent the body flexibility and geometry. This lengthy process was verified by comparing the structure's mass and fundamental natural frequencies as computed in DADS to the applicable acceptance criterion from Section 3.4. An example of this process was demonstrated on the rocket motor.

The details of the modal model verification reveal a two part process where first the I-DEAS model must be successfully measured against the acceptance criterion. Secondly the information exported to DADS must be measured against the same acceptance criterion to ensure that the exported process did alter the information. The rocket motor model was measured in I-DEAS against mass properties and frequency data as no lab static deflection data existed and no three dimensional FEM was available. The other major structural components relied on high fidelity three dimensional FEMs. The rocket motor was discretized by prescribing lumped masses at nodes. Elements based on cross sectional properties were prescribed. After much iteration, it was discovered that due to the composite layup the polar moment of inertia was one-half of the typical value. The model was modified to match the lab test scenario where mass and frequency data were produced and are compared in Tables 3.11 and 3.12 for verification. The successful comparison of the frequency data gives confidence to the smeared composite material properties. At this stage the model was modified to represent a typical empty rocket motor case. Next fixed boundary conditions were applied only to the aft slipper beam

48

interface and natural frequencies were solved for and exported to DADS. The mode shapes were processed for import allowing the resulting comparisons to be shown in Table 3.12 where no significant deviation is seen. This process was repeated for the remaining major structural components except three dimensional FEMs were used as the verification data source.

Table 3.11 Modal Model Empty Case Rocket Motor Mass Properties Comparison

Model	Weight (lb$_f$)	Ixx (lb$_f$ s^2 in)	Iyy (lb$_f$ s^2 in)	Izz (lb$_f$ s^2 in)
CAD Solid	203.15	1038.46	1033.47	31.00
DADS/Flex	202.68	1035.00	1030.00	30.85
Deviation %	-0.23	-0.33	-0.34	-0.48

Table 3.12 Modal Model Rocket Motor Frequency Comparison for Vibration Test, Mixon (2002b)

Model	Boundary Condition	Frequency (Hz) and Mode Shape				
Beam FEM	Free - Free	146 1st B V*	146 1st B L*	236 1st T DT*	381 2nd B V*	482 1st DT*
DADS/Flex	Free – Free	141 1st B V*	151 1st B L*	241 1st T DT*	396 2nd B V*	504 1st DT*
	Deviation %	-3.4	3.4	2.1	3.9	4.6

* V-Vertical; L-Lateral; DT-DownTrack; B-Bending; T-Torsional

3.4.2 Spring Mass Damper Representation

SMD representation was implemented by using the DADS beam element to describe the flexibility between discretized masses. The DADS beam element uses Euler-Bernoulli beam theory (LMS CADSI 2004) as its default to describe the stiffness between masses in all six-degrees-of-freedom. The use of the DADS beam element is similar to that of a finite element except that the DADS beam element is written in terms of relative deflection where the deflection and applied load of one beam end are relative to the other end. The values required by DADS for use in the Beam Force element are cross sectional area, area moment of inertia, and polar moment of inertia. Euler-Bernoulli beam theory is shown in Equation 3.6 and is valid for beam problems where the ratio of length over effective depth is greater than 10. It was shown for suddenly applied loads (Furlow 2004) that the Euler-Bernoulli beam theory was acceptable even though individual beam components did not meet this requirement as long as the entire structure met the length to depth ratio. The implementation of Euler-Bernoulli beam theory by DADS is shown in Appendix A and details a reduced 6 by 6 matrix reflecting DADS' use of a relative force and deflection implementation. For cross sections that varied between discretized masses a factoring method was used to modify the applied cross section properties. The factoring method accounts for the construction of multiple DADS Beam Force elements between masses each representing a portion of the entire structure between the masses. The typical treatment of springs in series was applied for each DOF that a particular stiffness represented. The goal was to produce equivalent values of area,

area moment of inertia, and polar moment of inertia so that one DADS Beam Force element could be prescribed between masses to represent the cross section variations. The general equation applied to determine each equivalent value is shown in Equation 3.7. This method was used on DADS SMD modeling of the rocket motor, payload, and slipper. This process was verified by determining the structure's mass, fundamental frequency, and static deflection and comparing them to the validation data. An example of this process is described for the major structural component rocket motor.

The rocket motor was discretized into 12 masses whose total values are shown in Table 3.13 and is identical to the acceptance criterion as the DADS model was discretized directly from the acceptance criterion. The structural stiffness was defined using DADS Beam Force elements. The mass properties of the entire model were processed and compared to the verification data. The frequency response was measured by altering the rocket motor case to reflect the test documented by Mixon (2002b) where torsional exciters, 40 lb_f each, were placed in both ends of the empty rocket motor case and a force exciter, 51.00 lb_f, was attached to the forward torsional exciter to apply transient loading to the rocket motor case. The entire test setup was suspended on bungee cables to represent a free-free condition. The same situation was recreated in DADS and the resulting natural frequencies compared to the acceptance criterion in Table 3.14 where a maximum deviation of 11.3% occurs. The application of this modeling process to the remaining major structural components yielded favorable comparisons and are provided in Appendix B. The simplicity of the

51

SMD modeling method is that it is not affected by boundary conditions as is the case

with modal methods. If verification is achieved for the SMD method in mass

properties, static deflection, and frequency for a particular set of boundary conditions,

then it should be acceptable for all applied boundary conditions and any error should

arise primarily from the accuracy of the method used for its structural flexibility.

$$EI\frac{\partial^4 y}{\partial x^4} + \rho A\frac{\partial^2 y}{\partial t^2} = q(x,t) \tag{3.6}$$

where

E is Young's modulus

I is the planar inertia about the deflected axis

ρ is the density

A is cross sectional area

q is an applied force

$$\psi_{Equivalent} = \frac{(\psi_i\psi_{i+1}\psi_{i+2}...\psi_n)L_{total}}{L_i(\psi_{i+1}\psi_{i+2}...\psi_n) + L_{i+1}(\psi_i\psi_{i+2}...\psi_n) + ... + L_n(\psi_i\psi_{i+1}...\psi_{n-1})} \tag{3.7}$$

where

ψ is beam force element cross section property : A, I_{jj}

L is length designated by subscript

total refers to the entire property from beam end to beam end

i is the number of beam sections

j is the axis of the beam element properties

n is the total number of beam sections

Table 3.13 SMD Model Mass Properties

Model	Weight (lb$_f$)	Ixx (lb$_f$ s in)	Iyy (lb$_f$ s in)	Izz (lb$_f$ s in)
CAD Solid	203.15	1038.46	1033.47	31.00
DADS SMD	203.16	1038.46	1033.47	31.00
Deviation %	0.00	0.00	0.00	0.00

Table 3.14 SMD Model Frequency Properties

Modal	Boundary Condition	Frequency (Hz) and Mode Shape				
Lab Data/ Beam FEM	Free - Free	146 1st B V*	146 1st B L*	236 1st T DT*	381 2nd B V*	482 1st DT*
DADS SMD	Free – Free	144 1st B V*	147 1st B L*	241 1st T DT*	424 2nd B V*	493 1st DT*
Deviation %		-1.4	0.7	2.1	11.3	2.3

* V-Vertical; L-Lateral; DT-DownTrack; B-Bending; T-Torsional

3.5 Sled Model Formation

The formation of a sled model consisted of assembling the major structural components of the sled using appropriate connections to join them. The assembly was accomplished in DADS by approximating the as-built function of the sled observed from test conditions. Since the major structural components represented directly determinable entities, there were several connections that were not directly determinable due to 3 dimensional structural effects and nonlinearities, chiefly

structural and boundary conditions. The areas that were analyzed and included in the model as connectors for the major structural components are shown in Figure 3.14. External loading, aerodynamic and thrust, were applied as described by Minto and Turnbull (2003) to duplicate the velocity profiles shown in Figure 3.15 (LSR) from 4.73 to 6.03 seconds (4,647- 9,465 fps) and Figure 3.16 (CO) from 1.46 to 2.20 seconds (5,327 –5,004 fps). Rocket motor mass and mass properties were varied linearly within DADS to account for propellant mass loss during thrusting.

3.5.1 Three Dimensional Structural Effects

The three dimensional structural effects were seen primarily in the lateral/roll motion of the payload as the deflection of its cross section changed significantly due to a very thin wall thickness and very stiff forward attachment point located at the bottom of the cross section. These effects were implemented in DADS by tuning its attachment stiffness so that its DADS response matched the corresponding three dimensional FEM response in I-DEAS. The other area of significant three dimensional structural effects was the aft end of the payload where an plate vibration effect was observed in the three dimensional FEM and was adjusted in the same manner in the DADS model by using tuned attachment stiffnesses.

3.5.2 Nonlinear Boundary Conditions

Nonlinear boundary conditions (BC) contribute significantly to the response of the model and were therefore carefully considered. The areas and types of nonlinear BCs
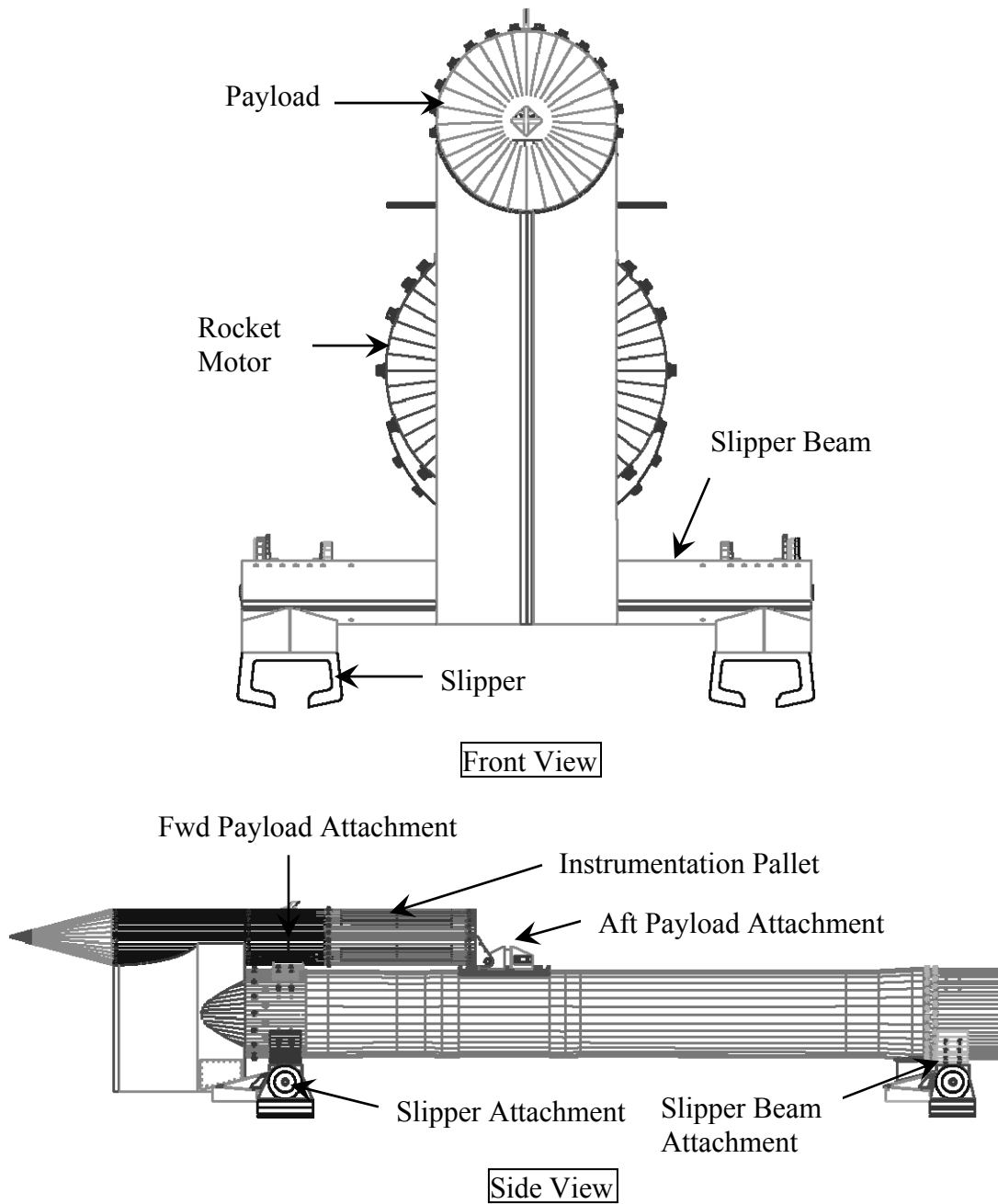
Figure 3.14 Sled Structural Connection Depiction
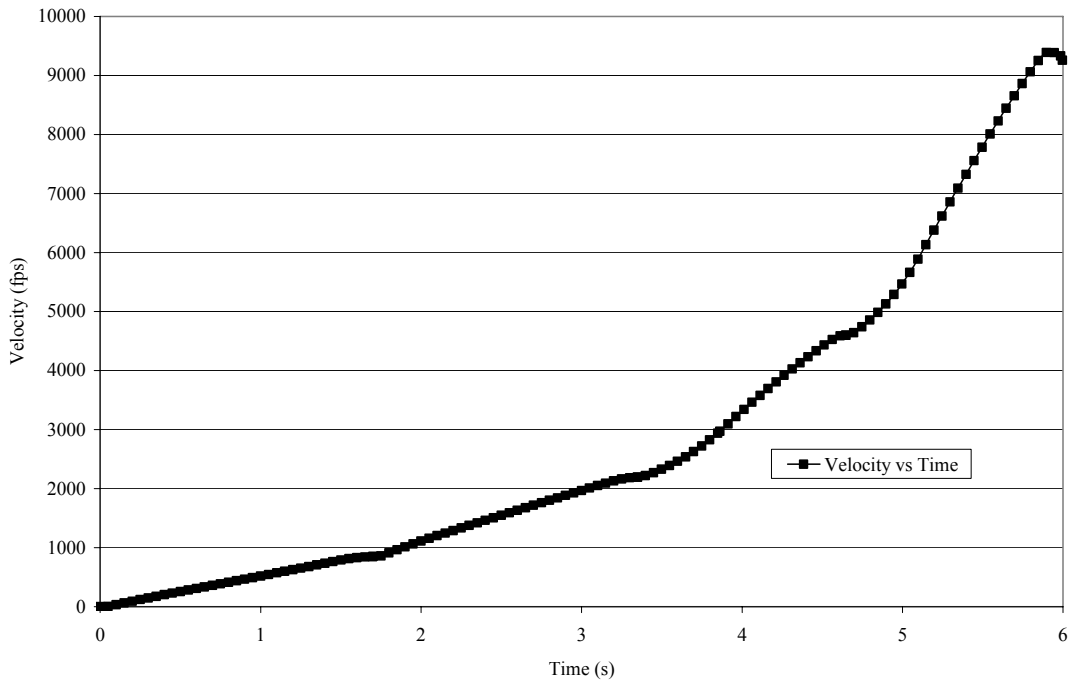
Figure 3.15 LSR Velocity Profile
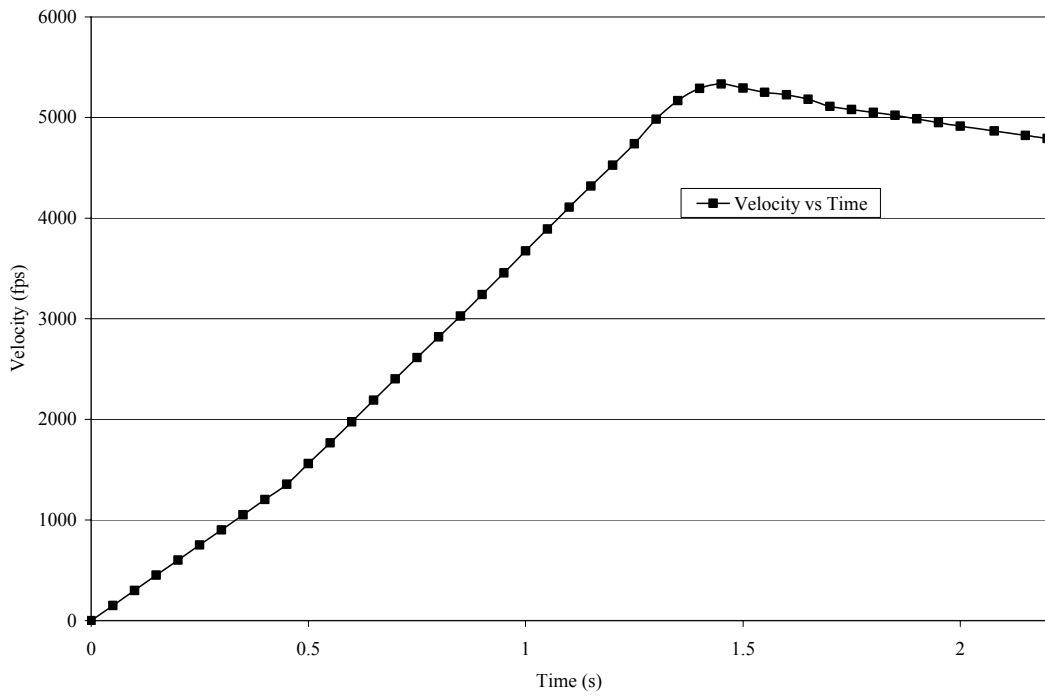
Figure 3.16 CO Velocity Profile

are listed in Table 3.15. The lateral vibration isolation at the connection of the slipper to the slipper beam represented a preloaded compression-only pair of differing stiffness nonlinear springs. This configuration is depicted in Figure 3.17 and shows an 80A durometer polyurethane pad of uncompressed length 0.56 in between the slipper beam and inner portion of the slipper with a 90A durometer polyurethane pad of uncompressed length 0.50 in. The implementation involved evaluation of the test time connecting bolt preload, in this case 8.5 kips, and determining the precompression length for both springs using Equation 3.8. It should be noted that the isolation materials 80A and 90A durometer polyurethane both have high damping values and nonlinear hardening stiffnesses as reported by Mixon (2002a) and shown in Figure 3.18. The stiffness in this connection; however, was linearized about the preload value of 8.5 kips as the load at this connection remains near the preload value during the test as reported by Turnbull and Minto (2003). The damping values were calculated to be 30 lb_f s/in for both pads.

A similar nonlinear boundary condition occurred at the aft payload attachment where a vibration isolation mechanism utilized an 80A durometer polyurethane pad as shown in Figure 3.19. On one side of the mechanism the pad was 1.00 in thick with an area of 7.07 in^2 and on the other side was a 0.50 in thick washer with an area of 0.76 in^2. This resulted in an effective one sided compression-only spring. Initially preload was applied to the thick pad but as the rocket motor fired motor expansion removed the preload and consequently none was modeled. The stiffness of the thick pad was set to 37,475 lb_f/in by applying the appropriate area and length to Mixon's

Table 3.15 Nonlinear Boundary Condition Summary

Nonlinear Boundary Condition Location	Type
Lateral vibration isolation at slipper/slipper beam interface	Nonlinear stiffness, unidirectional application
Lateral and axial vibration isolation between payload and rocket motor	Nonlinear stiffness, unidirectional application
Payload moment reduction mechanism	Gap in aft payload vertical support creates a nonlinear support that actuates only after gap is traversed in the positive or negative direction
Slipper gap	Gap between slipper and rail that allows contact once gap has been traversed
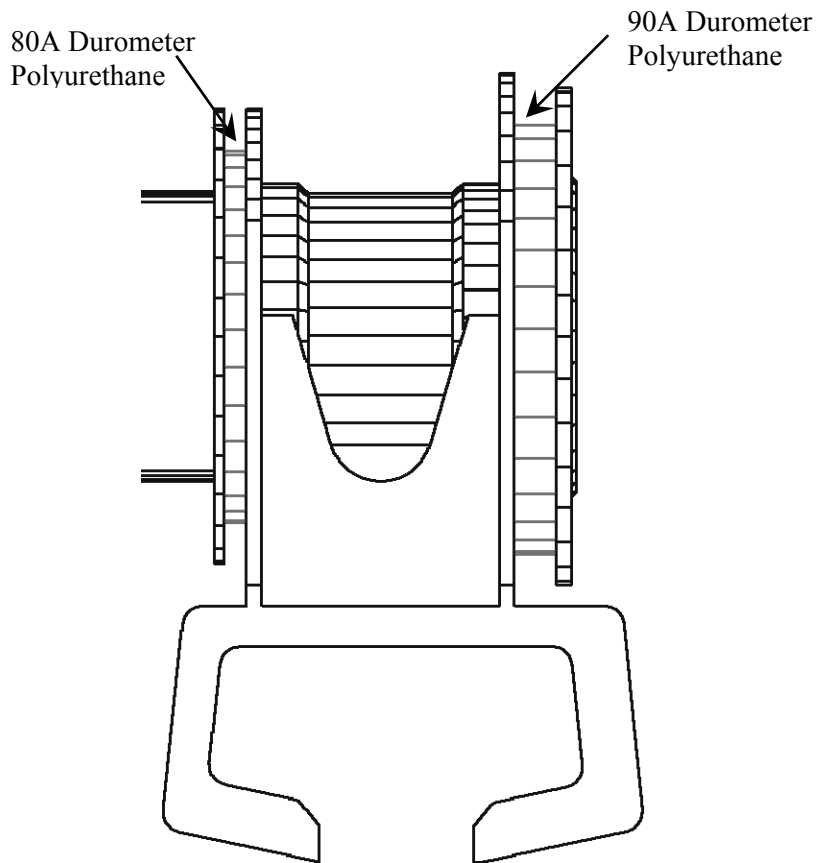
Figure 3.17 Lateral Slipper Vibration Isolation

$$\delta_{90A \text{ compressed}} = \frac{8.5 kips}{k_{90A}} - \delta_{90A \text{ Free}}$$

(3.8)

$$\delta_{80A \text{ compressed}} = \frac{8.5 kips}{k_{80A}} - \delta_{80A \text{ Free}}$$

where

$$k_{80A} = 45,559 \frac{lb_f}{in}$$

$$k_{90A} = 147,561 \frac{lb_f}{in}$$
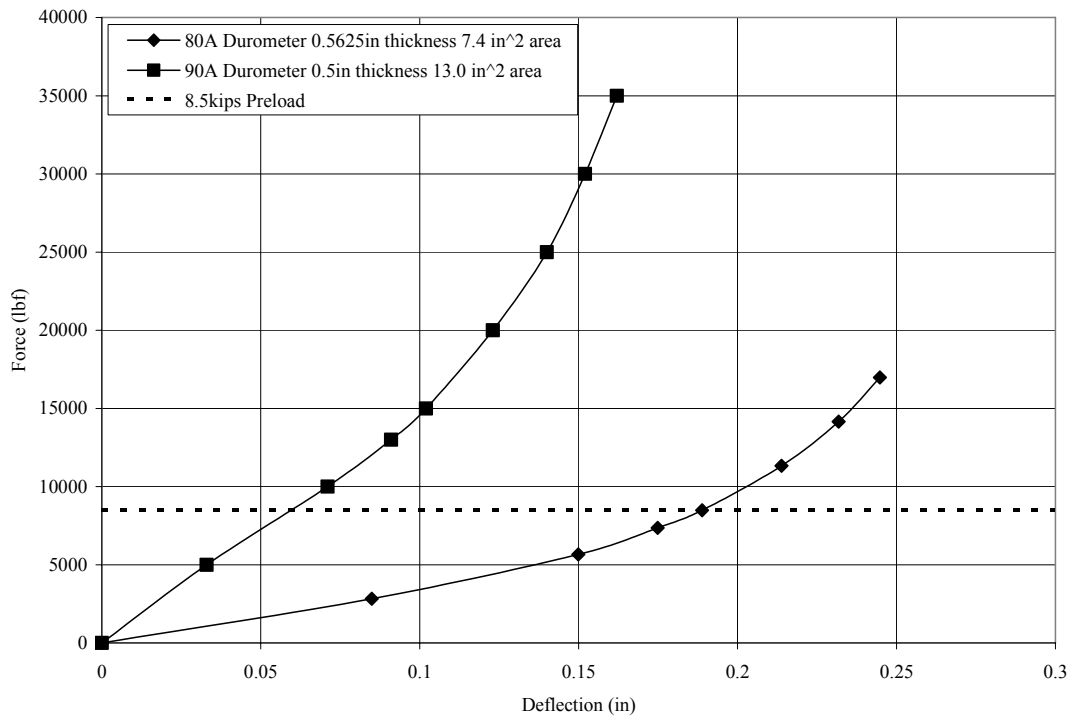
Figure 3.18 Nonlinear Polyurethane Force Deflection Test Data (Mixon 2002a)

(2002a) stress/strain curve for 80A durometer polyurethane.

The next area of nonlinearity occurred in the aft vertical payload attachment. The fabrication of this connection indicated a diameter of 0.80 in on the aft payload attachment bracket connected to the payload and a diameter of 0.76 in on aft payload

59

slider vertically connected to the rocket motor. This joint is designed to be a pivot about the lateral axis connected by a 0.75 in diameter bolt. This gives a vertical clearance of 0.028 in when the diameter of the bolt and clearance holes of the aft payload attachment bracket and aft payload slider are considered. This connection results in a nonlinear spring with characteristics shown in Figure 3.20 for a linear stiffness of 1,102,961 lb$_f$/in used in Equation 3.9. In effect there is no vertical force unless payload aft moves 0.06 in up or down from neutral. This concept is supported by analyzing the aft vertical force during the LSR test (Turnbull and Minto 2003).

$$k = \frac{AE}{L} = 1,102,961 \frac{\text{lb}_f}{\text{in}} \tag{3.9}$$

where

$A = \text{Area in compression}, 1.2 \text{ in}^2$

$E = \text{Young's Modulus}, 30E6 \frac{\text{lb}_f}{\text{in}^2}$

$L = \text{Length of matierial in compression}, 1.37 \text{ in}$

There was an attempt to utilize 80A durometer polyurethane vibration isolation in the aft payload lateral attachment but after studying both the force and acceleration test data it is apparent the as-designed vibration isolation system failed to perform as desired. The aft payload connecting mass weighs approximately 6-8 lb$_f$ and if not connected to the rocket motor would be loaded laterally only by lateral acceleration. The discrepancy in reporting the weight of this item is due to the addition of several undocumented items at run time which included accelerometers,

60
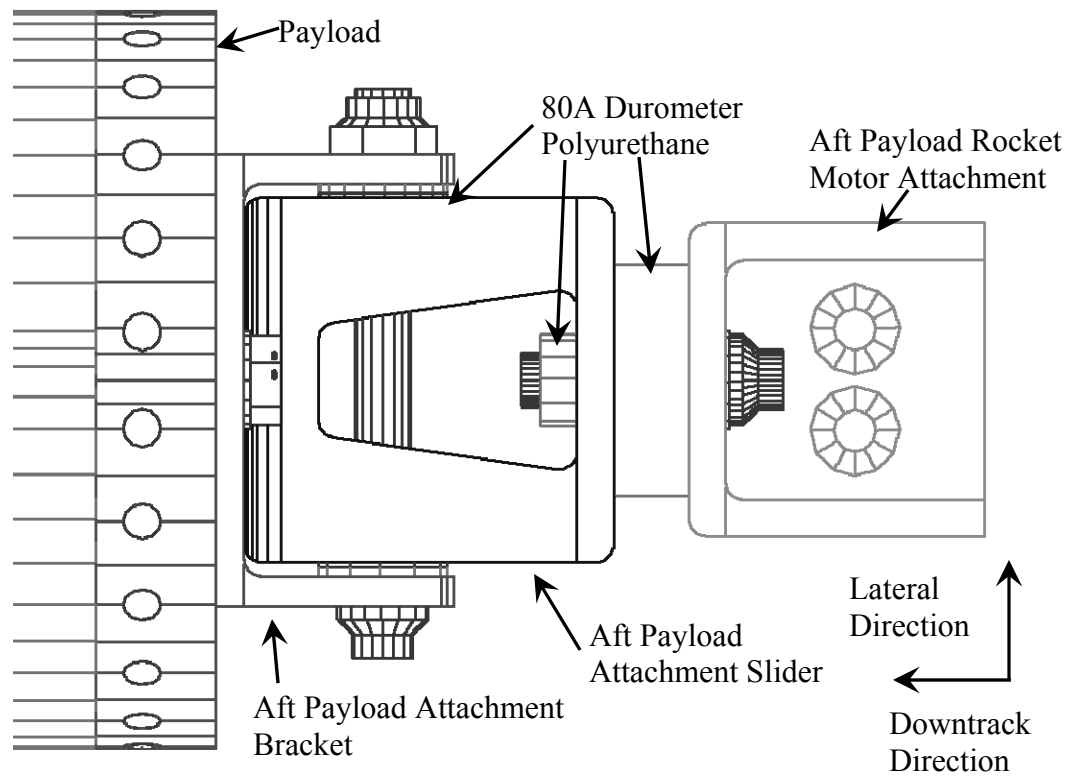
Figure 3.19 Aft Payload Downtrack and Lateral Vibration Isolation Mechanism
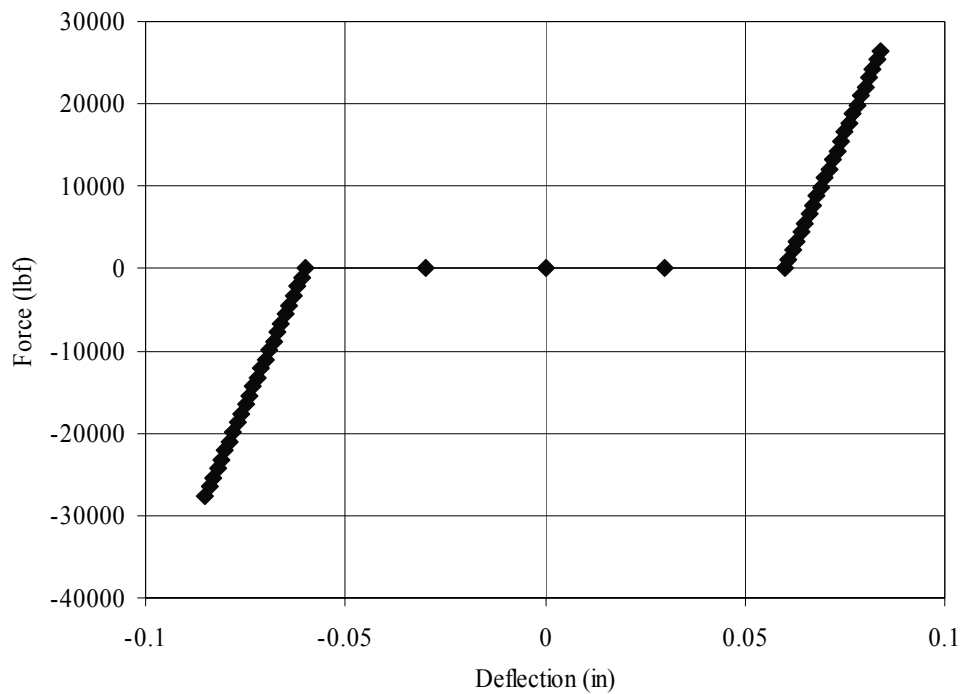
Figure 3.20 Gap Induced Nonlinear Stiffness at Payload Aft Vertical Attachment

strain gauges, and wiring; the original item weighed 5.7 lb_f. The typical local acceleration peak value in this area over the test duration is 35-50 Gs and results in a force of 210-400 lb_f when applied to the aft payload connecting mass. This value is near to the corresponding force measurement which was typically 200-700 lb_f. As a result the aft end of the payload was allowed to move freely through the aft payload connection gap.

An instrumentation pallet was installed on this sled to record, digitize, and telemeter data during the sled test. The instrumentation pallet consisted of electronic components hard mounted to two 0.25 in thick aluminum plates welded together to form a cruciform cross section inside of an aluminum cylinder as shown in Figure 3.21. The pallet was encased in polyurethane foam of varying density including 13, 15, and 35 lb_f/in^3. Since the pallet is much stiffer than the isolating foam it was modeled as a rigid point mass supported by translational springs on either end. The foam was idealized as a viscoelastic material where its stiffness and damping characteristics were determined from the lower curve of dynamic stress strain test data (General Plastics Manufacturing Company 2000). A precompression value of 0.25 in was used for the vertical and lateral directions and a precompression value of 1.72 in was used for the downtrack direction. The stiffness and damping values are provided in Table 3.16. The damping values are characteristic of 13 lb_f/in^3 foam and are derived from replicating the dynamic stress strain testing in DADS. The instrumentation mass properties listed in Table 3.17 are inclusive of the foam as detailed.
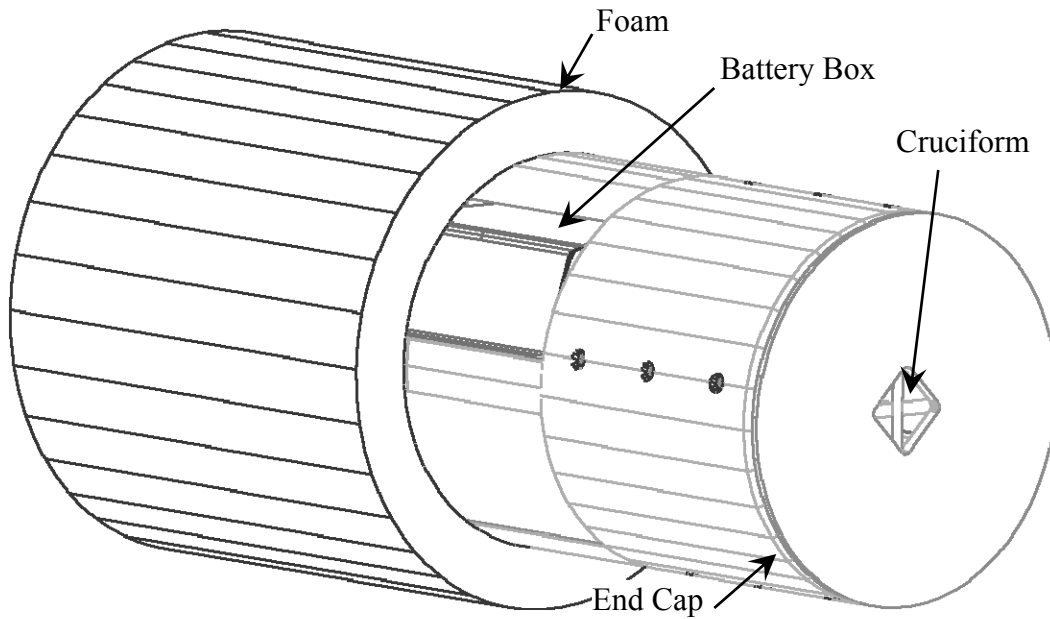
Figure 3.21 Instrumentation Pallet Depiction

Table 3.16 Instrumentation Pallet Foam Vibration Isolation Characteristics

Direction	Stiffness (lb_f/in)	Damping (lb_f s/in)
Vertical	1980	0.9
Lateral	1980	0.9
Downtrack	300	0.9

The most influential nonlinear boundary condition of the entire model is the slipper rail interface. The slipper and sled are constrained to the earth by the rail where slippers are of the same profile as the rail but over cut by an amount known as the slipper gap. This relationship is depicted in Figure 3.22. The boundary condition itself results in a quasi one-sided contact that allows the sled to respond in a free-free

Table 3.17 Instrumentation Pallet Rigid Mass Mass Properties

Component	Weight (lb$_f$)	Ixx (lb$_f$ s^2 in)	Iyy (lb$_f$ s^2 in)	Izz (lb$_f$ s^2 in)
Pallet	25.30	1.80	1.78	0.30
Foam	9.77	2.51	2.51	0.40
Composite	35.07	4.31	4.30	0.70
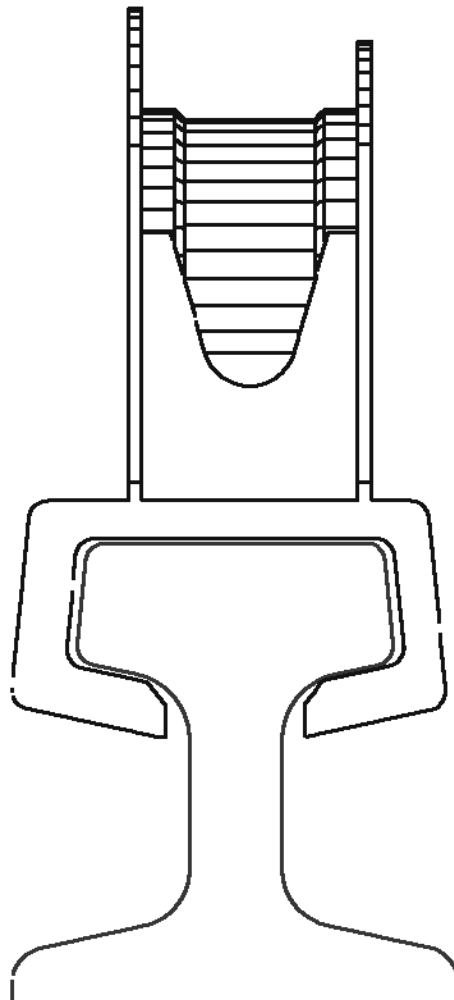
Figure 3.22 Slipper Rail Interface Showing Slipper Gap

mode when flying through the slipper gap and respond in a one-sided manner when in contact with the rail. To compound the matter further there are many combinations of this boundary condition as there is coupling due to the angled surfaces of the sides and bottom of the rail. This allows force propagation in both the vertical and lateral directions during lateral and vertical-up impacts. The actual contact between the two was discussed in detail in the preceding section and in short consists of force generation using stiffness and damping values to approximate the impact. This approximation was implemented in DADS using the Point-Seg-Rail contact element where each element consists of a single point on a slipper compliantly contacting a rigid rail. The rail profile depicted in Figure 3.4 was used to describe the rail cross section. Rail roughness, variations of the rail surfaces along the downtrack direction, was introduced using survey data processed for implementation into DADS. The survey data were acquired with a laser interferometric surveying system as part of the continuous rail alignment program carried on at the HHSTT. Rail downtrack measurements are accounted for using a Track Station (TS) terminology where TS 0.0 is the southernmost end of the HHSTT. The survey data was taken every 26 in and describes the deviation of the contact surface over which it is applied. The contact numbering scheme in Figure 3.4 shows two contact surfaces on the rail top (3 and 4), one contact surface on each of the lateral surfaces (2 and 5), and one contact surface on each of the rail head bottom surfaces (1 and 6). The two distinct surfaces on the rail top (3 and 4) were to account for fluctuations of rail head surface. The rail head bottom surfaces (1 and 6) used survey data from the corresponding rail head top

65

surface (3 and 4) as survey data from the rail head bottom is not measurable with current survey methods. The rail roughness and associated standard deviations are depicted in Figures 3.23, 3.24, 3.25, 3.26, and 3.27. The presence of three rail roughness profiles for B-rail opposed to two profiles for C-rail represents the available survey data at the time of this work.

3.5.3 External Loading, Aerodynamic and Thrusting

External loading was divided into lift, drag, and thrust. All three were applied to their respective directional components where the magnitude versus time was input into the model. For the LSR test the drag, Figure 3.28, lift, Figure 3.29, and thrust, Figure 3.30, were applied. For the CO test the drag, Figure 3.31, and lift, Figure 3.32, were applied.
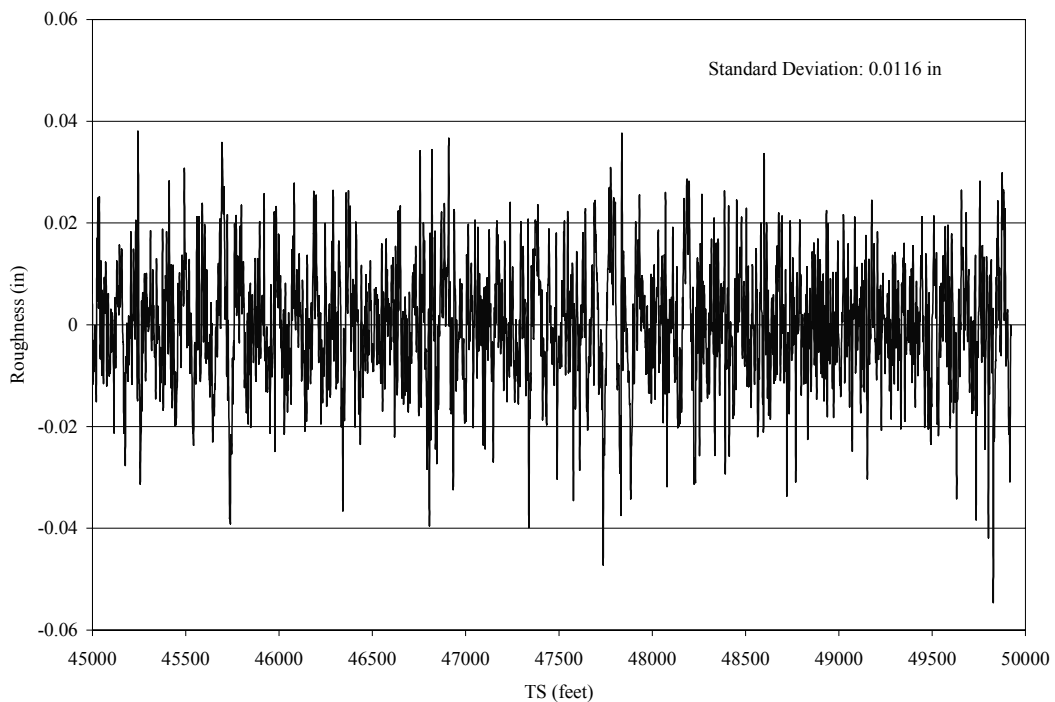
Figure 3.23 C-Rail East Vertical Roughness, DADS Contact Points 1, 3, 4, 6
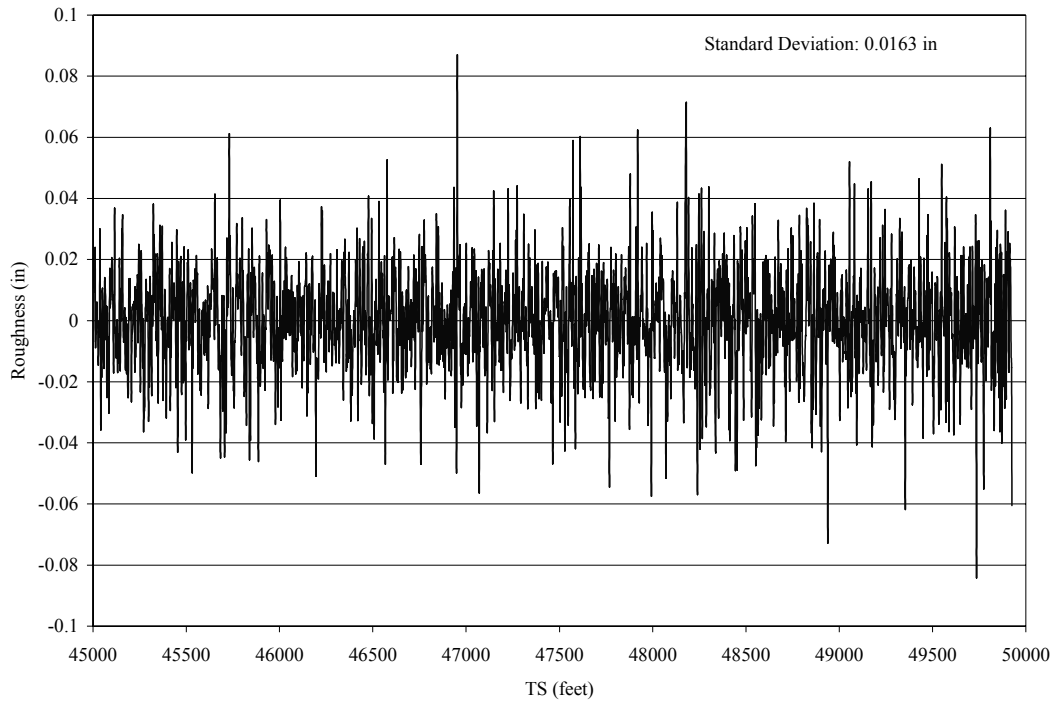
Figure 3.24 C-Rail East Lateral Roughness, DADS Contact Point 2
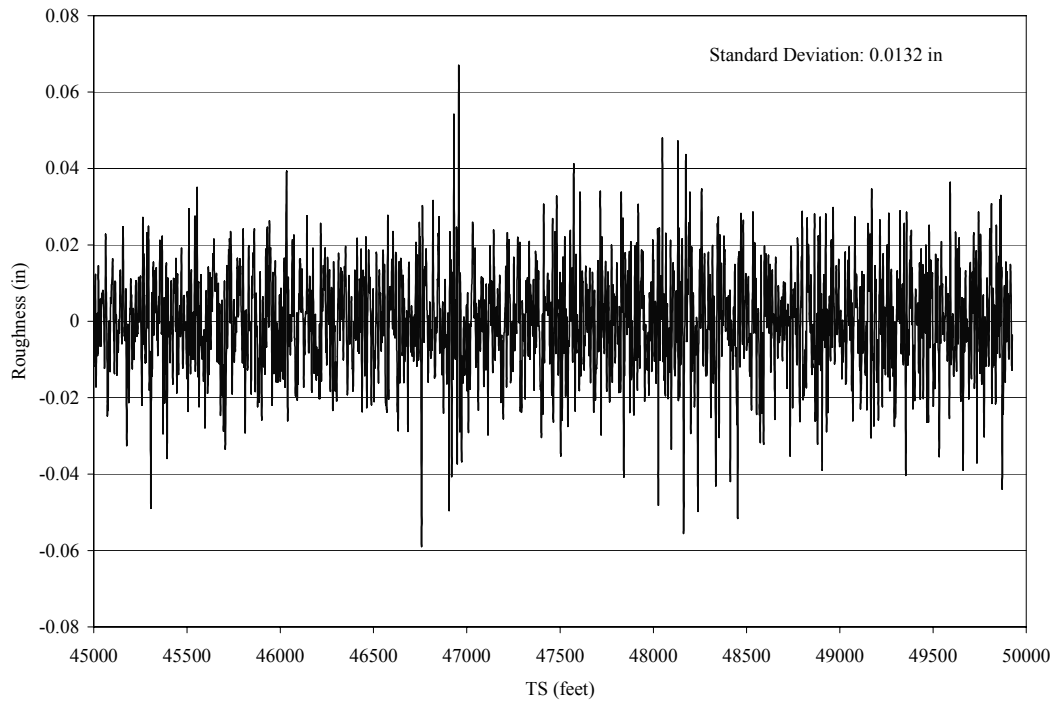
Figure 3.25 B-Rail West Lateral Roughness, DADS Contact Point 5
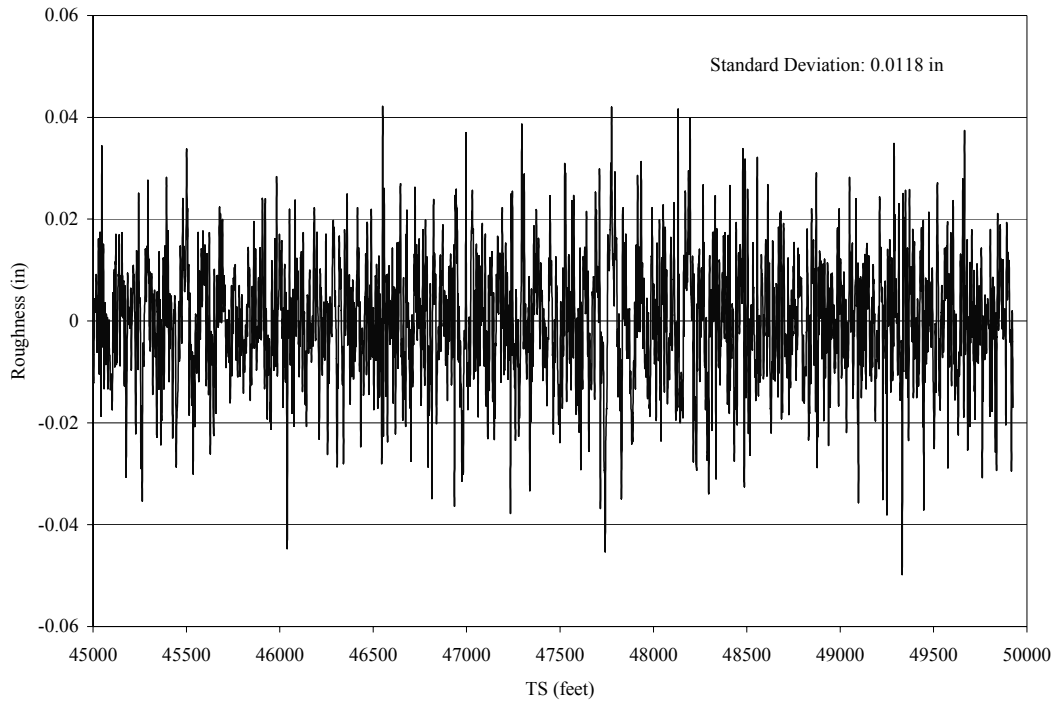
Figure 3.26 B-Rail East Vertical Roughness, DADS Contact Points 4 and 6
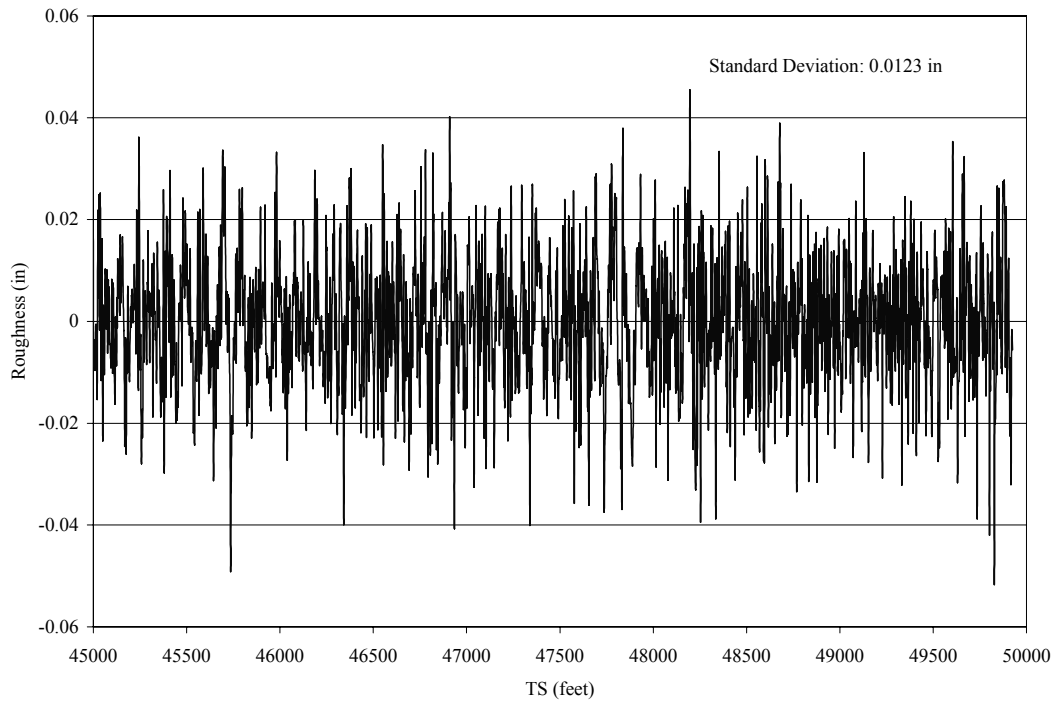
Figure 3.27 B-Rail West Vertical Roughness, DADS Contact Points 1 and 3
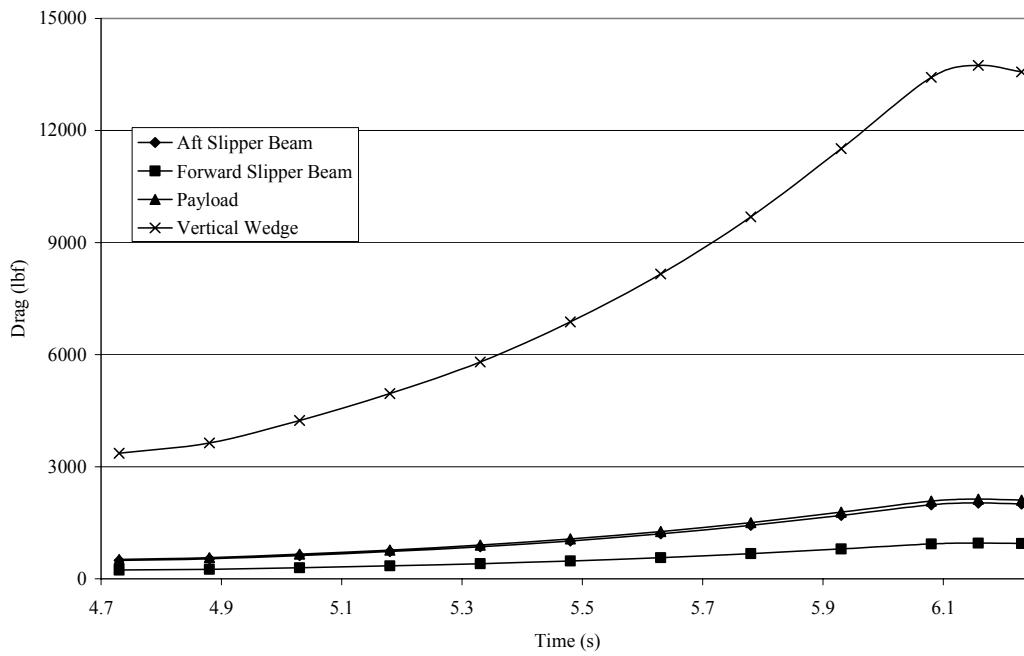
Figure 3.28 LSR Component Drag
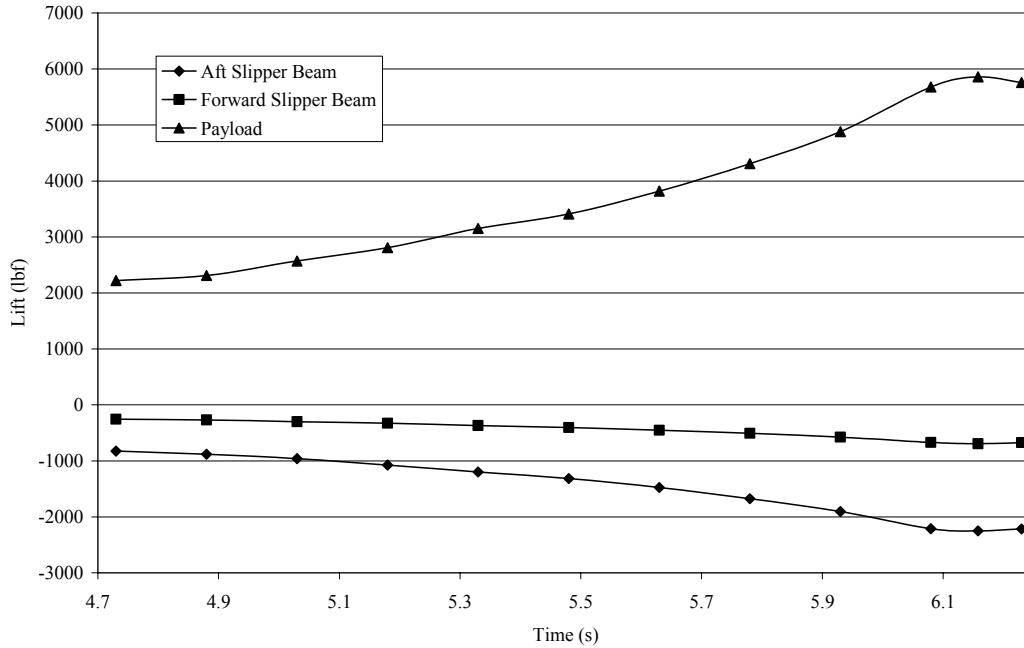
Figure 3.29 LSR Component Lift

69
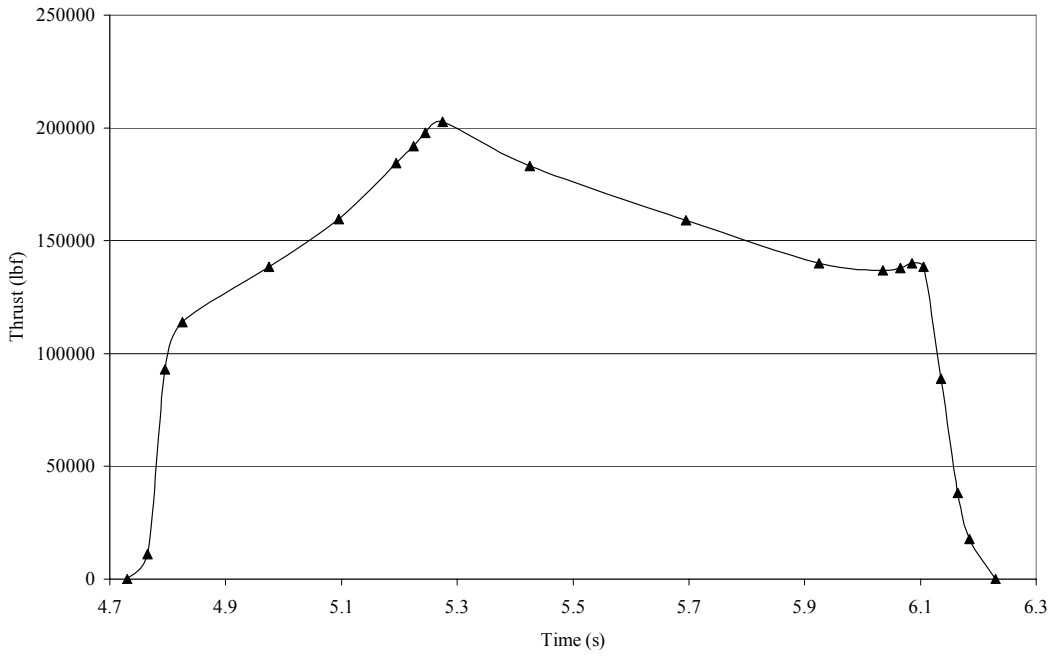
Figure 3.30 LSR Rocket Motor Thrust
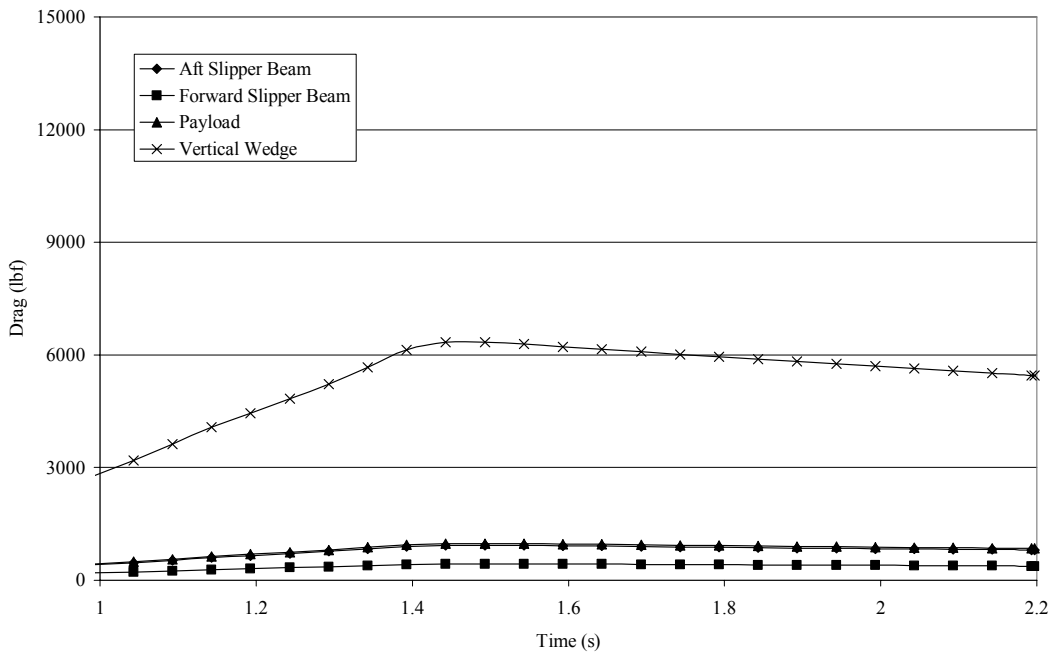
Figure 3.31 CO Component Drag
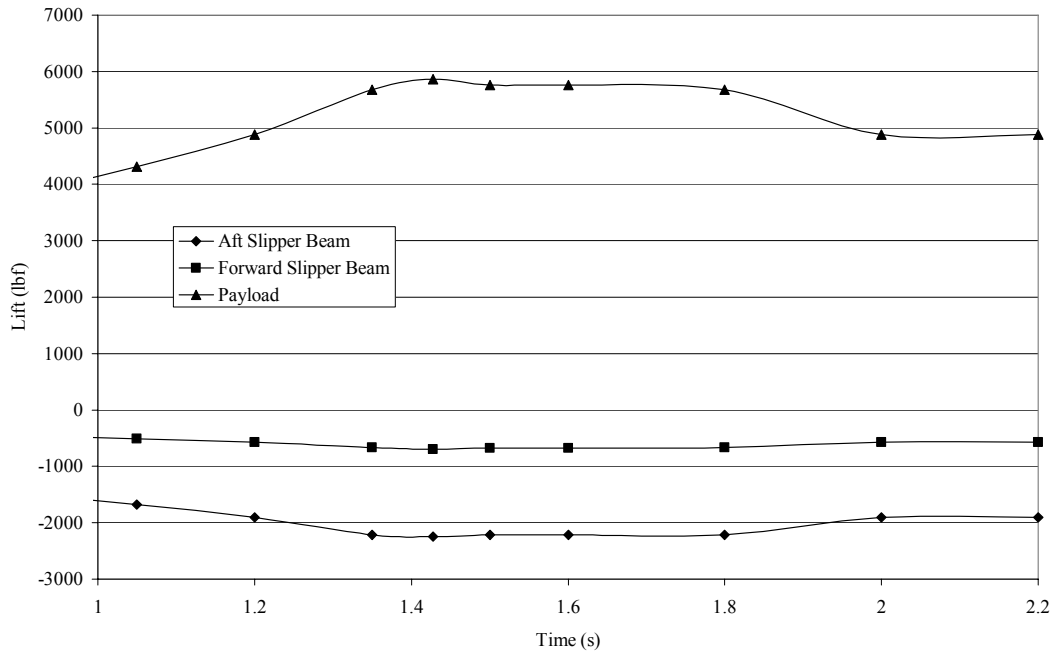
Figure 3.32 CO Component Lift

3.5.4 Rocket Motor Mass Variation

Rocket motor propellant mass was varied linearly within DADS for the LSR simulation during the thrust phase. DADS is a transient solver using numerical integration at each time step to solve the equations of motion, a zero mass property value would cause a matrix singularity. As a result of this, transient mass properties were at full value at the start of the simulation and linearly varied to a negligible value at the end of the simulation. The values used for the transient mass properties are produced from discretizing the propellant mass properties and are shown in Table 3.18. The propellant mass is non structural and has no effect on stiffness, but its effect on natural frequency of the rocket motor case is taken into account by varying the mass and inertia value.

71

Table 3.18 Propellant Mass Properties

Component Name	Mass (lbf s²/in)	Component Inertias (lbf s² in)			CG Location (in)		
		Ixx	Iyy	Izz	X	Y	Z
motor_f4	0.1098	2.04	2.04	3.58	0	0	122.80
motor_f3	0.2235	5.75	5.75	7.29	0	0	111.17
motor_f2a	0.1828	4.14	4.14	5.96	0	0	101.51
motor_f2	0.2062	5.02	5.02	6.72	0	0	93.76
motor_f1	0.2680	8.01	8.01	8.74	0	0	81.87
Motor	0.2865	9.11	9.11	9.34	0	0	68.22
motor_a1	0.2865	9.11	9.11	9.34	0	0	54.58
motor_a2	0.2865	9.11	9.11	9.34	0	0	40.93
motor_a3	0.2865	9.11	9.11	9.34	0	0	27.29
motor_a4	0.2408	6.57	6.57	7.85	0	0	13.64
Composite Total	2.9032	2643.09	2643.09	77.50	0	0	65.70

4. EVALUATION OF NUMERICAL MODEL AND OUTPUT CHARACTERISTIC STUDY

The narrow gauge sled model developed in DADS was studied in two areas: model validity and output characteristics. This was done to assess model quality against measured data sets and to give insight into model behavior with regard to input parameters to help determine initial model sensitivities and design drivers. The initial data set consisted of eleven channels of force, moment, and acceleration data from the LSR test (Turnbull and Minto 2003) where its collection points are schematically represented in Figure 4.1. The second data set consisted of sixteen channels of force, moment, and acceleration from a 5,343 fps velocity CO developmental test (Leadingham and Schauer 2001) where its collection points are schematically represented in Figure 4.2. The LSR test represented a maximum velocity case for test data and the CO test represented a lower velocity test where the sled was allowed to coast out while data were collected with the motor not burning. It should be noted that significant motor combustion instability effects were present while the motor was firing and arise from high amplitude internal pressure fluctuations occurring near 180 Hz. These effects are not modeled.

4.1 Evaluation of Numerical Model

The numerical model developed for DADS correlation required a comprehensive validation. The data from the LSR and CO tests was considered to be

Pyld Fwd Accelerations:

	STA	BL	WL
#139 Axial (PA)	52.52	0.00	28.34
#140 Lateral (PA)	53.12	0.60 (rt)	28.34
#141 Vertical (PA)	53.12	0.00	28.94

Pyld Aft Accelerations:

	STA	BL	WL
#123 Lateral (PA)	85.16	1.00 (lt)	27.82
#124 Vertical (PA)	85.16	1.60 (lt)	28.42

#112 Payload Pitch Bending Moment (SGB)
#113 Payload Yaw Bending Moment (SGB)
STA 39.93, BL 0.00, WL29.95

#115 Payload Aft Attachment Vertical Force (SGB)
#138 Payload Aft Attachment Lateral Force (SGB)
~STA 85.5 (Aft Hinge Axis STA 86.56, BL 0.00, WL 25.51)

Payload Front Attachment STA 50.0

STA 84.32

STA 0.00

WL 16.07

WL 29.95

WL 0.00

Aft Slipper Beam CL STA 170.58

Front Slipper Beam CL STA 49.83

#101 Front Slipper Beam Rocket Motor Attachment Vertical Force (SGB) BL 0.00, WL 3.75
#103 Front Slipper Right Lateral Force (IB) ~BL 13.1, WL 3.75

All sensors are based upon strain gage bridge installations.
IB = Instrumented Bolt (Commercial)
SGB = Strain Gage Bridge Circuit (Locally developed)
PA = Piezoresistive Accelerometer (Commercial)

CL = Centerline
(lt) = Left
(rt) = Right
Dimensions in inches

Figure 4.1 LSR Data Channel Schematic

Payload Fwd Data:

	STA	BL	WL
#112 Pitch Plane Bending Moment (SGB)	40.0	0.0	29.95
#114 Attachment Vertical Force (IB)	50.0	0.0	29.95
#113 Yaw Plane Bending Moment (SGB)	40.0	0.0	29.95
#121 Vertical Acceleration (PA)	20.6	0.0	29.95

#115 Payload Aft Attachment Pin Vertical Force (SGB)
#122 Payload Aft Axial Acceleration (PA)
~STA 86.0 (Hinge Axis BL 0.00 WL 25.51)

Station 0

WL 16.065

WL 29.95

WL 0.00

Forward Motor ~ STA 47.0, WL 16.07
#134 Vertical Acceleration (PA)
#136 Axial Acceleration (PA)

Aft Slipper Beam CL Sta. 170.8
#105 Motor Attachment Vertical Force (SGB)
#106 Right Lateral Force (SGB)
#107 Left Lateral Force (SGB)

Forward Slipper Beam CL Sta. 49.9, WL 3.75
#101 Motor Attachment Vertical Force (SGB) BL 0.0
#102 Motor Attachment Roll Moment (SGB) BL 0.0
#104 Left Lateral Force (IB) BL ~13.1 (lt)
#108 Right Roll Bending Moment (SGB) BL 5.08 (rt)
#109 Left Roll Bending Moment (SGB) BL 5.08 (lt)

IB=Instrumented Bolt
SGB=Strain Gage Bridge
PA=Piezoresistive Accelerometer

CL=centerline
(lt)=Left
(rt)=Right
Dimensions in inches

Figure 4.2 CO Data Channel Schematic

mildly stationary as most other high speed rocket sled data (Mixon 1971). The method used to compare the model data to the test data was to form statistical comparisons of each data channel in the time and frequency domains after applying a 3rd order digital bandpass filter, 10Hz to 4500Hz, in MATLAB. The time step for the DADS simulations was 1E-4 seconds to prevent aliasing and allow filtering up to 5,000 Hz giving an effective sampling rate of 10,000 Hz. Associated LSR data processing MATLAB scripts are located in Appendix C; the CO data processing scripts follow the exact algorithm but differ only to account for different channel names. The nature of the data also dictated that direct overlays of test and DADS data were not productive since any small shift in frequency or time step would generate significant deviations that were not reflective of the data comparison. Also the nature of rocket sled testing is that no two sled tests are the same since the sled impacts the rail in a random manner. Thus the vibration levels are similar for duplicate sleds but never observed to be identical. As a result the time and frequency domain comparisons were conducted in a velocity or frequency window for each respective domain. A weighted Root Mean Square (RMS) deviation Figure of Merit (FOM) system was used to measure the correlation of the DADS data to the test data. A FOM of 100% indicated complete correlation for that particular measurement. All individual FOMs were averaged with equal weighting to form a single composite FOM for the model in question for both the time and frequency domains.

4.1.1 Time Domain Comparison

The data comparison in the time domain consisted of parameterizing velocity over time and evaluating data over fixed velocity windows, 250 fps wide, to allow statistical properties to be extracted (Furlow 2006b). The reasoning behind windowing time domain data is twofold: first velocity windowing produces locally stationary data (Mixon 1971) allowing meaningful statistical evaluations, and second sled test vibration data is strongly velocity dependent (ISTRACON 1961, Hooser and Schwing 2000, and Mixon 1971). The standard deviation over the velocity window was then calculated using the default MATLAB algorithm. This process was accomplished for both test and DADS generated datasets. Linear curve fits for the test and DADS standard deviation data were calculated. The individual percentage deviation values of the DADS data from the test data curve fit were equally weighted by an amount whose summation equaled unity and the RMS of the weighted deviations was calculated and termed the RMS deviation for the particular data channel. A FOM was calculated as one hundred percent minus the RMS deviation and was used as a measure of correlation between the DADS and test data. This process was applied to all data channels annotated in Figures 4.1 and 4.2 and FOMs were produced for a DADS model and were then averaged into a single FOM to measure the correlation of that particular model. An example of the standard deviation (STD) vs. velocity overlay is shown in Figure 4.3 along with a sample of the calculations used to produce the data in Table 4.1.

STANDARD DEVIATION 101(Fwd SB Vertical Force)

$y = -4E-05x + 4.4626$

$y = 0.0017x - 5.5667$
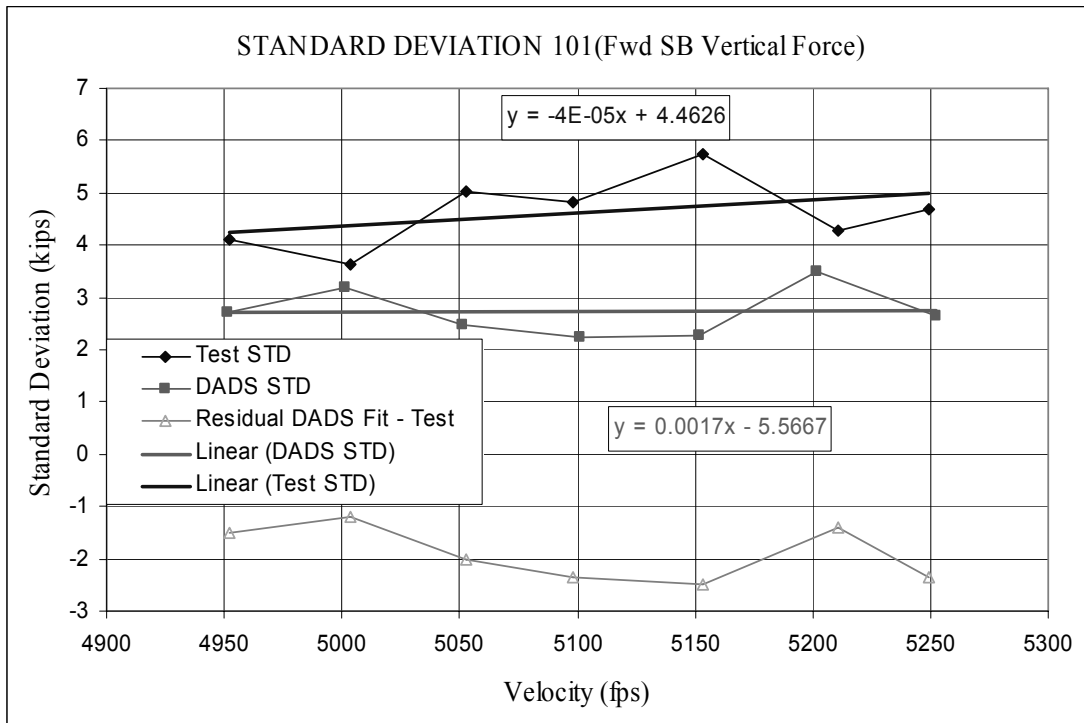
Figure 4.3 Time Domain Overlay, FOM 84.07%

Table 4.1 Time Domain Comparison Calculation

Test Data			DADS Data					%	%
Velocity	Stdev	Test Fit	Velocity	Stdev	DADS Fit			Weighted	Weighted
(fps)	(G)	(G)	(fps)	(G)	(G)	Residual	wt factors	Deviation	Deviation^2
5249.37	4.67	4.98	5252.05	2.63	2.73	-2.35	0.14	6.75	45.53
5211.10	4.27	4.89	5201.77	3.50	2.73	-1.39	0.14	4.07	16.52
5153.03	5.75	4.74	5151.44	2.26	2.72	-2.48	0.14	7.48	55.91
5097.75	4.84	4.60	5101.50	2.24	2.72	-2.36	0.14	7.32	53.61
5052.75	5.04	4.49	5051.43	2.48	2.71	-2.01	0.14	6.40	40.93
5003.84	3.64	4.36	5001.51	3.18	2.70	-1.18	0.14	3.87	14.97
4951.85	4.10	4.23	4951.55	2.72	2.70	-1.52	0.14	5.12	26.24
						0.53	1		15.93
						σ-res	Sum of weight factors		Rms % Dev

4.1.2 Frequency Domain Comparison

The data comparison in the frequency domain consisted of computing a Power

Spectral Density (PSD) of the data channel and then computing the RMS spectral

power within discrete frequency bands (Furlow 2006b). The use of discrete frequency bands allowed small frequency shifts to exist but not significantly affect the comparison and also to better characterize the response of the model or test hardware in the frequency domain. The computation of the RMS power consisted of numerically integrating the PSD over the discrete frequency band using a simple Romberg integration algorithm and taking the square root of the integral. The percentage deviation of the DADS-generated data from the test data was weighted by an amount equal to the normalized distribution of the test data RMS spectral power from 0 to 1000 Hz. This weighted distribution allows an efficient comparison of the DADS-generated data to the test data. The deviation at each discrete frequency band was computed into a single RMS deviation value which was then subtracted from one hundred to produce the FOM for the data channel in question. For each of the data channels the frequency FOM was averaged into a single FOM to represent the measure of correlation for the DADS model to the sled test. An example of the PSD overlay of DADS and test data is shown in Figure 4.4 and the calculations used to produce a FOM for the overlay is shown in Table 4.2. Discrepancies in total power values indicate one of two things: 1) an under representation of the system frequency response due to discretizing a continuous system, or 2) a shift in frequency response in the model where response is greater elsewhere than at the particular measurement location.

PSD 101 (Fwd SB Vertical Force)
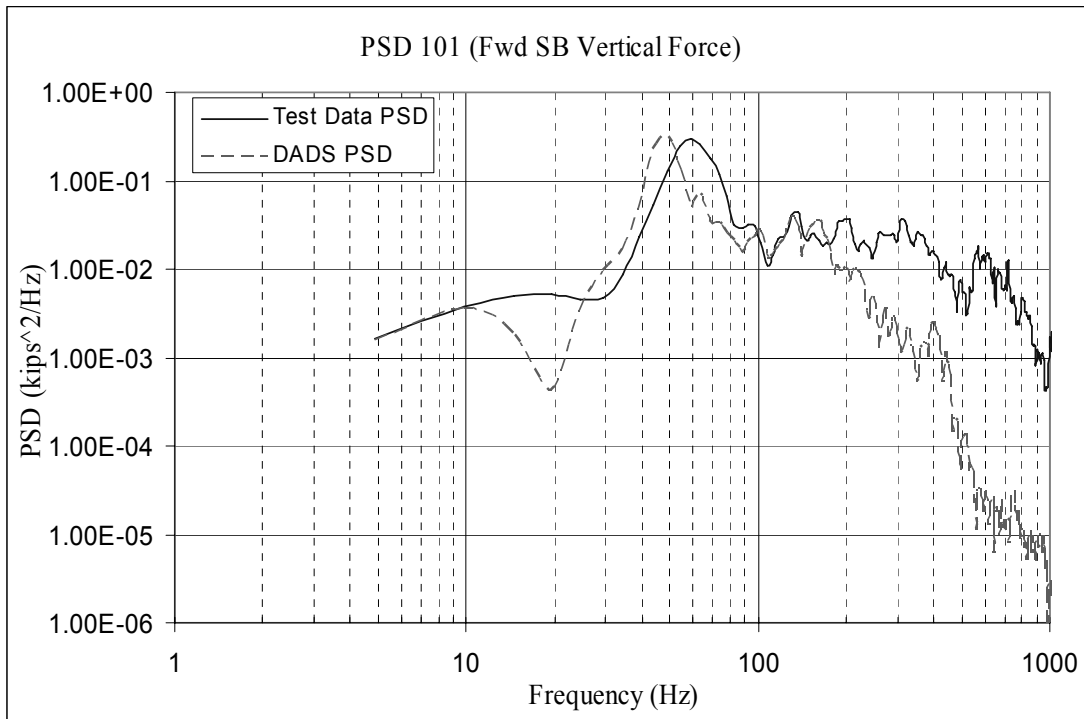
Figure 4.4 PSD Overlay, FOM 70.00%

4.1.3 Correlation Criteria

A FOM threshold was established for individual and composite FOM to define correlation. A FOM of 100% denoted complete correlation and is only achievable under artificial conditions since sled tests are nondeterministic. Thresholds for frequency and time domain composite and individual FOM values were established where greater than 80% for time domain FOM and greater than 70% for frequency domain FOM in the composite category denoted acceptable levels while specifying that no individual frequency domain FOM could be less than 50% and no individual time domain FOM could be below 70%. The additional constraint in the time domain correlation data comes from the fact that the ultimate goal of this

Table 4.2 RMS Power Calculation

Frequency (Hz)	Test Data		DADS Data		Weight Factors	% Weighted Deviation
	RMS Power (G rms)	% TTL RMS PWR	RMS Power (G rms)	% TTL RMS PWR		
9.77	0.13	0.03	0.13	0.05	0.031	-0.09
24.41	0.16	0.04	0.08	0.03	0.038	-1.89
48.83	0.63	0.15	1.29	0.46	0.147	15.49
97.66	1.79	0.42	0.74	0.26	0.419	-24.50
151.37	0.25	0.06	0.26	0.09	0.058	0.43
200.20	0.21	0.05	0.18	0.06	0.049	-0.74
249.02	0.16	0.04	0.06	0.02	0.038	-2.42
297.85	0.17	0.04	0.02	0.01	0.039	-3.42
351.56	0.19	0.05	0.01	0.00	0.045	-4.22
400.39	0.13	0.03	0.01	0.00	0.030	-2.74
454.10	0.08	0.02	0.01	0.00	0.018	-1.49
498.05	0.03	0.01	0.00	0.00	0.008	-0.79
546.88	0.03	0.01	0.00	0.00	0.008	-0.75
600.59	0.09	0.02	0.00	0.00	0.021	-2.14
654.30	0.07	0.02	0.00	0.00	0.016	-1.64
698.24	0.04	0.01	0.00	0.00	0.009	-0.90
751.95	0.04	0.01	0.00	0.00	0.010	-1.01
800.78	0.02	0.00	0.00	0.00	0.004	-0.42
854.49	0.02	0.01	0.00	0.00	0.005	-0.53
898.44	0.01	0.00	0.00	0.00	0.002	-0.21
952.15	0.01	0.00	0.00	0.00	0.002	-0.15
1000.98	0.00	0.00	0.00	0.00	0.001	-0.09
	4.26 Total Power		2.80 Total Power			30.00 Rms % Dev

study is to produce predictions for peak dynamic load and thus matching locally stationary peak values is more important than frequency characterization although the two are related. The only external sled forces that are not directly determinable are slipper rail impacts so considerable attention was paid to the FOMs associated with measurements near the slipper rail interface: channels 101 and 103 in Figure 4.1 and channels 101, 102, 104, 105, 106, 107, 108, and 109 in Figure 4.2.

4.2 Output Characteristic Study

The DADS model described in Section 3.5 was constructed to emulate the

LSR and CO tests and their FOMs were monitored for correlation. Also the output of

the DADS models were monitored during the correlation effort to gain insight into

model behavior and an initial understanding of design parameters that govern this

behavior. This study consisted of monitoring the FOMs produced in the correlation

to assess sensitivity to design parameter variation. Model refinement was employed

to ensure that the model ultimately converged to an acceptable value of FOMs for

each data channel monitored. Correlated models were produced, and general output

parameter sensitivities were noted during model refinement and flexible body

formulation.

4.2.1 Modal Model Characteristics

Modal model outputs were prescribed to correspond as closely as possible to

the test data locations shown in Figures 4.1 and 4.2. Nodes were used to track

displacement, velocity, and acceleration data; force and moment data were taken at

DADS-prescribed major structural component connection elements. Nodes are FEM

point masses and were discretized in I-DEAS where other masses were represented in

DADS as a point mass. The source of DADS data outputs are detailed in Tables 4.3

and 4.4 and show the particular method and measurement type. The DADS element

TSDA refers to a translational spring. The DADS element Bracket refers to an

analyst prescribed rigid connection of two masses. The DADS element Bushing

Table 4.3 LSR Modal Model Output Measurement

Channel Number	Measurement Type	DADS Element Type	DADS Model Element Name
101	Vertical Force	DADS TSDA	TSDA_MB_F
103	Lateral Force	DADS TSDA	TSDA_FRONT_BELL1b
112	Pitching Moment	DADS Bracket	BRACKET_PL_SRR_FRONT
113	Yawing Moment	DADS Bracket	BRACKET_PL_SRR_FRONT
115	Vertical Force	DADS Bushing, Pair	BUSH_LAT_SIM_ATCH_L/R
123	Lateral Acceleration	Node	PAYLOAD_FLEX_FLEX:node 59
124	Vertical Acceleration	Node	PAYLOAD_FLEX_FLEX:node 60
138	Lateral Force	DADS TSDA, Pair	TSDA_LAT_SIM_ATCH_R/L
139	Downtrack Acceleration	Node	PAYLOAD_FLEX_FLEX:node 62
140	Lateral Acceleration	Node	PAYLOAD_FLEX_FLEX:node 63
141	Vertical Acceleration	Node	PAYLOAD_FLEX_FLEX:node 64

refers to a flexible connection of two masses whose stiffnesses emulate a bushing.

All output measurements were sensitive to changes in the stiffness parameters of the connecting elements and slipper impact parameters. The LSR output channels 139, 140, and 141 and CO output channel 122 were the least sensitive to the parameter changes since they are physically remote from the slipper rail interaction and the sled loading is highly attenuated along this load path. High damping at the

Table 4.4 CO Modal Model Output Measurement

Channel Number	Measurement Type	DADS Element Type	DADS Model Element Name
101	Vertical Force	DADS TSDA	TSDA_MB_F
102	Roll Moment	DADS Bracket	BRACKET_MB_F
104	Lateral Force	DADS TSDA	TSDA_FRONT_BELL2b
105	Vertical Force	DADS TSDA	TSDA_MB_A
106	Lateral Force	DADS TSDA	TSDA_REAR_BELL1b
107	Lateral Force	DADS TSDA	TSDA_REAR_BELL2b
108	Roll Moment	DADS Bracket	BRACKET_MB_F
109	Roll Moment	DADS Bracket	BRACKET_MB_F
112	Pitching Moment	DADS Bracket	BRACKET_PL_SRR_FRONT
113	Yawing Moment	DADS Bushing, Pair	BRACKET_PL_SRR_FRONT
114	Vertical Force	DADS TSDA	TSDA_FRONT_PL_ATCH
115	Vertical Force	DADS Bracket	BRACKET_PL_SRR_AFT
121	Vertical Acceleration	Node	PAYLOAD_FLEX_FLEX:node23
122	Axial Acceleration	Node	PAYLOAD_FLEX_FLEX:node1
134	Vertical Acceleration	Node	SRR_FLEX:node29
136	Axial Acceleration	Node	SRR_FLEX:node29

slipper-rail interface and vibration isolation locations tended to inaccurately reduce acceleration levels and increase loading at the interfaces. The stiffness of the connection at measurement 115 was factored from its original expected value of 1,102,961 lb_f/in to 55,148 lb_f/in. It is noted that the actual condition of this joint was that a gap of unknown magnitude existed. Also the exact nature of this contact is not known during the LSR and CO tests, and thus some factoring is acceptable. Output sensitivity indicated that modal modeling was highly dependent upon mode shapes retained for sled modeling. DADS/Flex allows the analyst to choose which mode shapes to include for orthogonalization and these choices were made on the basis of retaining the lower fundamental frequencies in displacements of interest and ensuring that the DADS/Flex orthogonalization algorithm produced orthogonal mode shapes. There were instances with all modal representations where using all available mode shapes did not produce an orthogonal set and higher order mode shapes were rejected until the algorithm was successful. The degree to which this phenomena impacts accurate modal representations depends upon on the number of mode shapes retained to produce an orthogonalized set. The methodology followed herein is to include the maximum number of mode shapes while assuring the lower frequency mode shapes were retained. It should be noted that DADS is not able to successfully process an unorthogonalized set of modes shapes for flexile body analyses.

Principal strengths in using modal representation of flexible bodies is the ease of modeling in CAD packages, and specifically in I-DEAS, the formation of beam models includes the use of Timoshenko beam theory. The shear deflection effect, in

addition to the inclusion of higher order vibration effects via rotary inertia, is automatically included in this scenario. DADS simulation times were up to 50% less using modal representation than with the SMD representation.

Weaknesses include the dependency of the modal response on fixed boundary conditions which for linear systems is not an issue. For this sled with several instances of nonlinearity that are present in the interconnection of the major structural components, it is a problem that cannot be completely solved by substructuring. This forces the analyst to modify the parameters of connecting structures or major structural component boundary conditions to force a particular response.

4.2.2 SMD Model Characteristics

SMD model outputs were prescribed to coincide with test data locations shown in Figures 4.1 and 4.2. Masses were used to produce displacement, velocity, and acceleration data where force and moment data were taken at DADS prescribed major structural component connection elements. The source of DADS data outputs are detailed in Tables 4.5 and 4.6 and show the particular method and measurement type.

Principal strengths of modeling with the SMD scheme is the ability to construct a flexible body irrespective of boundary conditions. The resulting model will respond to nonlinear inputs or boundary conditions based upon its mass discretization and stiffness formulation. The flexibility representation chosen for this study is Euler-Bernoulli theory which is the default within DADS; any other theory

Table 4.5 LSR SMD Model Output Measurement

Channel Number	Measurement Type	DADS Element Type	DADS Model Element Name
101	Vertical Force	DADS Bushing	BUSHING.F_SB
103	Lateral Force	DADS TSDA	TSDA_FRONT_BELL 1b
112	Pitching Moment	DADS Beam Force Element	PL_5_PL_4
113	Yawing Moment	DADS Beam Force Element	PL_5_PL_4
115	Vertical Force	DADS Beam Force Element	PL_1_PL_AFT
123	Lateral Acceleration	Mass	SIM_ATCH_AFT_2
124	Vertical Acceleration	Mass	SIM_ATCH_AFT_2
138	Lateral Force	DADS Beam Force Element	PL_1_PL_AFT
139	Downtrack Acceleration	Mass	PL_3
140	Lateral Acceleration	Mass	PL_3
141	Vertical Acceleration	Mass	PL_3

would have to be entered via matrices in text files. Earlier work (Furlow 2004)

indicated some isolated instances of DADS solver instability and overall difficulty in

managing text file input stiffness matrices. The main concern with using Euler-

Bernoulli theory with relatively short length beams is that shear deflection may be

significant and that the resulting deflection error may propagate. It was shown for a

Table 4.6 CO SMD Model Output Measurement

Channel Number	Measurement Type	DADS Element Type	DADS Model Element Name
101	Vertical Force	DADS Bushing	BUSHING.F_SB
102	Roll Moment	DADS Bracket	BRACKET_MB_F
104	Lateral Force	DADS TSDA	TSDA_FRONT_BELL 2b
105	Vertical Force	DADS TSDA	BUSHING.A_SB
106	Lateral Force	DADS TSDA	TSDA_REAR_BELL1 b
107	Lateral Force	DADS TSDA	TSDA_REAR_BELL2 b
108	Roll Moment	DADS Beam Element	BEAM_F_SB_R_2
109	Roll Moment	DADS Beam Element	BEAM_F_SB_L_2
112	Pitching Moment	DADS Beam Element	PL_5_PL_4
113	Yawing Moment	DADS Beam Element	PL_5_PL_4
114	Vertical Force	DADS Bushing	BUSHING.PL_M_FOR
115	Vertical Force	DADS Beam Element	PL_1_PL_AFT
121	Vertical Acceleration	Mass	PL_CONE
122	Axial Acceleration	Mass	SIM_ATCH_AFT_2
134	Vertical Acceleration	Mass	M_FOR
136	Axial Acceleration	Mass	M_FOR

collection of short Euler-Bernoulli beams (Furlow 2004) that it was possible to obtain

deflections for the composite beam that were not affected by shear deflection effects.

4.3 Flexible Body Representation Selection

To proceed with the next phase of the study, wide scale parameter variation, a

reduced complexity model was to be constructed requiring the selection of a flexible

body representation. For the LSR test data set the best case FOM Summary is

presented in Table 4.7 for the modal representation and in Table 4.8 for the SMD

representation. It was very difficult to achieve a FOM Summary that met the

correlation criteria for the LSR test data set. This is partly due to unknown nonlinear

boundary conditions, unknown structural connections and from combustion

instability of the rocket motor. The combustion instability represented not only a

significant fluctuation in thrust but also a noticeable expansion and contraction of the

rocket motor cross section affecting data outputs at the payload attachment points.

The influence on the rocket motor cross sections is difficult to measure

experimentally and thus difficult to characterize and include in a numerical model.

The CO test data comparisons were more favorable as data were acquired during the

decelerating non-thrusting portion of the sled test that was free of combustion

instability. Thus a more direct comparison was made. The best case FOM summary

is shown for the modal representation in Table 4.9 and SMD representation is shown

in Table 4.10. The SMD flexible body formulation is the better choice for flexible

body representation as it exhibited the best overall FOM especially in the

measurement locations near the slippers and slipper beams and thus more accurately describes dynamic loading from the slipper-rail interface. The SMD flexible body formulation also displays more fidelity as it allows a more detailed description of structural response as boundary conditions, mode shape selection, and orthogonalization are not required for prescribing flexible body representation. The best case FOM summary is listed in Table 4.10 and meets the minimum criteria except for 113 which is away from the slippers and slipper beams. It should be noted for less complex bodies with linear connections the modal representation may be more desirable as its element formulation is superb and its solution time is generally lower than the SMD representation.

Table 4.7 LSR Modal FOM Summary

Channel	Description	FOM	
		Frequency	Time
101	Forward Slipper Beam Vertical Force	58.81	75.27
103	Forward Slipper Beam Lateral Force	69.07	79.05
112	Payload Pitch Bending Moment	63.23	84.12
113	Payload Yaw Bending Moment	64.68	87.29
115	Payload Aft Attachment Vertical Force	41.55	86.39
123	Payload Aft Lateral Acceleration	81.68	90.31
124	Payload Aft Vertical Acceleration	83.68	87.61
138	Payload Aft Attachment Lateral Force	83.12	90.33
139	Payload Forward Axial Acceleration	84.32	90.42
140	Payload Forward Lateral Acceleration	76.25	93.77
141	Payload Forward Vertical Acceleration	76.91	89.39
	Composite FOM	71.21	86.72

Table 4.8 LSR SMD FOM Summary

Channel	Description	FOM Frequency	FOM Time
101	Forward Slipper Beam Vertical Force	81.15	86.30
103	Forward Slipper Beam Lateral Force	61.19	55.82
112	Payload Pitch Bending Moment	33.61	86.47
113	Payload Yaw Bending Moment	64.23	90.84
115	Payload Aft Attachment Vertical Force	53.72	84.42
123	Payload Aft Lateral Acceleration	47.04	86.35
124	Payload Aft Vertical Acceleration	42.21	92.51
138	Payload Aft Attachment Lateral Force	64.42	85.64
139	Payload Forward Axial Acceleration	72.36	88.75
140	Payload Forward Lateral Acceleration	57.60	93.77
141	Payload Forward Vertical Acceleration	83.38	92.81
	Composite FOM	60.08	85.79

Table 4.9 CO Modal FOM Summary

Channel	Description	FOM Frequency	FOM Time
101	Forward Slipper Beam Vertical Force	63.85	82.63
102	Forward Slipper Beam Roll Moment	69.86	93.78
104	Forward Slipper Beam Left Lateral Force	83.51	91.49
105	Aft Slipper Beam Vertical Force	70.64	86.04
106	Aft Slipper Beam Right Lateral Force	84.54	87.95
107	Aft Slipper Beam Left Lateral Force	81.36	91.34
108	Forward Slipper Beam Right Roll Moment	78.90	88.65
109	Forward Slipper Beam Left Roll Moment	76.73	91.38
112	Payload Pitch Bending Moment	72.47	69.39
113	Payload Yaw Bending Moment	37.07	62.50
114	Payload Forward Vertical Force	69.14	70.74
115	Payload Aft Attachment Vertical Force	51.98	85.48
121	Payload Forward Vertical Acceleration	77.71	88.63
122	Payload Aft Axial Acceleration	81.52	86.24
134	Motor Forward Vertical Acceleration	76.40	80.63
136	Motor Forward Axial Acceleration	61.43	74.18
	Composite FOM	71.07	83.19

Table 4.10 CO SMD FOM Summary

Channel	Description	FOM Frequency	FOM Time
101	Forward Slipper Beam Vertical Force	70.00	84.07
102	Forward Slipper Beam Roll Moment	71.21	83.33
104	Forward Slipper Beam Left Lateral Force	78.33	95.72
105	Aft Slipper Beam Vertical Force	72.91	87.43
106	Aft Slipper Beam Right Lateral Force	86.03	90.04
107	Aft Slipper Beam Left Lateral Force	80.68	92.52
108	Forward Slipper Beam Right Roll Moment	69.61	91.76
109	Forward Slipper Beam Left Roll Moment	76.06	92.64
112	Payload Pitch Bending Moment	66.25	84.34
113	Payload Yaw Bending Moment	43.05	73.41
114	Payload Forward Vertical Force	69.37	74.64
115	Payload Aft Attachment Vertical Force	71.82	96.11
121	Payload Forward Vertical Acceleration	79.54	95.05
122	Payload Aft Axial Acceleration	71.61	95.52
134	Motor Forward Vertical Acceleration	77.77	76.27
136	Motor Forward Axial Acceleration	52.79	92.03
	Composite FOM	71.06	87.80

5. EVALUATION OF LARGE SCALE DESIGN
PARAMETER VARIATION

The parameter variation process was used to determine the sensitivity of the

sled model to different design inputs. After the DADS modeling process was

successfully correlated a reduced complexity model was produced with the correlated

modeling process. The model itself is similar to the third stage pusher sled used to

propel the LSR forebody to its maximum velocity. After constructing the reduced

complexity model its design parameters were varied and the corresponding solutions

were extracted. The design parameters were varied to encompass a range expected

during the normal course of track testing. Possible design parameter values included

a typical, high, and low to describe the range expected. Parameter variation was

accomplished in increasingly detailed steps indicative of the refinement needed to

ensure description of the dynamic loading outputs observed. For all parameter

variations, error tracking of the processed results was carried out to ensure that during

the execution of hundreds of simulations that excessive deflection and out of

tolerance downtrack velocity did not occur.

5.1 Construction of Reduced Complexity Parameter Variation Model

The numerical model developed for correlation in Chapter 4 served as a base

from which the reduced complexity parameter variation model was constructed.

Directly retained were the slippers along with their associated contact values which

were generated in Chapter 3 to describe slipper rail impact. The slipper beam

composition was made more uniform and the attachment was done through its neutral axis to help prevent extraneous deflection coupling in the vertical and lateral directions. Differences included a fixed mass for the sled body and no payload. The reduced complexity produced a sled configuration more applicable to general sled testing to ease the computational burden of the numerical solutions associated with wide scale parameter variation. Aerodynamic loading was omitted to allow a peak load that is purely dependent upon dynamic effects of the sled interacting with the rail and resulting frequency responses.

The thrust applied to the sled produced a constant acceleration required to propel the sled from 0 to 10,000 fps. The thrust is 105,275.4 lb_f and is intended to propel a 842.3 lb_f sled to 10,000 fps in 2.49 seconds at 125 Gs. The resulting reduced complexity model is depicted in Figure 5.1.

5.1.1 Sled Body

The sled body was modeled as a 136 in long cylindrical tube discretized into 12 equal evenly spaced masses having the mass properties shown in Table 5.1 for the typical mass values. The discretization was accomplished such that all masses had the same values representing an equal 11.33 in of the sled body length. The total mass and associated properties are the same as a final stage rocket motor used on the LSR and CO tests that is half way through its thrusting cycle. The thrust was applied at the forward most mass, m_for. The flexibility between the masses was prescribed with DADS Beam Force Elements using the constant property cross section detailed
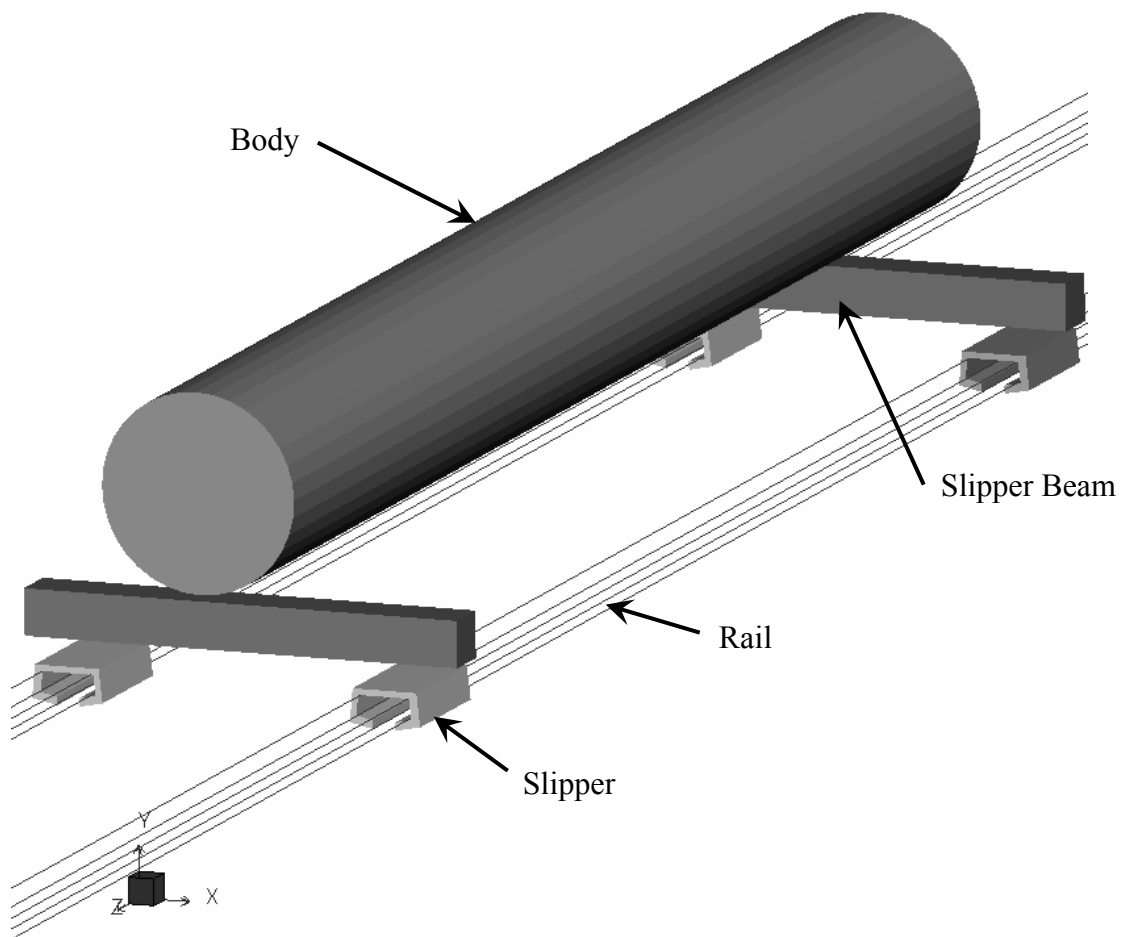
Figure 5.1 Reduced Complexity Model Depiction

in Table 5.2 and applied to associated elements in the model with a structural

damping ratio of 5.0% of critical. The flexibility was prescribed from the typical

cross section of the final stage rocket motor used on the LSR and CO tests which

represented 80% of the total cross sectional area as calculated along the length of the

body. It should be noted that the relationship of the polar moment of inertia to the

area moments of inertia for the rocket motor is maintained.

Table 5.1 Sled Body Mass Distribution

Name	Mass ($lb_f\,s^2$/in)	Location From Centerline and Body Aft End (in)			Mass Properties about CG ($lb_f\,s^2$ in)		
		X	Y	Z	Ixx	Iyy	Izz
m_for	0.138	0.00	0.00	130.33	14.617	14.409	2.347
m_f4	0.138	0.00	0.00	119.00	14.617	14.409	2.347
m_f3	0.138	0.00	0.00	107.67	14.617	14.409	2.347
m_f2a	0.138	0.00	0.00	96.33	14.617	14.409	2.347
m_f2	0.138	0.00	0.00	85.00	14.617	14.409	2.347
m_f1	0.138	0.00	0.00	73.67	14.617	14.409	2.347
m	0.138	0.00	0.00	62.33	14.617	14.409	2.347
m_a1	0.138	0.00	0.00	51.00	14.617	14.409	2.347
m_a2	0.138	0.00	0.00	39.67	14.617	14.409	2.347
m_a3	0.138	0.00	0.00	28.33	14.617	14.409	2.347
m_a4	0.138	0.00	0.00	17.00	14.617	14.409	2.347
m_aft	0.138	0.00	0.00	5.67	14.617	14.409	2.347

Table 5.2 Sled Body Flexibility

Name	Length (in)	Area (in^2)	Iy (in^4)	Iz (in^4)	J (in^4)	Young's Modulus (lb$_f$/in^2)	Poisson's Ratio
beam_for_f4							
beam_f4_f3							
beam_f3_f2a							
beam_f2a_f2							
beam_f2_f1							
beam_f1_mtr	11.33	13.398	377.743	377.743	377.743	11.75E6	0.28
beam_mtr_a1							
beam_a1_a2							
beam_a2_a3							
beam_a3_a4							
beam_a4_aft							

5.1.2 Slipper Beam

Both forward and aft slipper beams were modeled as 3.5 in by 3.5 in 0.375 in

thick annular box beams 36 in long. The beams were discretized into 13 equal

portions each having a length of 2.308 in as shown in Table 5.3. The flexibility

between the discretized masses was represented using DADS Beam force elements

applying the constant cross sectional properties shown in Table 5.4. The slipper

beams were modeled as Vascomax 300, a high nickel maraging steel, with a Young's

modulus of 27.5E6 lb_f/in^2 and a Poisson's ratio of 0.32. The flexibility was

implemented in DADS using the DADS Beam Force Element and applying the

corresponding values with a structural damping value of 3.0% of critical. Both the

forward and aft slipper beams were the same with regard to mass and flexibility

distribution.

5.1.3 Slippers

The slippers were retained directly from the correlation modeling effort for

the SMD LSR model (846th Test Squadron 2003) as they represented a successfully

employed real world standard that will be used in future narrow gauge testing. The

slipper was discretized into eight masses connected using DADS Beam Force

Elements as depicted in Figure 5.2 and listed in Table 5.5. Equivalent beam sections,

as detailed in Chapter 3, were employed in the slipper flexible body representation

and account for cross sectional changes from mass to mass. The beam section values

are shown in Table 5.6 and represent the implementation of Vascomax 300, a high

nickel maraging steel, with a Young's modulus of 27.5E6 lb_f/in^2 and a Poisson's ratio

of 0.32.

5.2 Design Parameter Formulation and Associated Values

The all inclusive list of design parameters from Chapter 3 is repeated below

Table 5.3 Slipper Beam Mass Distribution

Name	Mass (lb_f s^2/in)	Location From Centerline and Body Centerline (in)			Mass Properties about CG (lb_f s^2 in)		
		X	Y	Z	Ixx	Iyy	Izz
sb_l_6	0.00793	28.846	0.000	0.000	0.026	0.017	0.017
sb_l_5	0.00793	26.538	0.000	0.000	0.026	0.017	0.017
sb_l_4	0.00793	24.231	0.000	0.000	0.026	0.017	0.017
sb_l_3	0.00793	21.923	0.000	0.000	0.026	0.017	0.017
sb_l_2	0.00793	19.615	0.000	0.000	0.026	0.017	0.017
sb_l_1	0.00793	17.308	0.000	0.000	0.026	0.017	0.017
sb_c	0.00793	15.000	0.000	0.000	0.026	0.017	0.017
sb_r_1	0.00793	12.692	0.000	0.000	0.026	0.017	0.017
sb_r_2	0.00793	10.385	0.000	0.000	0.026	0.017	0.017
sb_r_3	0.00793	8.077	0.000	0.000	0.026	0.017	0.017
sb_r_4	0.00793	5.769	0.000	0.000	0.026	0.017	0.017
sb_r_5	0.00793	3.462	0.000	0.000	0.026	0.017	0.017
sb_r_6	0.00793	1.154	0.000	0.000	0.026	0.017	0.017

Table 5.4 Slipper Beam Flexibility

Name	Length (in)	Area (in^2)	Iy (in^4)	Iz (in^4)	J (in^4)	Young's Modulus (lb$_f$/in^2)	Poisson's Ratio
beam_sb_l_6							
beam_sb_l_5							
beam_sb_l_4							
beam_sb_l_3							
beam_sb_l_2							
beam_sb_l_1							
beam_sb_c	2.307	4.688	7.739	7.739	15.479	30.00E6	0.32
beam_sb_r_1							
beam_sb_r_2							
beam_sb_r_3							
beam_sb_r_4							
beam_sb_r_5							
beam_sb_r_6							

Figure 5.2 DADS Slipper Depiction of Front Right Slipper

for ease of reference and is intended to show a comparison between it and the list of

reduced/combined design parameters in Table 5.7.

    1) Slipper Gap, Vertical and Lateral

    2) Rail Roughness, Vertical and Lateral

3) Slipper Beam Stiffness

4) Rocket Motor Stiffness

5) Component Connection Structural Characteristics

6) Component Weight

7) Structural Damping

8) Vibration Isolation

9) Component Material

10) Thrust

11) Aerodynamic Lift and Drag Forces

12) Velocity

13) Slipper Rail Contact

14) Combustion Instability

For design parameters such as slipper gap and rail roughness there are values specified by HHSTT operating procedures (846th Test Squadron 2006) that designate a precise value range. The minimum and maximum values from this range were used in Table 5.7. The formation of total sled free-free natural frequencies accounts for component material, material distribution, and component stiffness for each major structural component. Lateral slipper vibration isolation is accounted for in the formation of the lateral natural frequency because it is considered a spring in series with the axial stiffness of the slipper beam. It should be noted that complexity reduction in this area included modeling the vibration isolation of equal linear type material on both sides of the slipper; thus eliminating the need for a highly complex and nonlinear representation of this joint as a set of nonlinear preloaded springs.

Table 5.5 Slipper Mass Distribution

| Name | Mass (lb$_f$ s^2/in) | Location From Centerline and Body Centerline (in) | | | Mass Properties about CG (lb$_f$ s^2 in) | | |
		X	Y	Z	Ixx	Iyy	Izz
slip_cent	0.008	-0.070	-5.857	0.000	0.067	0.068	0.002
slip_con	0.004	0.590	-4.012	0.000	0.033	0.033	0.0004
slip_low_in	0.005	-4.323	-4.041	0.000	0.042	0.042	0.001
slip_mid_h_in	0.009	-3.641	-5.868	0.000	0.073	0.075	0.003
slip_mid_h_out	0.034	-1.809	-2.271	0.000	0.330	0.291	0.167
slip_low_out	0.010	-1.625	0.000	0.000	0.020	0.020	0.020
slip_mid_lo_in	0.005	0.708	-5.139	0.000	0.0389	0.038	0.001
slip_mid_l_out	0.006	-4.435	-5.107	0.000	0.048	0.048	0.001

5.2.1 Sled Mass

Sled weight refers directly to the sled mass and associated mass properties. The high and low values are representative of composite sled values where the body is varied from mass properties representing unexpended (high), half-expended (typical), and expended (low) LSR final stage rocket motor mass. Consideration was given to the fact that mass distribution was important to the performance of the sled and was not varied by just simply scaling the mass moments of inertia. The

Table 5.6 Slipper Flexibility

Name	Length (in)	Area (in^2)	Iy (in^4)	Iz (in^4)	J (in^4)	Mass 1	Mass 2
beam_s_cent _in	2.22	5.00	41.77	41.67	0.18	slip_cent	slip_mid _h_in
beam_s_cent _out	2.70	5.00	41.77	41.67	0.18	slip_mid_ h_out	slip_cent
beam_s_mid _out	1.07	6.88	57.60	57.60	0.27	slip_mid_l _out	slip_mid _h_out
beam_s_low _out	0.79	7.26	60.84	60.51	0.31	slip_mid_l _out	slip_low_ out
beam_s_mid _in	1.13	5.19	43.37	43.25	0.11	slip_mid_ h_in	slip_mid _lo_in
beam_s_low _in	0.78	7.00	58.67	58.38	0.28	slip_low_i n	slip_mid _lo_in

variations of mass and mass moments of inertia were somewhat counterintuitive because the discretized mass inertia values were tuned so that the composite body values matched the LSR rocket motor equivalent. The sled mass high, typical, and low values are shown in Table 5.8.

5.2.2 Slipper Gap

Slipper gap definition is: 'Total slipper gap is defined as the distance from one slipper bearing surface to the rail surface with the opposite slipper bearing surface in contact with the rail. Both vertical and horizontal gap shall be checked.' (846th Test Squadron 2006). Currently the slipper gap range is from 0.125 +/- 0.015 in and represents the typical, high, and, low values respectively to be used in the parameter variation study.

Table 5.7 Reduced Design Parameter Listing

Name	Designation	Values		
		Low	Typical	High
Sled Mass (lb$_f$)	DP$_1$	383.3	842.0	1,301
Slipper Gap (in)	DP$_2$	0.110	0.125	0.140
STD Rail Roughness, Vertical (in)	DP$_3$	0.0083	0.0119	0.0155
STD Rail Roughness, Lateral (in)	DP$_4$	0.0103	0.0147	0.0191
ω Sled V* (Hz)	DP$_5$	41.0	79.9	200
ω Sled L* (Hz)	DP$_6$	44.0	84.5	168
ω Sled TOR* (Hz)	DP$_7$	45.0	85.9	161
Velocity (fps) (windowed Δv=250 fps)	DP$_8$	0.0	5,000	10,000

* V–Vertical; L–Lateral; TOR–Torsional

Table 5.8 Reduced Complexity Sled Mass Properties

Case	Weight (lb$_f$)	Mass (lb$_f$ s^2/in)	CG (in)			Mass Properties about CG (lb$_f$ s^2 in)		
			X	Y	Z	Ixx	Iyy	Izz
Low	383.37	0.9931	0	-7.57	68.55	1967.97	1984.82	123.92
Typical	842.20	2.1816	0	-3.45	68.25	4708.14	4692.67	221.12
High	1301.02	3.3701	0	-2.23	68.16	6445.43	6422.10	268.26

5.2.3 Rail Roughness

Rail roughness was applied in the same manner prescribed in Chapter 3 with the values used in correlation modeling representing typical values as surveyed from TS 44,845 to 49,926 on B and C rails. The high and low values were represented by +/- 30% deviation of the typical values. This variation will be applied through simple scaling of the corresponding rail roughness within the DADS model. The corresponding standard deviation values for the rail roughness profiles and corresponding contact points are shown in Table 5.9 and Figure 3.4 and represent standard deviation values as seen in Figures 3.23, 3.24, 3.25, 3.26, 3.27.

5.2.4 Sled Natural Frequency

The sled natural frequencies listed in Table 5.7 refer to modal analysis

Table 5.9 Rail Roughness Standard Deviation Values

Case	Standard Deviation (in)	Direction	DADS Contact Points
High	0.0155		
Typical	0.0119	Vertical	1,3,4,6
Low	0.0083		
High	0.0191		
Typical	0.0147	Lateral	2,5
Low	0.0103		

solutions of the sled with free-free boundary conditions. The natural frequencies are

the fundamental, 1st, in their respective directions. This is allows a design engineer to

produce a basic FEM of an early stage sled design and quickly determine the natural

frequencies for entry into the dynamic load prediction tool. The boundary conditions

are prescribed with two intentions: First, to create an easily applied standard so that

few discrepancies can exist when the dynamic load prediction tool is applied.

Second, to account for the fact that the product of the tool, force, is applied to the sled

CG where the dynamic loading is assumed to come from the slipper/rail interaction

and the load path is from the slipper to the sled CG. This designation of boundary

conditions and resulting natural frequencies may appear somewhat artificial because

during a test the sled encounters a combination of free-free and fixed translational one

sided boundary conditions. However, the intent is to establish a standard by which all

sleds may be easily measured and a well defined stiffness and mass distribution for

the entire system can be accurately established. The corresponding reduced

complexity parameter variation model will respond to any boundary condition

combination encountered in the DADS simulation accomplishing the goal of

establishing a common, easily measured input parameter.

5.2.5 Velocity

The velocity profile desired for each design parameter variation simulation is

from rest to 10,000 fps. This is to simulate a realistic range of narrow gauge

velocities and will be determined by a scaled thrust value to ensure that acceleration

is the same for each simulation. The velocity is achieved by applying a constant

acceleration of 125 Gs for 2.49 seconds. The thrust values applied to achieve

maximum velocity are shown in Table 5.10.

Table 5.10 Reduced Complexity Model Thrust Values

Case	Sled Weight Value (lb$_f$)	Thrust Values (lb$_f$)
High	1,301	162,625.00
Typical	842	105,275.38
Low	383	47,921.63

5.3 η Force Formation

The output values of the DADS reduced complexity model simulations

consisted of forces at the four slipper beam interface locations over the simulation

time. The formation of η force comes directly from solving the translational dynamic

equilibrium equations, Equations 5.1 and 5.2, as derived from Figure 5.3 in both the

vertical and lateral directions. Two forces at each location were output from DADS

for processing in MATLAB where the data were filtered using a 10 Hz high pass

filter and then combined into a resolved force at the sled CG. The data were

windowed producing standard deviation and peak values for velocity window values

every 250 fps to ensure that locally stationary data was used in statistical calculations.

The data were compared as accomplished previously by Mixon (1971), Hooser

(1989), and Nedimovic (2004) to determine if the maximum force value over each

$$\Sigma F_y = F_{\eta \text{ vertical}} = \eta_{vertical} W = \sum_{i=1}^{4} F_{yi} = F_{fr} + F_{fl} + F_{ar} + F_{al} \qquad (5.1)$$

where
f is front
a is aft
r is right
l is left

$$\Sigma F_x = F_{\eta \text{ lateral}} = \eta_{lateral} W = \sum_{i=1}^{4} F_{xi} = F_{fr} + F_{fl} + F_{ar} + F_{al} \qquad (5.2)$$

where
f is front
a is aft
r is right
l is left

velocity window was governed by the peak or three times the standard deviation. It

was determined that the data peaks were the governing data set as was reported by

Mixon (1971) and were subsequently used to construct the envelope function to

bound the data. The envelope function was computed using a simple algorithm that

began at a zero force value at zero velocity and searched the data set for a relative

high value that returned a greater than or equal to zero value of slope computed from

the current relative high value. Once another relative high value was found, it was

recorded and set as the current relative high value. This process was repeated until

the maximum velocity was reached. At the end of the process if no other relative

high value had been found the current relative high value was projected to the

maximum velocity point to ensure that the entire data set had been bounded. The

number of relative high values varies with each simulation result set. To make

108
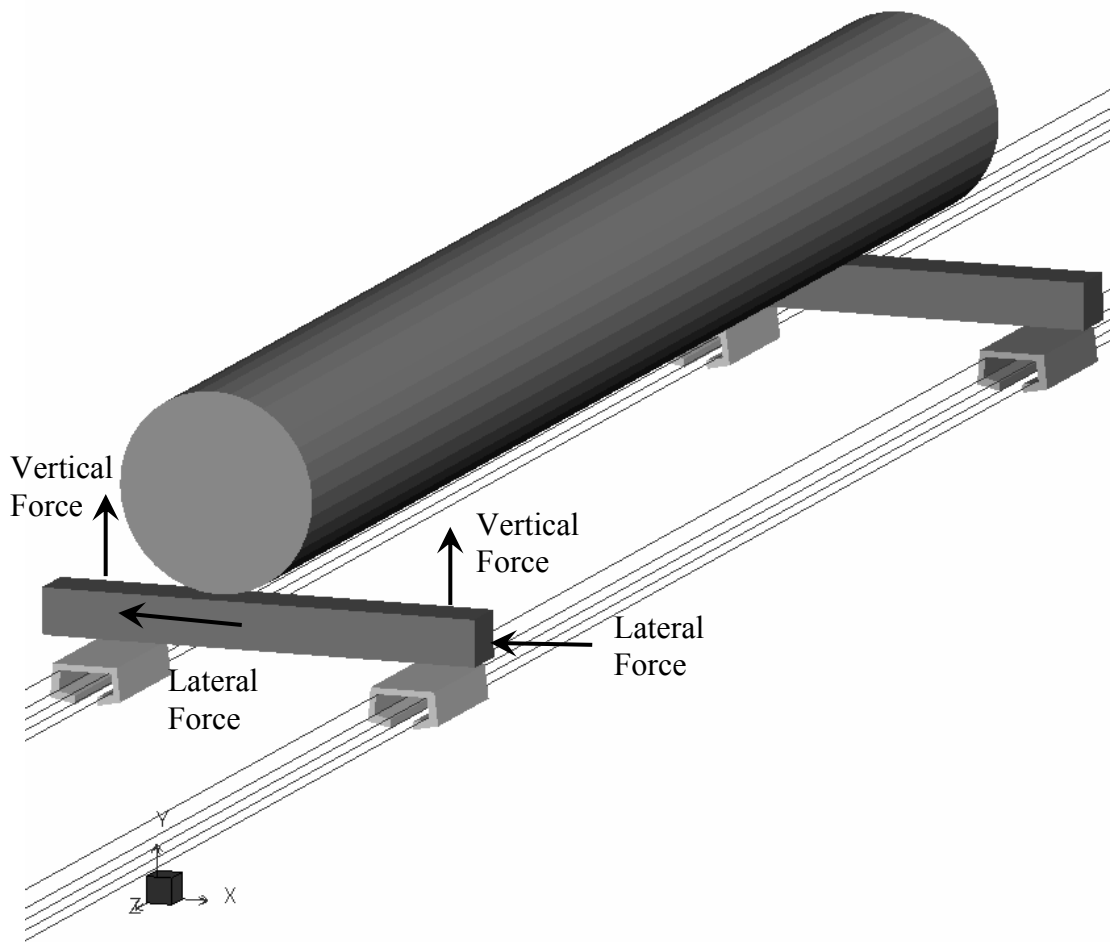
Figure 5.3 Force Depiction of η Forces from Reduced Complexity Model

comparisons more direct, the envelope curve was written over the entire windowed

velocity set to make the envelope a piecewise linear function of windowed velocity as

shown for the vertical, all-typical design parameter set shown in Figure 5.4. The

MATLAB commands associated with processing the parameter variation solution

data appear in Appendix D.

A variability study was conducted to determine the variation of η force with
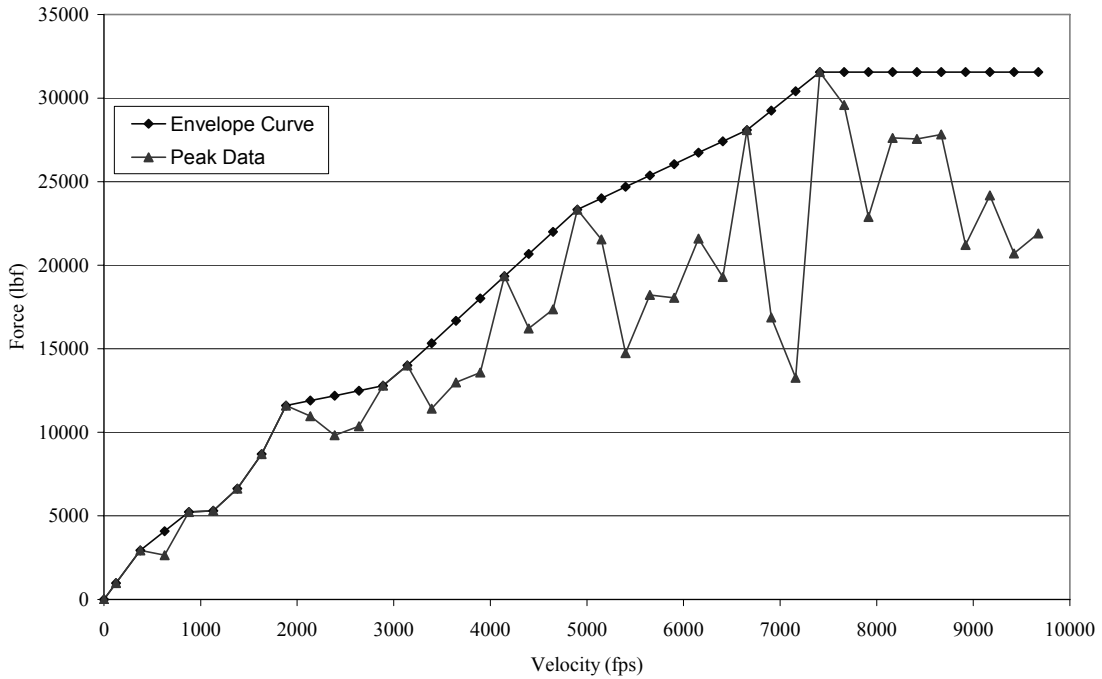
Figure 5.4 Envelope Function Depiction Vertical All-Typical Data Set

regard to random sets of equivalent rail roughness. Six solutions were accomplished

where the vertical rail roughness profiles on B- and C-Rails were shifted forward and

backward in TS respectively at 6 inch increments from typical. The first solution of

this variability study featured all of the typical values of the design parameters. The

next five solutions featured rail roughness shifting. The η force associated with these

studies was computed and the vertical and lateral results from the six solutions were

compared. The vertical force variation was bounded by a band of ±1.7 multiplied by

the standard deviation about the mean. The lateral force variation was bounded by a

band of ±1.9 multiplied by the standard deviation about the mean.

The application of η forces at the sled CG was done to ensure a conservative

approach to load distribution, not from a standpoint of a locally high value for a

110

subsequent stress analysis but from a standpoint of moment distribution. At the

HHSTT, a significant departure from previous practices was documented by Mixon

and Hooser (2002) stating that from its inception until the 1980's, λ loading had

always been applied as a point load at the sled CG. With the advent and widespread

use of FEM software, λ loading has been applied as a distributed load across all

masses as they have been discretized based upon the model's node distribution. The

load application difference is subtle but the resulting shear and moment distributions

across the sled structure are not. To illustrate this phenomenon consider the bounding

load cases of a point load, F, applied at the center of a beam of length L pinned at

each end and a distributed load of the same total magnitude applied to the same beam

with the same boundary conditions. The shear and moment diagrams for each case

appear in Figures 5.5 and 5.6 respectively. The distributed load case was chosen as it

represents a theoretical limit to a discretized FEM representation of a simple beam.

The maximum moment for both cases occurs at beam center and is FL*0.25 for the

point load case and FL*0.125 for the distributed load case. The point load case

produces a maximum moment 100% greater than the distributed load case. Thus η

and λ should be applied at the sled CG as to ensure proper moment calculation.

5.4 Design Parameter Variation

The reduced model was cycled through the design parameters listed in Table

Figure 3.6 where the solution of all typical parameter values was completed, followed

by solutions of different combinations of the high and low parameter values in three
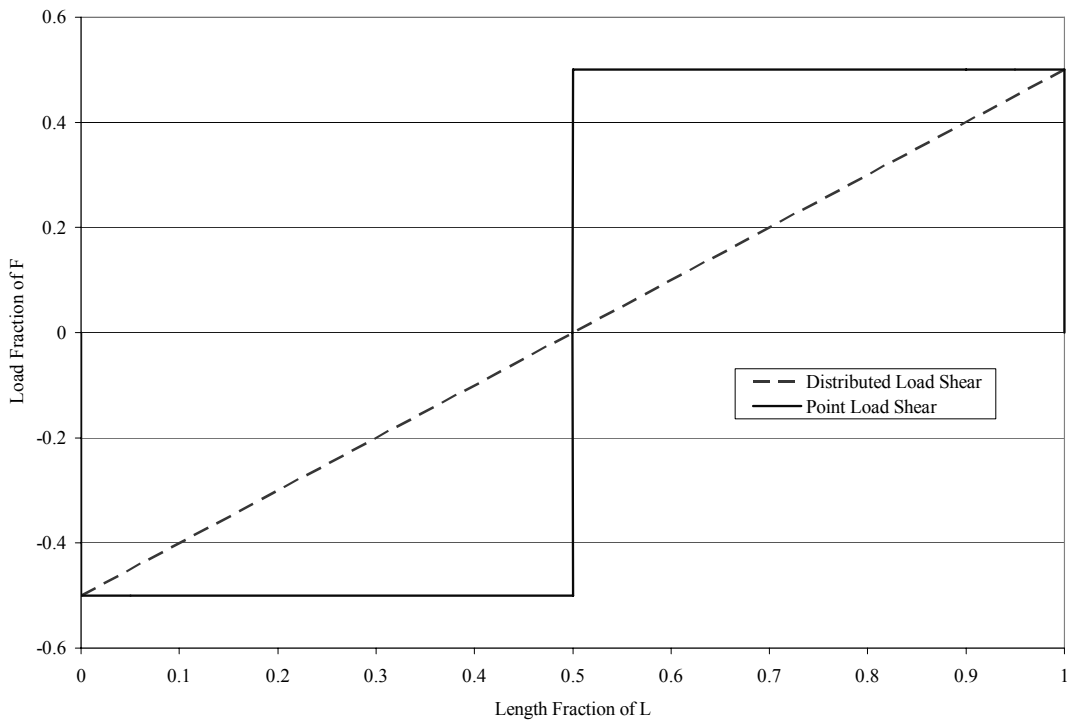
Figure 5.5 Comparison of Point Load and Distributed Load Shear Diagrams
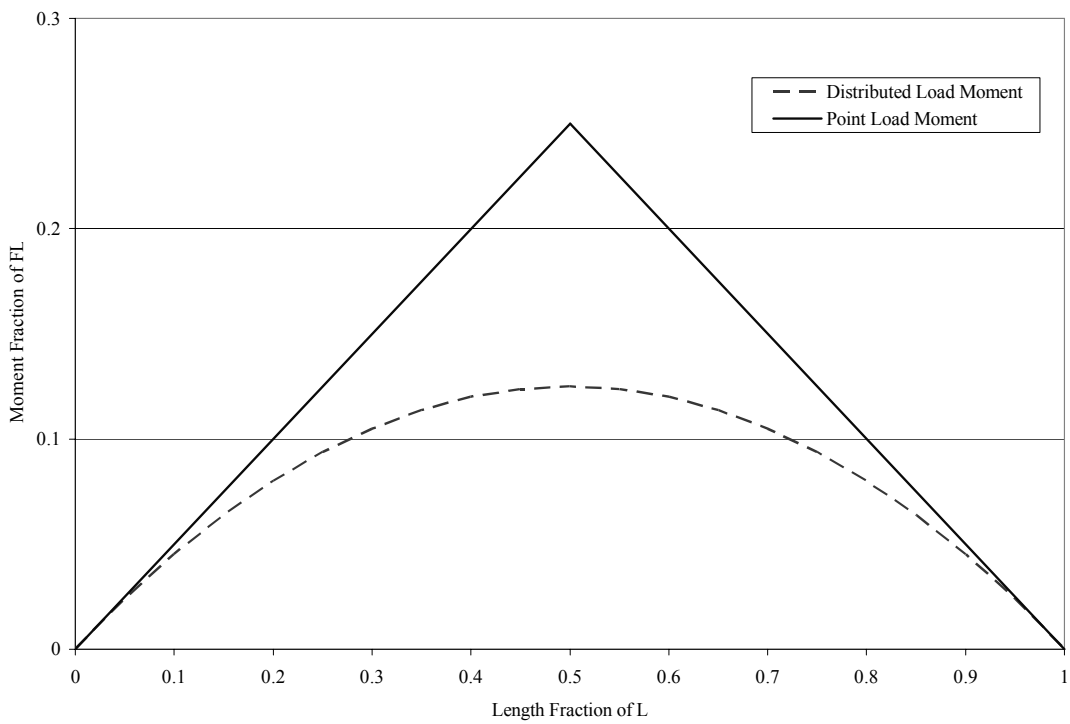
Figure 5.6 Comparison of Point Load and Distributed Load Moment Diagrams

112

steps of increasing detail. The first step consisted of individually varying the 1st

seven design parameters over their high and low values while holding all other design

parameters (except velocity) at their respective typical values resulting in 14 total

simulations. This initial step produced a comparison against typical values giving

insight into the effects of individual parameter variation. It also established an initial

parameter variation to identify any noncontributing parameters so that they could be

excluded from any subsequent parameter variations reducing the number of possible

simulations. The threshold criteria are defined as the percentage change, 10%, over

the entire velocity profile in resolved force at the CG in the vertical or lateral

direction for one parameter variation of its extremum values while all others are held

at their respective typical value. Any percentage change above the threshold denotes

a contributing parameter. Any change less than the threshold criteria denotes a non

contributing parameter. The intermediate parameter variation consisted of varying all

parameters through all possible combinations of their high and low values resulting in

128 total combinations describing the extremum space of parameter combinations.

The final parameter variation consisted of varying the remaining combinations of

remaining design parameters after applying the threshold criteria or logical simulation

number reduction from parameter dependence. The design parameter variation

served two purposes: first to identify contributing parameters, secondly to generate

data from which the dynamic load prediction tool could be constructed. A naming

convention was developed to easily detect the design parameter variation being

employed. The low value of a particular design parameter is represented by the

number 1, the typical value by the number 2, and the high value by the number 3.
There are eight design parameters total for each simulation. Velocity, the eighth
design parameter, is used as the independent variable in analyzing the resulting forces
so consideration of the seven other parameters is needed in the code formation. The
convention is written as a seven digit number where the left-most digit corresponds to
the seventh design parameter and the right-most digit to the first design parameter as
referenced by Table 5.7. Each digit can be a 1, 2, or 3 and represents the low, typical,
or high designation or the parameter value. Table 5.11 gives examples of convention
usage for arbitrary design parameter combinations. From this point on, design
parameter combinations will be referenced using this nomenclature.

Table 5.11 Design Parameter Combination Convention example

Design Parameter Value							Convention Value
7	6	5	4	3	2	1	
ω Sled Tor (Hz)	ω Sled L (Hz)	ω Sled V (Hz)	STD RR L (in)	STD RR V (in)	Slipper Gap (in)	Sled Weight (lb$_f$)	
85.9 Typical	84.5 Typical	79.9 Typical	0.0147 Typical	0.0119 Typical	0.125 Typical	842.0 Typical	2222222
85.9 Typical	84.5 Typical	79.9 Typical	0.0147 Typical	0.0155 High	0.125 Typical	842.0 Typical	2222322
45.0 Low	84.5 Typical	79.9 Typical	0.0191 High	0.0083 Low	0.125 Typical	842.0 Typical	1223122

* V - Vertical; L – Lateral; Tor – Torsional; RR – Rail Roughness

5.4.1 Initial Design Parameter Variation

The initial design parameter variation consisted of individually varying the seven design parameters through their high and low values, meaning that one parameter was varied by a 1 or 3 while the other six were held at the typical value of 2. The initial parameter variation results indicated that all design parameters were significant in either vertical or lateral force. There were instances where one force in one direction was insignificant while the other was significant so that the parameter variation in question could not be discarded. This result is significant in that it validates the initial selection of design parameters and range of corresponding variables. The all-typical design parameter case was plotted against the design parameter variations for this initial set and includes both vertical and lateral forces on the same plot. The resulting plots are shown in Figures 5.7-5.20.

Common to all results was the presence of a force transition point which is defined as the departure of the η forces from λ forces, this force transition is either higher or lower than the λ force, with the majority of the departures being lower. Typically the transition occurred between 800 and 2000 fps. Also shown was the variation of the ratio of lateral to vertical dynamic forces which has been traditionally held to 0.6. These phenomena are documented by Mixon and Hooser (2002, Figure 16) and Hooser (1989, Figure 4.5) for a wide array of sled configurations representing a correspondingly wide array of sled design parameters. Error tracking did not indicate that any of the simulations were out of tolerance.
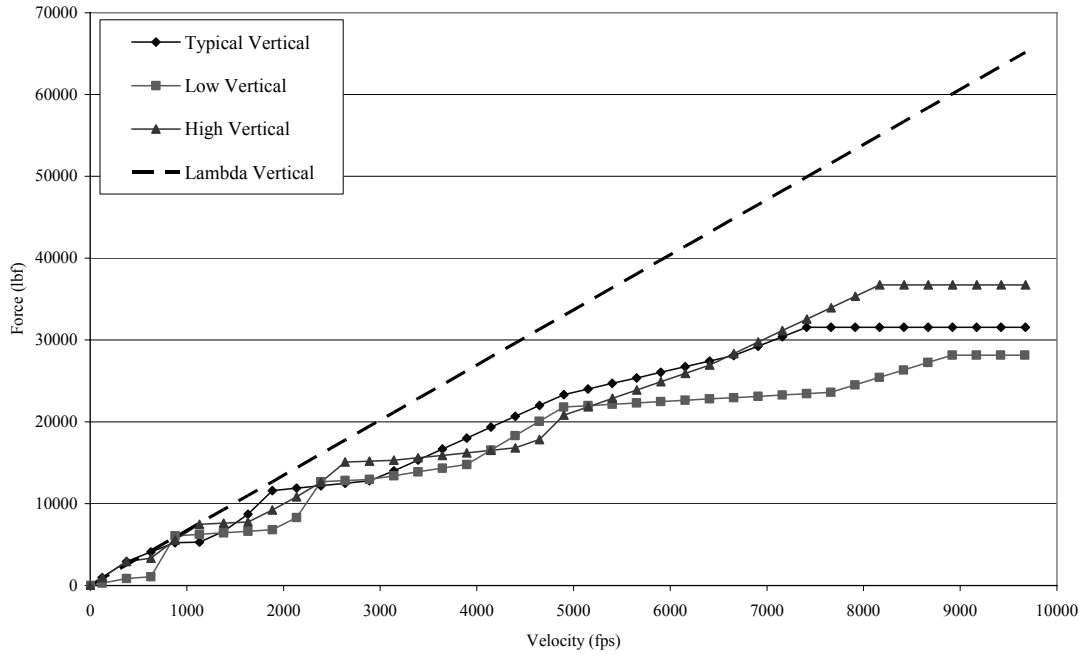
Figure 5.7 Initial Parameter Variation Vertical Force Results: Mass
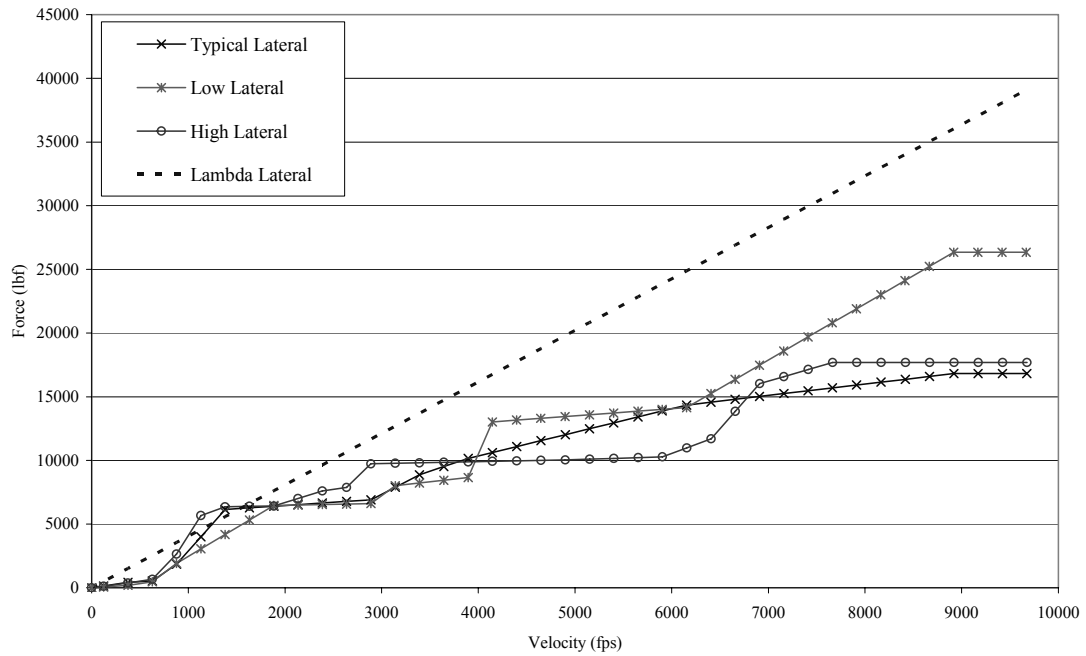
Figure 5.8 Initial Parameter Variation Lateral Force Results: Mass

116
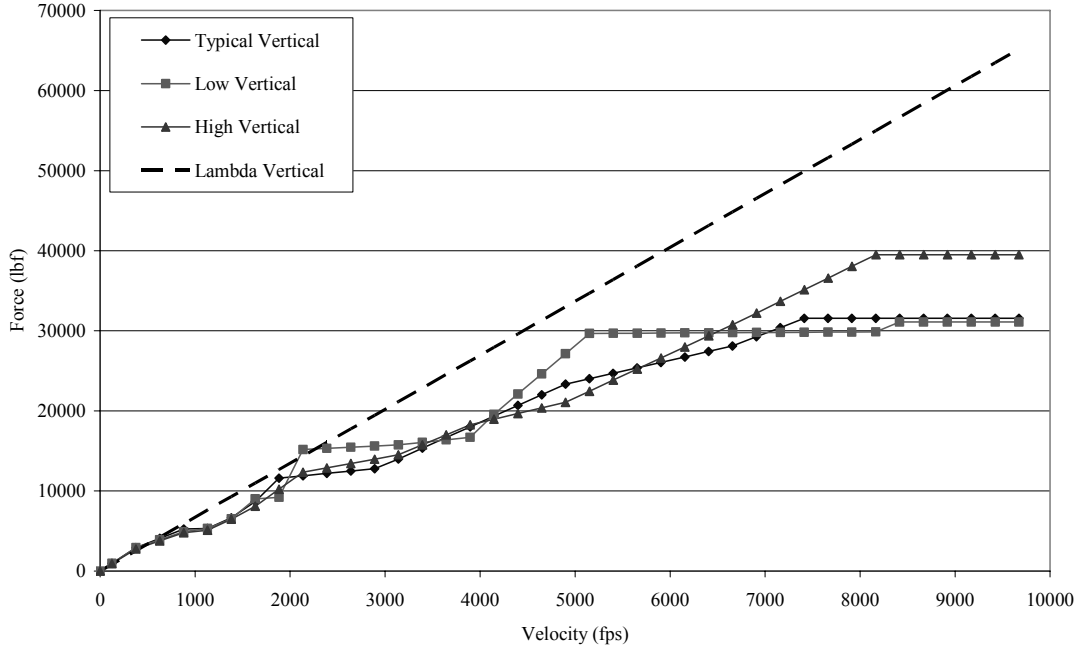
Figure 5.9 Initial Parameter Variation Vertical Force Results: Slipper Gap
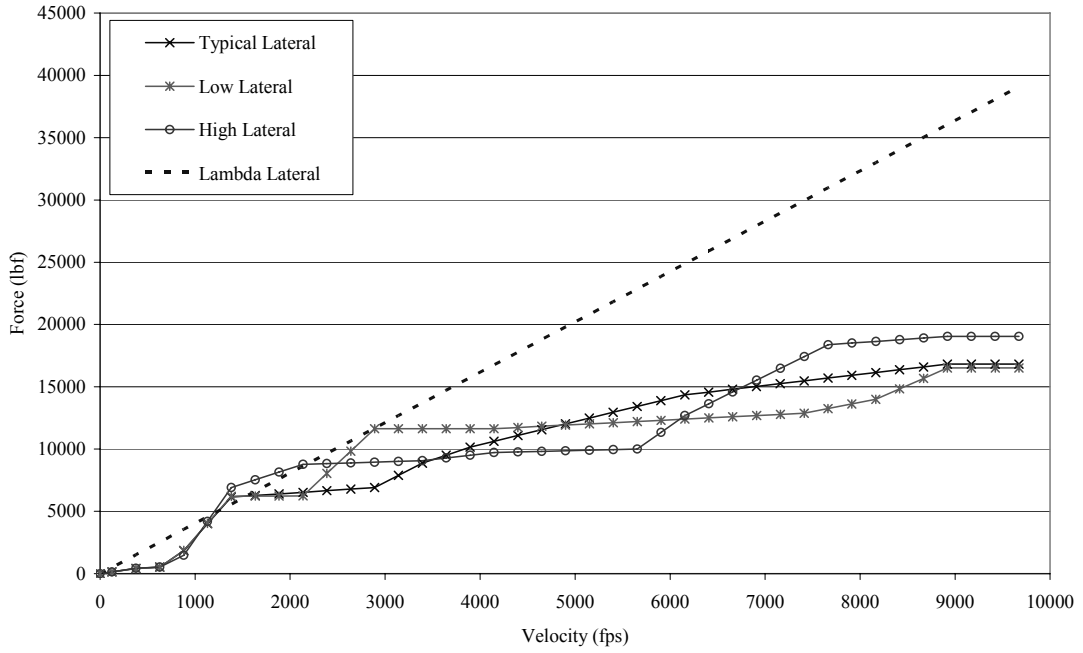
Figure 5.10 Initial Parameter Variation Lateral Force Results: Slipper Gap
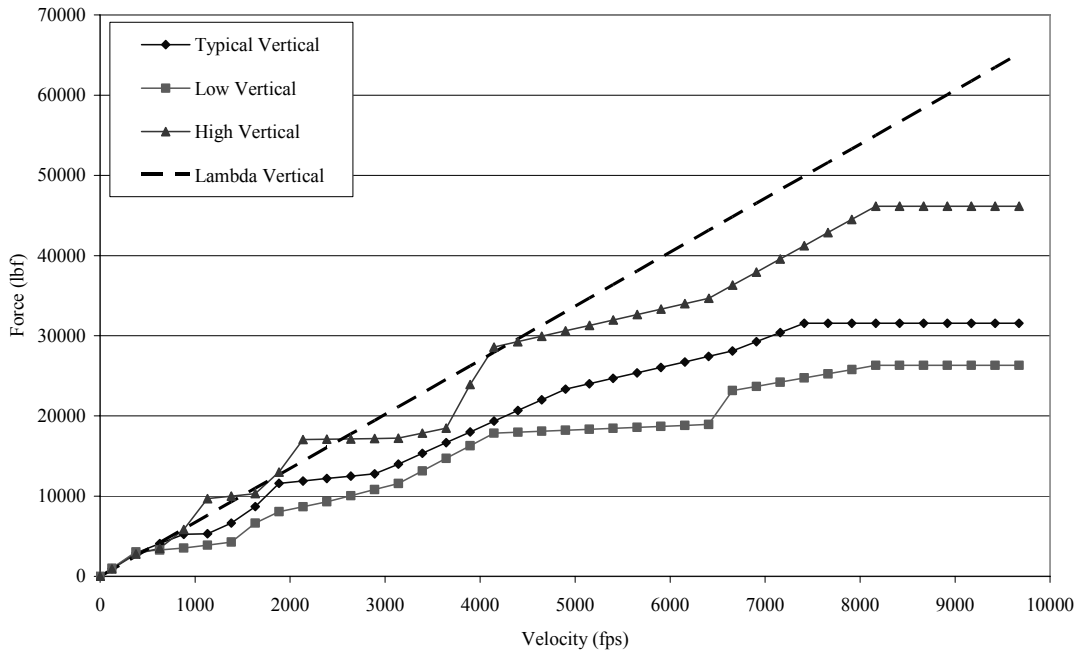
Figure 5.11 Initial Parameter Variation Vertical Force Results: Vertical Rail
Roughness
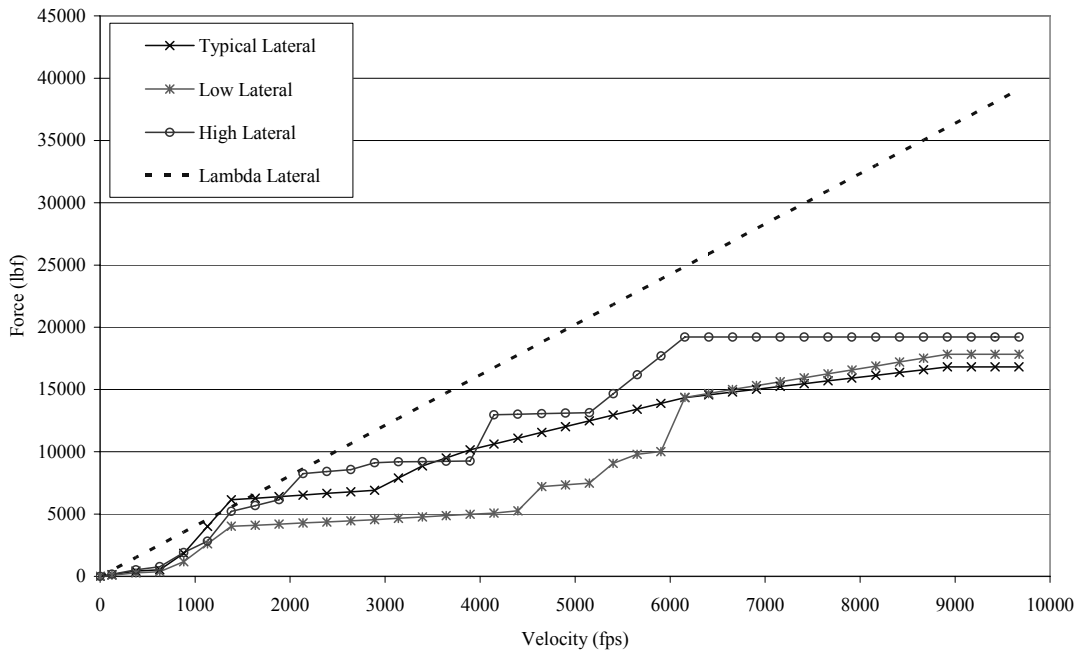
Figure 5.12 Initial Parameter Variation Lateral Force Results: Vertical Rail
Roughness
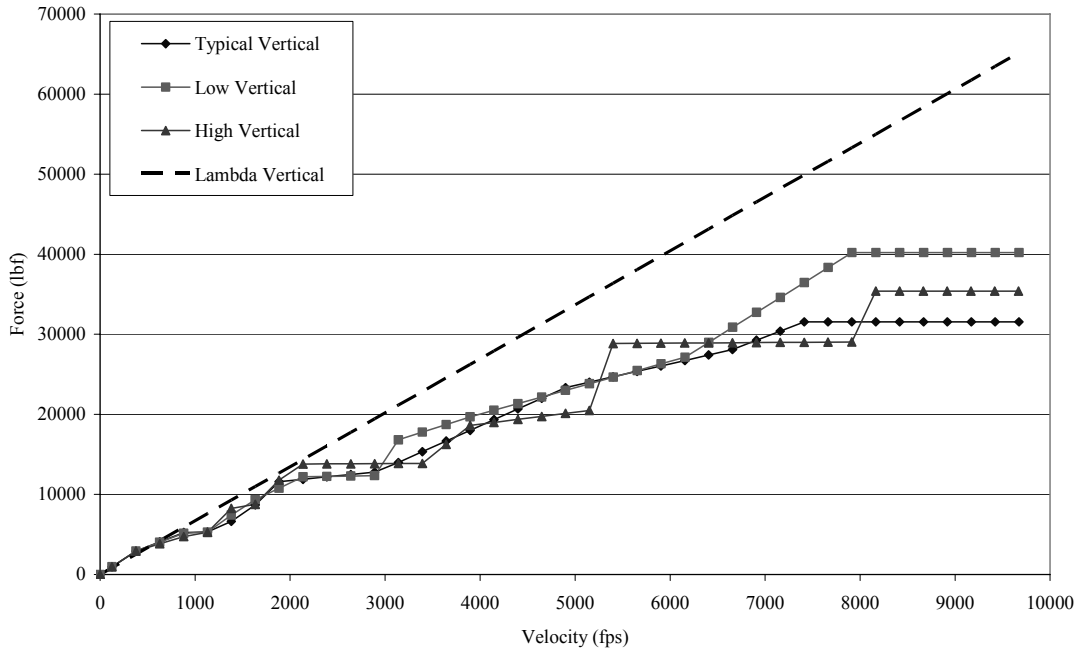
Figure 5.13 Initial Parameter Variation Vertical Force Results: Lateral Rail
Roughness
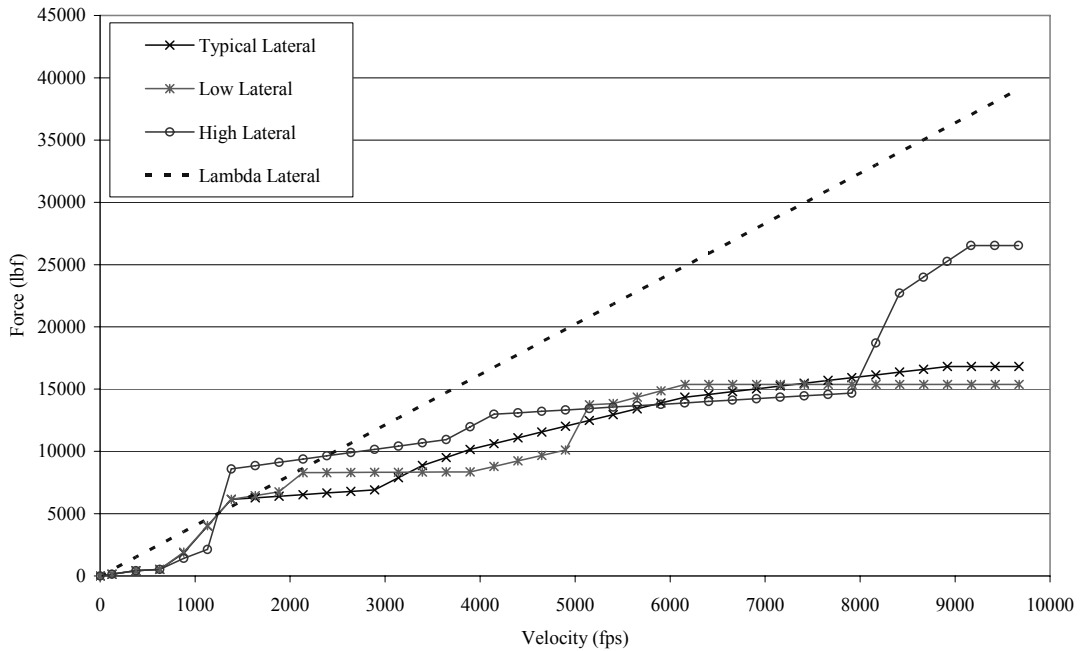
Figure 5.14 Initial Parameter Variation Lateral Force Results: Lateral Rail Roughness

119
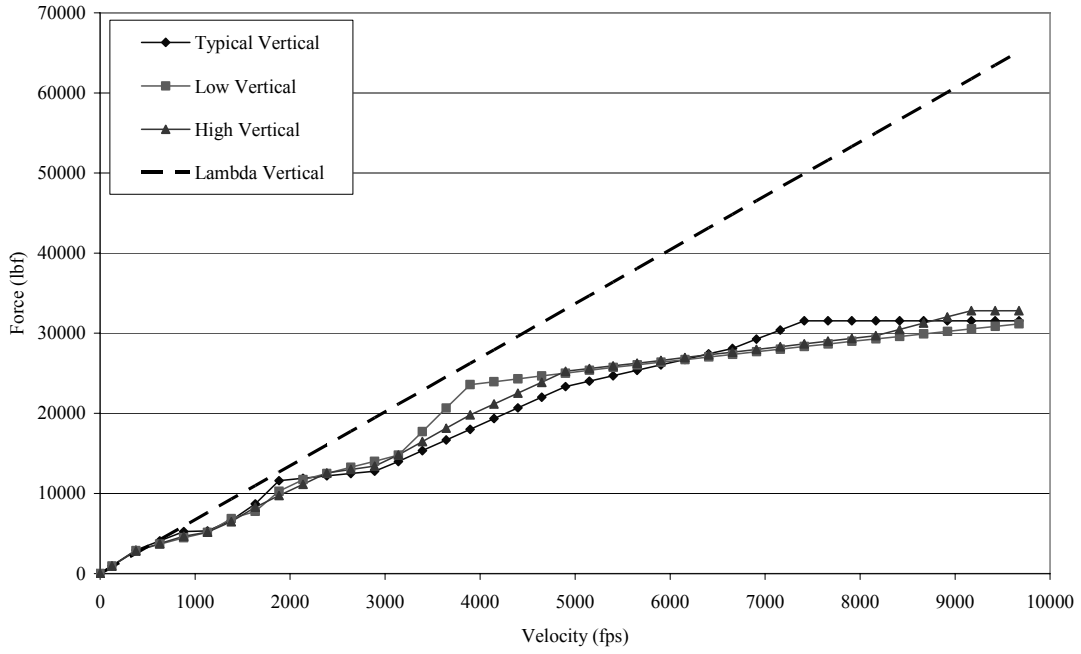
Figure 5.15 Initial Parameter Variation Vertical Force Results: Vertical Natural
Frequency
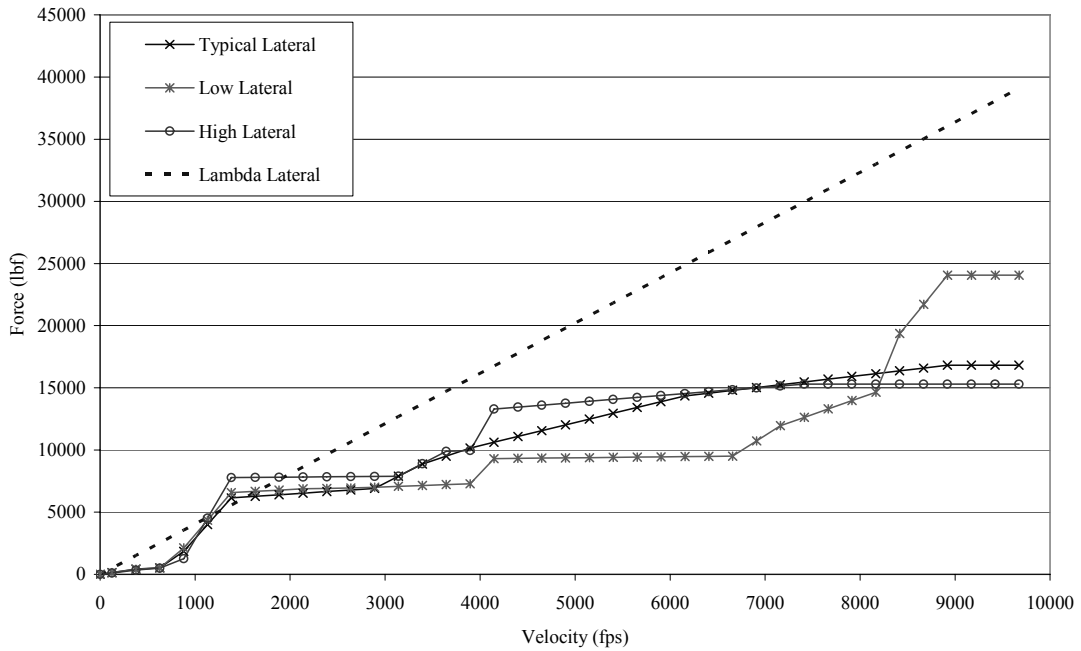
Figure 5.16 Initial Parameter Variation Lateral Force Results: Vertical Natural
Frequency

120
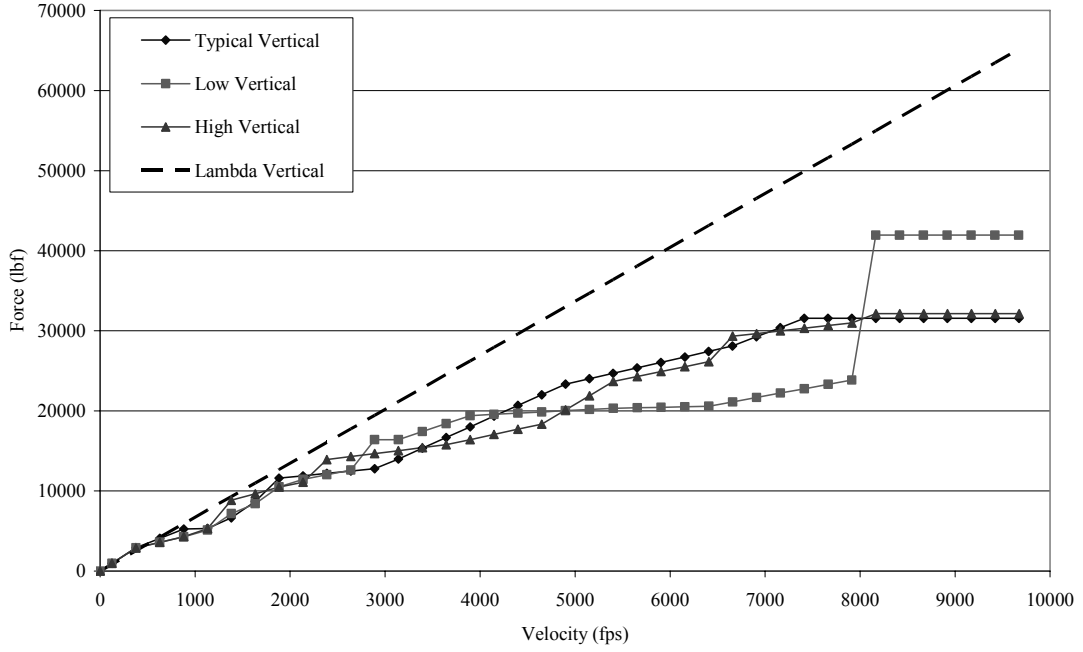
Figure 5.17 Initial Parameter Variation Vertical Force Results: Lateral Natural
Frequency
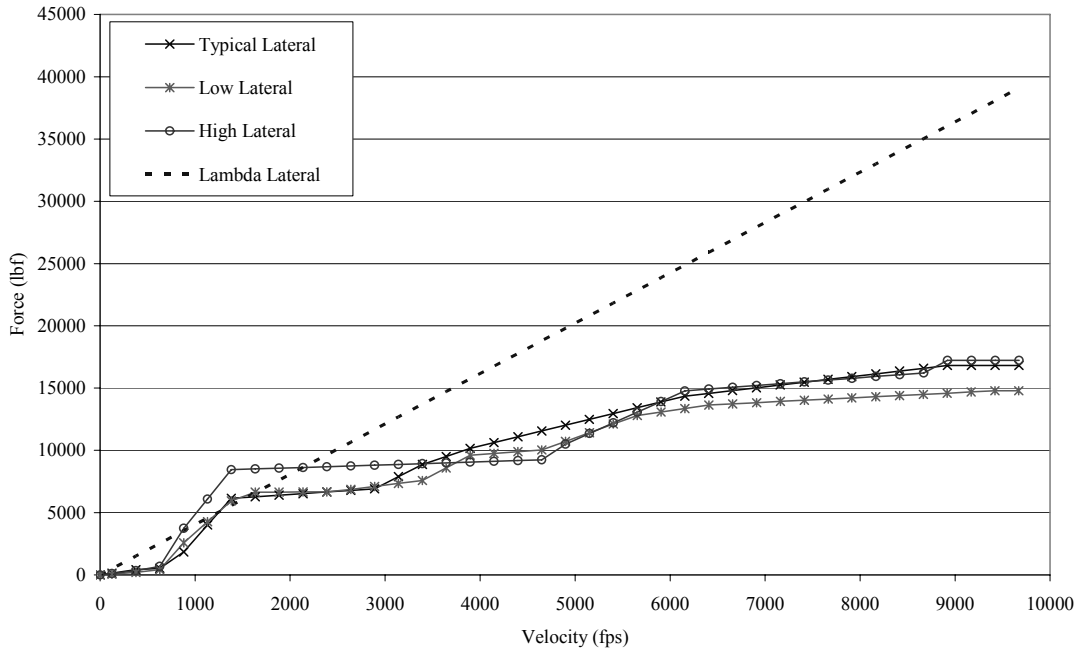
Figure 5.18 Initial Parameter Variation Lateral Force Results: Lateral Natural
Frequency

121
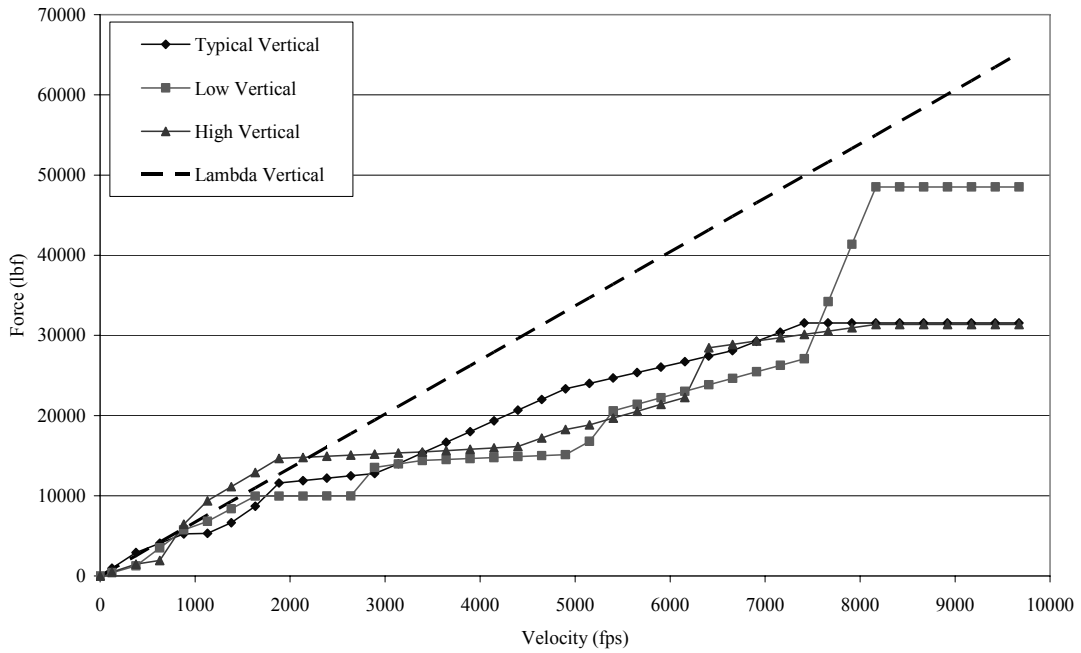
Figure 5.19 Initial Parameter Variation Vertical Force Results: Torsional Natural Frequency
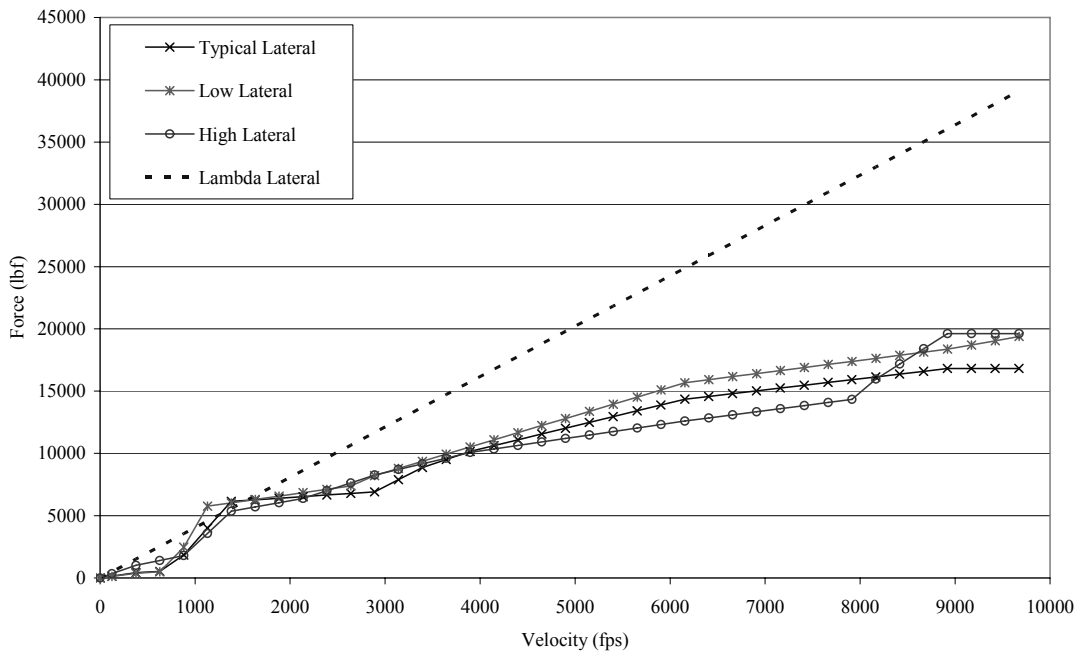
Figure 5.20 Initial Parameter Variation Lateral Force Results: Torsional Natural Frequency

122

5.4.2 Intermediate Design Parameter Variation

The intermediate design parameter variation was accomplished to define the extremum space of the design parameters and attempt to encompass the anticipated peak values of the vertical and lateral η forces. The subsequent formation of a design tool would, at a minimum, have to include the all-typical, initial, and intermediate solutions to be able to interpolate a desired point from within the design parameter space. As a result, the intermediate design parameter variation consisted of varying all combinations of the high and low values for all seven design parameters resulting in 128 total solutions as shown in Table 5.12. The simulation index consisted of all binary combinations of a seven digit number using 1s and 3s. Analysis of these results consisted of a cursory visual comparison to the typical values and was deemed acceptable based on the performance of the initial parameter variation results and that error tracking did not indicate that any of the simulations were out of tolerance.

Table 5.12 Intermediate Design Parameter Variation Values

Design Parameter	7	6	5	4	3	2	1
Value	1	1	1	1	1	1	1
	3	3	3	3	3	3	3

5.4.3 Final Design Parameter Variation

The final design parameter variation study was accomplished to give greater detail to areas of interest bounded by the intermediate design parameter and initial

design parameter studies. The total number of possible simulations was 2187 or 3^7.

Instead of running all possible combinations it was decided that a reduced set of 192

total simulations would be used in this final stage. This reduced set was defined by

analyzing the initial design parameter variations results and then applying a bounding

influence technique. This technique was applied by visually analyzing Figures 5.7-

5.13 individually and then determining which values of the design parameters were

influential in either the maximum or minimum values of the corresponding η force.

It was considered absolutely necessary to consider the vertical and lateral forces

simultaneously as the bounding design parameters for each force were not always the

same. An example of this phenomenon is best illustrated in Figure 5.10 where the

variation of rail roughness is shown. Above 6,000 fps there is a significant increase

in the η force in the vertical direction for a low lateral rail roughness value and above

8,000 fps there is significant in crease in the η force in the lateral direction for a high

lateral rail roughness value. The lower parameter value bounds the maximum vertical

values while the higher parameter bounds the maximum value for the lateral force

direction. After a careful study of the figures, the bounding design parameter values

were determined and are shown in Table 5.13. The inclusion of all three parameter

values for design parameter 7 indicates that the complete influence of the design

parameter values and that the η curves are intertwined as shown in Figure 5.13. From

the set of 192 total simulations it was found 32 had been previously solved so 160

unique solutions were required to complete this task. Error tracking did not indicate

that any of the results were out of tolerance.

Table 5.13 Final Design Parameter Variation Values

Design Parameter	7	6	5	4	3	2	1
Value	1	1	1	1	1	1	1
	2	2	2	3	3	3	3
	3	N/A	N/A	N/A	N/A	N/A	N/A

6. DEVELOPMENT OF CORRELATION OF PREDICTED LOAD AND DESIGN PARAMETERS

The ultimate goal of this study is the production of a design tool which can effectively correlate the input variables to the output forces so that the designer may effectively apply the design tool during the sled design process. The functional relationship sought is represented for a given η force in Equation 6.1. This was accomplished by correlating the design parameters to the η forces produced by the efforts documented in Chapter 5. Several correlation methods were studied including linear multivariate least squares regression, nonlinear multivariate least squares regression, nondimensional analysis, and multivariate interpolation. The motivation behind the studying of regression methods was the possibility of arriving at a closed form solution which may be applied either by hand or within a simulation environment in a variety of applications whereas an interpolation method is somewhat fixed as the algorithm must be programmed. Since the design tool will ultimately be employed in an environment where its function must be expedient, any implementation must be acutely representative of the data produced in Chapter 5 and easily employed so that it will not suffer the same fate as that of SIMP and SLEDYNE.

$$F_\eta = f(DP_8, DP_7, DP_6, DP_5, DP_4, DP_3, DP_2, DP_1) \tag{6.1}$$

6.1 Linear Least Squares Regression

To begin the correlation effort a basic multivariate least squares regression was accomplished on the η force data set. The assumed solution took the form shown in Equation 6.2. The regression coefficients were solved using Equation 6.3 by inverting the summation matrix and multiplying it by the right hand side summation vector (Volk 1958). The regression coefficients are shown in Table 6.1. The correlation coefficient, r^2, was calculated using Equation 6.4 and yielded the values of 0.82 and 0.76 for the vertical and lateral η forces respectively. These values, both less than 0.99, indicate an inadequate regression which was due in part to the piecewise linear nature of the η force over velocity and nonlinear variation of other design parameters. The motivation behind this effort was to establish a basis from which to launch a nonlinear regression study to investigate a closed form data correlation. The individual correlation coefficients, r, were calculated using Equation 6.5 and are shown in Table 6.2 for each of the design parameters. From the results in Table 6.2 it is obvious that the linear correlation is poor for design parameters mass, slipper gap, rail roughness lateral (vertical only), vertical, lateral and torsional sled natural frequency and better for design parameters rail roughness vertical, rail roughness lateral (lateral only), and velocity. This information is useful in determining in how to vary the assumed curve fit for a nonlinear regression analysis since higher correlation coefficients imply that the respective variable is better represented by the method used.

$$y = a + b_1 x_1 + b_2 x_2 + b_3 x_3 + \ldots + b_8 x_8 \tag{6.2}$$

where

y is the dependent variable, η force

x_i are the design parameters values

a, b_i are regression coefficients

i is the index 1,...,8

$$\begin{bmatrix} N & \sum x_1 & \sum x_2 & \sum x_3 & \ldots & \sum x_8 \\ \sum x_1 & \sum x_1^2 & \sum x_1 x_2 & \sum x_1 x_3 & \ldots & \sum x_1 x_8 \\ \sum x_2 & \sum x_1 x_2 & \sum x_2^2 & \sum x_2 x_3 & \ldots & \sum x_2 x_8 \\ \ldots & \ldots & \ldots & \ldots & \ldots & \ldots \\ \sum x_8 & \sum x_8 x_1 & \sum x_8 x_2 & \sum x_8 x_3 & \ldots & \sum x_8^2 \end{bmatrix} * \begin{Bmatrix} a \\ b_1 \\ b_2 \\ \ldots \\ b_8 \end{Bmatrix} = \begin{Bmatrix} \sum y \\ \sum x_1 y \\ \sum x_2 y \\ \ldots \\ \sum x_8 y \end{Bmatrix} \tag{6.3}$$

where

N is the total number of data points

$$r^2 = \frac{\sum' c^2}{\sum' y^2} \tag{6.4}$$

where

$$\sum' c^2 = b_1 \sum' x_1 y + b_2 \sum' x_2 y + \ldots + b_8 \sum' x_8 y$$

$$\sum' x_i y = \sum (x_i - \overline{x_i})(y - \overline{y})$$

$$\sum' y^2 = \sum (y - \overline{y})^2$$

$\overline{y_i}$ is the mean of y_i

x_i are the design parameters values

y is output force

$$r_{x_i y} = \frac{\sum' x_i y}{\left(\sum' x_i^2 \sum' y^2 \right)^{0.5}} \tag{6.5}$$

where

$$\sum' x_i y = \sum (x_i - \overline{x_i})(y - \overline{y})$$

$$\sum' x_i^2 = \sum (x_i - \overline{x_i})^2$$

$\overline{x}_i$ is the mean of x_i

x_i are the design parameters values

y is output force

i is the index 1,...,8

Table 6.1 Linear Multivariate Least Squares Regression Coefficients

Regression Coefficients	Design Parameter	Force Direction	
		Vertical	Lateral
a		-16049.8	-9628.8
b_1	Sled Mass	2.26	1.98
b_2	Slipper Gap	-75754.7	-40411.0
b_3	Vertical Rail Roughness	1997732.8	574909.9
b_4	Lateral Rail Roughness	48638.5	471002.2
b_5	$\omega_{Vertical}$	-1.28	0.29
b_6	$\omega_{Lateral}$	1.40	9.59
b_7	$\omega_{Torsional}$	12.65	3.85
b_8	Velocity	4.06	2.21

Table 6.2 Linear Multivariate Least Squares Correlation Coefficients

Regression Coefficients	Design Parameter	Individual Correlation Coefficient Values, r	
		Vertical	Lateral
b_1	Sled Mass	0.07	0.01
b_2	Slipper Gap	-0.07	-0.07
b_3	Vertical Rail Roughness	0.45	0.24
b_4	Lateral Rail Roughness	0.01	0.24
b_5	$\omega_{Vertical}$	-0.00	0.01
b_6	$\omega_{Lateral}$	0.01	0.06
b_7	$\omega_{Torsional}$	0.04	0.03
b_8	Velocity	0.77	0.79

6.2 Nonlinear Least Squares Regression

The nonlinear least squares regression was studied to better characterize the η force curves and to investigate a closed form relationship between the design parameters and the output η forces. A nonlinear regression analysis gives rise to a vast number of possible relationships of design parameters and assumed curve fits. For the current study the nonlinear forms were limited to polynomial or power forms.

6.2.1 Polynomial Form

The polynomial form was implemented to explore the correlation of different exponent values in a linear combination of design parameters or by using exponent values and nonlinear combinations of design parameters. The first part of this study focused on combinations of different exponent values for the polynomial while the second part focused on different nonlinear combinations of variables.

In the first part the exponent values were cycled through the range of 1, 2, and 3 for all possible values (high, typical, and low) for all eight design parameters in the form of Equation 6.6. The individual correlation coefficients for each prediction were tracked to determine if a particular fit was acceptable. After cycling the exponents through the prescribed range it was found that none of the individual correlation coefficients reached an acceptable value as indicated by their ranges shown in Table 6.3.

$$y = a + b_1 x_1^{n_1} + b_2 x_2^{n_2} + b_3 x_3^{n_3} + ... + b_8 x_8^{n_8} \tag{6.6}$$

where

y is the dependent variable, η force

x_i are the design parameters values

a, b_i are regression coefficients

n_i are the exponents

i is the index 1,...,8

The second part of the nonlinear regression effort utilized single variable combinations of all possible combinations of the design parameters of the form given in Equation 6.7. Following the least squares methodology depicted in Equation 6.3

131

Table 6.3 Polynomial Individual Correlation Coefficient Ranges

Design Parameter	DP_1	DP_2	DP_3	DP_4	DP_5	DP_6	DP_7	DP_8
High Value	0.11	0.08	0.45	0.25	0.02	0.06	0.04	0.79
Low Value	0.07	0.07	0.24	0.00	0.00	0.00	0.03	0.67

the initial formation shown in Equation 6.7 yielded correlation coefficients, r^2, of 0.71 vertical and 0.71 lateral, showing that this correlation was better but still not within an acceptable range. Equation 6.7 was modified slightly by changing the beginning index of j from i to 1 which resulted in Equation 6.8. The slight change in indices adds a factor of 2 to the $x_i x_j$ terms where $i \neq j$. This modification significantly improved the correlation coefficients to 0.90 vertical and 0.82 lateral. This change was the first regression based effort to yield acceptable r^2 values that included contributions from all eight design parameters. Studying the individual correlation coefficients, it was seen for the vertical direction that variables containing the design parameters rail roughness vertical and velocity were influential in this form. For the lateral direction variables containing design parameters mass, rail roughness vertical, rail roughness lateral, and velocity were influential in this form. The r^2 values near 0.9 indicate a positive representation of the majority of η data but fail to represent all individual cases. In some cases, η force is under predicted by as much as 50% thus disqualifying this regression method.

$$y = a + \sum_{i=1}^{8} \sum_{j=i}^{8} x_i x_j + b_1 x_1 + b_2 x_2 + b_3 x_3 + b_4 x_4 + b_5 x_5 + b_6 x_6 + b_7 x_7 + b_8 x_8 \qquad (6.7)$$

132

$$y = a + \sum_{i=1}^{8}\sum_{j=1}^{8} x_i x_j + b_1 x_1 + b_2 x_2 + b_3 x_3 + b_4 x_4 + b_5 x_5 + b_6 x_6 + b_7 x_7 + b_8 x_8 \tag{6.8}$$

6.2.2 Power Form

The power form was implemented as shown in Equation 6.9. The exponent values were solved by taking the log of both sides, implementing a least squares regression of the logarithmic values, and then solving for the exponent values. The least squares method was performed on Equation 6.10 and yielded the exponent values shown in Table 6.4. R^2 values for this form were 0.99 vertical and 0.98 lateral. The resulting correlation coefficient values associated with each design parameter are shown in Table 6.5 and prove to be excellent for velocity, but unacceptable for other parameters. The high correlation values for velocity are partially due to the fact that the method automatically forces the prediction of 0 force at 0 velocity. There is some significant deviation of the prediction from the η extremum values for some cases (see Figures 6.1 and 6.2). Thus this method is unacceptable for use as a correlation tool in the current study although it was the most accurate direct linear least squares regression method.

$$F_\eta = e^a W^{b_1} SG^{b_2} RR_V^{b_3} RR_L^{b_4} \omega_V^{b_5} \omega_L^{b_6} \omega_{TOR}^{b_7} V^{b_8} = e^a x_1^{b_1} x_2^{b_2} x_3^{b_3} x_4^{b_4} x_5^{b_5} x_6^{b_6} x_7^{b_7} x_8^{b_8} \tag{6.9}$$

$$\log(F_\eta) = a + b_1 \log(x_1) + b_2 \log(x_2) + b_3 \log(x_3) + b_4 \log(x_4) + \\ b_5 \log(x_5) + b_6 \log(x_6) + b_7 \log(x_7) + b_8 \log(x_8) \tag{6.10}$$

Table 6.4 Power Form Exponent Values

Regression Exponent Values	Design Parameter	Force Direction	
		Vertical	Lateral
a		36.91	16.07754
b_1	Sled Mass	0.1356	0.18275
b_2	Slipper Gap	-0.255	-0.3363
b_3	Vertical Rail Roughness	0.9885	0.66742
b_4	Lateral Rail Roughness	0.0438	0.42874
b_5	$\omega_{Vertical}$	-0.01009	0.00366
b_6	$\omega_{Lateral}$	0.00588	0.0616
b_7	$\omega_{Torsional}$	0.0625	0.05653
b_8	Velocity	1.083	1.0708

6.3 Nondimensional Analysis

Nondimensional analysis is a method which employs groupings of dependent

and independent variables to examine meaningful relationships among all of the

variables in a nondimensional form. This method is employed extensively in the

thermal fluids area of study where well known dimensionless parameters such as

Reynolds number and Nusselt number have been developed using nondimensional

134

Table 6.5 Power Form Individual Coefficient Values

Regression Coefficients	Design Parameter	Individual Correlation Coefficient Values, r	
		Vertical	Lateral
b_1	Sled Mass	0.03	0.04
b_2	Slipper Gap	-0.01	-0.01
b_3	Vertical Rail Roughness	0.11	0.07
b_4	Lateral Rail Roughness	0.02	0.05
b_5	$\omega_{Vertical}$	-0.00	0.00
b_6	$\omega_{Lateral}$	0.00	0.12
b_7	$\omega_{Torsional}$	0.01	0.01
b_8	Velocity	0.99	0.98

techniques specifically the Buckingham Pi (Π) Theorem. The Π Theorem outlined

by White (1994) will be used in this portion of the study. The application of the Π

theorem to solid mechanics is not widespread but was employed recently in

Smzerekovsky's (2004) study of hypervelocity impact. The Π theorem in general

consists of evaluating the function and number of dependent and independent

variables and then listing the dimensions of each variable. Applying this to the

function in question, Equation 6.1, the variables and associated dimensions are shown
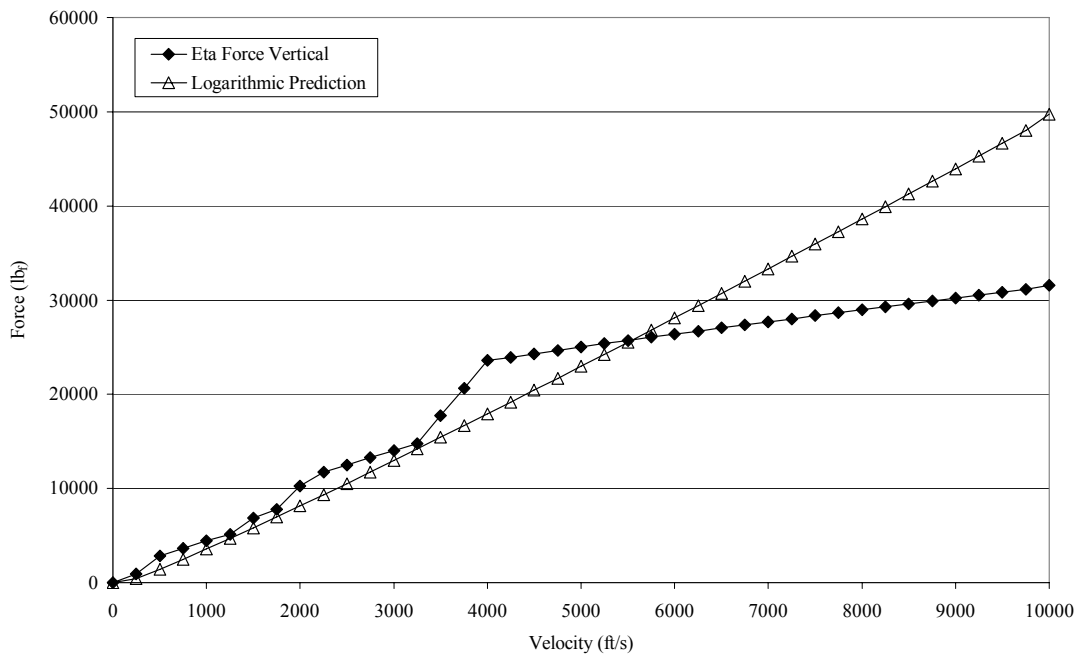
Figure 6.1 2212222 Vertical Best Power Form Prediction vs η Force
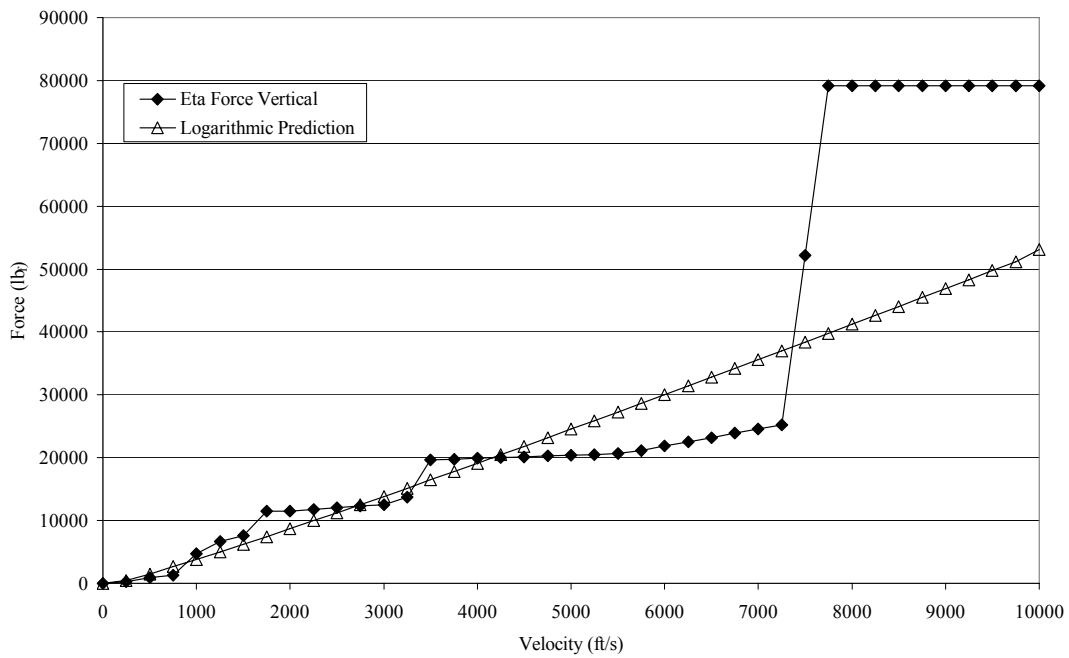
Figure 6.2 1111331 Vertical Worst Power Form Prediction vs η Force

in Table 6.6. There are 9 variables and choosing a dimensional system of mass, M, length, L, and time, T, there are 3 dimensions. Following White's (1994) treatment there should be 6 distinct Π parameters. Using the repeatable groupings of Velocity, Weight, and Slipper Gap, the 6 Πs are written in Equation 6.11 and represent essentially nondimensional values of design parameters and output force. It is interesting to note that from the initial collection of 1 dependent variable and 8 independent variables that there are now 6 Π values that represent 1 dependent variable and 5 independent variables which is a reduction in the amount of original variables. The exponential values for each Π were next solved to satisfy the nondimensional requirement, the results of which are presented in Table 6.7 and applied in Equation 6.12. At this step in the process, a relationship is sought between the dependent variable, Π_1, and the independent variables, Π_{2-6}, shown in Equation 6.13 and is analogous to Equation 6.1. Beginning with the initial relative success of the power form the relationship in Equation 6.14 was pursued. The particular formation was developed to satisfy several known aspects of the data; velocity and vertical rail roughness are proportional to the vertical output force while slipper gap is inversely proportional to vertical output force. The resulting relationship returned a spread of data that proved to be too wide even after graphical representation with exponential scaling. The best result in each respective force application direction is presented in Figures 6.3 and 6.4. The resulting data spread represented a situation where a closed form mathematical relationship was not possible. Other power combinations were pursued that featured cubic powers of velocity and quintic powers

137

of slipper gap whose results met with the same unacceptable spread of data. The next

relational attempt was to run the nondimensional parameters through the same gamut

of least squares regression methods used in the preceding sections. The best attempt

was the logarithmic regression which produced r^2 values of 0.54 vertical and 0.29

lateral, thus representing an inadequate regression of the non dimensional values.

Table 6.6 Design Parameter Dimensional Analysis

Design Parameter	Output	DP_1	DP_2	DP_3	DP_4	DP_5	DP_6	DP_7	DP_8
Variable	F_η	W	SG	RR_V	RR_L	ω_V	ω_L	ω_{TOR}	V
Dimension	MLT^{-2}	MLT^{-2}	L	L	L	T^{-1}	T^{-1}	T^{-1}	LT^{-1}

$$\Pi_1 = V^a W^b SG^c F = L^a T^{-a} M^b L^b T^{-2b} L^c MLT^{-2} = M^0 L^0 T^0$$
$$\Pi_2 = V^d W^e SG^f RR_V = L^d T^{-d} M^e L^e T^{-2e} L^f L = M^0 L^0 T^0$$
$$\Pi_3 = V^g W^h SG^i RR_L = L^g T^{-g} M^h L^h T^{-2k} L^i L = M^0 L^0 T^0$$
$$\Pi_4 = V^j W^k SG^l \omega_V = L^j T^{-j} M^k L^k T^{-2k} L^l T^{-1} = M^0 L^0 T^0$$
$$\Pi_5 = V^m W^n SG^o \omega_L = L^m T^{-m} M^n L^n T^{-2n} L^o T^{-1} = M^0 L^0 T^0$$
$$\Pi_6 = V^p W^q SG^r \omega_{TOR} = L^p T^{-p} M^q L^q T^{-2q} L^r T^{-1} = M^0 L^0 T^0$$

(6.11)

Table 6.7 Π Exponent Values

	Π_1	Π_2	Π_3	Π_4	Π_5	Π_6
	$a = 0$	$d = 0$	$g = 0$	$j = -1$	$m = -1$	$p = -1$
Exponent Values	$b = -1$	$e = 0$	$h = 0$	$k = 0$	$n = 0$	$q = 0$
	$c = 0$	$f = -1$	$i = -1$	$l = 1$	$o = 1$	$r = 1$

$$\Pi_1 = \frac{F}{W}$$

$$\Pi_2 = \frac{RR_V}{SG}$$

$$\Pi_3 = \frac{RR_L}{SG}$$

$$\Pi_4 = \frac{SG\omega_V}{V} \tag{6.12}$$

$$\Pi_5 = \frac{SG\omega_L}{V}$$

$$\Pi_6 = \frac{SG\omega_{TOR}}{V}$$

$$\Pi_1 = f(\Pi_2, \Pi_3, \Pi_4, \Pi_5, \Pi_6) \tag{6.13}$$

$$\Pi_1 = \frac{\Pi_2 \Pi_4}{\Pi_3 \Pi_5 \Pi_6} = \frac{RR_V \omega_V V}{RR_L \omega_L \omega_{TOR} SG} \tag{6.14}$$
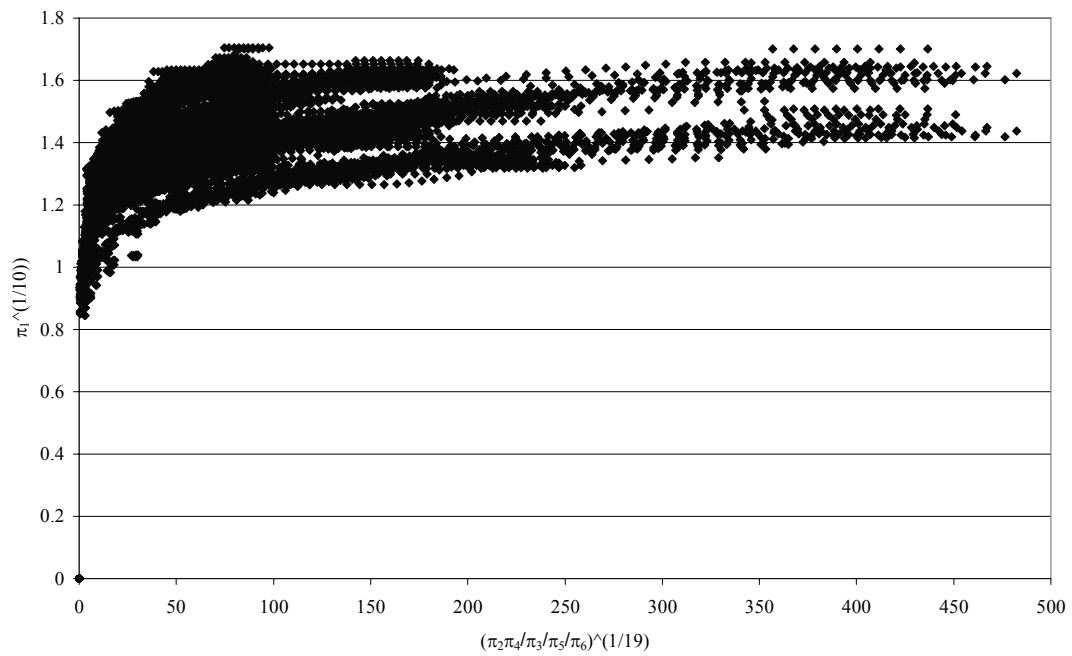
Figure 6.3 Vertical Π Theorem Analysis

139
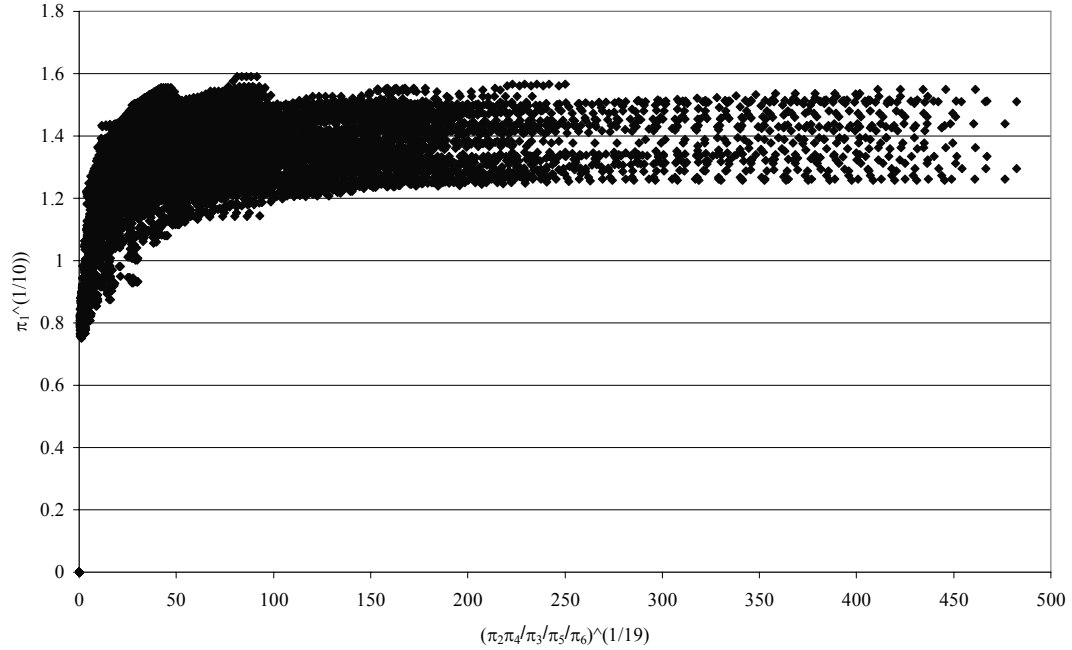
Figure 6.4 Lateral Π Theorem Analysis

6.4 Multivariate Interpolation

Multivariate interpolation is a method of computing a correlated value from a multidimensional data table of input design parameters and associated η force output values. The point of interest is bounded by input variables higher and lower in value. The output values associated with each set of input variables is then used to linearly interpolate the value of the point of interest to produce the desired output value. Multivariate interpolation is basically a local application of linear regression as the point of interest is a weighted average of the adjacent bounding points. On the other hand, a regression method is influenced by values of all points in the data. A multivariate interpolator meticulously considers weighted averages between distinct points in a data table where a regression equation would be applicable to all points

140

throughout the table. Multivariate interpolation, if properly applied, is accurate for almost all data types since it is bounded while regression techniques seek to satisfy an assumed mathematical relationship for the entire data set. In the current study, the nonlinear nature of the η force data makes multivariate regression the correct choice for the η force prediction tool.

For clarity, two examples are presented. The first consists of a 2-dimensional example that requires four sets of data points to bound the desired point. The high values will be designated by a 1 and the low values by a 0 and the interpolated values by 0.5. There are output values associated with each data point set. The desired point is designated by a value of (0.5,0.5) with the 2-dimensional example displayed in Figure 6.5. Pairs of data point sets are interpolated as shown by the interpolation points which in turn are interpolated to return the desired point designated in the figure by a square. Equation 6.15 was applied to the pairs of data points to perform the interpolation. As applied and conducive to the piecewise linear nature of the data, the interpolation method was implemented as a two dimensional recursive interpolation.

A second example, 3-dimensional, appears in Figure 6.6 and demonstrates the extension of the 2-dimensional example with the addition of another dimension and by the transformation of the interpolation space from a square to a cube. The interpolation is accomplished using Equation 6.15 and is easily adapted for use by considering pairs of adjacent points and stepping towards the desired location. Again the high values are designated by a 1 and the low values by a 0. The desired point is
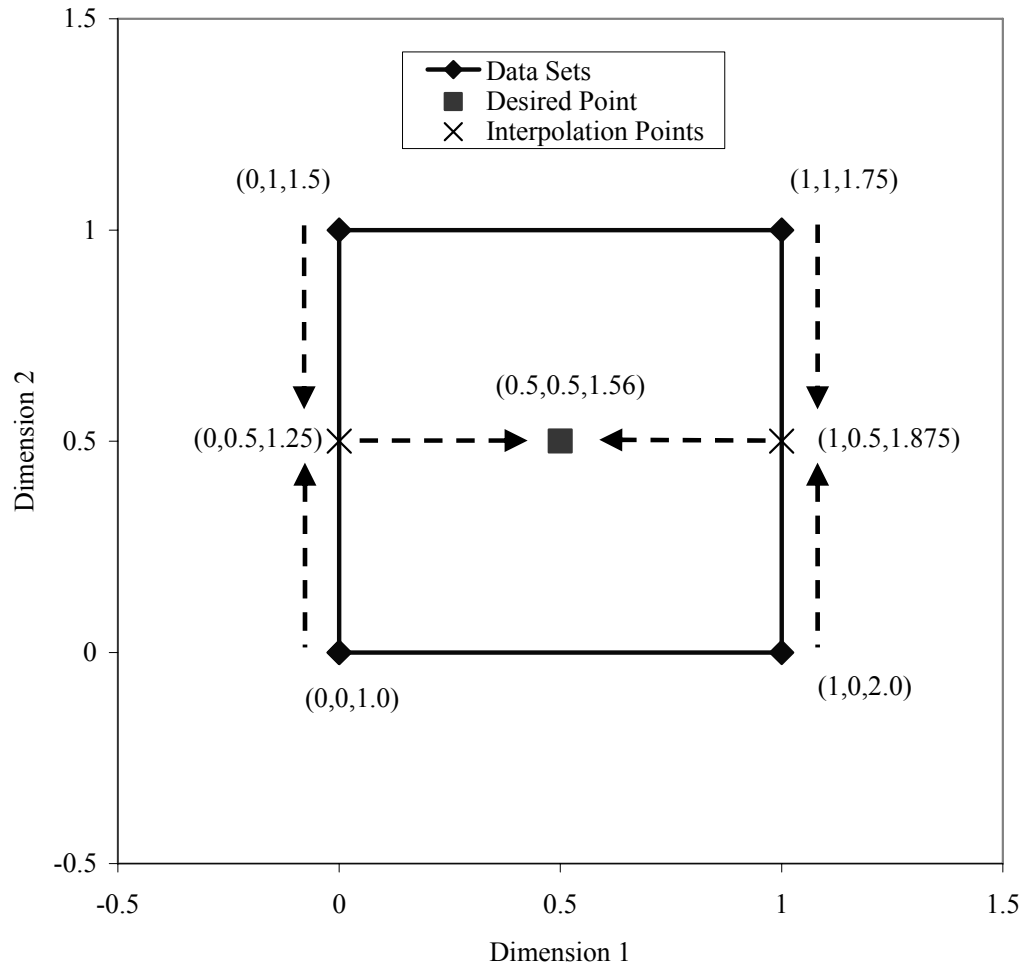
Figure 6.5 2-Dimensional Interpolation Example Depiction

$$y_{desired} = \left(\frac{y_h - y_l}{x_h - x_l} \right)(x_{desired} - x_h) + y_h \qquad (6.15)$$

(0.5, 0.5, 0.5) and is ultimately found to be 1.88. The interpolation process may be

performed between any eight points; in this study, it was more efficient to perform

the interpolation between adjacent points which are for this example the circles and

then interpolated to the points designated by the Xs. These four points were then

interpolated to the two hexagons and finally to the square; this process is detailed in
Table 6.8. The total number of bounding points for the three dimensional case is 8
points indicating a trend of 2^n where n is the number of dimensions or parameters
needed to bound the desired point.
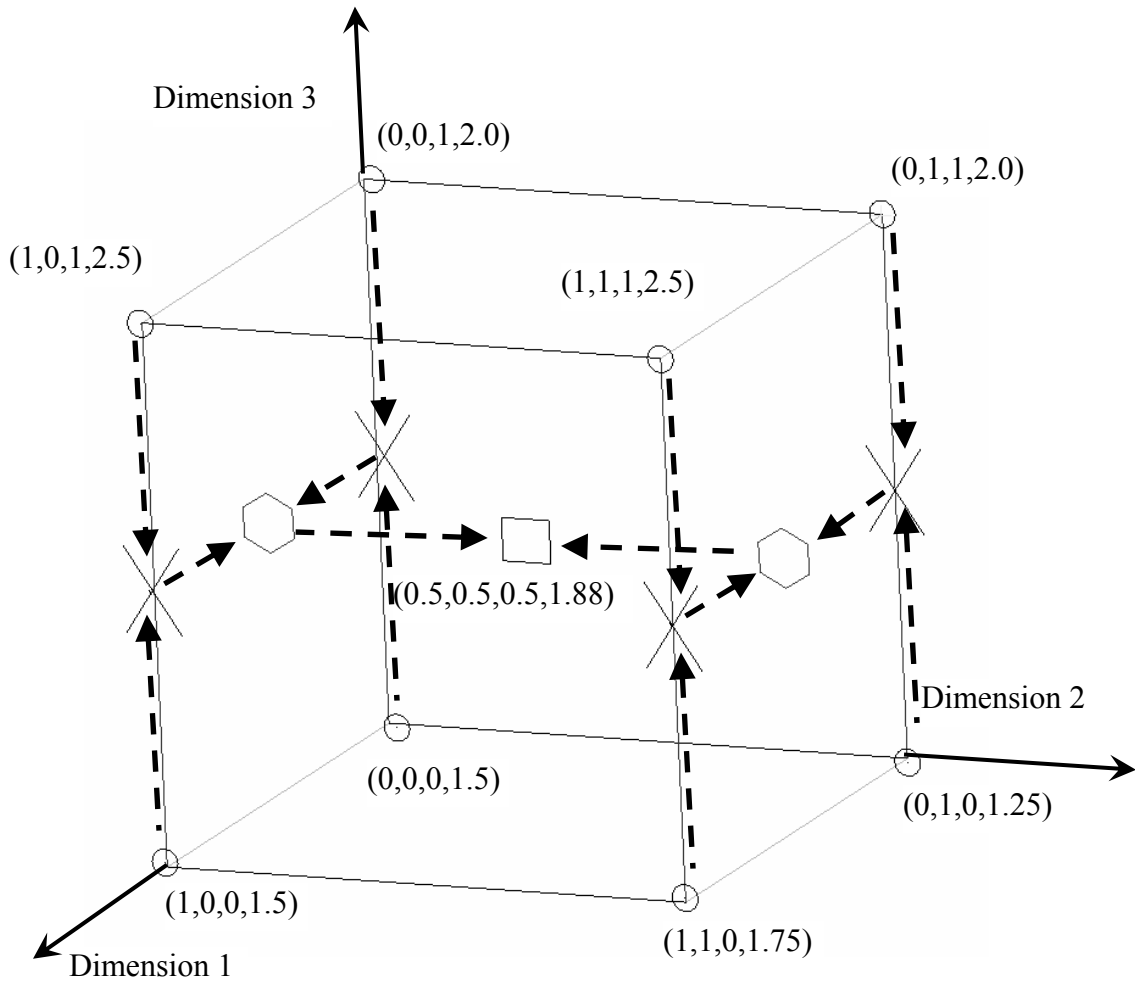
Figure 6.6 3-Dimensional Interpolation Example Depiction

Table 6.8 Three Dimensional Interpolation Detail

Dimensions			
(X_1,X_2,X_3,Y)	(X_1,X_2,X_3,Y)	(X_1,X_2,X_3,Y)	(X_1,X_2,X_3,Y)
(0,0,0,1.5)	(0,0,0.5,1.75)	(0.5,0,0.5,1.875)	(0.5,0.5,0.5,1.875)
(0,0,1,2.0)			
(1,0,0,1.5)	(1,0,0.5,2.00)		
(1,0,1,2.5)			
(0,1,0,1.25)	(0,1,0.5,1.625)	(0.5,1,0.5,1.875)	
(0,1,1,2.0)			
(1,1,0,1.75)	(1,1,0.5,2.125)		
(1,1,1,2.5)			
Circle	X	Hexagon	Square
Symbol			

Extending the interpolation to higher dimensions, ultimately 8, a systematic approach is warranted due to the many calculations needed to perform data sorting and adjacent point interpolation. The total number of data points needed to bound the desired point is 2^8 or 256. The interpolation algorithm was implemented on the data set produced in Chapter 5 in a Microsoft© Excel spreadsheet and was found to be

144

accurate and expedient. The shortest runtimes for the spreadsheet were 20 seconds to return dynamic loads for a full 8 dimensional design parameter set. The spreadsheet functioned such that if a design parameter set coincided with a η force database point then the vertical and lateral η force database values were returned. Further testing showed that the spreadsheet properly interpolated η force values for single parameter variations.

A concern when using an interpolation method is that representing a design parameter set outside the range of the original data set requires extrapolation. To alleviate this concern, the maximum velocity range was linearly extrapolated to 10,250 fps from the original value of 10,000 fps. Slipper gap values should not exceed the range specified by regulation (846th Test Squadron 2006) and rail roughness is always be adequately bounded by current design parameter range based on actual measurements. A remaining concern is the inclusion of natural frequency of the sled since it is difficult to predict the values produced during a sled development cycle. The typical range expected from the reduced complexity model was taken directly from the LSR sled with no payload since this design is the most likely candidate to experience high velocity ranges for the foreseeable future. However the range of natural frequencies studied herein is not all encompassing. Thus, the question remains: how are natural frequency values outside of this range to be accounted for? In the event that the desired design parameter values were in the unbounded space, the highest adjacent value was returned in place of the interpolated value and the user was notified of such. For situations where η limits are greatly

145

exceeded, or completely unbounded the most logical and conservative approach was to prescribe the maximum η force value and notify the user. It is seen that for almost all-typical design parameter values that η forces were less than their λ or SIMP counterparts. When η force design parameter ranges were exceeded and extreme conservatism was desired then the next most accurate force prediction tool was λ or SIMP. However, given the inaccurate nature of these two methods it would be advisable to use only λ with the condition that the answer would be highly conservative for values of typical rail roughness only.

7. COMPARISON OF PREDICTED LOAD TO PREVIOUS LOAD PREDICTION METHODS

The η force generated in the course of this study was compared to methods commonly used to predict design loads including λ, SIMP, and SLEDYNE. The comparison was conducted in two parts, a general comparison of force magnitude predicted with the various techniques and then a comparison of sled designs produced using the different methods to evaluate the effectiveness of the new prediction method. SLEDYNE was successfully recompiled in a Microsoft® Windows environment; however, the required COSMIC NASTRAN® input files could not be generated for the comparison study, and no previously designed narrow gauge sleds using SLEDYNE were located. These complications made SLEDYNE unusable for a comparison tool but since it is a detailed FEM implementation of the same method used to develop SIMP, the comparison is made for both within the context of SIMP.

7.1 Force Magnitude Comparison

The comparison of the magnitudes of design forces predicted by η, λ, and SIMP was conducted to determine the accuracy of each method and to develop familiarity comparing η forces to those from more well known methods. SIMP and λ force values were calculated alongside η force values during parameter variation data processing to give an accurate comparison. In the majority of the cases studied, for typical values of rail roughness, SIMP and λ forces were larger in magnitude than η forces after the force transition point is reached (see Section 5.4.1). There are a few

cases where η forces exceed λ and SIMP forces, these typical rail roughness cases and associated values shown in Table 7.1. It is seen in Table 7.1 that in the situation when one force direction of η exceeds λ or SIMP, the other direction tends to be lower leading to sled designs which may ultimately contain lower mass. The ratio of lateral to vertical force as dictated in the formation of λ, typically 0.6, is not observed in the case of η where the ratio varies from 0.07 to 1.8 and is dictated by velocity, rail roughness and slipper gap. The lateral to vertical force ratio for η forces is directly related to the mechanisms that cause η lateral and η vertical to increase or decrease. The same study of SIMP derived forces yields a range of 0.22 to 0.28; however, the lateral values of SIMP generated forces did not correlate well to test data and subsequently tend to under predict lateral forces (Mixon 1971). In studies of LSR and CO test data (Turnbull and Minto 2003, Leadingham and Schauer 2001) the ratio of lateral to vertical force varies and ranges from 0.07 to 1.4.

It was found during the design parameter variation study of η that combinations of certain design parameters yielded higher η forces. These sets were not the same for the vertical and lateral force directions. The maximum η force values are shown in Table 7.2 and occurred at design parameter values of 3123313 vertical and 3313313 lateral. It was documented previously and verified currently that rail roughness and slipper gap are highly influential in the magnitude of dynamic loading. As can be seen in Table 7.2, the high values of rail roughness, and the lower value of slipper gap return the maximum η forces at maximum velocity. Maximum force occurring at maximum velocity had been noted from the earliest studies of

dynamic loading (ISTRACON Handbook 1961, Mixon 1971).

Table 7.1 Selected η Comparisons to λ and SIMP at 10,000 fps

| | η Peak | | λ Peak | | SIMP Peak | |
Case	Vertical (lb_f)	Lateral (lb_f)	Vertical (lb_f)	Lateral (lb_f)	Vertical (lb_f)	Lateral (lb_f)
2222221	28,158	26,348	30,670	18,402	48,548	11,329
2222223	36,740	17,689	104,080	62,448	47,923	10,414
1222222	48,516	19,379	67,376	40,426	48,357	10,771

Table 7.2 Maximum η Force Values at 10,000 fps

Case	η Vertical (lb_f)	η Lateral (lb_f)
3123313	89,094	22,379
3313313	59,669	53,414

7.1.1 Vertical Force Comparison

At higher sled velocities, the comparison of the vertical η forces to those predicted by SIMP and λ follow the general trend that higher values of vertical rail roughness standard deviation yielded high η forces than the corresponding values of SIMP and λ. This is due to the choice of the high value of vertical rail roughness, 30% greater than surveyed, and to the fact that SIMP and λ are derived from typical

149

rail roughness conditions and do not account for changes in rail roughness deviation. The best example is shown in Figure 7.1 where η vertical 1111331 and 1111131 are plotted against corresponding λ and SIMP values. Intuitively smaller slipper gap, high vertical sled natural frequency, and smaller mass amplify the effect of high vertical rail roughness. This is a natural conclusion since λ and SIMP are derived for fixed slipper gaps and depend directly on mass to calculate loading. The mass variation effect is less in SIMP than in λ since with λ it is a linear relationship and with SIMP it is a $Mass^{0.25}$ term. The vertical sled natural frequency effect is less in SIMP than in λ since SIMP can account for some flexibility variation. When all parameters are typical, 2222222, η is less than λ and SIMP as shown in Figure 7.2.
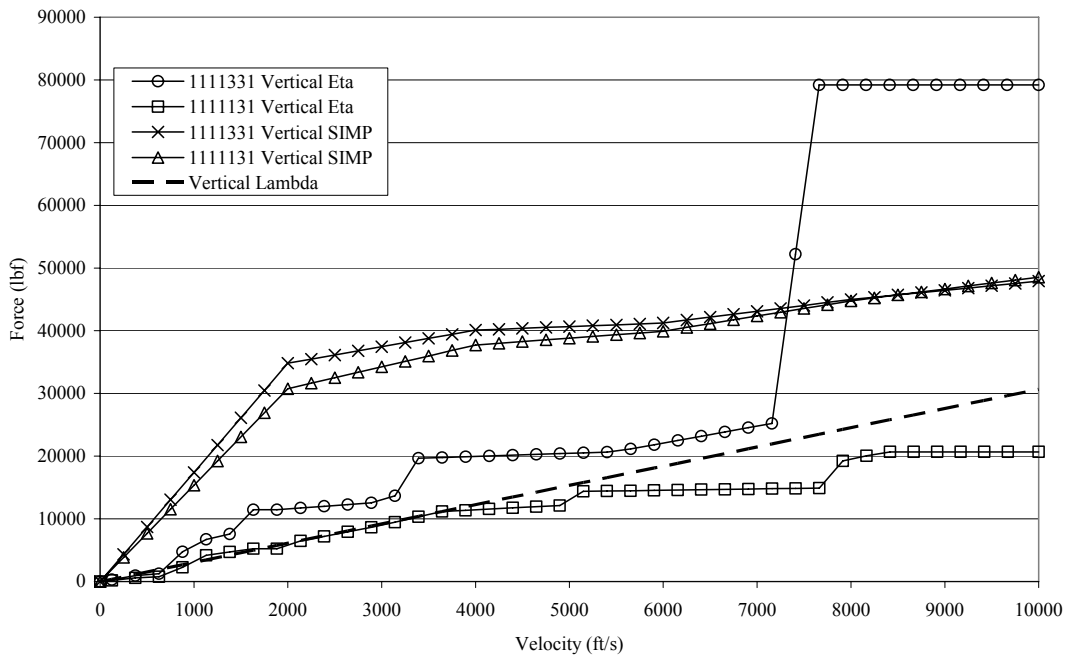
Figure 7.1 Vertical Force Extreme Case, 1111331, Comparison
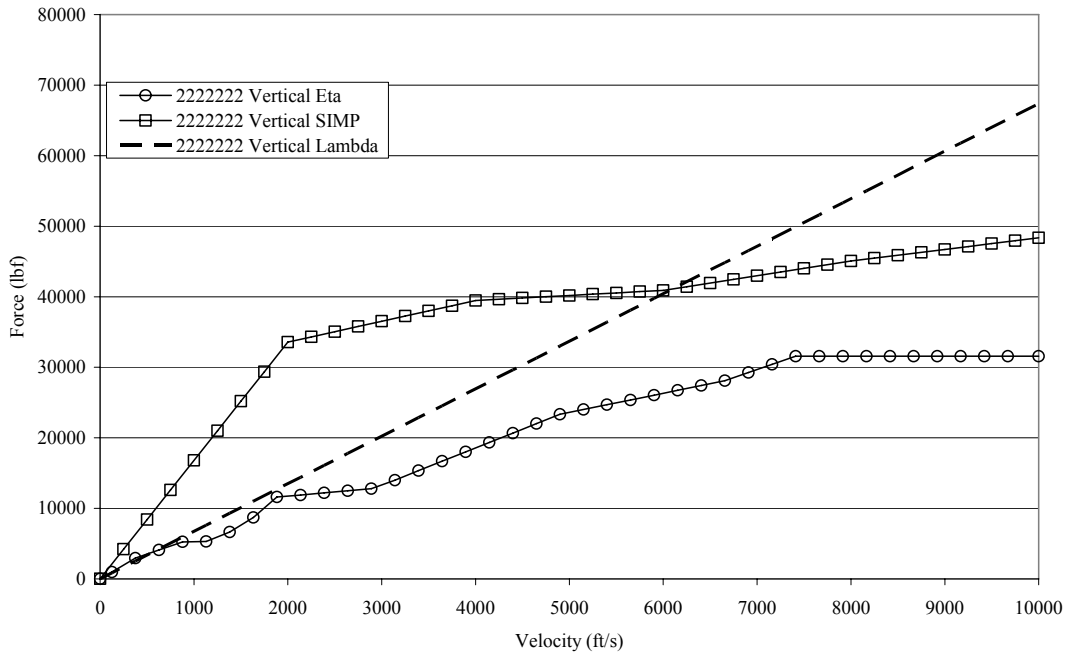
Figure 7.2 Vertical Force Typical Case, 2222222, Comparison

7.1.2 Lateral Force Comparison

The comparison of η forces in the lateral direction to those generated from SIMP and λ follow the similar general trends reported in the study of the vertical force comparison. Standard deviation of lateral rail roughness was the primary driving factor behind the deviation of η from SIMP and λ. Increases in slipper gap tended to lessen the effect and conversely decreases in slipper gap tended to amplify the effect. Increases in sled velocity caused increases in η forces as was the case with λ and SIMP. Combinations of high natural frequencies and high rail roughness tended to increase η loading. The amplification effect was similar to that seen for lower and higher gap. There was significant coupling of the lateral and vertical loading in the sense that lateral η was sensitive to changes in vertical sled parameters

151

such as vertical rail roughness values and vertical sled natural frequency. The

coupling trend was more evident than was observed in the vertical direction.

In general, η was lower than λ for typical and low values of rail roughness as

shown in Figure 7.3 for the extreme case of 1111133. Since λ depends directly on

sled mass but does not consider rail roughness, λ was less than η for low mass values

as shown in Figure 7.4 for the extreme case of 2222221. In general, SIMP was

significantly less than η for all higher velocity cases studied. This substantial result is

due to SIMP not being correlated to lateral test data since it did not consider lateral

rail survey data and did not accurately characterize lateral slipper rail contact. It is

seen in hypersonic test data from the LSR test (Minto and Turnbull 2003) that lateral

and vertical dynamic effects are similar in magnitude. It should be remembered that

λ and SIMP are fixed in many of their parameters when compared to η. In the all-

typical, 2222222, case comparison, Figure 7.5, η proves to be lower at every velocity

other than 1,500 fps where η slightly exceeds λ. η is lower than SIMP for velocities

under 4000 fps.

7.2 Sled Design Comparison

To further illustrate the comparison among the force prediction methods a

mock sled design was performed to accentuate the differences between η, λ, and

SIMP. The reduced complexity model narrow gauge was chosen as the sled

configuration for consideration. The slipper beam material is normalized 4130 steel

(Department of Defense 2003) whose properties are given in Table 7.3 while the sled

152
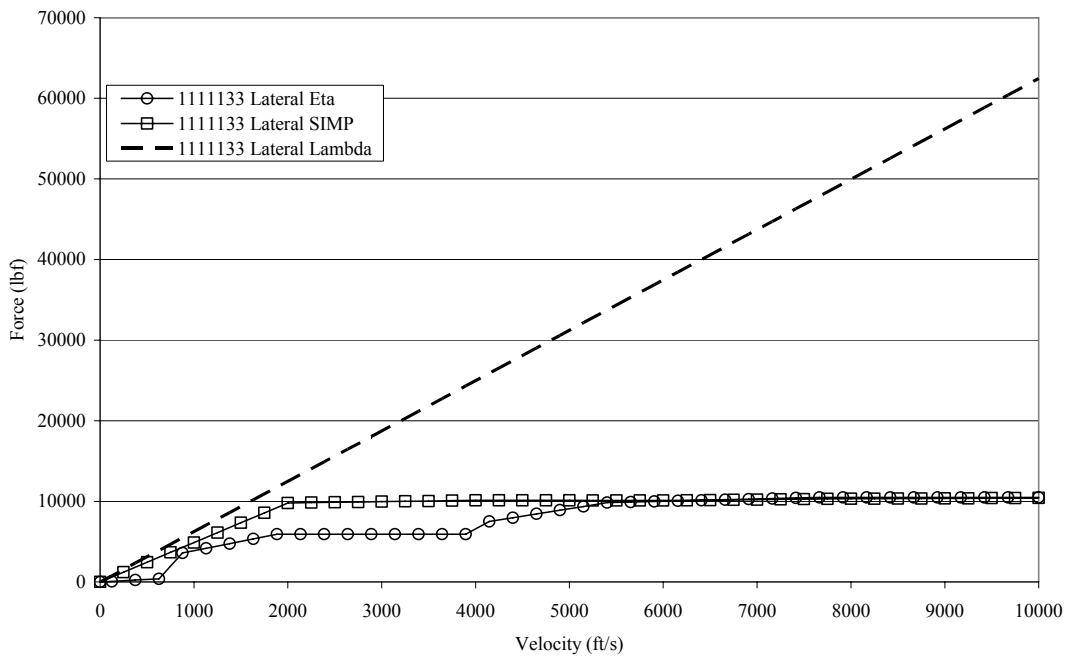
Figure 7.3 Lateral Force Extreme Case, 1111133, Comparison
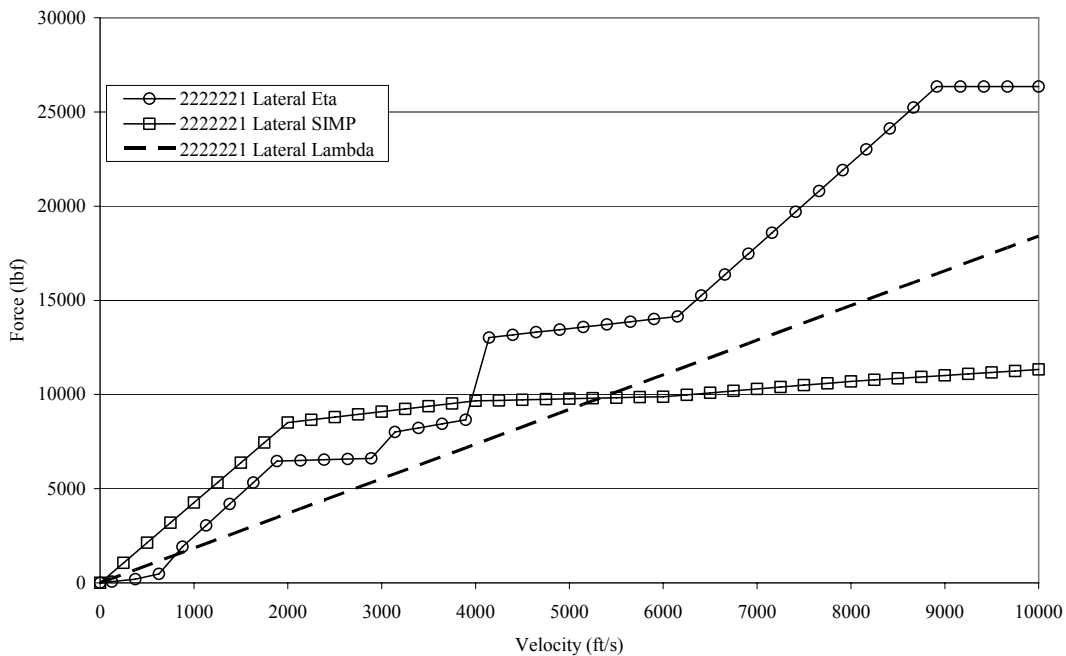
Figure 7.4 Lateral Force Extreme Case, 2222221, Comparison

153
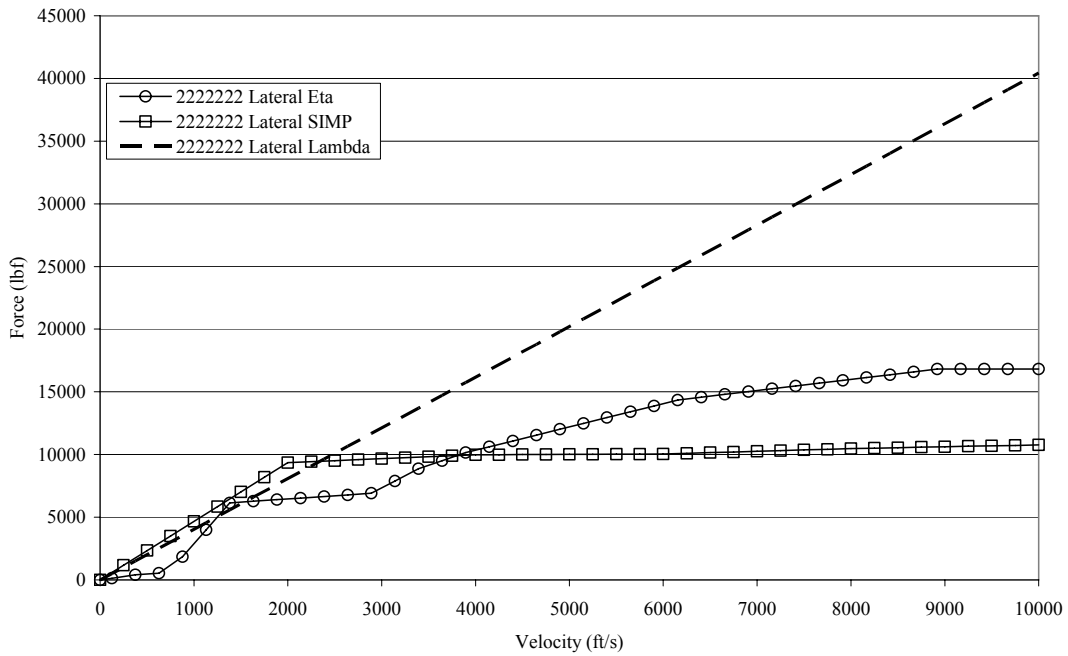
Figure 7.5 Lateral Force Typical Case, 2222222, Comparison

Table 7.3 Slipper Beam Material Specification

Young's Modulus (psi)	Poisson's Ratio	Density (lb_f/in^3)	Yield Stress (psi)	Ultimate Stress (psi)
29E6	0.32	0.283	70E3	90E3

body design material is a composite whose properties are given in Table 7.4. The

comparison to be made here was more than a basic ratio of loading for η and SIMP

since it will take into consideration the mass distribution which is dictated by the

capacity to successfully resist the resulting load distribution within the structure. The

comparison was further defined by setting the parameters to their typical values from

the η force formation study as shown in Table 7.5.

Table 7.4 Sled Body Material Specification

Young's Modulus (psi)	Poisson's Ratio	Density (lb$_f$/in^3)	Yield Stress (psi)	Ultimate Stress (psi)
11.8E6	0.28	0.067	60E3	60E3

Table 7.5 Design Parameters for Mock Sled Design

Design Parameter	DP$_1$	DP$_2$	DP$_3$	DP$_4$	DP$_5$	DP$_6$	DP$_7$	DP$_8$
Variable	W (lbf)	SG (in)	RR$_V$ (in)	RR$_L$ (in)	ω_V (Hz)	ω_L (Hz)	ω_{TOR} (Hz)	V (fps)
Value	842.0	0.125	0.0119	0.0147	79.9	84.5	85.9	9,500

The goal of the design comparison was to conduct a concept feasibility-level design of the sled structure as depicted in Figure 7.6 to minimize weight and optimize vonMises stress within the sled body and slipper beams. Initial study dimensions are listed in Table 7.6 and initial weight detailed in Table 7.7. The stress analysis was limited to basic beam analyses of the sled body and slipper beam and did not entail a detailed study of their connections or local three dimensional effects. The stress values were maximum values of beam bending, axial and shear resolved into their corresponding vonMises values. To further simplify the process, the thickness of the sled body and slipper beams were the varied parameters. Indirectly this caused shifts in weight and thus resulted in design iterations. Subject to the desire of the analyst, these iterations were reasonably curtailed in the present study. A Factor of Safety (FS) of 1.0 was applied to the yield stress and used to compute a Margin of Safety (MS) as shown in Equation 7.1 (Krupovage, Mixon, Bush 1991).

155
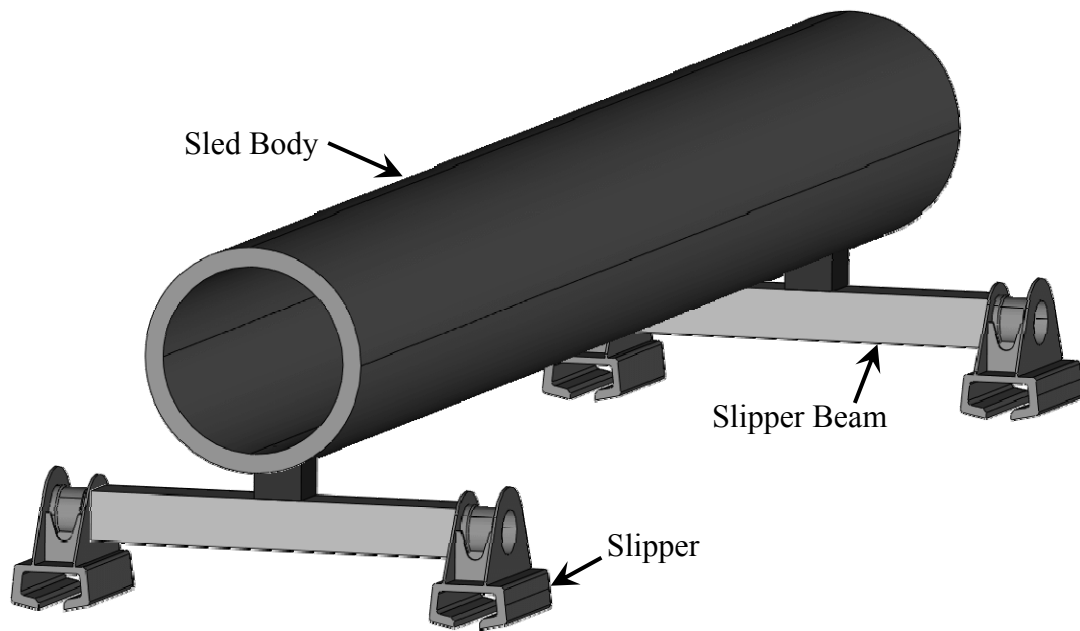
Figure 7.6 Design Study Sled Structure

Table 7.6 Initial Study Dimensions

Parameter	Slipper Beam Height (in)	Slipper Beam Width (in)	Slipper Beam Thickness (in)	Sled Body Radius (in)	Sled Body Thickness (in)
Value	3.5	3.5	0.375	8.06	1.354

Table 7.7 Initial Study Weight Detail

Component	Sled Body	Slipper Beam (2 total)	Slippers (4 total)	Miscellaneous	Total
Weight (lb$_f$)	573.856	95.513	132.00	40.631	842.00

$$MS = \frac{\sigma_{Allowable}}{\sigma_{Design}} - 1$$

$$\sigma_{Allowable} = \frac{\sigma_{Yield}}{FS}$$

(7.1)

where

σ_{Yield} is the material yield stress

7.2.1 λ Design Study

The λ mock sled design considers only weight and velocity to form the λ force associated with the sled design. The method of calculating the λ force (Krupovage et al. 1991) is shown in Equation 7.2 for a narrow gauge sled and produced initial force values of 63,992 lb_f vertical and 38,395 lb_f lateral utilizing the parameters given in Table 7.8. During the course of design iteration, it was apparent that adding material to the slipper beam to withstand the vonMises stress levels caused a linear load increase while the stress levels decreased cubically. The final study dimensions are shown in Table 7.9 and correspond to a total sled weight of 847.75 lb_f which is an increase of 5.75 lb_f over the initial design. The resulting shear and moment diagrams for the slipper beam and sled body appear in Figures 7.7-7.10. This design resulted in a MS of 0.0 at the forward slipper beam midpoint with final design loads of 66,330 lb_f vertical and 39,798 lb_f lateral.

$$F_{\lambda Vertical} = \lambda W = 0.008 * V * W$$

$$F_{\lambda Lateral} = 0.6 * F_{\lambda Vertical}$$

(7.2)

where

λ is the narrow gage λ factor, 0.008

W is sled weight

V is velocity

Table 7.8 λ Initial Design Parameters

λ Design Parameter	Sled Weight (lb$_f$)	Velocity (fps)	λ factor
	842.0	9,500	0.008

Table 7.9 λ Final Study Dimensions

Parameter	Slipper Beam Height (in)	Slipper Beam Width (in)	Slipper Beam Thickness (in)	Sled Body Radius (in)	Sled Body Thickness (in)
Value	3.5	3.5	0.598	8.06	1.25
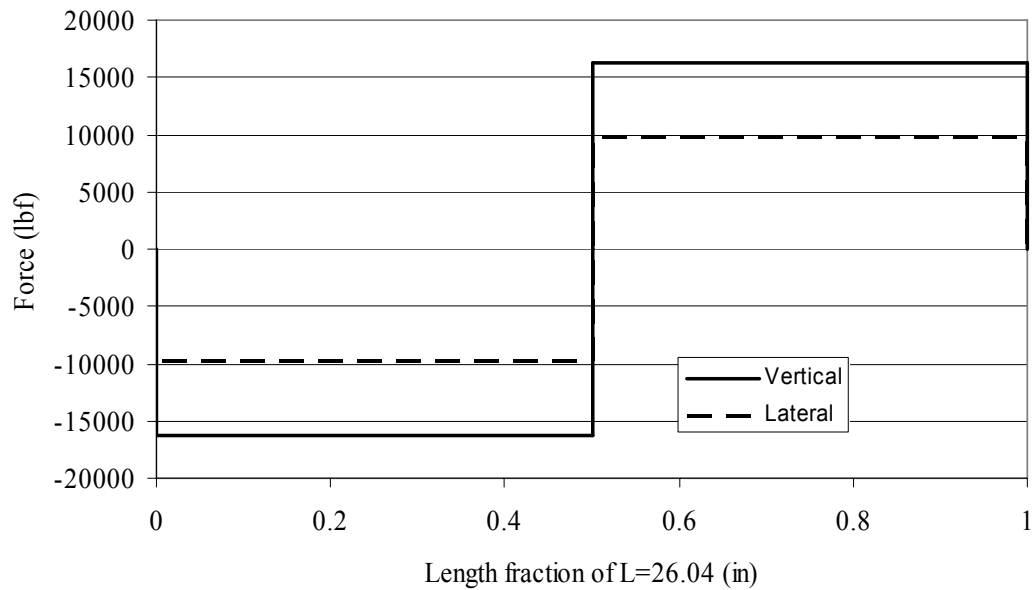
Figure 7.7 λ Slipper Beam Shear Diagram
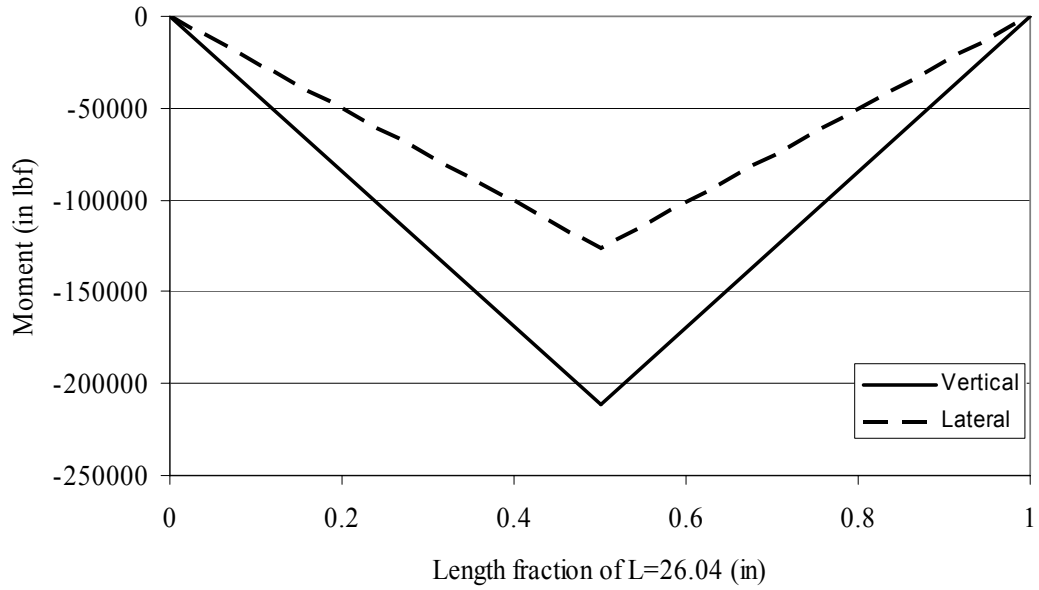
Figure 7.8 λ Slipper Beam Moment Diagram

Figure 7.9 λ Sled Body Shear Diagram

159
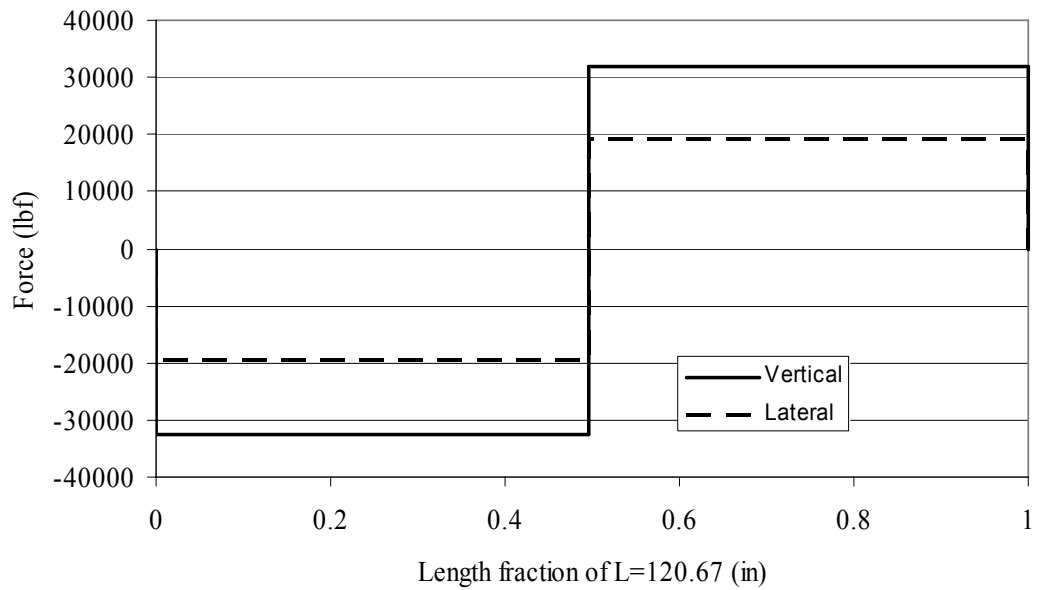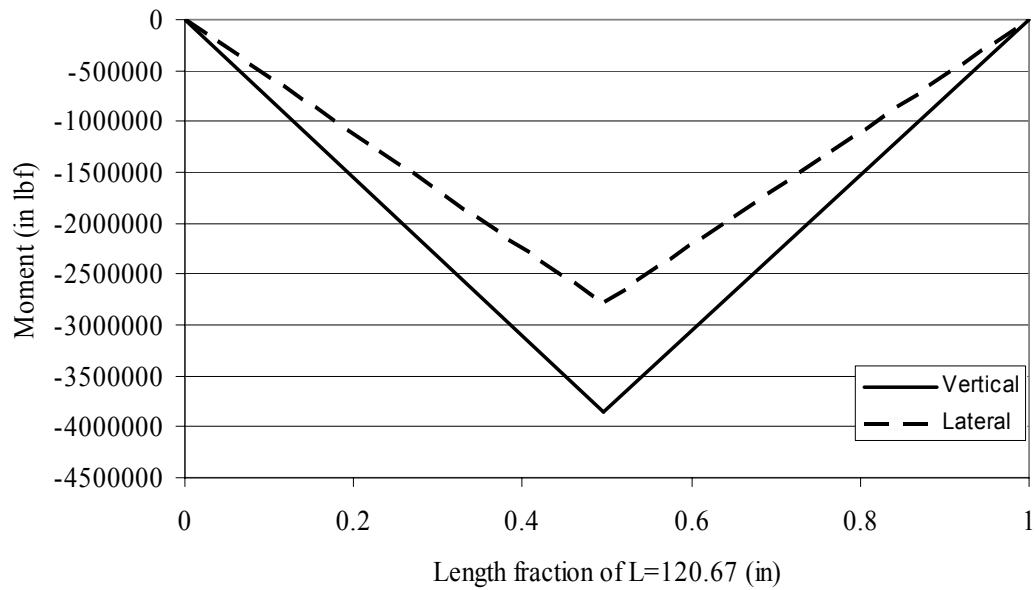
Figure 7.10 λ Sled Body Moment Diagram

7.2.2 SIMP Design Study

The SIMP force calculation was completed by applying the SIMP process to the design under consideration. The initial SIMP parameters appear in Table 7.10 and served as the starting point for this design study. After iteration, the final SIMP design parameters, Table 7.11, were produced and applied as an illustration of the load determination accomplished in 7 steps (Krupovage et al. 1991) for the current design. The first step of the SIMP process was the identification of SIMP parameters. The vertical slipper stiffness was defined as the deflection of the slipper beam at its mid span when considering the most likely linear boundary conditions which are that of a simply supported beam. This is justified since no significant deflection occurs until both slippers are engaged with the rail and no moment support is reasonable for these conditions since beam deflection will not cause the slipper to rotate through the

160

Table 7.10 SIMP Initial Design Parameters

SIMP Design Parameter	Sled Mass ($\mathrm{lb_f\,s^2/in}$)	Length CG to Slipper (in)	Pitching MMOI (in $\mathrm{lb_f\,s^2}$)	Yawing MMOI (in $\mathrm{lb_f\,s^2}$)	Vertical Slipper Stiffness ($\mathrm{lb_f/in}$)	Lateral Slipper Stiffness ($\mathrm{lb_f/in}$)
Front	2.181	59.94	4,708.14	4,692.14	860,732	146,332
Aft	2.181	60.73	4,708.14	4,692.14	860,732	146,332

Table 7.11 SIMP Final Design Parameters

SIMP Design Parameter	Sled Mass ($\mathrm{lb_f\,s^2/in}$)	Length CG to Slipper (in)	Pitching MMOI (in $\mathrm{lb_f\,s^2}$)	Yawing MMOI (in $\mathrm{lb_f\,s^2}$)	Vertical Slipper Stiffness ($\mathrm{lb_f/in}$)	Lateral Slipper Stiffness ($\mathrm{lb_f/in}$)
Front	2.022	59.94	4,653.78	4,639.34	5,82041	145,377
Aft	2.022	60.73	4,653.78	4,639.34	5,82041	145,377

slipper gap and bind. The lateral stiffness is the active stiffness of the slipper beam that resists the lateral movement of the sled. In this case, it is the longitudinal stiffness of half of the slipper beam and the stiffness of the outside vibration isolation material. The equivalent stiffness value of the springs in series is defined as the lateral slipper stiffness. The second step involved the computation of four effective mass distributions utilizing Equation 7.3. These values are given in Table 7.12 and were based upon a pinned-pinned 1st mode modal mass representation of the sled. The third step was to calculate the associated effective frequency using Equation 7.4

and yielded the data in Table 7.13. The fourth step was the calculation of lift-to-weight ratios which was 0 for the vertical value with the lateral case being held to the lowest value of 1. Steps 5 and 6 involved the determination and use of a design impact velocity using the downtrack velocity and effective impact velocity values

$$M_{effFV} = \frac{M}{1 + \dfrac{Ml_F^2}{I_P}}$$

$$M_{effAV} = \frac{M}{1 + \dfrac{Ml_A^2}{I_P}}$$

$$M_{effFL} = \frac{M}{1 + \dfrac{Ml_F^2}{I_Y}}$$

$$M_{effAL} = \frac{M}{1 + \dfrac{Ml_A^2}{I_Y}}$$

(7.3)

Table 7.12 SIMP Effective Mass Values

$M_{eff\,FV}$ (lb$_f$ s^2/in)	$M_{eff\,FL}$ (lb$_f$ s^2/in)	$M_{eff\,AV}$ (lb$_f$ s^2/in)	$M_{eff\,AL}$ (lb$_f$ s^2/in)
0.789	0.777	0.788	0.775

$$f_{FV} = \frac{1}{2\pi}\sqrt{\frac{K_{FV}}{M_{effFV}}}$$

$$f_{AV} = \frac{1}{2\pi}\sqrt{\frac{K_{AV}}{M_{effAV}}}$$

$$f_{FL} = \frac{1}{2\pi}\sqrt{\frac{K_{FL}}{M_{effFL}}}$$

$$f_{AL} = \frac{1}{2\pi}\sqrt{\frac{K_{AL}}{M_{effAL}}}$$

(7.4)

from Step 3, Table 7.14. The downtrack velocity value for the present study was

9,500 fps. The original SIMP monorail data for the velocity cases of 8,000 fps and

10,000 fps, reported by Greenbaum, Garner, and Platus (1973), were used to

interpolate to the velocity under consideration. The resulting impact velocities were

utilized in Equation 7.5 to calculate the maximum slipper force and are given in Table

7.15. The calculation of the maximum slipper force was multiplied by a numeric

constant of 5 as prescribed by Greenbaum et al. (1973) to include a conservative

factor of 2.5 for a thrusting monorail sled. This methodology was shown to be overly

conservative (Mixon 2006). Since the current application was on a non-thrusting

narrow gauge and that Mixon (1999b, 1999c) successfully used a numeric factor of 2

Table 7.13 SIMP Effective Impact Frequency

f_{FV} (Hz)	f_{AV} (Hz)	f_{FL} (Hz)	f_{AL} (Hz)
136.68	137.78	68.36	68.91

Table 7.14 SIMP Effective Impact Velocity

v_{FV} (in/s)	v_{AV} (in/s)	v_{FL} (in/s)	v_{AL} (in/s)
32.5	33.0	12.8	13.5

$$F_{FV} = 2\pi f_{FV} v_{FV} M_{effFV}$$
$$F_{AV} = 2\pi f_{AV} v_{AV} M_{effAV}$$
$$F_{FL} = 2\pi f_{FL} v_{FL} M_{effFL}$$
$$F_{AL} = 2\pi f_{AL} v_{AL} M_{effAL}$$

(7.5)

Table 7.15 SIMP Maximum Slipper Force

F_{FV} (lb$_f$)	F_{AV} (lb$_f$)	F_{FL} (lb$_f$)	F_{AL} (lb$_f$)
22030	22190	4332	4533

on a thrusting narrow gauge pusher much stiffer than the current study, a numeric

factor of 2 was used in Equation 7.5. Studying Equation 7.5 it was apparent that there

was no coupling of the vertical and lateral forces other than mass distribution

relationships. The data from step 6 was used in step 7 to produce inertial loading

which could then be applied to either discrete or continuous mass systems. In the

current study, the data output from step 6 was sufficient to produce the shear and

moment diagrams in Figures 7.11-7.14. Substituting Equations 7.3 and 7.4 into 7.5

and assuming the relationship of impact velocity to impact frequency given in

Equation 7.6, it can be shown from a quantitative viewpoint that SIMP is essentially a

function of stiffness, K, effective mass, M_{eff}, downtrack Velocity, V_d, lift-to-weight

ratio, L/W, and a constant as shown in Equation 7.7. The relationship in Equation 7.7

shows the dependence upon mass to be much less than that of λ and that SIMP is

more a function of V_d and L/W. Applying the stress analysis based upon the shear

and moment diagrams and from the iteration of structure variations through the SIMP

process, the final study dimension values were obtained and are shown in Table 7.16.

They represented a decrease in weight of 61.52 lb$_f$ from the initial design giving a

final sled weight of 780.48 lb$_f$. The minimum MS of 0.00 was located at both slipper

beam mid-spans. During the design iteration process, it was observed that reducing

164
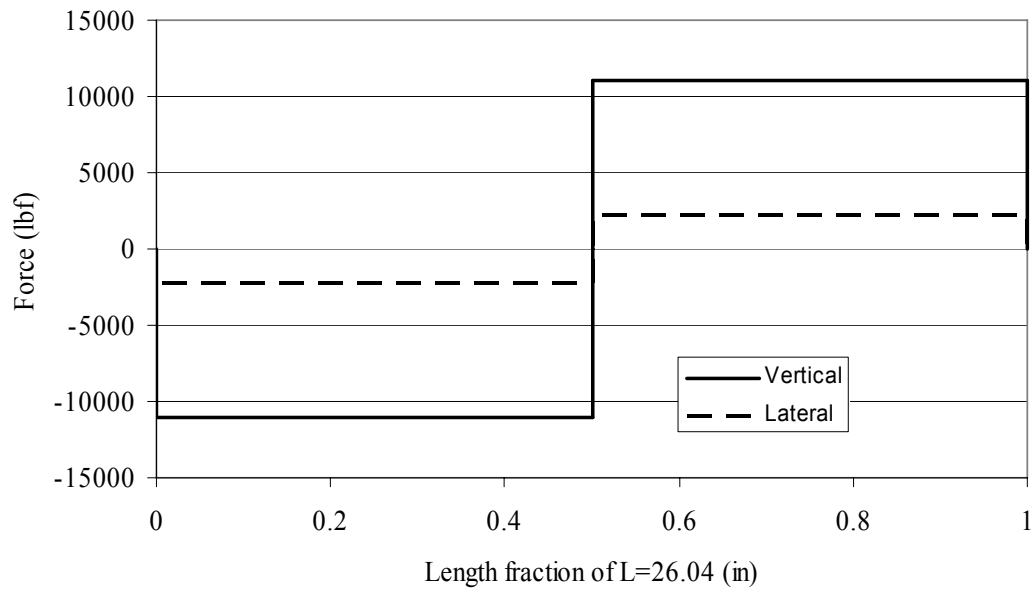
Figure 7.11 SIMP Slipper Beam Shear Diagram
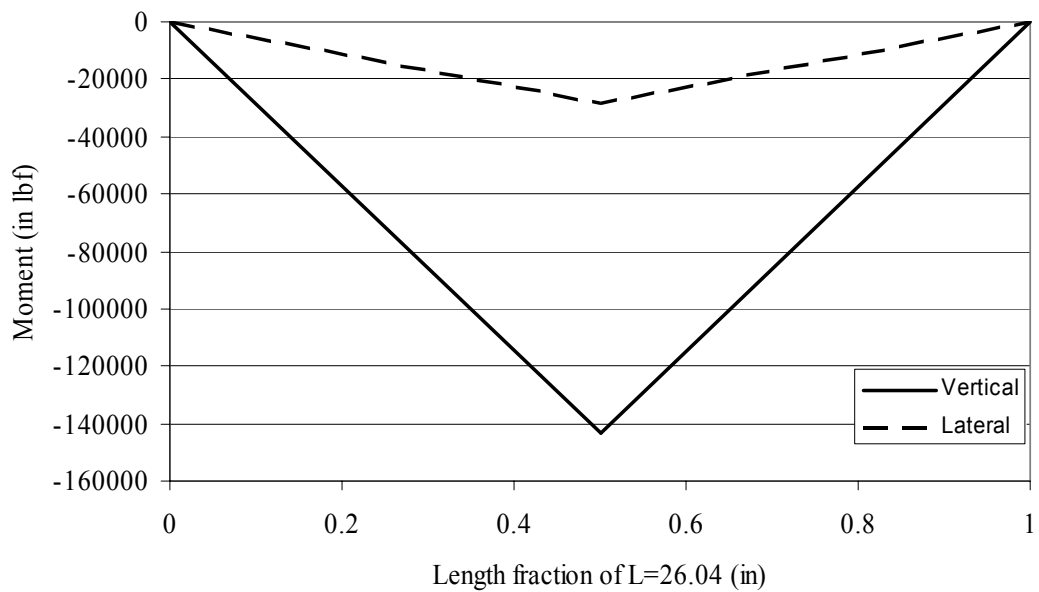
Figure 7.12 SIMP Slipper Beam Moment Diagram
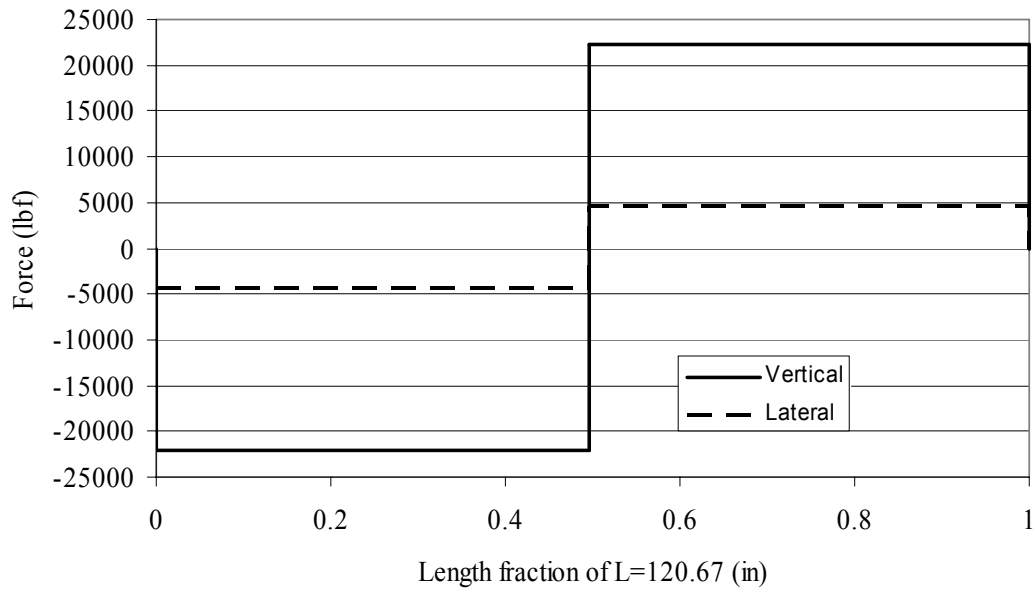
Figure 7.13 SIMP Sled Body Shear Diagram
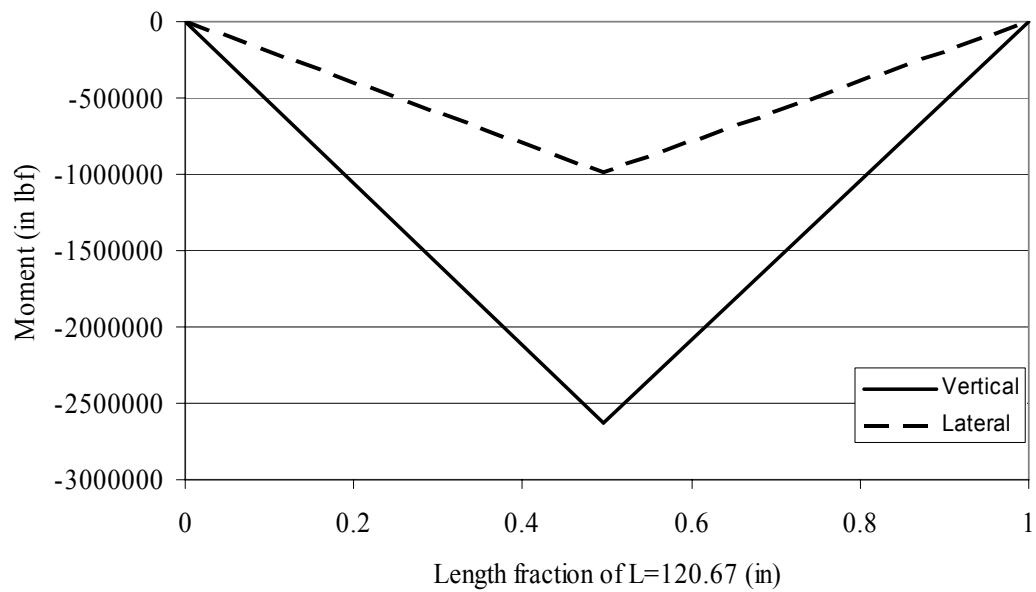
Figure 7.14 SIMP Sled Body Moment Diagram

$$v = \text{constant} * V_D * \frac{L}{W} \left(\frac{K}{M_{eff}} \right)^{0.25} \tag{7.6}$$

where
V is the slipper impact velocity

166

V_d is the downtrack velocity
L/W is the Lift to Weight ratio
K is the applicable stiffness
M_{eff} is the effective mass

$$F = K^{0.75} * M_{eff}^{0.25} V_D \frac{L}{W} \text{constant} \qquad (7.7)$$

where
F is the general SIMP force

Table 7.16 SIMP Final Study Dimensions

Parameter	Slipper Beam Height (in)	Slipper Beam Width (in)	Slipper Beam Thickness (in)	Sled Body Radius (in)	Sled Body Thickness (in)
Value	3.5	3.5	0.35	8.06	1.21

weight in the slipper beam increased flexibility which when coupled with the

corresponding weight reduction served to reduce the vonMises stress level. The

relationship of slipper impact velocity to slipper impact frequency is a higher slipper

impact frequency corresponds to a higher impact velocity which linearly increases

SIMP loading as shown in Equation 7.5.

7.2.3 η Design Study

        The η force design study consisted of entering the design parameters given in

Table 7.5 into the interpolation tool and applying the resulting loads to the sled. The

process of η force calculation involves the monitoring of interrelated design

parameters of mass, DP_1, and sled natural frequencies, DP_5, DP_6, DP_7. These specific

design parameters are affected by the variation of the study dimensions and are what ultimately contributes to the variation of the η force. This is most efficiently accomplished using a FEM software package or spreadsheet application as changes in structural members result in changes in the associated mass and usually the natural frequencies of the sled. There are situations where the 1st fundamental frequency of a particular component is higher than the 1st fundamental frequency of the system. Thus the associated frequency design parameter does not change with the mass of the system. This phenomenon must be closely monitored with a FEM package to ensure that all frequency content is not overlooked. The initial vertical and lateral loading was 29,728 lb$_f$ and 21,948 lb$_f$ respectively. After iteration, the final design parameters shown in Table 7.17 correspond to the final study dimensions shown in Table 7.18. This yielded the shear and moment diagrams shown in Figures 7.15-7.18. The final sled weight of 767.91 lb$_f$ shows a decrease in weight of 74.09 lb$_f$ from the initial design. The minimum MS of 0.0 was located at the slipper beam midpoint.

7.2.4 Comparison of Design Study Results

The results of the sled design comparison appear in Tables 7.19-7.21 and show that η produces a basic sled design with lower resultant dynamic loading and correspondingly lower weight giving opportunity for better sled performance. Tables 7.19 and 7.20 summarize and compare the peak moment values for the three methods found in Figures 7.8, 7.10, 7.12, 7.14, 7.16, and 7.18. The application of the λ method was very direct and efficient as shown by Equation 7.2. The efficiency of

168

Table 7.17 η Final Design Parameters for Mock Sled Design

Design Parameter	DP_1	DP_2	DP_3	DP_4	DP_5	DP_6	DP_7	DP_8
Variable	W (lbf)	SG (in)	RR_V (in)	RR_L (in)	ω_V (Hz)	ω_L (Hz)	ω_{TOR} (Hz)	V (fps)
Value	767.9	0.125	0.0119	0.0147	79.9	84.5	85.9	9,500

Table 7.18 η Final Study Dimensions

Parameter	Slipper Beam Height (in)	Slipper Beam Width (in)	Slipper Beam Thickness (in)	Sled Body Radius (in)	Sled Body Thickness (in)
Value	3.5	3.5	0.216	8.06	1.26
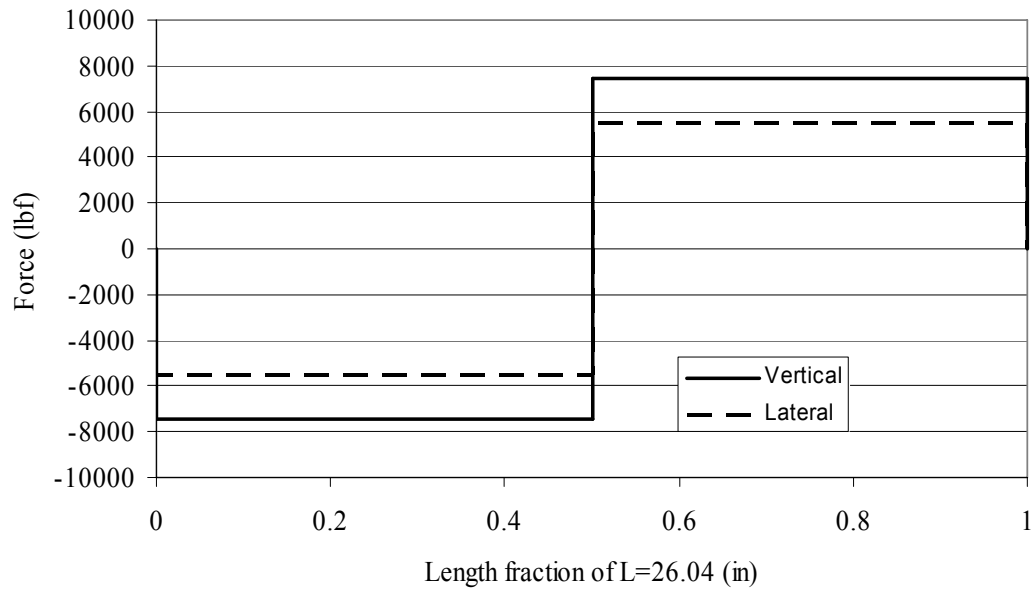
Figure 7.15 η Slipper Beam Shear Diagram
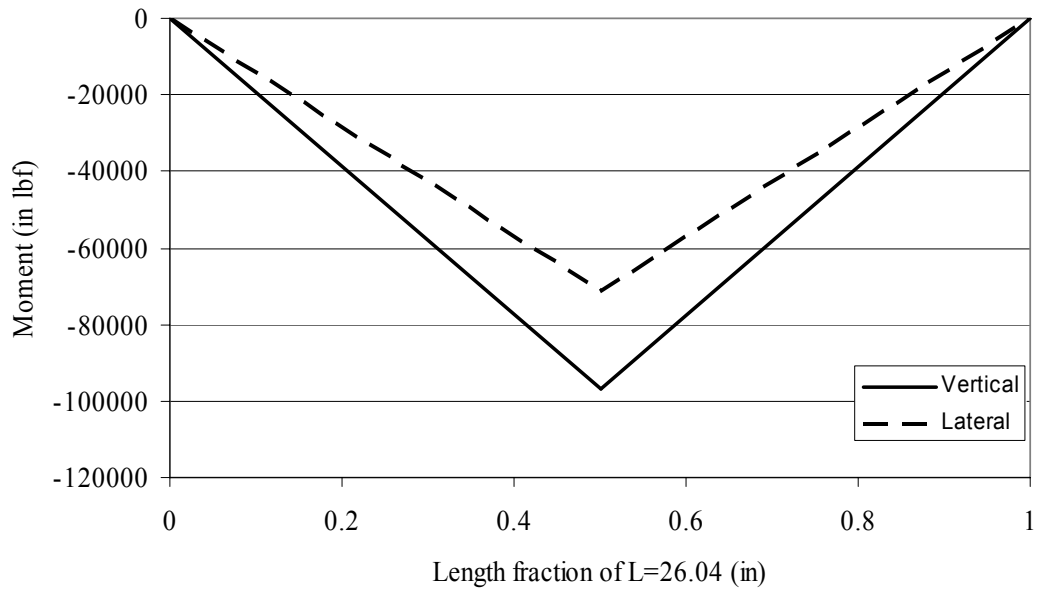
Figure 7.16 η Slipper Beam Moment Diagram
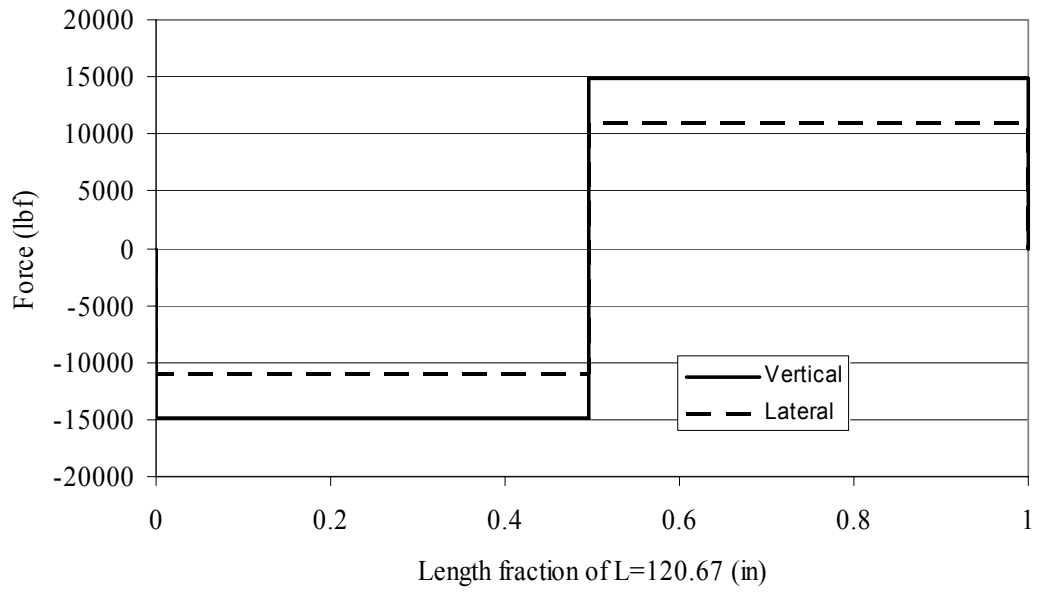
Figure 7.17 η Sled Body Shear Diagram
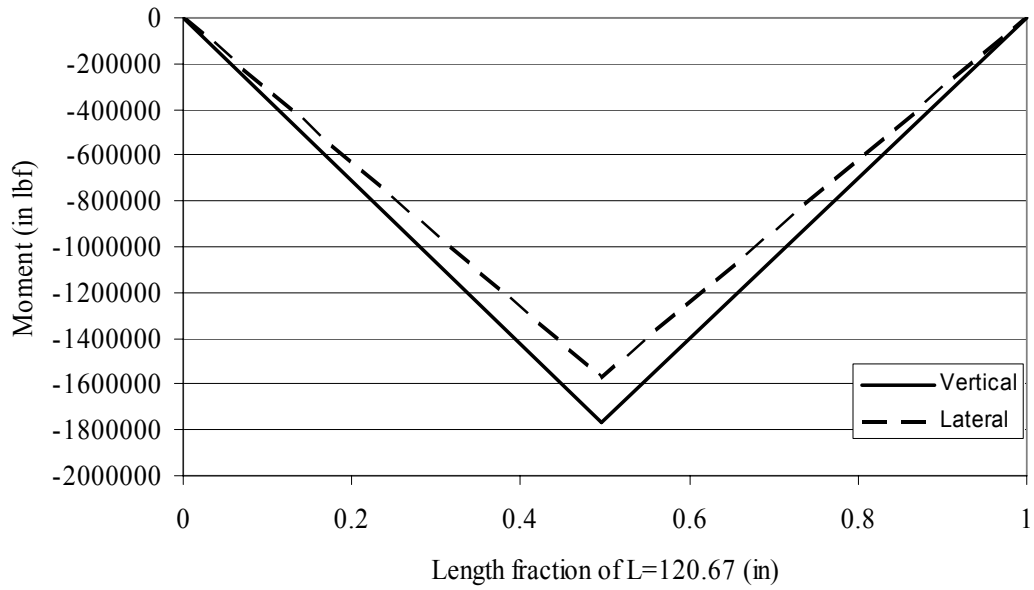
Figure 7.18 η Sled Body Moment Diagram

Table 7.19 Slipper Beam Peak Moment Values

Method	Lateral (in lb$_f$)	Vertical (in lb$_f$)
λ	-126,656	-211,093
SIMP	-28,203	-143,419
η	-71,441	-97,766

Table 7.20 Sled Body Peak Moment Values

Method	Lateral (in lb$_f$)	Vertical (in lb$_f$)
λ	-2,793,329	-3,861,933
SIMP	-988,903	-2,623,842
η	-1,577,358	-1,770,329

Table 7.21 Final Design Study Results Comparison

Method	Sled Weight (lb$_f$)	ΔWeight from Initial (lb$_f$)	CG Force Vertical (lb$_f$)	CG Force Lateral (lb$_f$)
λ	847.75	+5.75	66,330	38,658
SIMP	780.48	-61.52	44,221	8,865
η	767.91	-74.09	29,728	21,948

use is overshadowed by the resulting over-prediction of loads when compared to SIMP and η forces. The λ design study yielded a sled with a 1.0% increase in weight over the initial value while SIMP and η yielded weight decreases of 7.3% and 8.8% respectively. The load comparison is a better indicator of the differences in the methods. With respect to η, λ over predicts 123.1% vertical and 76.1% lateral and SIMP over predicts 48.8% vertical and under predicts 59.6% lateral. The preceding study of λ, SIMP, and η shows that λ tends to over predict dynamic force with increasing velocity. Ultimately infinite velocity would lead to infinite loading and does not consider other design parameters. This over prediction yields conservative designs with unnecessarily strong and heavy components that greatly reduce performance in the hypersonic velocity realm of sled testing. The application of SIMP is a lengthy seven-step process that is suited to automation in a spreadsheet application. However the current method requires reading impact velocity and frequency charts which are only available as SLEDYNE generated output tables. The inclusion of rail roughness and slipper gap is available from SLEDYNE through its

relationship of these values to slipper impact frequency and velocity. Unfortunately SLEDYNE is practically unusable in its current state with the inability to produce current slipper impact frequency and velocity charts making it a method with fixed parameters with regard to rail properties. It should be noted that the slipper impact frequency and velocity tables used in this study were originally developed for a monorail sled since no comprehensive narrow gauge study had been completed at the time of their production. Typically, monorail sleds have a worse vibration environment than narrow gauge sleds. Also, in every study of dynamic sled loading the downtrack sled velocity is a significant and often the dominant parameter in dynamic load prediction so the use of charts specific to particular downtrack velocities makes SIMP somewhat cumbersome in its use. It should be noted that there is a limit within SIMP where dynamic loading goes to 0 as impact frequency approaches 0. This aspect if considered alone could yield a sled component with unrealistic flexibility. The fact remains that for realistic design parameters SIMP produces loads in the vertical direction are realistic and suited to help produce optimized designs. In the lateral direction SIMP under predicts loads by nearly 60% compared to η. The η formation is more efficient than SIMP since it uses a FEM tool to produce the natural frequencies that the analyst does by hand with SIMP. Both methods give the analyst some latitude in choosing significant frequency components and rely on an in-depth knowledge of the mass distribution and stiffness of the sled system, where λ uses only mass and velocity. Both SIMP and η are found to deviate from the lateral to vertical ratio of 0.6 as documented by Krupovage et al. (1991).

173

Iteration through the η method showed that dynamic loading was dependent upon all structural aspects of the sled including mass and stiffness distribution. SIMP in this application is constrained to the flexibility of the slipper beam for its frequency content, and thus any variations in the sled body do not affect SIMP loading. λ produced loading is entirely deficient in taking into account sled body flexibility.

7.3 CO Test Data Comparison

A comparison of η force to corresponding CO test data resolved from slipper beam force at the sled CG was conducted to evaluate the effectiveness of η in predicting dynamic load. Of all the tests studied only the CO test returned data suitable for resolving at the sled CG in the vertical direction. Figure 7.19 details the application of the η for typical values of all design parameters except mass/weight which for this case was 770 lb$_f$. The velocity region shown is represents maximum velocity of the CO test. η force successfully bounds the force data in all but three areas. These areas are associated with probable noise spikes from the original data trace.
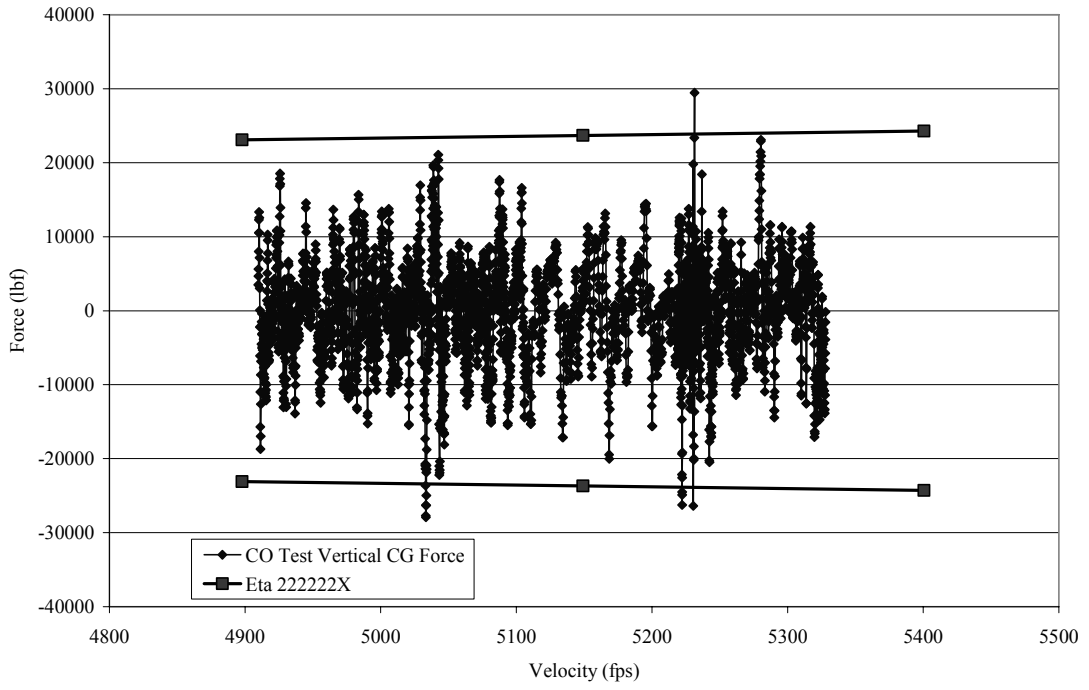
Figure 7.19 CO Test Vertical Force Comparison

8. DISCUSSION OF RESULTS

Several results from the execution of this study were deemed significant and worthy of documentation. There were original results generated that contributed to the advancement of narrow gauge sled design in the area of dynamic modeling and load prediction since lateral slipper rail contact and resulting force data were studied in detail for the first time. Further, this study represents the first large scale numerical study of a narrow gauge sled system.

8.1 Major Findings

Several major findings related to the modeling and prediction of dynamic loading of narrow gauge sleds were revealed in this study.

8.1.1 λ and SIMP Limits of Applicability

An initial review of the literature and examination of previous loading methods showed that λ and SIMP had narrow limits of applicability. λ was found to be applicable to similar test data points from which it was derived and SIMP was found to be applicable to vertical loading. There were several instances from actual test data that illustrated how λ was not accurate in predicting narrow gauge dynamic loading. In most instances, λ over predicted loading but, for a few cases under predicted loading when compared to test data (Mixon and Hooser 2002). Additionally, both methods, SIMP and λ, were found to over predict loading for the

176

all-typical case, 2222222, when compared to η at higher velocities. Outside of their narrow range of applicability, both methods return erroneous results.

8.1.2 Applicability of Dynamic Structural Modeling Approaches

Suitable structural modeling assumptions were discovered for direct representation of narrow gauge sleds in DADS for the purposes of successful transient dynamic modeling. Two investigations were conducted into the implementation of modal and SMD representations of structural components. The SMD representation employed Euler-Bernoulli beam theory to represent the structural flexibility between discretized masses. The modal representation utilized mode shapes and natural frequencies built using Timoshenko beam theory to define structural flexibility. For linear boundary conditions the modal representation was found to be acceptable while the SMD system was acceptable regardless of boundary conditions and was subsequently used in correlation modeling. The robustness of the SMD representation was well-suited for the nonlinear hypervelocity environment experienced during simulated tests of the narrow gauge sled in this study. Correlation modeling showed that the SMD representation also quickly correlated in areas near the slipper rail interface better representing the dynamic load generation of the slipper-rail interface.

8.1.3 Slipper Rail Impact Characterization

Slipper rail impact for the slipper configuration particular to a narrow gauge

177

sled was found to be the primary basis of the dynamic load generation in the sled. From a nonlinear FEM study, slipper rail contact values were returned for three distinct impact configurations; and for the first time, lateral contact characterization was described. It showed a significant amount of rail head torsional displacement which absorbs considerable amounts of linear slipper momentum. During the course of correlation modeling, it was not until suitable contact stiffness and damping values were deduced and implemented into the entire sled model that the correlation numbers reached acceptable values. This was evidenced by the high correlation values, average FOMs of 75.6 frequency and 85.2 standard deviation, in the vicinity of the slipper beam and rocket motor near the slipper beam attachments.

8.1.4 Importance of Modeling of Sled Nonlinearities

Nonlinearities in modeling such as nonlinear stiffness and contact were critical to the production of a correlated model. Sled motion and subsequent loading is heavily influenced by the nonlinear contact scenario generated by the movement of the sled through the slipper gap during a test. During the course of correlation modeling it was discovered that sled movement and loading was also influenced by the accurate modeling of the nonlinearities elsewhere on the sled. The extent of accurate correlation modeling was dictated locally by the analyst's ability to account for these other nonlinear features. The following nonlinear features were found to be influential: slotted contact between aft payload and rocket motor and nonlinear stiffness in the payload and sled vibration isolation systems.

178

8.1.5 Importance of Accurate Damping Modeling

During the course of developing the correlation model, the values of damping associated with the payload and sled vibration isolation systems were found to be important. Prescribing an artificially high damping value leads to an under prediction of acceleration and the generation of artificially high forces at the area under consideration, as well as throughout the entire sled system. It also rendered realistic stiffness values irrelevant as the damping mechanism dominated the force generation. Hypersonic sled systems are particularly sensitive to excessive damping values as high velocity values abound and the problem can quickly escalate. It was also seen that excessive damping for some isolated instances appeared to be suitable; however, when other modeling parameters were varied slightly the excessive damping produced erroneous results.

8.1.6 Utility of Figure of Merit (FOM)

During the course of correlation modeling it was found that that the most efficient way to compare numerical data to test data was to use FOM comparisons at test measurement locations. The use of weighted averages in the frequency domain was particularly useful since convergence was more meaningful as individual FOM values increased. The use of standard deviation as the time domain value was well suited to the current study since peak force prediction was the ultimate goal of the study lending itself to the direct measure of model validity in this area.

8.1.7 Identification of Appropriate Design Parameters and Corresponding Ranges

Design parameter variation of a reduced complexity model was done to address generic sled designs of the immediate future at the HHSTT by choosing typical values associated with an LSR forebody sled with the payload removed and then by varying the associated parameters through a realistic expected range. It was found that the range employed was acceptable and also that some prudence in choosing the number and value of the design parameters is warranted since the resulting number of possible simulations is quite large and time consuming to complete. The total number of possible simulations in the current study was 2187 where on a five processor system the average run time of one simulation was 9.1 hours making the solution of all simulations roughly 166 days. Selectively choosing a reduced set of 303 simulations, representing the extremum η force values, reduced the solution time to 23 days.

8.1.8 Superiority of Multivariate Interpolation to Correlate Design Parameters to η Forces

Study of the parameter variation solutions indicated that a basic multivariate least squares correlation produces reasonable correlation but not in sufficient detail for a designer to accurately predict dynamic loading. This is due to the nonlinear nature of the dynamic load data and from the piecewise linear nature with which the data were reported as it varied over velocity. The piecewise linear nature is from the enveloping of the data to afford some conservatism in the formation of η force since

it bypassed certain velocity ranges where the dynamic load locally decreased. The

most accurate representation of η force resulted from multivariate interpolation.

8.1.9 Influence of Design Parameters on Dynamic Loading

Velocity was found to be the most influential design parameter in the

magnitude of dynamic load since increases in velocity always cause an increase in

dynamic load. This is a natural conclusion and supported by other studies of this

nature (ISTRACON 1961, Mixon 1971, Hooser and Mixon 2002) and experimental

work (Hooser 1989, Leadingham and Schauer 2001, Turnbull and Minto 2003). It

was also found that rail roughness (vertical and lateral), slipper gap, and translational

sled natural frequency were the main contributing factors in the dynamic loads. η

force values when compared to corresponding values from λ and SIMP methods were

significantly lower for both force directions except for some instances of lateral

SIMP. After velocity, rail roughness was shown to be the second most influential

design parameter since the high value of rail roughness is extreme, 30% higher than

typical or surveyed data.

8.2 Significance and Contribution of Current Study

The significance of this study is the advancement of the modeling of

hypersonic narrow gauge sleds, specifically in the representation of the structural

members and characterization of slipper rail contact. The method of structural

modeling was unique since it was the first attempt to use a method directly and

entirely related to the structural geometry and material of the particular component and was able to bypass, in all cases but one, laboratory testing to verify the model. There was significant information produced that verified the proper modeling of slipper rail contact in the vertical direction which directly lead to a greater assurance that characterization of the lateral impact scenario was also properly modeled. These modeling efforts were verified by the first successful comprehensive correlation of a hypersonic narrow gauge sled using an expanded form of the correlation technique introduced by Hooser and Schwing (2000).

The second area of contribution was in the area of dynamic load prediction. The general method was first used by Mixon (1971) and involved the use of a verified model to numerically expand the input parameters to extrapolate a numerical model to produce dynamic load predictions. The current study applied this technique to a narrow gauge sled system in a hypervelocity environment and produced vertical and lateral force data in the form of η forces. This is the first known narrow gauge sled dynamic load prediction tool developed from in depth correlation studies of such a system.

9. CONCLUSIONS

The current study tested and selected two methods of structural representation, SMD and modal, and developed and implemented a new slipper rail contact scheme to build numerical models of hypervelocity narrow gauge sleds. These models were developed to the point that an acceptable correlation, based on frequency and standard deviation FOM numbers, was returned. The modeling method and corresponding assumptions were applied to a reduced complexity narrow gauge sled model where eight critical design parameters were identified. The eight design parameters: mass, slipper gap, rail roughness vertical, rail roughness lateral, sled natural frequency vertical, sled natural frequency lateral, sled natural frequency torsional, and velocity, were varied through strategic combinations of their corresponding high, low, and typical values. The resulting dynamic load data, η force, was studied and compared to previous load prediction methods, λ and SIMP. For direct comparisons, η force was found to be generally lower than previous methods and resulted in a more efficient basic sled design in terms of total sled weight.

9.1 Existing Theory Review of Dynamic Load Prediction

The review of existing theory indicated that closed form dynamic load prediction had been attempted λ (ISTRACON Handbook 1961) and SIMP (Greenbaum, Garner, Platus 1973, Mixon 1971). Some success was met with λ

becoming the standard at the HHSTT for monorail, narrow gauge, and dual rail sleds. λ was shown to be typically conservative but for certain conditions, it under predicted dynamic loading (Mixon and Hooser 2002). The principal deficiencies of SIMP are its non-correlation in the lateral direction, and its inability to produce slipper impact velocities and frequencies indicative of varied slipper gaps and rail roughness.

9.2 Numerical Model Development

Numerical modeling development was accomplished by creating two distinct DADS sled models based on different structural representations. Slipper rail impact was developed in PRONTO, studied, and implemented in both DADS models. Connections between major structural components were implemented in the DADS models to complete the numerical modeling process.

9.2.1 Modeling Assumptions

For the current study the following items were assumed to exist: elastic slipper rail contact, flexible major structural components, rough rail, and rigid rail. The following items were assumed to either be nonexistent or to be not critical to numerical sled modeling in this effort: plastic deformation at slipper rail contact, slipper gouging, significant aerodynamic or frictional heating, frictional slipper wear, and a flexible rail. This selection of modeling assumptions was intended to capture the majority effect of relevant structural dynamics that characterize a rocket sled traversing the rail.

9.2.2 Slipper Rail Impact Results

Finite element modeling of the slipper and rail in PRONTO, a nonlinear FEM package, was accomplished to help uncover the true nature of slipper rail impact. The study centered on approaching a flexible rail from three directions typical to slipper rail impact: vertical down, lateral, and vertical up at typical impact velocities: 10 ips, 25 ips, 50 ips, and 100 ips. The downtrack velocity of the slipper was 5,000 fps, the approximate velocity midpoint of the LSR test. The results of the vertical impacts resulted in the vertical up and down directions losing slightly more translational momentum, COR of 0.5 and 0.4 respectively, than the classic sphere on plate COR of 0.7. The lateral impact case showed significant rail head torsional motion which allowed the slipper to expend roughly twice the translational momentum of the vertical impacts, COR of 0.2. The resulting slipper rail contact parameters were implemented in DADS for a rigid rail and the corresponding results correlated to those in PRONTO.

9.2.3 DADS Implementation

Both structural representations were implemented in DADS in addition to the contact characterization derived from the PRONTO results. Stiffness and damping values associated with structural connections of the major structural components were prescribed along with a rough rigid rail described by survey data. Appropriate lift, drag, and thrust values were applied so that the sled simulated the LSR and CO tests.

9.3 Evaluation of Numerical Model

The numerical model was evaluated to gauge its accuracy against measured data sets from the LSR and CO tests so that the underlying modeling assumptions could be verified. The validation of the numerical, DADS generated, data to the test data was accomplished through the use of frequency and time domain comparisons. The data was band pass filtered from 10 Hz to 4500 Hz and then converted to a velocity windowed data set and the standard deviation over the velocity window was computed every 250 fps to constitute the time domain comparison. The standard deviation values were compared to the curve fit of the correspondingly processed test data and the RMS weighted average deviation was returned as the time domain FOM.

The frequency domain comparison consisted of band pass filtering and then converting the data to the frequency domain using an FFT algorithm and then integrating the data to evaluate the RMS power of the data at intervals of every 50 Hz. The deviation of the DADS data from the correspondingly processed test data was weighted using the test data ratio of RMS power at each frequency interval and the RMS deviation was returned to form the frequency FOM. FOM values for eleven data channels were averaged and used in the correlation of the DADS model to the test data. Correlation criteria were that the average frequency FOM was greater than 70 with no individual value less than 50 and the average time domain FOM was greater than 80 and no individual value less than 70. The SMD structural representation was found to most readily meet the criteria with average FOM values of 60.08 frequency, 85.79 STD, and 71.06 frequency, 87.80 STD for the LSR and CO

tests respectively. The exception given to the SMD frequency FOM for the LSR test is due to the in ability to characterize rocket motor combustion instability and from the excellent FOM numbers near the slipper rail interface.

9.4 Evaluation of Large Scale Design Parameter Variation

The modeling assumptions validated by evaluating the numerical model were implemented in a reduced complexity model indicative of a LSR forebody sled with the payload removed and the fuel half expended. Eight design parameters were identified that represented the most critical dynamic load contributors. The design parameters were then assigned typical, low, and high values indicative of reasonable variations of each. The design parameters associated with slipper gap and rail roughness were assigned typical values as surveyed or prescribed by HHSTT policy. The high and low values of slipper gap were prescribed by limits found in HHSTT policy where the high and low limits of rail roughness were prescribed by a ± 30% variation. The design parameters associated with the mass of the sled were varied to represent the rocket motor of the LSR forebody sled at full burnout and at motor ignition. The velocity of the sled was varied from rest to 10,000 fps. The remaining design parameters associated with sled natural frequency were evaluated at values typical to the half expended LSR forebody and then at values representing a high and low of ± 50% respectively. Velocity was the independent variable over which force data was evaluated so simulations involving design parameters involved the monitoring of only seven design parameters. The design parameters were varied and

187

simulations run through cycled combinations to return η force data in the vertical and

lateral directions. The initial design parameter variation consisted of the all typical,

2222222, case where initial force values were evaluated. The next variation included

varying the design parameters by setting only one design parameter to either extreme,

1 or 3, and keeping all others at the typical value of 2. This variation was

accomplished to determine the effect of the design parameters as individual values

were cycled through their extreme values. The next variation consisted of all possible

combinations of the high and low values, 1 and 3, 128 simulations total. This

variation was accomplished to establish an extremum set defining loading at the

design parameter bounding values. The final design parameter variation consisted of

varying the design parameters through a reduced set of design parameter values

where noncontributing design parameter values were excluded. This variation was

accomplished to round out the study by investigating any possible excessive dynamic

loads without completing the overbearing number of simulations, 2187, possible with

the variation of all parameters involved 3^7. This final set initially numbered 192 but

since 32 simulations had been previously completed the total number of simulations

was reduced to160.

9.5 Correlation of Predicted Load and Design Parameters

The correlation of the numerically generated force data to the design

parameters was begun by forming η forces from the peak values of the DADS data.

η force is an envelope function that bounds the peaks of the data as plotted over

188

velocity causing η to be piecewise linear over velocity and the other design parameters. The correlation of η was initiated using linear regression to investigate the possibility of a closed form solution to relate the design parameters to the vertical and lateral η forces. This attempt was not successful and the implementation of a multivariate interpolation technique was employed to relate design parameter values to output η force. The use of a multivariate interpolator does not immediately make the relationship of the design parameters to the η forces apparent but does guarantee that the values of calculated η force are an accurate representation of the DADS data and makes η useful to design engineers.

9.6 Comparison to Previous Methods

The η force values were compared to the corresponding values calculated from the λ and SIMP methods. It was found that η returned lower values of dynamic load for velocities above the force transition point typically between 800 fps and 2,000 fps.   For the all typical case, 2222222, η was shown to be significantly lower than λ at high velocities and consistently lower than SIMP for all velocities in the vertical direction and under 4,000 fps in the lateral direction. The lower values of SIMP were due to SIMP not being correlated in the lateral direction due to inadequate slipper rail impact characterization. It was shown that η was able to account for the changes in rail roughness, while λ and SIMP utilize fixed typical values of rail roughness and slipper gap. As expected, η force values increased with a large rail roughness increase of 30%. A basic sled design which consisted of a sled body and

189

slipper beams was completed for each method. The basic sled design was analyzed

and redesigned based upon each of the three methods. It was seen that the λ–based

design yielded a mass increase of 1% over the baseline, the SIMP-based design

resulted in a mass decrease of 7.3% and the η-based design resulted in a mass

decrease of 8.8%. When compared to η, λ over predicts design loads by 123.1%

vertical and 76.1% lateral; SIMP over predicts loads by 48.8% vertical and under

predicts by 59.6%. Again the reason for the under prediction of SIMP is from

inaccurate characterization of the lateral slipper rail impact.

9.7 Future Work

There is great opportunity to pursue further work in the general area of

hypersonic sled dynamic load prediction and into many other related areas.

Recommendations for further study include expanding the formation of η force

calculation into the areas of monorail and dual rail sled systems. Since there have

been many more sled tests and consequently more and various types of sleds

constructed for these two configurations than for narrow gauge systems, the breadth

and depth of study and correlation would lead to a comprehensive dynamic load

prediction. Monorail and dual rail sled systems represent a marked departure in

design philosophy from each other and narrow gauge sled systems; however, the

proper application of the dynamic load prediction method outlined in this work would

return useful data from which a suitable load prediction database could be

constructed. Narrow gauge results show λ and SIMP to be inadequate in accurately

predicting dynamic loading over the wide range of design parameters encountered during the range of HHSTT test applications. Further work into the area of narrow gauge dynamic load prediction would include analyzing narrow gauge sleds that deviate from the typical slipper beam and sled body design, where the more rigid truss structure type sleds are studied. This type of study would effectively build upon the established η force narrow gauge database.

Structural modeling may be optimized by studying discretization limits of a robust beam theory such as the Timoshenko theory to reduce the number of discretized masses necessary to construct an accurate DADS sled model. This was accomplished to some extent in the current study but it is likely that further reductions may be realized by detailing the lower limit of discretized masses needed in DADS.

Further studies into the nature of the slipper rail impact for different structural representations of slippers in general would uncover the driving mechanism behind slipper impact and could eventually lead to improved slipper isolation mechanisms. It could also lead to engineered slippers with increased flexibility that would help reduce dynamic loading through momentum exchange with the rail.

Additional work into the correlation of the input design parameters to output η forces can be accomplished where the nonlinear nature of the output data may be captured by nonlinear methods into a closed form. A successful closed form outcome is doubtful but its completion would be valuable enough to sled designers and load analysts alike that the required work would be warranted. A closed form solution built from accurate loading data would immediately make dynamic load

characterization apparent and useful.

9.8 Concluding Remarks

The results of this study have shown that accurate modeling and

characterization of a narrow gauge sled was accomplished and that comprehensive

correlation to test data was achieved. Numerical modeling based upon this

correlation effort was accomplished to produce a new method of predicting dynamic

loading in the lateral and vertical directions based upon high fidelity numerical sled

tests. The resulting data were correlated in a form similar to λ in ease of use while

retaining the capability to return accurate results. This effort gives sled designers a

new capability to confidently produce optimized narrow gauge sled designs.

APPENDIX A

FEMS AND RESULTING COMPARISONS
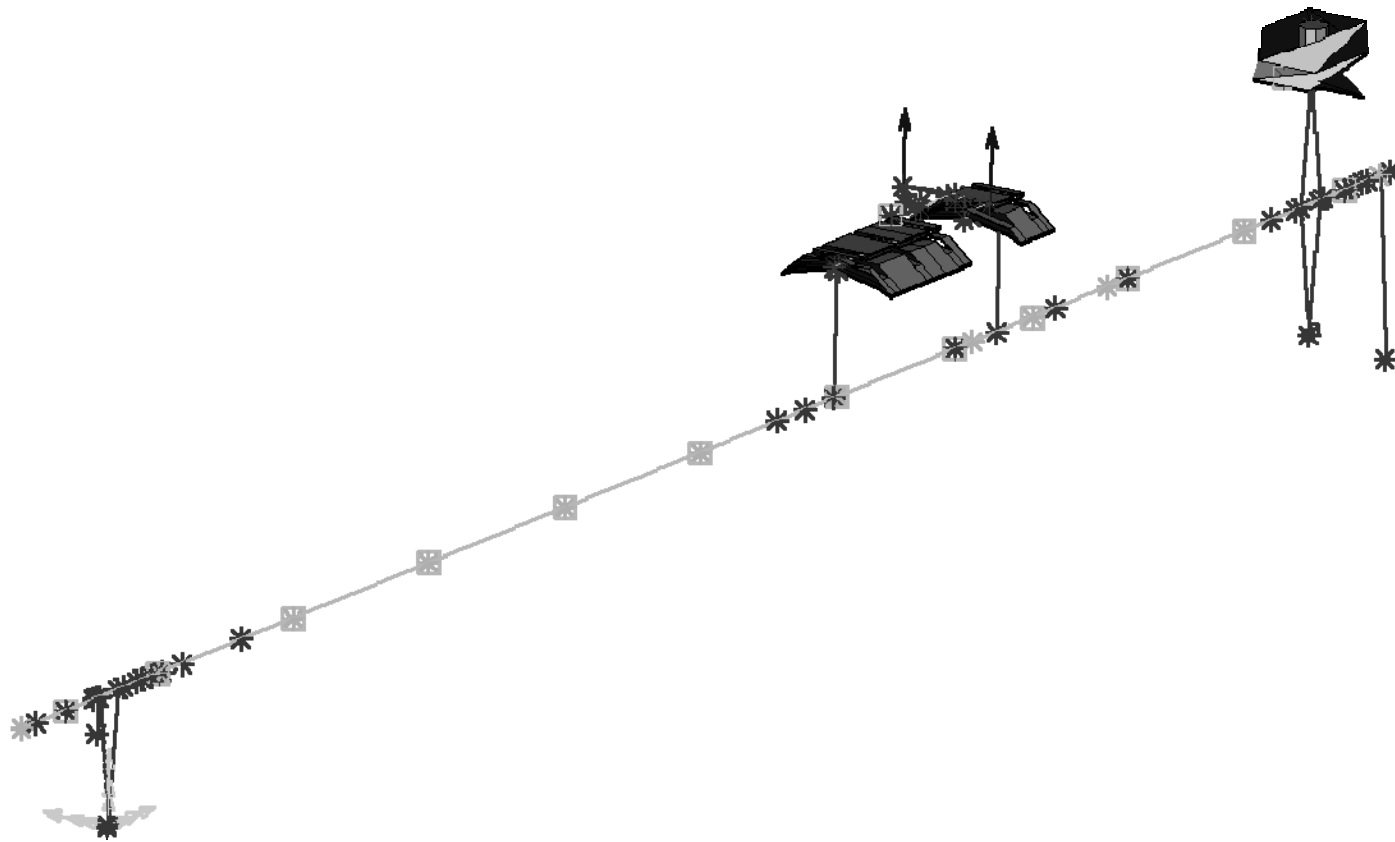
Figure A.1 Rocket Motor Beam FEM
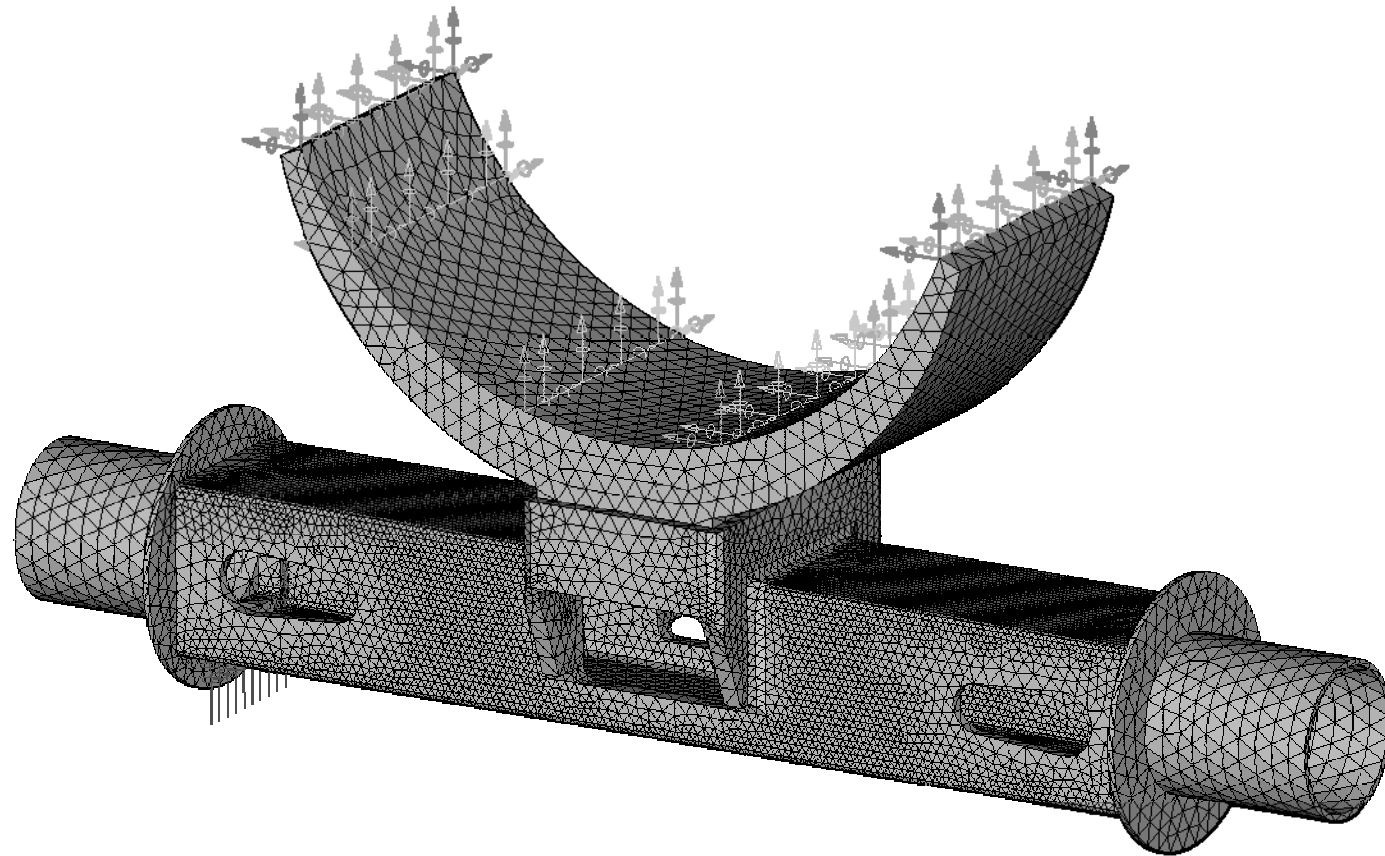
Figure A.2 Slipper Beam Three Dimensional FEM
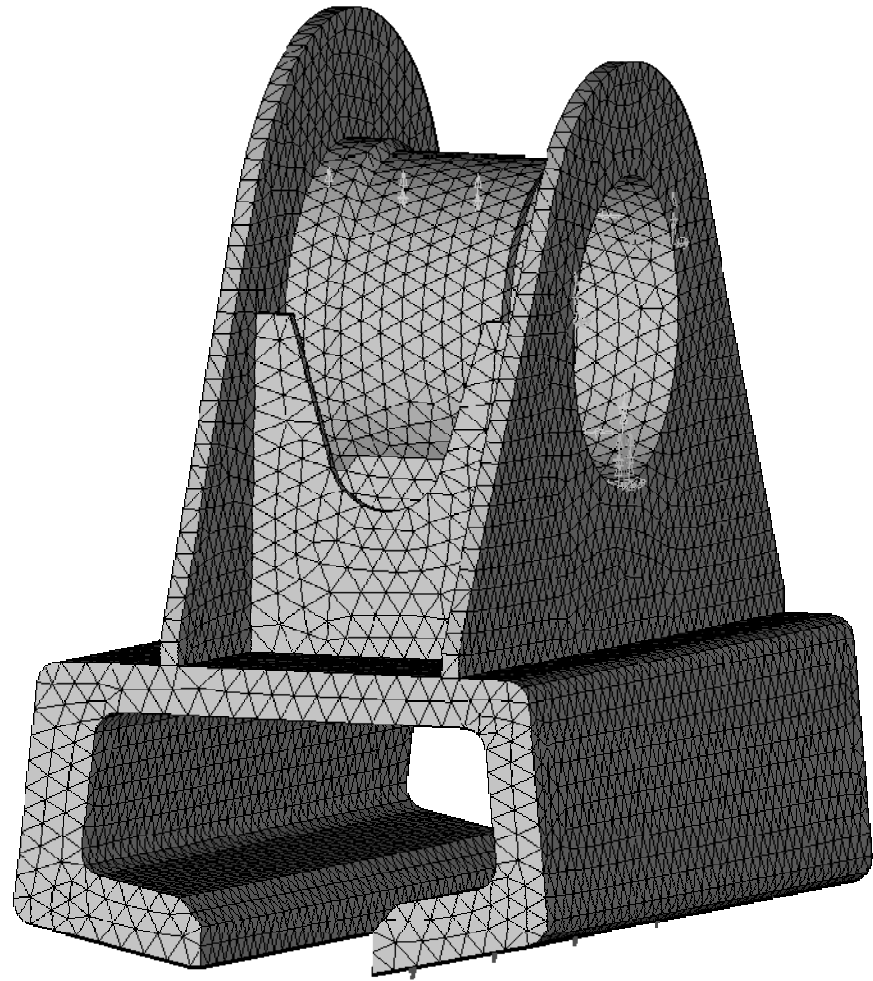
Figure A.3 Slipper Three Dimensional FEM
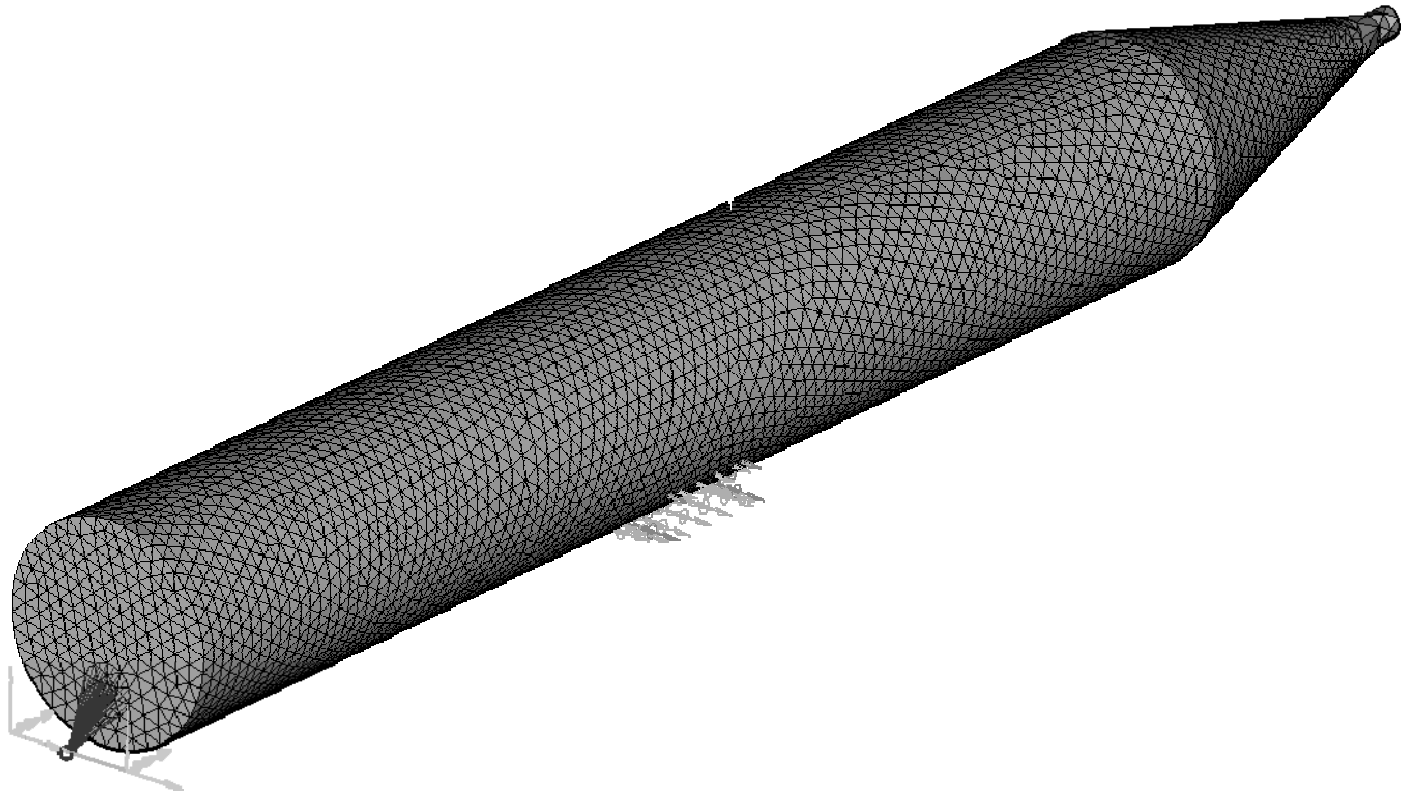
Figure A.4 Payload Three Dimensional FEM

Table A.1 Modal Model Payload Mass Properties Comparison

Model	Weight (lb_f)	Ixx $(lb_f \, s^2 \, in)$	Iyy $(lb_f \, s^2 \, in)$	Izz $(lb_f \, s^2 \, in)$
3D Solid	145.43	194.00	194.00	7.78
DADS/Flex	141.14	185.1	184.9	5.71
Deviation %	-2.9	-4.5	-4.7	26.6

Table A.2 Modal Model Payload Frequency Comparison

Model	Boundary Condition	Frequency (Hz) and Mode Shape				
3D FEM	Fixed (FWD) – Free (AFT)	151 1st B V*	152 1st B L*	803 2nd B V*	833 2nd B L*	3500 1st DT*
DADS/Flex	Fixed (FWD) – Fixed (AFT)	134 1st B V*	160 1st B L*	767 2nd B V*	833 2nd B L*	3487 1st DT*
Deviation %		-11.2	5.3	-4.5	0.0	-0.4

* V-Vertical; L-Lateral; DT-DownTrack; B-Bending; T-Torsional

Table A.3 Modal Model Slipper Beam Mass Properties Comparison

Model	Weight (lb$_f$)	Ixx (lb$_f$ s^2 in)	Iyy (lb$_f$ s^2 in)	Izz (lb$_f$ s^2 in)
3D Solid	49.68	1.29	5.29	5.85
DADS/Flex	49.91	1.17	5.30	5.89
Deviation %	0.5	-9.3	0.2	0.7

Table A.4 Modal Model Slipper Beam Frequency Comparison

Model	Boundary Condition	Frequency (Hz) and Mode Shape				
3D FEM	Fixed at Slipper Beam Center	259 SS V*	487 SS DT*	650 C DT*	732 1st C V*	1850 1st T*
DADS/Flex	Fixed at Slipper Beam Center	273 SS V*	566 SS DT*	799 C DT*	682 1st C V*	1512 1st T*
Deviation %		5.5	16.2	22.9	-6.8	-18.3

* V-Vertical; L-Lateral; DT-DownTrack; SS-See Saw; T-Torsional; C-Cantilever

Table A.5 Modal Model Slipper Mass Properties Comparison

Model	Weight (lb_f)	Ixx $(\text{lb}_f\,\text{s}^2\,\text{in})$	Iyy $(\text{lb}_f\,\text{s}^2\,\text{in})$	Izz $(\text{lb}_f\,\text{s}^2\,\text{in})$
3D Solid	27.06	0.803	0.770	0.521
DADS/Flex	25.99	0.616	0.595	0.504
Deviation %	4.0	-23.3	-22.7	-3.3

Table A.6 Modal Model Slipper Frequency Comparison

Model	Boundary Condition	Frequency (Hz) and Mode Shape	
3D FEM	Fixed at SB interface	708 B L*	2280 B V*
DADS/Flex	Fixed (FWD) – Fixed (AFT)	770 B L*	2065 B V*
Deviation %		8.8	-9.4

* V-Vertical; L-Lateral; B-Bending

Table A.7 Spring Mass Damper Model Payload Mass Properties Comparison

Model	Weight (lb$_f$)	Ixx (lb$_f$ s^2 in)	Iyy (lb$_f$ s^2 in)	Izz (lb$_f$ s^2 in)
3D Solid	145.25	194.00	194.00	7.79
DADS/SMD	145.25	205.70	205.70	7.87
Deviation %	0.0	6.0	6.0	1.0

Table A.8 Spring Mass Damper Model Payload Frequency Comparison

Model	Boundary Condition	Frequency (Hz) and Mode Shape				
3D FEM	Fixed (FWD) – Fixed (AFT)	151 1st B V*	152 1st B L*	803 2nd B V*	833 2nd B L*	3500 1st DT*
DADS/SMD	Fixed (FWD) – Fixed (AFT)	158 1st B V*	141 1st B L*	803 2nd B V*	660 2nd B L*	3400 1st DT*
Deviation %		4.6	-7.2	0.0	-20.7	-2.9

* V-Vertical; L-Lateral; DT-DownTrack; B-Bending; T-Torsional

Table A.9 Spring Mass Damper Model Slipper Beam Mass Properties Comparison

Model	Weight (lb$_f$)	Ixx (lb$_f$ s^2 in)	Iyy (lb$_f$ s^2 in)	Izz (lb$_f$ s^2 in)
3D Solid (no Yoke)	32.23	0.34	4.55	4.54
DADS/SMD	32.23	0.34	4.76	4.76
Deviation %	0.0	0.0	4.6	4.8

Table A.10 Spring Mass Damper Model Slipper Beam Frequency Comparison

Model	Boundary Condition	Frequency (Hz) and Mode Shape				
3D FEM (no yoke)	Fixed at Slipper Beam Center	279 SS V*	578 SS DT*	697 1st C DT*	750 1st C V*	1900 1st T*
DADS/SMD	Fixed at Slipper Beam Center	270 SS V*	580 SS DT*	650 1st C DT*	780 1st C V*	2700 1st T*
Deviation %		3.2	0.3	-6.7	4.0	42.0

* V-Vertical; L-Lateral; DT-DownTrack; SS-See Saw; T-Torsional; C-Cantilever

Table A.11 Spring Mass Damper Model Slipper Mass Properties Comparison

Model	Weight (lb$_f$)	Ixx (lb$_f$ s^2 in)	Iyy (lb$_f$ s^2 in)	Izz (lb$_f$ s^2 in)
3D Solid	27.06	0.803	0.770	0.521
DADS/SMD	26.93	0.759	0.697	0.482
Deviation %	-0.5	-5.5	-9.5	-7.5

Table A.12 Spring Mass Damper Model Slipper Frequency Comparison

Model	Boundary Condition	Frequency (Hz) and Mode Shape	
3D FEM	Fixed at SB interface	708 B L*	2280 B V*
DADS/Flex	Fixed (FWD) – Fixed (AFT)	683 B L*	2080 B V*
Deviation %		-3.5	-8.8

* V-Vertical; L-Lateral; B-Bending

APPENDIX B

FLEXIBLE BODY STIFFNESS FORMULATION

Timoshenko Beam Theory Finite Element Stiffness Formulation (Przemieniecki 1968)

$$
205
\begin{Bmatrix}
F_{x1} \\ F_{y1} \\ F_{z1} \\ M_{x1} \\ M_{y1} \\ M_{z1} \\ F_{x2} \\ F_{y2} \\ F_{z2} \\ M_{x2} \\ M_{y2} \\ M_{z2}
\end{Bmatrix}
=
\begin{bmatrix}
\dfrac{EA}{l} & & & & & & & & & & & \\[2ex]
0 & \dfrac{12EI_z}{l^3(1+\phi_y)} & & & & & & & & & & \\[2ex]
0 & 0 & \dfrac{12EI_y}{l^3(1+\phi_z)} & & & & \textit{Symmetric} & & & & & \\[2ex]
0 & 0 & 0 & \dfrac{GJ}{l} & & & & & & & & \\[2ex]
0 & 0 & \dfrac{6EI_y}{l^2(1+\phi_z)} & 0 & \dfrac{(4+\phi_z)EI_y}{l(1+\phi_z)} & & & & & & & \\[2ex]
0 & \dfrac{6EI_z}{l^2(1+\phi_y)} & 0 & 0 & 0 & \dfrac{(4+\phi_y)EI_z}{l(1+\phi_y)} & & & & & & \\[2ex]
\dfrac{-EA}{l} & 0 & 0 & 0 & 0 & 0 & \dfrac{EA}{l} & & & & & \\[2ex]
0 & \dfrac{-12EI_z}{l^3(1+\phi_y)} & 0 & 0 & 0 & \dfrac{-6EI_z}{l^2(1+\phi_y)} & 0 & \dfrac{12EI_z}{l^3(1+\phi_y)} & & & & \\[2ex]
0 & 0 & \dfrac{-12EI_y}{l^3(1+\phi_z)} & 0 & \dfrac{-6EI_y}{l^2(1+\phi_z)} & 0 & 0 & 0 & \dfrac{12EI_y}{l^3(1+\phi_z)} & & & \\[2ex]
0 & 0 & 0 & \dfrac{-GJ}{l} & 0 & 0 & 0 & 0 & 0 & \dfrac{GJ}{l} & & \\[2ex]
0 & 0 & \dfrac{-6EI_y}{l^2(1+\phi_z)} & 0 & \dfrac{(2-\phi_z)EI_y}{l(1+\phi_z)} & 0 & 0 & 0 & \dfrac{6EI_y}{l^2(1+\phi_z)} & 0 & \dfrac{(4+\phi_z)EI_y}{l(1+\phi_z)} & \\[2ex]
0 & \dfrac{-6EI_z}{l^2(1+\phi_y)} & 0 & 0 & 0 & \dfrac{(2-\phi_y)EI_z}{l(1+\phi_y)} & 0 & \dfrac{-6EI_z}{l^2(1+\phi_y)} & 0 & 0 & 0 & \dfrac{(4+\phi_y)EI_z}{l(1+\phi_y)}
\end{bmatrix}
\begin{Bmatrix}
u_1 \\ v_1 \\ w_1 \\ \theta_{u1} \\ \theta_{v1} \\ \theta_{w1} \\ u_2 \\ v_2 \\ w_2 \\ \theta_{u2} \\ \theta_{v2} \\ \theta_{w2}
\end{Bmatrix}
$$

where

u, v, w are the translational displacements in the x, y, and z directions respectively

$\theta_u, \theta_v, \theta_w$ are the rotational displacements about the x, y, and z directions respectively

F_{ij} is the force in the i direction at the j end of the beam

M_{ij} is the moment in the i direction at the j end of the beam

E is Young's modulus

G is shear modulus

I_i is the planar moment of inertia about the i axis

J is the polar moment of inertia

l is the length of the beam

A is the cross sectional area of the beam

$$\Phi_z = \frac{12EI_z}{GA_{sy}l^2} \quad \& \quad \Phi_y = \frac{12EI_y}{GA_{sz}l^2}$$

A_{si} is the area acting in shear in the i direction or :

$A_{si} = A\Xi$

Ξ is the Timoshenko shear coefficient

Euler-Bernoulli Beam Theory as Implemented by LMS DADS (LMS CADSI 2004)

$$
\begin{Bmatrix} F_x \\ F_v \\ F_z \\ M_x \\ M_v \\ M_z \end{Bmatrix} =
\begin{bmatrix}
\dfrac{EA}{l} & 0 & 0 & 0 & 0 & 0 \\
0 & \dfrac{12EI_z}{l^3} & 0 & 0 & 0 & \dfrac{-6EI_z}{l^2} \\
0 & 0 & \dfrac{12EI_y}{l^3} & 0 & \dfrac{6EI_y}{l^2} & 0 \\
0 & 0 & 0 & \dfrac{GI_x}{l} & 0 & 0 \\
0 & 0 & \dfrac{6EI_y}{l^2} & 0 & \dfrac{4EI_y}{l} & 0 \\
0 & \dfrac{-6EI_z}{l^2} & 0 & 0 & 0 & \dfrac{4EI_z}{l}
\end{bmatrix}
\begin{Bmatrix} u \\ v \\ w \\ \theta_u \\ \theta_v \\ \theta_w \end{Bmatrix}
$$

where

u, v, w are the translational displacements in the x, y, and z directions respectively

$\theta_u, \theta_v, \theta_w$ are the rotational displacements about the x, y, and z directions respectively

F_{ij} is the force in the i direction at the j end of the beam

M_{ij} is the moment in the i direction at the j end of the beam

E is Young's modulus

G is shear modulus

I_i is the planar momeent of inertia about the i axis

l is the length of the beam

A is the cross sectional area of the beam

APPENDIX C

MATLAB CORRELATION DATA PROCESSING SCRIPTS

data_master.m Main Program File


```
% data master
% this script calls both processing scripts for DADS
% and mission data and then calls the plotting script

% Mission data processing, doesn't need to be run all
% of the time
sw_md=input('Process mission data? ');
if sw_md, data_proc, end

% DADS data processing
sw_dd=input('Process DADS data? ');
if sw_dd, data_proc_dads, end

% Plot this data
pp=input('Plot this data? ');
if pp, data_plot, end
```


Published with MATLAB® 7.0

data_proc.m Test Data Processing Script

```
% This script is designed to process data from the
% 80X-G1 mission by filtering, then rearranging the
% data into velocity windowed format and performing
% PSD analysis.  Finally the data is written into
% *.txt files This script does not perform any data
% decimation
% S Furlow

clear all

% Load raw data from file

data=load('D80XG1F_no_head.txt');

data_end=60394;
% Assign data more meaningful names

d_141=data(10001:80001,13);
d_140=data(10001:80001,12);
d_139=data(10001:80001,11);
d_138=data(10001:80001,10);
d_137=data(10001:80001,9);
d_124=data(10001:80001,8);
d_123=data(10001:80001,7);
d_115=data(10001:80001,6);
d_113=data(10001:80001,5);
d_112=data(10001:80001,4);
d_103=data(10001:80001,3)-8.5;
d_101=data(10001:80001,2);
t=data(10001:80001,1);

% Load velocity
dum=load('80x_g1_data.txt');
vel=dum(:,2);
vel_size=numel(vel)
if vel_size<70001
    for i=vel_size+1:70001,
        vel(i)=vel(vel_size)+100;
    end
end

% Filter Data
```

```
dt=t(2)-t(1);
fs=1/dt;
nyq=fs/2;
wn=[10/nyq,4500/nyq];
[B,A] = BUTTER(3,wn);

d_101_f = filter(B,A,d_101);
d_103_f = filter(B,A,d_103);
d_112_f = filter(B,A,d_112);
d_113_f = filter(B,A,d_113);
d_115_f = filter(B,A,d_115);
d_123_f = filter(B,A,d_123);
d_124_f = filter(B,A,d_124);
d_138_f = filter(B,A,d_138);
d_139_f = filter(B,A,d_139);
d_140_f = filter(B,A,d_140);
d_141_f = filter(B,A,d_141);

% Build Velocity Windowed data
d_vel=250;
j=1;
vel_i=vel(1);
for i=1:numel(vel),
    if (vel(i)-vel_i)>d_vel,
        index(j)=i;
        j=j+1;
        vel_i=vel(i);
    end
end

index_vel_end=j;

for i=1:index_vel_end-2,
    vel_a(i)=mean(vel(index(i):index(i+1)));
    d_101_f_std(i)=std(d_101_f(index(i):index(i+1)));
    d_103_f_std(i)=std(d_103_f(index(i):index(i+1)));
    d_112_f_std(i)=std(d_112_f(index(i):index(i+1)));
    d_113_f_std(i)=std(d_113_f(index(i):index(i+1)));
    d_115_f_std(i)=std(d_115_f(index(i):index(i+1)));
    d_123_f_std(i)=std(d_123_f(index(i):index(i+1)));
    d_124_f_std(i)=std(d_124_f(index(i):index(i+1)));
    d_138_f_std(i)=std(d_138_f(index(i):index(i+1)));
    d_139_f_std(i)=std(d_139_f(index(i):index(i+1)));
    d_140_f_std(i)=std(d_140_f(index(i):index(i+1)));
    d_141_f_std(i)=std(d_141_f(index(i):index(i+1)));
```

```
dum_101=sort(abs(d_101_f(index(i):index(i+1))),'de
scend');
dum_103=sort(abs(d_103_f(index(i):index(i+1))),'de
scend');
dum_112=sort(abs(d_112_f(index(i):index(i+1))),'de
scend');
dum_113=sort(abs(d_113_f(index(i):index(i+1))),'de
scend');
dum_115=sort(abs(d_115_f(index(i):index(i+1))),'de
scend');
dum_123=sort(abs(d_123_f(index(i):index(i+1))),'de
scend');
dum_124=sort(abs(d_124_f(index(i):index(i+1))),'de
scend');
dum_138=sort(abs(d_138_f(index(i):index(i+1))),'de
scend');
dum_139=sort(abs(d_139_f(index(i):index(i+1))),'de
scend');
dum_140=sort(abs(d_140_f(index(i):index(i+1))),'de
scend');
dum_141=sort(abs(d_141_f(index(i):index(i+1))),'de
scend');

d_101_f_p1(i)=dum_101(1);
d_103_f_p1(i)=dum_103(1);
d_112_f_p1(i)=dum_112(1);
d_113_f_p1(i)=dum_113(1);
d_115_f_p1(i)=dum_115(1);
d_123_f_p1(i)=dum_123(1);
d_124_f_p1(i)=dum_124(1);
d_138_f_p1(i)=dum_138(1);
d_139_f_p1(i)=dum_139(1);
d_140_f_p1(i)=dum_140(1);
d_141_f_p1(i)=dum_141(1);

d_101_f_p2(i)=dum_101(2);
d_103_f_p2(i)=dum_103(2);
d_112_f_p2(i)=dum_112(2);
d_113_f_p2(i)=dum_113(2);
d_115_f_p2(i)=dum_115(2);
d_123_f_p2(i)=dum_123(2);
d_124_f_p2(i)=dum_124(2);
d_138_f_p2(i)=dum_138(2);
d_139_f_p2(i)=dum_139(2);
```

```
    d_140_f_p2(i)=dum_140(2);
    d_141_f_p2(i)=dum_141(2);
end

% Frequency analysis
t_off=43751;
[P_101_f,F_101] =
PWELCH(d_101_f(1+t_off:8600+t_off),[],[],[],fs);
[P_103_f,F_103] =
PWELCH(d_103_f(1+t_off:14445+t_off),[],[],[],fs);
[P_112_f,F_112] =
PWELCH(d_112_f(1+t_off:15099+t_off),[],[],[],fs);
[P_113_f,F_113] =
PWELCH(d_113_f(1+t_off:15099+t_off),[],[],[],fs);
[P_115_f,F_115] =
PWELCH(d_115_f(1+t_off:14445+t_off),[],[],[],fs);
[P_123_f,F_123] =
PWELCH(d_123_f(1+t_off:15099+t_off),[],[],[],fs);
[P_124_f,F_124] =
PWELCH(d_124_f(1+t_off:15099+t_off),[],[],[],fs);
[P_138_f,F_138] =
PWELCH(d_138_f(1+t_off:14445+t_off),[],[],[],fs);
[P_139_f,F_139] =
PWELCH(d_139_f(1+t_off:15099+t_off),[],[],[],fs);
[P_140_f,F_140] =
PWELCH(d_140_f(1+t_off:15099+t_off),[],[],[],fs);
[P_141_f,F_141] =
PWELCH(d_141_f(1+t_off:15099+t_off),[],[],[],fs);

% Export data
fid =fopen('d_101_psd.txt','w');
fprintf(fid,'%6.4f  %12.6f\n',[F_101,P_101_f]');
fid =fopen('d_103_psd.txt','w');
fprintf(fid,'%6.4f  %12.6f\n',[F_103,P_103_f]');
fid =fopen('d_112_psd.txt','w');
fprintf(fid,'%6.4f  %12.6f\n',[F_112,P_112_f]');
fid =fopen('d_113_psd.txt','w');
fprintf(fid,'%6.4f  %12.6f\n',[F_113,P_113_f]');
fid =fopen('d_115_psd.txt','w');
fprintf(fid,'%6.4f  %12.6f\n',[F_115,P_115_f]');
fid =fopen('d_123_psd.txt','w');
fprintf(fid,'%6.4f  %12.6f\n',[F_123,P_123_f]');
fid =fopen('d_124_psd.txt','w');
fprintf(fid,'%6.4f  %12.6f\n',[F_124,P_124_f]');
fid =fopen('d_138_psd.txt','w');
```

```
fprintf(fid,'%6.4f   %12.6f\n',[F_138,P_138_f]');
fid =fopen('d_139_psd.txt','w');
fprintf(fid,'%6.4f   %12.6f\n',[F_139,P_139_f]');
fid =fopen('d_140_psd.txt','w');
fprintf(fid,'%6.4f   %12.6f\n',[F_140,P_140_f]');
fid =fopen('d_141_psd.txt','w');
fprintf(fid,'%6.4f   %12.6f\n',[F_141,P_141_f]');
fid =fopen('d_101_f_v.txt','w');
fprintf(fid,'%6.4f   %12.6f %12.6f %12.6f\n',...
[vel_a',d_101_f_std',d_101_f_p1',d_101_f_p2']');
fid =fopen('d_103_f_v.txt','w');
fprintf(fid,'%6.4f   %12.6f %12.6f %12.6f\n',...
[vel_a',d_103_f_std',d_103_f_p1',d_103_f_p2']');
fid =fopen('d_112_f_v.txt','w');
fprintf(fid,'%6.4f   %12.6f %12.6f %12.6f\n',...
[vel_a',d_112_f_std',d_112_f_p1',d_112_f_p2']');
fid =fopen('d_113_f_v.txt','w');
fprintf(fid,'%6.4f   %12.6f %12.6f %12.6f\n',...
[vel_a',d_113_f_std',d_113_f_p1',d_113_f_p2']');
fid =fopen('d_115_f_v.txt','w');
fprintf(fid,'%6.4f   %12.6f %12.6f %12.6f\n',...
[vel_a',d_115_f_std',d_115_f_p1',d_115_f_p2']');
fid =fopen('d_123_f_v.txt','w');
fprintf(fid,'%6.4f   %12.6f %12.6f %12.6f\n',...
[vel_a',d_123_f_std',d_123_f_p1',d_123_f_p2']');
fid =fopen('d_124_f_v.txt','w');
fprintf(fid,'%6.4f   %12.6f %12.6f %12.6f\n',...
[vel_a',d_124_f_std',d_124_f_p1',d_124_f_p2']');
fid =fopen('d_138_f_v.txt','w');
fprintf(fid,'%6.4f   %12.6f %12.6f %12.6f\n',...
[vel_a',d_138_f_std',d_138_f_p1',d_138_f_p2']');
fid =fopen('d_139_f_v.txt','w');
fprintf(fid,'%6.4f   %12.6f %12.6f %12.6f\n',...
[vel_a',d_139_f_std',d_139_f_p1',d_139_f_p2']');
fid =fopen('d_140_f_v.txt','w');
fprintf(fid,'%6.4f   %12.6f %12.6f %12.6f\n',...
[vel_a',d_140_f_std',d_140_f_p1',d_140_f_p2']');
fid =fopen('d_141_f_v.txt','w');
fprintf(fid,'%6.4f   %12.6f %12.6f %12.6f\n',...
[vel_a',d_141_f_std',d_141_f_p1',d_141_f_p2']');

fid = fopen('d_101_f.txt','w');
fprintf(fid,'%6.4f %6.4f %12.6f\n',[t,vel,d_101_f]');
fid = fopen('d_103_f.txt','w');
fprintf(fid,'%6.4f %6.4f %12.6f\n',[t,vel,d_103_f]');
```

214

```matlab
fid = fopen('d_112_f.txt','w');
fprintf(fid,'%6.4f %6.4f %12.6f\n',[t,vel,d_112_f]');
fid = fopen('d_113_f.txt','w');
fprintf(fid,'%6.4f %6.4f %12.6f\n',[t,vel,d_113_f]');
fid = fopen('d_115_f.txt','w');
fprintf(fid,'%6.4f %6.4f %12.6f\n',[t,vel,d_115_f]');
fid = fopen('d_123_f.txt','w');
fprintf(fid,'%6.4f %6.4f %12.6f\n',[t,vel,d_123_f]');
fid = fopen('d_124_f.txt','w');
fprintf(fid,'%6.4f %6.4f %12.6f\n',[t,vel,d_124_f]');
fid = fopen('d_138_f.txt','w');
fprintf(fid,'%6.4f %6.4f %12.6f\n',[t,vel,d_138_f]');
fid = fopen('d_139_f.txt','w');
fprintf(fid,'%6.4f %6.4f %12.6f\n',[t,vel,d_139_f]');
fid = fopen('d_140_f.txt','w');
fprintf(fid,'%6.4f %6.4f %12.6f\n',[t,vel,d_140_f]');
fid = fopen('d_141_f.txt','w');
fprintf(fid,'%6.4f %6.4f %12.6f\n',[t,vel,d_141_f]');

fclose('all')
```

Published with MATLAB® 7.0

data_proc_dads.m DADS Data processing script

```matlab
% This script is designed to process DADS generated
% data of the 80X-G1 mission by filtering, then
% rearranging the data into velocity windowed
% format and performing PSD analysis.  Finally the
% data is written into *.txt files This script does
% not perform any data decimation.
% S Furlow

clear all

% Load raw data from file

filename=input('Enter complete file name of data
file (no header)');
data=load(filename);

data_end=15000;
% Assign data more meaningful names

vel=data(:,14);
d_141=data(:,12);
d_140=data(:,11);
d_139=data(:,10);
d_138=data(:,9)/1000;
d_124=data(:,8);
d_123=data(:,7);
d_115=data(:,6)/1000;
d_113=data(:,5)/1000;
d_112=data(:,4)/1000;
sw_103=1;
offset_133=input('Enter preload offset for 103
should be in kips (8.5) ');
d_103=(data(:,13)/1000-offset_133)*sw_103+(1-
sw_103)*(data(:,3)/1000*17.99876*2.9e7/0.125);
d_101=data(:,2)/1000;
t=data(:,1)+4.696;

% Filter Data
dt=t(2)-t(1);
fs=1/dt;
nyq=fs/2;
wn=[10/nyq,4500/nyq];
```

216

```
[B,A] = BUTTER(3,wn);

d_101_f = filter(B,A,d_101);
d_103_f = filter(B,A,d_103);
d_112_f = filter(B,A,d_112);
d_113_f = filter(B,A,d_113);
d_115_f = filter(B,A,d_115);
d_123_f = filter(B,A,d_123);
d_124_f = filter(B,A,d_124);
d_138_f = filter(B,A,d_138);
d_139_f = filter(B,A,d_139);
d_140_f = filter(B,A,d_140);
d_141_f = filter(B,A,d_141);

% Build Velocity Windowed data
d_vel=250;
j=1;
vel_i=vel(1);
for i=1:numel(vel),
    if (vel(i)-vel_i)>d_vel,
        index(j)=i;
        j=j+1;
        vel_i=vel(i);
    end
end

index_vel_end=j;

for i=1:index_vel_end-2,
    vel_a(i)=mean(vel(index(i):index(i+1)));
  d_101_f_std(i)=std(d_101_f(index(i):index(i+1)));
  d_103_f_std(i)=std(d_103_f(index(i):index(i+1)));
  d_112_f_std(i)=std(d_112_f(index(i):index(i+1)));
  d_113_f_std(i)=std(d_113_f(index(i):index(i+1)));
  d_115_f_std(i)=std(d_115_f(index(i):index(i+1)));
  d_123_f_std(i)=std(d_123_f(index(i):index(i+1)));
  d_124_f_std(i)=std(d_124_f(index(i):index(i+1)));
  d_138_f_std(i)=std(d_138_f(index(i):index(i+1)));
  d_139_f_std(i)=std(d_139_f(index(i):index(i+1)));
  d_140_f_std(i)=std(d_140_f(index(i):index(i+1)));
  d_141_f_std(i)=std(d_141_f(index(i):index(i+1)));
    dum_101=sort(abs(d_101_f(index(i):index(i+1))),'
descend');
    dum_103=sort(abs(d_103_f(index(i):index(i+1))),'
descend');
```

217

```
dum_112=sort(abs(d_112_f(index(i):index(i+1)))),
'descend');

dum_113=sort(abs(d_113_f(index(i):index(i+1)))),
'descend');
dum_115=sort(abs(d_115_f(index(i):index(i+1)))),
'descend');
dum_123=sort(abs(d_123_f(index(i):index(i+1)))),
'descend');
dum_124=sort(abs(d_124_f(index(i):index(i+1)))),
'descend');
dum_138=sort(abs(d_138_f(index(i):index(i+1)))),
'descend');
dum_139=sort(abs(d_139_f(index(i):index(i+1)))),
'descend');
dum_140=sort(abs(d_140_f(index(i):index(i+1)))),
'descend');
dum_141=sort(abs(d_141_f(index(i):index(i+1)))),
'descend');

d_101_f_p1(i)=dum_101(1);
d_103_f_p1(i)=dum_103(1);
d_112_f_p1(i)=dum_112(1);
d_113_f_p1(i)=dum_113(1);
d_115_f_p1(i)=dum_115(1);
d_123_f_p1(i)=dum_123(1);
d_124_f_p1(i)=dum_124(1);
d_138_f_p1(i)=dum_138(1);
d_139_f_p1(i)=dum_139(1);
d_140_f_p1(i)=dum_140(1);
d_141_f_p1(i)=dum_141(1);

d_101_f_p2(i)=dum_101(2);
d_103_f_p2(i)=dum_103(2);
d_112_f_p2(i)=dum_112(2);
d_113_f_p2(i)=dum_113(2);
d_115_f_p2(i)=dum_115(2);
d_123_f_p2(i)=dum_123(2);
d_124_f_p2(i)=dum_124(2);
d_138_f_p2(i)=dum_138(2);
d_139_f_p2(i)=dum_139(2);
d_140_f_p2(i)=dum_140(2);
d_141_f_p2(i)=dum_141(2);
end
```

```matlab
% Frequency analysis
[P_101_f,F_101] =
PWELCH(d_101_f(1:8600),[],[],[],fs);
[P_103_f,F_103] =
PWELCH(d_103_f(1:13000),[],[],[],fs);
[P_112_f,F_112] =
PWELCH(d_112_f(1:13000),[],[],[],fs);
[P_113_f,F_113] =
PWELCH(d_113_f(1:13000),[],[],[],fs);
[P_115_f,F_115] =
PWELCH(d_115_f(1:13000),[],[],[],fs);
[P_123_f,F_123] =
PWELCH(d_123_f(1:13000),[],[],[],fs);
[P_124_f,F_124] =
PWELCH(d_124_f(1:13000),[],[],[],fs);
[P_138_f,F_138] =
PWELCH(d_138_f(1:13000),[],[],[],fs);
[P_139_f,F_139] =
PWELCH(d_139_f(1:13000),[],[],[],fs);
[P_140_f,F_140] =
PWELCH(d_140_f(1:13000),[],[],[],fs);
[P_141_f,F_141] =
PWELCH(d_141_f(1:13000),[],[],[],fs);

% Export data
fid = fopen('d_101_psd_dads.txt','w');
fprintf(fid,'%6.4f   %12.6f\n',[F_101,P_101_f]');
fid = fopen('d_103_psd_dads.txt','w');
fprintf(fid,'%6.4f   %12.6f\n',[F_103,P_103_f]');
fid = fopen('d_112_psd_dads.txt','w');
fprintf(fid,'%6.4f   %12.6f\n',[F_112,P_112_f]');
fid = fopen('d_113_psd_dads.txt','w');
fprintf(fid,'%6.4f   %12.6f\n',[F_113,P_113_f]');
fid = fopen('d_115_psd_dads.txt','w');
fprintf(fid,'%6.4f   %12.6f\n',[F_115,P_115_f]');
fid = fopen('d_123_psd_dads.txt','w');
fprintf(fid,'%6.4f   %12.6f\n',[F_123,P_123_f]');
fid = fopen('d_124_psd_dads.txt','w');
fprintf(fid,'%6.4f   %12.6f\n',[F_124,P_124_f]');
fid = fopen('d_138_psd_dads.txt','w');
fprintf(fid,'%6.4f   %12.6f\n',[F_138,P_138_f]');
fid = fopen('d_139_psd_dads.txt','w');
fprintf(fid,'%6.4f   %12.6f\n',[F_139,P_139_f]');
fid = fopen('d_140_psd_dads.txt','w');
fprintf(fid,'%6.4f   %12.6f\n',[F_140,P_140_f]');
```

```
fid = fopen('d_141_psd_dads.txt','w');
fprintf(fid,'%6.4f   %12.6f\n',[F_141,P_141_f]');

fid = fopen('d_101_f_v_dads.txt','w');
fprintf(fid,'%6.4f   %12.6f %12.6f
%12.6f\n',[vel_a',d_101_f_std',d_101_f_p1',d_101_f_
p2']');
fid = fopen('d_103_f_v_dads.txt','w');
fprintf(fid,'%6.4f   %12.6f %12.6f
%12.6f\n',[vel_a',d_103_f_std',d_103_f_p1',d_103_f_
p2']');
fid = fopen('d_112_f_v_dads.txt','w');
fprintf(fid,'%6.4f   %12.6f %12.6f
%12.6f\n',[vel_a',d_112_f_std',d_112_f_p1',d_112_f_
p2']');
fid = fopen('d_113_f_v_dads.txt','w');
fprintf(fid,'%6.4f   %12.6f %12.6f
%12.6f\n',[vel_a',d_113_f_std',d_113_f_p1',d_113_f_
p2']');
fid = fopen('d_115_f_v_dads.txt','w');
fprintf(fid,'%6.4f   %12.6f %12.6f
%12.6f\n',[vel_a',d_115_f_std',d_115_f_p1',d_115_f_
p2']');
fid = fopen('d_123_f_v_dads.txt','w');
fprintf(fid,'%6.4f   %12.6f %12.6f
%12.6f\n',[vel_a',d_123_f_std',d_123_f_p1',d_123_f_
p2']');
fid = fopen('d_124_f_v_dads.txt','w');
fprintf(fid,'%6.4f   %12.6f %12.6f
%12.6f\n',[vel_a',d_124_f_std',d_124_f_p1',d_124_f_
p2']');
fid = fopen('d_138_f_v_dads.txt','w');
fprintf(fid,'%6.4f   %12.6f %12.6f
%12.6f\n',[vel_a',d_138_f_std',d_138_f_p1',d_138_f_
p2']');
fid = fopen('d_139_f_v_dads.txt','w');
fprintf(fid,'%6.4f   %12.6f %12.6f
%12.6f\n',[vel_a',d_139_f_std',d_139_f_p1',d_139_f_
p2']');
fid = fopen('d_140_f_v_dads.txt','w');
fprintf(fid,'%6.4f   %12.6f %12.6f
%12.6f\n',[vel_a',d_140_f_std',d_140_f_p1',d_140_f_
p2']');
fid = fopen('d_141_f_v_dads.txt','w');
fprintf(fid,'%6.4f   %12.6f %12.6f
```

```
%12.6f\n',[vel_a',d_141_f_std',d_141_f_p1',d_141_f_
p2']');

fid = fopen('d_101_f_dads.txt','w');
fprintf(fid,'%6.4f %6.4f
%12.6f\n',[t,vel,d_101_f]');
fid = fopen('d_103_f_dads.txt','w');
fprintf(fid,'%6.4f %6.4f
%12.6f\n',[t,vel,d_103_f]');
fid = fopen('d_112_f_dads.txt','w');
fprintf(fid,'%6.4f %6.4f
%12.6f\n',[t,vel,d_112_f]');
fid = fopen('d_113_f_dads.txt','w');
fprintf(fid,'%6.4f %6.4f
%12.6f\n',[t,vel,d_113_f]');
fid = fopen('d_115_f_dads.txt','w');
fprintf(fid,'%6.4f %6.4f
%12.6f\n',[t,vel,d_115_f]');
fid = fopen('d_123_f_dads.txt','w');
fprintf(fid,'%6.4f %6.4f
%12.6f\n',[t,vel,d_123_f]');
fid = fopen('d_124_f_dads.txt','w');
fprintf(fid,'%6.4f %6.4f
%12.6f\n',[t,vel,d_124_f]');
fid = fopen('d_138_f_dads.txt','w');
fprintf(fid,'%6.4f %6.4f
%12.6f\n',[t,vel,d_138_f]');
fid = fopen('d_139_f_dads.txt','w');
fprintf(fid,'%6.4f %6.4f
%12.6f\n',[t,vel,d_139_f]');
fid = fopen('d_140_f_dads.txt','w');
fprintf(fid,'%6.4f %6.4f
%12.6f\n',[t,vel,d_140_f]');
fid = fopen('d_141_f_dads.txt','w');
fprintf(fid,'%6.4f %6.4f
%12.6f\n',[t,vel,d_141_f]');

fclose('all')
```

Published with MATLAB® 7.0

data_plot.m Data Plotting Script for basic data overlay of DADS and Test

Data

```matlab
clear all

% Plot ?
pl=1;

% Variable array
name=[101,103,112,113,115,123,124,138,139,140,141];

% Load and plot file data
for i=1:numel(name),
  % Velocity Data for Plots of DADS and Mission
  filename=['d_',num2str(name(i)),'_f_dads.txt'];
  d1=load(filename);
  x2_d(:,i)=d1(:,2);y5_d(:,i)=d1(:,3);

  filename=['d_',num2str(name(i)),'_f.txt'];
  d2=load(filename);
  x2(:,i)=d2(:,2);y5(:,i)=d2(:,3);

  % Mean and STD Data for Plots of DADS and Mission

  filename=['d_',num2str(name(i)),'_psd_dads.txt'];
  d3=load(filename);
  x_d(:,i)=d3(:,1);y_d(:,i)=d3(:,2);

  filename=['d_',num2str(name(i)),'_psd.txt'];
  d4=load(filename);
  x(:,i)=d4(:,1);y(:,i)=d4(:,2);

  % PSD data for Plots of DADS and Mission
  filename=['d_',num2str(name(i)),'_f_v_dads.txt'];
  d5=load(filename);
  x1_d(:,i)=d5(:,1);y1_d(:,i)=d5(:,2);
  y2_d(:,i)=d5(:,3);y3_d(:,i)=d5(:,4);

  filename=['d_',num2str(name(i)),'_f_v.txt'];
  d6=load(filename);
  x1(:,i)=d6(:,1);y1(:,i)=d6(:,2);
  y2(:,i)=d6(:,3);y3(:,i)=d6(:,4);

  fclose('all');
```

```
if pl,
   figure,subplot(2,1,1),
   plot(x2_d(:,i),y5_d(:,i),'b',x2(:,i),y5(:,i),'r
   '),legend('DADS','Mission data'),
   xlabel('Velocity (fps)'),
   ylabel('Unit'),title(num2str(name(i)));
   hold on,
   subplot(2,1,2),plot(x1_d(:,i),y1_d(:,i),'b',x1_
   d(:,i),y2_d(:,i),'b+',x1_d(:,i),y3_d(:,i),'b+',
   x1(:,i),y1(:,i),'r',x1(:,i),y2(:,i),'r+',x1(:,i
   ),y3(:,i),'r+'),
   legend('DADS STD','DADS Max','DADS
   Min','Mission data','Mission Max','Mission
   Min'),
   xlabel('Vel (fps)'),
   ylabel('Unit'),title(num2str(name(i)));

   figure,plot(x_d(:,i),y_d(:,i),'b',x(:,i),y(:,i)
   ,'r'),
   legend('DADS','Mission data'),
   xlabel('Freq (Hz)'),
   ylabel('Unit^2/Hz'),title(num2str(name(i)));
   end
   clear x
   clear y
   clear x_d
   clear y_d
end
```

Published with MATLAB® 7.0

APPENDIX D

MATLAB PARAMETER VARIATION DATA PROCESSING

SCRIPTS

```matlab
function []=param_proc(filename,plot_out)
% param_proc(filename,plot) where filename is a string
% and must be entered using single quotes --> 'filename'
% plot --> plot option
% This function is designed to process data from the
% parameter variations filtering, then rearranging the
% data into velocity windowed format
% Finally the data is written into *.txt files.
% This script does not perform any data decimation
% S Furlow

if filename=='2222222',
    dads_head_off(filename);
else
    dads_head_off_dat(filename);
end

if filename(1,7)=='2',
    effective_weight=719.043
    % sled weight (lbf) being acted upon by eta forces
elseif filename(1,7)=='3',
    effective_weight=1177.863
    % sled weight (lbf) being acted upon by eta forces
elseif filename(1,7)=='1',
    effective_weight=260.213
    % sled weight (lbf) being acted upon by eta forces
else
    disp('Error in file input: file not recognized')
end


% Open no header file and process data
data=load(strcat(filename,'_nh.dat'));


% Assign data more meaningful names
t=data(:,1);
velocity=data(:,2);
fy_s_aft_rt_in=data(:,3);
fy_s_aft_rt_out=data(:,4);
fy_s_aft_lt_out=data(:,5);
```

225

```
fy_s_aft_lt_in=data(:,5);
fy_s_aft_lt_in=data(:,6);
fy_s_frt_rt_in=data(:,7);
fy_s_frt_rt_out=data(:,8);
fy_s_frt_lt_out=data(:,9);
fy_s_frt_lt_in=data(:,10);
fx_s_frt_rt_out=data(:,11);
fx_s_frt_rt_in=data(:,12);
fx_s_frt_lt_out=data(:,13);
fx_s_frt_lt_in=data(:,14);
fx_s_aft_rt_out=data(:,15);
fx_s_aft_rt_in=data(:,16);
fx_s_aft_lt_out=data(:,17);
fx_s_aft_lt_in=data(:,18);
m_xx=data(:,19);
m_yy=data(:,20);
m_zz=data(:,21);

% Filter Data
dt=t(2)-t(1);
fs=1/dt;
nyq=fs/2;
wn=[10/nyq,0.9];
[B,A] = BUTTER(3,wn);

fy_s_aft_rt_in_f=
filter(B,A,fy_s_aft_rt_in);%fy_s_aft_rt_in
fy_s_aft_rt_out_f =
filter(B,A,fy_s_aft_rt_out);%fy_s_aft_rt_out
fy_s_aft_lt_out_f =
filter(B,A,fy_s_aft_lt_out);%fy_s_aft_lt_out
fy_s_aft_lt_in_f =
filter(B,A,fy_s_aft_lt_in);%fy_s_aft_lt_in
fy_s_frt_rt_in_f =
filter(B,A,fy_s_frt_rt_in);%fy_s_frt_rt_in
fy_s_frt_rt_out_f =
filter(B,A,fy_s_frt_rt_out);%fy_s_frt_rt_out
fy_s_frt_lt_out_f =
filter(B,A,fy_s_frt_lt_out);%fy_s_frt_lt_out
fy_s_frt_lt_in_f =
filter(B,A,fy_s_frt_lt_in);%fy_s_frt_lt_in
fx_s_frt_rt_out_f =
filter(B,A,fx_s_frt_rt_out);%fx_s_frt_rt_out
fx_s_frt_rt_in_f =
filter(B,A,fx_s_frt_rt_in);%fx_s_frt_rt_in
```

226

```matlab
fx_s_frt_lt_out_f =
filter(B,A,fx_s_frt_lt_out);%fx_s_frt_lt_out
fx_s_frt_lt_in_f =
filter(B,A,fx_s_frt_lt_in);%fx_s_frt_lt_in
fx_s_aft_rt_out_f =
filter(B,A,fx_s_aft_rt_out);%fx_s_aft_rt_out
fx_s_aft_rt_in_f =
filter(B,A,fx_s_aft_rt_in);%fx_s_aft_rt_in
fx_s_aft_lt_out_f =
filter(B,A,fx_s_aft_lt_out);%fx_s_aft_lt_out
fx_s_aft_lt_in_f =
filter(B,A,fx_s_aft_lt_in);%fx_s_aft_lt_in
m_xx_f = filter(B,A,m_xx);%m_xx
m_yy_f = filter(B,A,m_yy);%m_yy
m_zz_f = filter(B,A,m_zz);%m_zz

% Construct Slipper reaction forces
% Vertical Aft
fy_s_aft_rt=fy_s_aft_rt_in_f+fy_s_aft_rt_out_f;
fy_s_aft_lt=fy_s_aft_lt_out_f+fy_s_aft_lt_in_f;

fy_s_aft=fy_s_aft_rt+fy_s_aft_lt;

% Vertical Front
fy_s_frt_rt=fy_s_frt_rt_in_f+fy_s_frt_rt_out_f;
fy_s_frt_lt=fy_s_frt_lt_out_f+fy_s_frt_lt_in_f;

fy_s_frt=fy_s_frt_rt+fy_s_frt_lt;

% Vertical total
fy_s=fy_s_aft+fy_s_frt;

% Lateral Front
fx_s_frt_rt=fx_s_frt_rt_out_f+fx_s_frt_rt_in_f;
fx_s_frt_lt=fx_s_frt_lt_out_f+fx_s_frt_lt_in_f;

fx_s_frt=fx_s_frt_rt+fx_s_frt_lt;

% Lateral Aft
fx_s_aft_rt=fx_s_aft_rt_out_f+fx_s_aft_rt_in_f;
fx_s_aft_lt=fx_s_aft_lt_out_f+fx_s_aft_lt_in_f;

fx_s_aft=fx_s_aft_rt+fx_s_aft_lt;

% Lateral Total
```

```matlab
fx_s=fx_s_frt+fx_s_aft;

% eta formation
% Sled being acted upon by eta consists of sled body and
% slipper beams and weighs
% Vertical
eta_v=fy_s./effective_weight;
eta_l=fx_s./effective_weight;

% Build Velocity Windowed data
d_vel=250;
j=1;
vel_i=velocity(1);
index(j)=1;
for i=1:numel(velocity),
    if (velocity(i)-vel_i)>=d_vel,
        j=j+1;
        index(j)=i;
        vel_i=velocity(i);
    end
end

index_vel_end=j;

for i=1:index_vel_end-1,

    vel_a(i)=mean(velocity(index(i):index(i+1)));

    eta_v_std(i)=3*std(eta_v(index(i):index(i+1)));
    eta_l_std(i)=3*std(eta_l(index(i):index(i+1)));
    m_xx_f_std(i)=3*std(m_xx_f(index(i):index(i+1)));
    m_yy_f_std(i)=3*std(m_yy_f(index(i):index(i+1)));
    m_zz_f_std(i)=3*std(m_zz_f(index(i):index(i+1)));

    eta_v_p(i)=max(abs(eta_v(index(i):index(i+1))));
    eta_l_p(i)=max(abs(eta_l(index(i):index(i+1))));
    m_xx_f_p(i)=max(abs(m_xx_f(index(i):index(i+1))));
    m_yy_f_p(i)=max(abs(m_yy_f(index(i):index(i+1))));
    m_zz_f_p(i)=max(abs(m_zz_f(index(i):index(i+1))));

end


% Build envelope curve for data
% Build on vertical data first
```

```
j=1;
peak_eta_v(1)=0;
% force the zero-zero condition at zero velocity
peak_vel_v(1)=0;
index(1)=1;
dum_slope=0;
eta_v_p(1)=mean([0.0000,eta_v_p(2)]);
% this step removes the artifical peak at low velocity
for i=2:numel(eta_v_p),
    if
slope(eta_v_p(i),vel_a(i),eta_v_p(index(j)),vel_a(index(j
)))>=dum_slope,
        j=j+1;
        index(j)=i;
        peak_eta_v(j)=eta_v_p(i);
        peak_vel_v(j)=vel_a(i);
    end
end
if eta_v_p(i)<peak_eta_v(j),
    peak_eta_v(j+1)=peak_eta_v(j); % Plateau for the
remainder of the velocity
    peak_vel_v(j+1)=vel_a(i);
end

% Build on lateral data next
j=1;
peak_eta_l(1)=0;
% force the zero-zero condition at zero velocity
peak_vel_l(1)=0;
index(1)=1;
dum_slope=0;
eta_l_p(1)=mean([0.0000,eta_l_p(2)]);
% this step removes the artifical peak at low velocity
for i=2:numel(eta_l_p),
    if
slope(eta_l_p(i),vel_a(i),eta_l_p(index(j)),vel_a(index(j
)))>=dum_slope,
        j=j+1;
        index(j)=i;
        peak_eta_l(j)=eta_l_p(i);
        peak_vel_l(j)=vel_a(i);
    end
end
if eta_l_p(i)<peak_eta_l(j),
    peak_eta_l(j+1)=peak_eta_l(j);
```

229

```
        % Plateau for the remainder of the velocity
        peak_vel_l(j+1)=vel_a(i);
end

% Write Piecewise linear envelope function based on peak
% values to account for all velocity values as found in
% vel_a
j=2;y2v=peak_eta_v(j);,x2v=peak_vel_v(j);y1v=peak_eta_v(j
-1);x1v=peak_vel_v(j-1);sl_v=slope(y2v,x2v,y1v,x1v)
k=2;y2l=peak_eta_l(k);x2l=peak_vel_l(k);y1l=peak_eta_l(k-
1);x1l=peak_vel_l(k-1);sl_l=slope(y2l,x2l,y1l,x1l);
for i=1:numel(vel_a),
    if vel_a(i)==peak_vel_v(j)&i~=numel(vel_a),
        j=j+1;
        y2v=peak_eta_v(j);x2v=peak_vel_v(j);
        y1v=peak_eta_v(j-1);x1v=peak_vel_v(j-1);
        sl_v=slope(y2v,x2v,y1v,x1v);
    end
    if vel_a(i)==peak_vel_l(k)&i~=numel(vel_a),
        k=k+1;
        y2l=peak_eta_l(k);x2l=peak_vel_l(k);
        y1l=peak_eta_l(k-1);x1l=peak_vel_l(k-1);
        sl_l=slope(y2l,x2l,y1l,x1l);
    end
    eta_v_out(i)=sl_v*(vel_a(i)-x1v)+y1v;
    eta_l_out(i)=sl_l*(vel_a(i)-x1l)+y1l;
end

% Prepare data for output and plot against peak curves
% and lambda, check
% plot option variable
eta_vel_out=vel_a;
if plot_out,
    lam_v=.008*eta_vel_out;
    lam_l=0.6*.008*eta_vel_out;
    figure,plot(vel_a,eta_v_p,'b-
',peak_vel_v,peak_eta_v,'r--')
    hold on,plot(eta_vel_out,eta_v_out,'k-
',eta_vel_out,lam_v,'r+'),title(strcat(filename,'_Vertica
l')),xlabel('Velocity (fps)'),ylabel('Factor (G)')
    figure,plot(vel_a,eta_l_p,'b-
',peak_vel_l,peak_eta_l,'r--')
    hold on,plot(eta_vel_out,eta_l_out,'k-
',eta_vel_out,lam_l,'r+'),title(strcat(filename,'_Lateral
')),xlabel('Velocity (fps)'),ylabel('Factor (G)')
```

```
end

% Output data to file
sf=size(filename);
for i=1:sf(1,2),
    num_index(1,i)=str2num(filename(1,i));
end

fid=fopen(strcat(filename,'.vef'),'w');
fprintf(fid,'%f %f %f
\n',[0.00000000;0.00000000;0.00000000]);
fid2=fopen(strcat(filename,'.eta'),'w');
[param_value]=param_ident(num_index);
write_out=[param_value(1,1);param_value(1,2);param_value(
1,3);param_value(1,4);param_value(1,5);param_value(1,6);p
aram_value(1,7);0.00000000;0.00000000;0.00000000;0.000000
00;0.00000000];
fprintf(fid2,'%f %f %f %f %f %f %f %f %f %f %f %f
\n',write_out);
dd=size(eta_vel_out)
for j=1:dd(1,1),
    fprintf(fid,'%f %f %f
\n',[eta_vel_out(j,:);eta_v_out(j,:);eta_v_out(j,:)*effec
tive_weight]);

end
fclose(fid);

for j=1:dd(1,2),

write_out=[param_value(1,1);param_value(1,2);param_value(
1,3);param_value(1,4);param_value(1,5);param_value(1,6);p
aram_value(1,7);eta_vel_out(1,j);eta_v_out(1,j);eta_l_out
(1,j);eta_v_out(1,j)*effective_weight;eta_l_out(1,j)*effe
ctive_weight];
    fprintf(fid2,'%f %f %f %f %f %f %f %f %f %f %f %f
\n',write_out);
end
fclose(fid2);
j

fid=fopen(strcat(filename,'.lef'),'w');
fprintf(fid,'%f %f %f
\n',[0.00000000;0.00000000;0.00000000]);
dd=size(eta_vel_out);
```

```
for j=1:dd(1,1),
    fprintf(fid,'%f %f %f
\n',[eta_vel_out(j,:);eta_l_out(j,:);eta_l_out(j,:)*effec
tive_weight]);
end

 fclose(fid);
```

REFERENCES

846th Test Squadron (2006). *SQUADRON OPERATING INSTRUCTION 10-3*. Holloman AFB, NM: Author.

846th Test Squadron (2003). *SRR FOREBODY FINAL ASSEMBLY, Engineering Drawing Layout*. Holloman AFB, NM: Author.

Abbot, P. W. (1967). "Vibration Environment of the Holloman Impact Test Sled (HIT) Second Stage", ATM NO 348-44.1-6, 6585th Test Group Holloman AFB, NM.

Baker, W. E. and Turnbull, D. A. (1999). "Track Response to Simulated Slipper Impacts" Report from Mixon Technologies Inc. under Contract #F08635-99-C-0023.

Cinnamon, J. D. (2006). "Analysis and Simulation of Hypervelocity Gouging Impacts", Doctoral Dissertation, Air Force Institute of Technology.

Department of Defense. (2003). "Metallic Materials and Elements for Aerospace Vehicle Structures: MIL-HDBK-5J" Department of Defense Handbook.

Eskridge, S. E. (1998). "Development of Consistent Nonlinear Models of Flexible Body Systems", Master's Thesis, Texas Tech University.

Furlow, J. S. (2006a). "DADS Contact Formulation Using PRONTO FEM Results", *Southern New Mexico Technology Symposium,* 20 Apr 2006, Alamogordo, NM.

Furlow, J. S. (2006b). "Dynamic Data Comparison of a Narrow Gauge Sled: Numerical Data vs Test Data", *Southern New Mexico Technology Symposium,* 20 Apr 2006, Alamogordo, NM .

Furlow, J. S. (2004). "DADS Flexible Body Formulation Study" Engineering Seminar, Holloman High Speed Test Track, Oct 2004.

General Plastics Manufacturing Company (2000). *Shock Mitigation Using Last-A-Foam High Density Flexible Foams*. Tacoma, WA: Author.

Graf, K. F., Mahig, J., Wu, T. S., Barnes, R. A., Kowal, C. R. (1966). "Study of Track Failure Criteria", Report from The Ohio State University Research Foundation under USAF Contract No. AF 29(600)-5178.

Greenbaum, G. A., Garner, T. N., and Platus, D. L. (1973). "Development of Sled Structural Design Procedures", AFSWC-TR-73-22, 6585th Test Group, Holloman AFB, NM.

Gruttmann, F. and Wagner W. (2001). Shear Correction Factors in Timoshenko's Beam Theory for Arbitrary Shaped Cross-Sections, *Computational Mechanics, 27,* 199-207.

Haug, E. J. (1989). *Computer Aided Kinetics and Dynamics of Mechanical Systems, Volume I: Basic Methods*. Boston: Allyn and Bacon.

Herakovich, C. T. (1998). *Mechanics of Fibrous Composites*. New York: John Wiley and Sons Inc.

Hooser, C. D. (1989). "Narrow-Gage Rocket Sled Design Criteria Investigation", Master's Thesis, New Mexico State University, 1989.

Hooser, M. D. (2002a). "Rail and Deflection During the 80X-F1 HUP Sled Run", Holloman High Speed Test Track Technical Report, 12 June 2002.

Hooser, M. D. (2002b). "The Holloman High Speed Test Track Gone Soft: Recent Advances in Hypersonic Test Track Vibration Environment", *21st AIAA Aerodynamic Measurement Technology and Ground Testing Conference*, St. Louis, MO, AIAA 2002-3035.

Hooser, M. D. (2000). "Simulation of a 10,000 Foot per Second Ground Vehicle", *21st AIAA Advanced Measurement Technology and Ground Testing Conference*, 19-22 June 2000, Denver, CO, AIAA 2000-2290.

Hooser, M. D. and Mixon L. C. (2000). "Comparison of Sled Impact Momentum and Rail Momentum", Holloman High Speed Test Track Technical Report, 1 March 2000.

Hooser, M. D. and Mixon L. C. (1998). "Rail Modal Tests", Holloman High Speed Test Track Technical Report, 6 April 1998.

Hooser, M. D. and Schwing, A. (2000). "Validation of Dynamic Simulation Techniques at the Holloman High Speed Test Track", *38th Aerospace Sciences and Meeting Exhibit*, 10-13 January 2000, Reno, NV, AIAA 2000-0155.

ISTRACON Handbook, (1961). Istracon Report No. 60-1, Interstation Supersonic Track Conference, Structures Working Group, Air Force Systems Command. Holloman Air Force Base: Printing & Publications Distribution Division, AFMDC.

Krupovage, D. J., Mixon, L. C., and Bush, J. D. (1985). "Design Manual for Dual Rail, Narrow Gage, and Monorail Rocket Sleds", Holloman High Speed Test Track.

Krupovage, D. J., Mixon, L. C., and Bush, J. D. (1991). "Design Manual for Dual Rail, Narrow Gage, and Monorail Rocket Sleds Revised", Holloman High Speed Test Track.

Leadingham M. A. and Schauer S. A. (2001). *Data Report for the Hypersonic Upgrade Program (HUP) Super Roadrunner Over/Under (SRR O/U)*, 08 February 2001.

LMS CADSI. (1999). *DADS/Flex Manual*. Coralville, IA: Author.

LMS CADSI. (2004). *DADS Reference Manual*. Coralville, IA: Author.

Minto, D. W. (2004). "CTEIP Funded Advances in Hypersonic Testing at The Holloman High Speed Test Track", *24th AIAA Aerodynamic Measurement Technology and Ground Testing Conference*, Portland, OR, AIAA-2004-2740.

Minto, D. W. (2002). "The Holloman High Speed Test Track Hypersonic Upgrade Program Status", *22nd AIAA Aerodynamic Measurement Technology and Ground Testing Conference*, St. Louis, MO, AIAA-2002-3034.

Minto, D. W. (2000). "Recent Increase in Hypersonic Test Capabilities at the Holloman High Speed Test Track", *38th Aerospace Sciences Meeting & Exhibit*, Reno, NV, AIAA-2000-0154.

Mixon, L. C. (2006). Personal Communication. Holloman AFB, NM. 8 August 2006.

Mixon, L. C. (2002a). *Technical Report: Independent Analysis of the 6 Pupfish Pusher Lateral Isolation System* (Contract# F08635-99-C-0023), 23 January 2002.

Mixon, L. C. (2002b). *Technical Report: Super Roadrunner Composite Case Modal Test Report* (Contract# F08635-99-C-0023), 1 February 2002.

Mixon, L. C. (1999a). *Technical Report: Initial Nike and SRR DADS Modeling Parameters* (Contract# F08635-99-C-0023), 01 June 1999.

Mixon, L. C. (1999b). *Technical Report: Design for Flexibility and Not Strength* (Contract# F08635-99-C-0023), 01 September 1999.

Mixon, L. C. (1999c). *Technical Report: Draft Loads Study on the 6 Pupfish Narrow Gage Pusher Sled* (Contract# F08635-99-C-0023), 01 December 1999.

Mixon, L. C. (1971). "Sled Design Techniques", AFSWC-TR-71-3, 6585th Test Group, Holloman AFB, NM, Feb 1971.

Mixon, L. C. and Hooser, C. D. (2002). *Technical Report: PAC3 Long Body Program Failure Analysis* (Contract# F08635-99-C-0023), 2 September 2002.

Nedimovic, P. H. (2004). "Dynamic Load Analysis for Design", Masters Project Report, New Mexico State University.

Przemieniecki, J. S. (1968). *Theory of Matrix Structural Analysis*. New York: McGraw Hill.

Szmerekovsky, A. G. (2004). "The Physical Understanding of the Use of Coatings to Mitigate Hypervelocity Gouging Considering Real Test Sled Dimensions", Doctoral Dissertation, Air Force Institute of Technology.

Stronge, W. J. (2000). *Impact Mechanics*. Cambridge: Cambridge University Press.

Timoshenko, S. P., Young, D. H. and Weaver, W. (1974). *Vibration Problems in Engineering*. New York John Wiley and Sons.

Tischler, V. A., Venkayya, V. B., and Palazotto, A. N. (1981). "Dynamic Analysis of High Speed Rocekt Sleds", *ASME Design Engineering Technical Conference*, Hartford, CN, 81-DET-42.

Turnbull D. A. and Minto D. W. (2003). *Data Report for the Hypersonic Upgrade Program (HUP) Super Roadrunner Over/Under (SRR O/U) Record Sled Land-Speed & Payload-Energy Test*, 20 May 2003.

Unigraphics Solutions Inc. (2002) *I-DEAS User's Guide*, Plano, TX: Author.

White, F. M. (1994). *Fluid Mechanics* (3rd ed.). New York: McGraw-Hill, Inc.

Volk, W. (1958). *Applied Statistics for Engineers*. New York: McGraw-Hill Book Company, Inc.

Zukas, J. A., Nicholas, T., Swift, H. F., Greszczuk, L, B. (1982). *Impact Dynamics*. New York: John Wiley and Sons.